Stony Brook University

Synthesis, characterization, and morphology-dependent investigation of 0D and 1D formulations of various classes of nanomaterials

A Dissertation Presented

by

Hongjun Zhou

to

The Graduate School

in Partial Fulfillment of the

Requirements

for the Degree of

Doctor of Philosophy

in

Chemistry

Stony Brook University

August 2009

Stony Brook University

The Graduate School

Hongjun Zhou

We, the dissertation committee for the above candidate for the

Doctor of Philosophy degree,

hereby recommend acceptance of this dissertation.

Professor Stanislaus S. Wong - Dissertation Advisor

Associate Professor, Department of Chemistry

Professor Joseph W. Lauher - Chairperson of Defense

Professor, Department of Chemistry

Professor Philip M. Johnson - Third Member of Academic Committee

Professor, Department of Chemistry

Dr. Radoslav Azdic - Outside Member

Senior Chemist, Department of Chemistry,

Brookhaven National Laboratory

This dissertation is accepted by the Graduate School

Lawrence Martin

Dean of the Graduate School

Abstract of the Dissertation

Synthesis, characterization, and morphology-dependent investigation of 0D and 1D formulations of various classes of nanomaterials

By

Hongjun Zhou

Doctor of Philosophy

In

Chemistry

Stony Brook University

2009

Nanomaterials have attracted extraordinary attention due to their unique size, shape-dependent physical properties (i.e., mechanical, optical, magnetic and electric properties). Although a tremendous amount of work has been accomplished in the field of nanoscience, there are still challenges including (i) the precise control of size, dimensionality, composition and assembly at the nanoscale, (ii) the development of an environmentally friendly, energy effective synthesis method, (iii) the rational design and fabrication of novel nanomaterials and nanocomposites, and (iv) a deep understanding of the relationship between size, shape and physical properties. In my graduate research, various classes of nanomaterials were synthesized by environmentally friendly methods and their unique properties were also explored. Specifically, the synthesis of $Bi_2Ti_2O_7$ nanotubes by sol-gel technique were discussed in Chapter II. Shape control of submicron sized $BaZrO_3$ cubes and spheres were achieved via molten salt synthesis (Chapter III). The effects of parameters selection in the molten salt synthesis of $BaZrO_3$ particles were also explored. A nontoxic, low temperature, and cost effective template method was applied to fabricating various one-dimensional nanomaterials, i.e., transition- metal oxides (ZnO, CuO, and α-Fe_2O_3 in Chapter IV), ternary-metal oxides, multiferroic $MnWO_4$ (in Chapter V), and noble metals (Ag, Au, and Pt, in Chapter VI). Finally, a multifunctional nanostructure was fabricated by the self-assembly technique (in Chapter

VII), involving building blocks such as silica nanotubes and functional nanoparticles (CdSe and Fe_3O_4). The ability to make various nanomaterials with control over uniformity, size and morphology is extremely important in the field of nanoscience and will enable many research opportunities in this area.

Dedicated to my grandfather

Table of Contents

List of Figures

List of Tables

List of Abbrevations

0D	zero-dimensional
1D	one-dimensional
2D	two-dimensional
4-CP	4-chlorophenol
AAO	anodized aluminum oxide
AFM	atomic force microscopy
ALD	atomic layer deposition
BLA	barrier layer alumina
CTAB	cetlytrimethylammonium bromide
CVD	chemical vapor deposition
DRAM	dynamic random access memory
DSSC	dye sensitized solar cell
DWCNT	double-walled carbon nanotube
EDS	energy dispersive X-ray spectroscopy
EM	electromagnetic waves
FC	field cooled
FE	field emission
FET	field emission transistors
FFT	fast Fourier transform
h	hour
HPA	hexylphosphonic acid
HRTEM	high resolution transmission electron microscopy
IR	infrared spectroscopy
JCPDS	Joint Committee on Powder Diffraction Standards
LED	light emitting diode
MCM	mobile crystalline material
MEMS	microelectromethanical
MIMIC	micromolding in capillaries
min	minute
MOS	metal oxide semiconductor
MPMS	magnetic property measurement system
MRI	magnetic resonance imaging
MSS	molten salt synthesis
MWCNT	multi-walled carbon nanotube
nm	nanometer
NPs	nanoparticles
ORR	oxygen reduction reaction

PC	polycarbonate
PDMS	polydimethylsiloxane
PGM	platinum group metal
PL	photoluminescence
PVD	physical vapor deposition
PVP	poly(vinyl pyrrolidone)
QD	quantum dot
Q-XRD	quantitative X-Ray diffraction
RDE	roating disk electrode
REM	replica molding
RHE	reversible hydrogen electrode
SAED	selected-area electron diffraction
SAMs	self assembled monolayers
SEM	scanning electron microscopy
SPM	scanning probe microscopy
SQUID	superconducting quantum interference device
STM	scanning tunneling microscopy
SWCNT	single-walled carbon nanotube
TEM	transmission electron microscopy
TEOS	tetraethyl orthosilicate
UV-Vis	ultra-violet visible
VLS	vapor-liquid-solid
XPS	X-ray photoelectron spectroscopy
XRD	X-ray diffraction
ZFC	zero field cooled
μCP	microcontact printing
μTM	microtransfer molding

Acknowledgements

Foremost, I would like to express my sincere gratitude to my advisor Professor Stanislaus S. Wong for the continuous support of my Ph.D study and research, and for his patience, guidance, motivation, enthusiasm, advice and wisdom. He provided me unflinching encouragement and support in various ways. His truly scientific intuition exceptionally inspired and enriched my growth as a student, a researcher and a scientist.

Besides my advisor, I would like to thank the rest of my committee: Professor Joseph W. Lauher and Professor Philip M. Johnson, for their encouragement, insightful comments, and help. I am also grateful to Professor Radoslav Adzic for serving in my committee as an outside member.

Many thanks go in particular to Dr. Yuanbing Mao, for his valuable advice and help when I was at the early stage of my research. I would also like to thank the members (former and current) of the Wong group: Sarbajit, Mandakini, Jingyi, Tirandai, T.-J., Fen, Alex, John, Xiaohui, Amanda, and Chris, for their help, advice and understanding.

I gratefully acknowledge the support and assistance given to me by students, faculty, and technical support during my research. To Dr. Jim Quinn (Materials Science, SUNY) and Dr. Susan van Horn (Life science, SUNY), I would like to thank for their help with electron microscopy. I am grateful to Dr. Dezhi Wang (Physics, Boston College) and Dr. Eli Sutter (CFN, BNL) for the help with high resolution microscopy, to Professor M. C. Aronson, Dr. Mikhail Feygensen and Yuen Yiu (Physics, SUNY) for their assistance with magnetic measurements, as well as to Professor Radoslav R. Adzic and Dr. Wei-Ping Zhou (Chemistry, BNL) for their work with electrochemical measurements.

Special thanks go to Chemistry Department, SUNY, where I did my Ph. D study and research. Also, I am grateful to everyone in the Main office for their valuable help.

Last but not the least, I thank my parents and parents-in law for their persistent support and understanding. And I am especially grateful for their love and care of my son, Lucas. I would also like to thank my wife, Lu, for her confidence in me, love and support. I thank my son for the happiness he brings to me every second.

List of Publications

- **H. Zhou**, J. Chen, E. Sutter, M. Feygensen, M. C. Aronson, and S. S. Wong, "Multifunctional magnetic, luminescent silica-encapsulated composite nanotubes. ", **2009**, in preparation
- S. Berweger, C. C. Neacsu, Y. Mao, **H. Zhou**, S. S. Wong, and M. B. Raschke, "Optical nanocrystallography with tip-enhanced phonon Raman spectroscopy.", *Nature Nanotechnology*, **2009,** in press
- **H. Zhou,** W. Zhou, R. Adzic, and S. S. Wong, "Enhanced electrocatalytic performance of one-dimensional metal nanorods and arrays generated via an ambient, surfactantless synthesis. ", *J. Phys. Chem. C* **2009**, 113, 5460-5466
- **H. Zhou** and S. S. Wong, "A facile, ambient synthesis of industrially relevant one-dimensional transition metal oxide nanowires and nanowire arrays." *ACS Nano*, **2008**, 2, 944-958
- **H. Zhou**; Y. Li; M. C. Aronson and S. S. Wong, "Ambient template synthesis of multiferroic $MnWO_4$ nanowires and nanowire arrays." *J. Solid State Chem.* **2008**, 181, 1539-1545
- **H. Zhou**; Y. Mao and S. S. Wong, "Probing structure-parameter correlations in the molten salt synthesis of $BaZrO_3$ perovskite submicrometer-sized particles." *Chem. Mater.* **2007,** 19, 5238-5249
- Y. Mao; T.-J. Park; F. Zhang; **H. Zhou** and S. S. Wong, "Environmentally friendly methodologies of nanostructure synthesis." *Small* **2007**, 3, 1122-1139 (invited review)
- **H. Zhou**; Y. Mao and S. S. Wong, "Shape control and spectroscopy of crystalline $BaZrO_3$ perovskite particles." *J. Mater. Chem.* **2007**, 17, 1707-1713
- **H. Zhou**; T.-J. Park and S. S. Wong, "Synthesis, characterization, and photocatalytic properties of pyrochlore $Bi_2Ti_2O_7$ nanotubes." *J. Mater. Res.* **2006**, 21, 2941-2947 (focused issue)

List of Presentations

- "Probing structure-parameter correlations in the molten salt synthesis of $BaZrO_3$ perovskite submicrometer-sized particles", oral presentation, ACS Spring, Apr. 08, New Orleans
- "A general, versatile method to synthesize 1-D transition metal oxide arrays", poster, ACS Spring, Apr. 08, New Orleans
- "Shape control and spectroscopy of crystalline $BaZrO_3$ perovskite particles." oral presentation, ACS Fall, Aug. 07, Boston
- "Synthesis, characterization and photocatalytic properties of pyrochlore $Bi_2Ti_2O_7$ nanotubes." poster, ACS Fall, Aug. 07, Boston
- "Synthesis, characterization and photocatalytic properties of pyrochlore $Bi_2Ti_2O_7$ nanotubes." poster, MRS Fall, Nov. 06, Boston
- "Synthesis and characterization of $BaZrO_3$ nanocrystals." poster, MRS Fall, Nov. 05, Boston

List of Patents

- **H. Zhou** and S. S. Wong, "Methods of controlling the morphology of perovskite submicron-sized particles.", in preparation
- **H. Zhou** and S. S. Wong, "Methods of making binary metal oxide nanostructures and methods of controlling morphology of same.", in preparation
-

Chapter I Background: Synthesis and Properties of Nanomaterials

1.1 What is nanotechnology?

"Nano" is a prefix in the SI system of units denoting a factor of 10^{-9}. It is often used in prefixing when time and length units encountered. It was confirmed in 1960 and comes from the Greek νᾶνος, meaning dwarf. When used in words such as nanotechnology or nanomaterials, it means a nanometer. A nanometer (nm) represents a distance of one-billionth of a meter. To obtain a better understanding of how small a nanometer is, Figure 1.1, which compares the size difference from a person (around 1.75 m) all the way down to a hydrogen atom (around 0.1 nm),[1] is shown.

1.1.1 Definition

The word "nanotechnology" was first introduced in the late 1970s. It is sometimes shortened to "nanotech", and refers to a field whose theme is the control of matter on the atomic and molecular scales.

Currently, there is diverse opinion as to what exactly is nanotechnology. Some believe that the synthesis of nano-sized materials constitutes nanotechnology. Some believe that the research into the microstructure of materials using electron microscopy is nanotechnology. Drug delivery, e.g., by putting drugs outside/inside carbon nanotubes, is considered as nanotechnology as well. Microelectromechanical system (MEMS) and lab-on-a-chip have at times been portrayed as nanotechnology.

Although many definitions for nanotechnology exist, most research groups use the National Nanotechnology Initiative (NNI) definition. The following defining features of nanotechnology have been hammered out:

1. Nanotechnology involves research and technology development at the 1nm-to-100nm range.

2. Nanotechnology creates and uses structures that have novel properties because of their small size.

3. Nanotechnology builds on the ability to control or manipulate at the atomic scale.

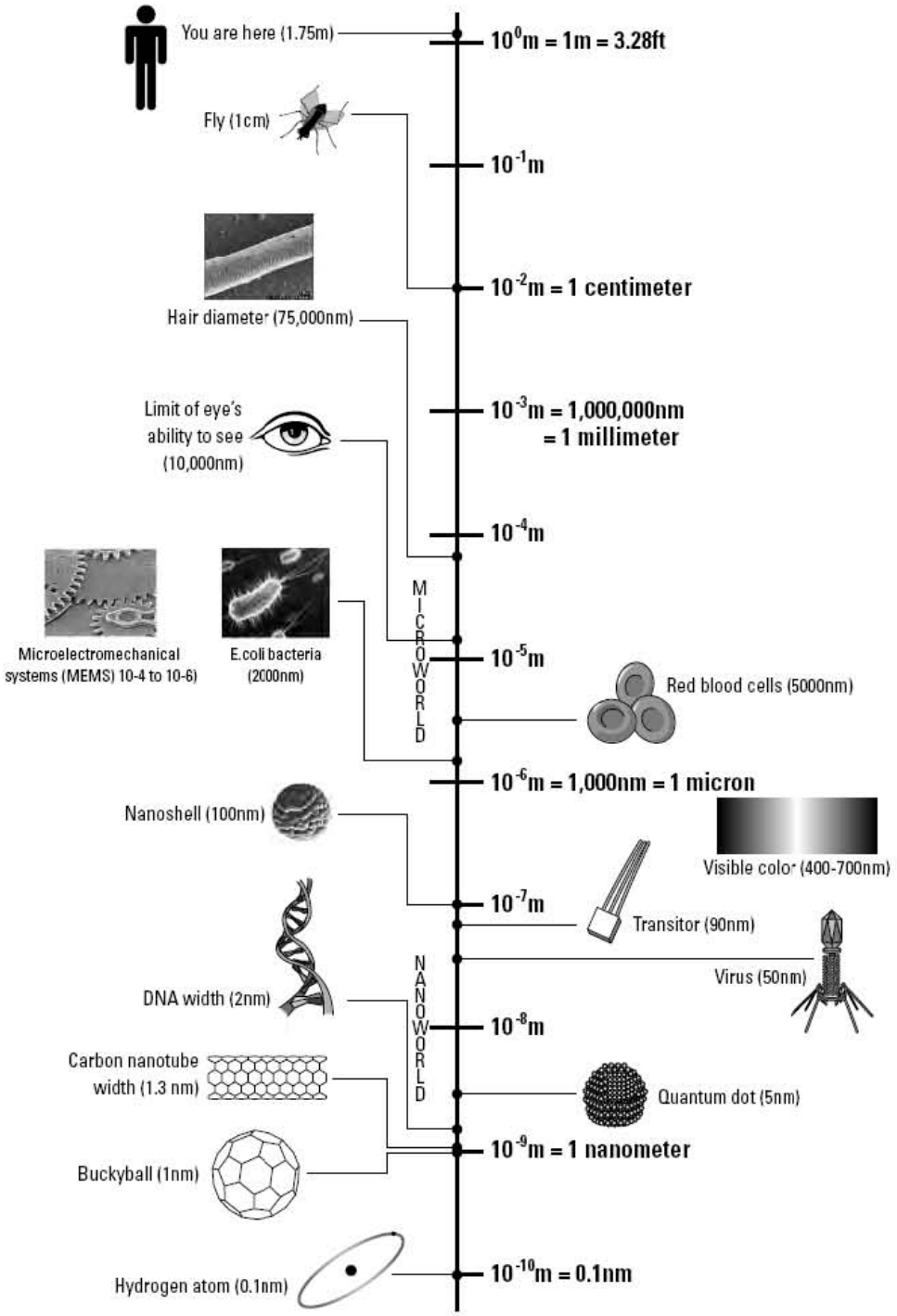

Figure 1.1 Size comparisons, from a person (measuring 1.75 meters,or approximately 5 ft. 7 in.) all the way down to the hydrogen atom (0.1 nm).[1]

In general, nanotechnology is concerned with materials and systems whose structures and components exhibit novel and significantly improved physical, chemical and biological properties, phenomena, and processes due to their nanoscale size.[2]

1.1.2 History of nanotechnology

The study of materials at the nanometer scale can be traced back for centuries, strating with the usage of gold and silver metal nanoparticles. A famous artifact from Roman Period (30 BC-640 AD) called the Lycurgus cup resides in the British Museum in London.[3, 4] What makes this cup unique is that its color changes from green (when illuminated from the outside) to red (when illuminated from within). Transmission electron microscopy (TEM) reveals that the glass contains nanoparticles of gold and silver. In the medieval period, gold and silver nanoparticles were used in stained glass so as to render them colorful (ruby red and deep yellow respectively). These metal nanoparticles have also been used to color pottery in the Renaissance.

In 1827, the first successful photograph was produced, in which silver nanoparticles were made after decomposition of silver halides by light and served as pixels of the photographic image. In 1857, Michael Faraday discovered and prepared the first metallic colloids, which were stable for almost a century before being destroyed during World War II.[5] In 1931, the first electron microscope was developed by German scientists Max Knott and Ernst Ruska, which was an important first step in the development of techniques and instrumentation that would eventually enable research at the nanoscale.[6, 7] Following this, the invention and development of field-ion electron microscopy in 1951, transmission electron microscopy (TEM), scanning tunneling microscopy (STM), and atomic force microscopy (AFM) have opened up new possibilities for the characterization, measurement, and manipulation of nanostructures and nanomaterials. In 1959, Richard P. Feynman made his famous speech, entitled "There's Plenty of Room at the Bottom.", in which he cited a number of interesting ramifications of a general ability to manipulate matter on an atomic scale.[8] The word "nanotechnology" was first used by Nario Taniguchi in 1974 to describe machining with tolerances of less than a micron. In 1985, Robert F. Curl Jr., Harold W. Kroto, and Richard E. Smalley[9] discovered buckminster fullerenes, i.e. soccer-ball-shaped molecules made of carbon and measuring roughly 0.7 nm wide. In 1991, Sumio Iijima[10] discovered a new form of carbon called carbon nanotubes, which consisted of several tubes nested inside each other. Two to three years later, single-walled carbon nanotubes were observed which were just 1-2 nanometers in diameter.

1.2 What are nanomaterials?

Nanomaterials are materials with morphological features smaller than a one tenth of a micrometer in at least one dimension.[11] Specifically they are those with at least one dimension falling in the nanometer scale.

1.2.1 Zero-dimensional (0D) nanomaterials: Nanoparticles

Nanoparticles maintain a size between 1 and 100 nanometers including all single crystalline, polycrystalline and amorphous particles with possible morphologies, such as spheres, cubes and platelets. Nanocrystals of metals, oxides, and semiconductors have been studied intensely in the last several years by different chemical and physical methods.[12-14] In the past decade, the realization that the electronic, optical, magnetic, and chemical properties of nanocrystals depend on their size has motivated intense research in this area.

Semiconducting nanoparticles (e.g. CdSe, CdTe, PbSe) were also called quantum dots (QDs), which confine electrons and holes in all three directions giving rise to a discrete energy spectrum. In an unconfined (bulk) semiconductor, an electron-hole pair is typically bound within a characteristic length called the Bohr exciton radius. If the electron and hole are constrained further, then the semiconductor's properties change. This effect is a form of quantum confinement, and it is a key feature in many emerging electronic structures. Therefore quantum dots possess properties that are between those of bulk semiconductors and those of discrete molecules. Quantum dots have been widely used in transistors, solar cells, LEDs, and diode lasers. They have also been investigated as agents for medical imaging.[15-19]

Typical preparation methods of nanoparticles include coprecipitation, sol-gel, microemulsion, hydrothermal, templated, and biomimetic syntheses.[20-25] Although most of methods are in solution phase, nanoparticles can also be fabricated by vapor phase reactions.[26]

1.2.2 One-dimensional (1D) Nanomaterials: Nanowires and Nanorods

1D nanomaterials are those materials that are nanoscale in two dimensions. Nanowires, nanorods, nanotubes and nanobelts constitute an important class of 1D nanomaterials. As compared with bulk materials, 1D nanoscale materials, with their large surface areas and possible quantum confinement effects, exhibit distinct thermal, mechanical, optical, electronic and magnetic properties. In most cases, 1D nanomaterials are superior to their bulk counterparts. They have attracted interest in applications ranging from field effect transistors (FETs), lasers, sensors, solar cells, optical switches and so on.[27-31] They are also good models to study the relationships between electrical transport, optical and other properties, constrained by dimensionality and size confinement.

There are six main synthesis strategies for 1D nanomaterials:

(1) dictation by the anisotropic crystallographic structure of a solid (e.g. Se, Te, $Na_2Mo_6Se_6$);[32, 33]

(2) confinement by a liquid droplet as in the vapor-liquid-solid process (e.g. nanoparticle catalysts in a CVD technique);[34-37]

(3) directionality through use of a template (e.g. channels in porous materials, self-assembled molecular structures, existing 1D nanostructures);[38-41]

(4) kinetic control provided by a capping agent (e.g. hexylphosphonic acid (HPA) for CdSe rods; poly(vinyl pyrrolidone) (PVP) for Ag nanowires);[42, 43]

(5) self-assembly of 0D nanostructures (e.g. Au nanoparticles self-assembled into chains);[44]

(6) size reduction of a 1D microstructure (e.g. anisotropic etching of single crystal Si to form V-shaped grooves which can be used as a template with which to grow nanowires coupled with other techniques).[45]

1.2.3 Two-dimensional nanomaterials: Thin Films

Thin films are thin material layers ranging from a nanometer to several micrometers in thickness. They are widely used for electronic semiconducting devices and optical coatings. Recently, ferromagnetic thin films were applied for computer memory and drug delivery applications. A ceramic thin film coating can help protect substrate materials against corrosion, oxidation and wear.[46, 47]

The deposition techniques have been a subject of intensive study for almost a century. Many techniques have been developed and used in industry. These techniques include physical vapor deposition (PVD), chemical vapor deposition (CVD), atomic layer deposition (ALD), self-assembly, Langmuir-Blodgett film formation, electrochemical deposition and sol-gel methodologies.

1.2.4 Special nanomaterials

There are a number of important nanomaterials whose syntheses and properties are unique. Most of these are "man-made" and do not exist in Nature.

1.2.4.1 Carbon fullerenes and nanotubes

A carbon fullerene is normally referred to as a molecule with 60 carbon atoms, C_{60}, but also includes larger fullerenes C_n ($n>60$) such as C_{70}, C_{76}, C_{78}. The fullerene was discovered in 1985 by Robert Curl, Harold Kroto and Richard Smalley at the University of Sussex and Rice University, who named it after Richard Buckminster Fuller, whose geodesic domes it resembles. Fullerenes are usually synthesized by applying an arc discharge between graphite electrodes in approximately 200 torr of He gas.[48, 49] Because of the uniqueness of the C_{60} molecule and its ability to undergo a variety of chemical reactions, fullerene chemistry has been a very active research field.

Since their discovery in 1991 by Iijima and coworkers, carbon nanotubes have been investigated by many researchers all over the world. Their large length (up to several microns) and small diameter (a few nanometres) result in a large aspect ratio. They can be seen as the nearly one-dimensional form of fullerenes. These include single-walled carbon nanotube (SWCNT), double-walled carbon nanotube (DWCNT) and multi-wall carbon nanotube (MWCNT) motifs. Carbon nanotubes can be synthesized by

arc discharge, laser ablation, pyrolysis, chemical vapor deposition (CVD) and electrochemical methods. Carbon nanotubes afford a wide spectrum of applications. Examples include energy storage, molecular electronics, nanoprobes and sensors, catalysis, flow sensors, drug delivery and nanocomposites.[49-53]

1.2.4.2 Micro and mesoporous meterials

Porous materials can be classified into three kinds in terms of their size. According to IUPAC notation, microporous materials have pore diameters of less than 2 nm and macroporous materials possess pore diameters of greater than 50 nm. The mesoporous category thus lies in the middle (i.e. 2 nm < d < 50 nm).

The first ordered mesoporous materials synthesized were MCM-41 and MCM-48, which are both aluminosilicates. Mesoporous materials possess many important technological applications such as use as supports, sieves, adsorbents and nanoscale chemical reactors. They are mainly created with a combination of self-assembled surfactants as templates and of simultaneous sol-gel condensation around the template itself.[54, 55]

Classical microporous materials include zeolites which are also aluminosilicates and were first discovered in 1756. They have a three-dimensional framework structure with uniformly sized pores of molecular dimensions, typically ranging from ~0.3 to 1 nm in diameter. Zeolites have many applications such as catalysts, adsorbents, and molecular sieves. They are normally prepared by hydrothermal synthesis techniques. Their production typically involves the use of water, a silica source, an alumina source, a mineralizing agent and a structure-directing agent.[56, 57]

1.2.4.3 Organic-inorganic hybrids

Organic-inorganic hybrids are materials in which inorganic and organic components interpenetrate each other at the nanometer scale. The self-assembly of organic molecules can lead to a complex structural hierarchy which can easily be tuned by subtle modifications in the molecular structure of the individual component. Inorganic materials, on the other hand, very often show highly desirable materials' properties which are complementary to those of organic and organo-polymeric systems. Organic-inorganic hybrids specifically combine such properties with a hierarchical structure formation. The sol-gel technique is normally used for making these hybrids.[58, 59]

1.2.4.4 Nanocomposites

Nanocomposites include multiphase solid materials wherein one of the phases has a dimension of less than 100 nm.[60, 61] The mechanical, electrical, optical, electrochemical, and catalytic properties of the nanocomposite will differ markedly from that of the component materials. For example, adding carbon nanotubes into a polymer matrix greatly improves the electrical and thermal conductivity. Other kinds of nanoparticulates may result in enhanced optical properties, dielectric properties or mechanical properties such as stiffness and strength. In general, the nanoscale reinforcement is dispersed into the matrix during processing.

1.3 Synthesis Methods

Many techniques, including both top-down and bottom-up approaches, have been developed for the synthesis of nanomaterials. The terms "top-down" and "bottom-up' were first applied to the field of nanotechnology by the Foresight Institute in 1989 in order to distinguish between molecular manufacturing (which can be used to mass-produce large atomically precise objects) and conventional manufacturing (which can mass-produce large objects that are not atomically precise). Bottom-up approaches create complex assemblies from smaller components (like molecules), whereas top-down approaches create nanoscale devices by using larger, externally-controlled ones to direct their assembly. Top-down approaches include milling (attrition), repeat quenching, lithography, and ink-jet printing. Bottom-up approaches are far more popular in the synthesis of nanoparticles. An example would involve nanoparticles synthesized from either the liquid or vapor phase by homogeneous nucleation, or by heterogeneous nucleation on substrates. Generally speaking, bottom-up approaches are able to produce materials or devices in parallel and are much cheaper than top-down methods, but could potentially be overmatched as the size and complexity of the desired assembly increases.

There are many ways to categorize these techniques. One of the easiest ways is to divide them into chemical and physical methods, respectively, depending on whether the composition has been changed or not.

1.3.1 Chemical Methods

1.3.1.1 Precipitation from solution

Many of the earliest syntheses of nanoparticles were achieved by the precipitation of sparingly soluble products from aqueous solutions followed by thermal decomposition of those products to oxides. This method has become very popular in making metallic, semiconducting, and oxide nanoparticles.

This technique can be explained using a nucleation-growth mechanism (see Figure 1.2). When the concentration of solute increases as a function of time, no nucleation would occur even above the equilibrium solubility. The nucleation occurs only when the supersaturation level reaches a certain value above the solubility value. After the initial nucleation process, the concentration of the growth species decreases. When the concentration is lower than this specific value, nucleation stops. However, growth, which starts from the moment nuclei appear, will still proceed until the concentration decreases down to the equilibrium concentration or solubility.[62]

For the synthesis of nanomaterials with a uniform size distribution, it is best if all nuclei are formed at the same time so that they can possess same or similar sizes. Moreover, all of the nuclei will then undergo the same growth. Hence it is desirable to have nucleation occur in a very short period of time. In practice, the concentration of the growth species is increased abruptly to a very high supersaturation and then quickly brought below the minimum concentration for nucleation. Since the size distribution of the initial nuclei may be altered depending on the kinetics of the subsequent growth

process, the growth process should be appropriately controlled to obtain uniformly sized nanoparticles.

A good example involves the synthesis of CdSe semiconductor nanoparticles.[63] First, temporally discrete nucleation can be obtained by a rapid increase in concentration upon injection, resulting in an abrupt supersaturation. Second, Ostwald ripening during aging at increased temperatures promotes the growth of large particles at the expense of small ones, narrowing the size distribution. Third, size selective precipitation can be applied to further enhance the size uniformity. Other examples include the syntheses of Au and Ag nanoparticles.

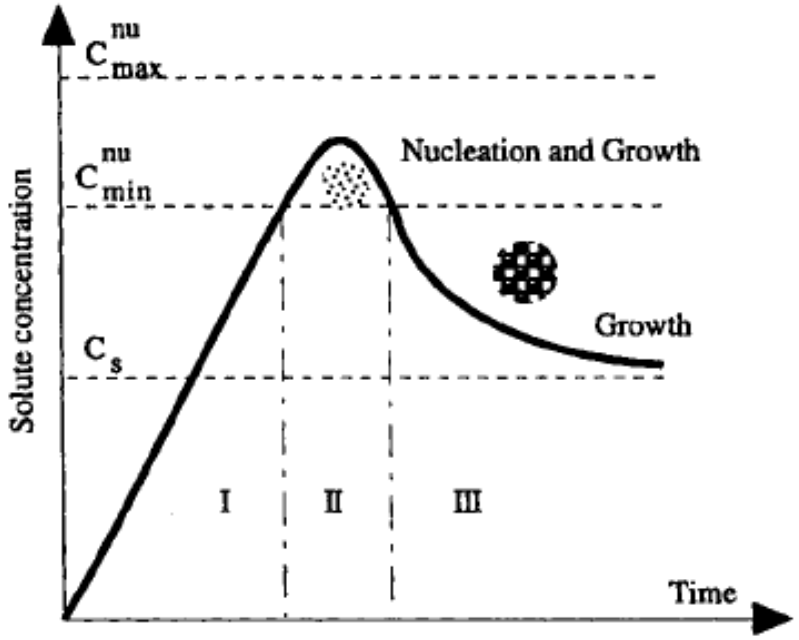

Figure 1.2 Schematic illustrating the processes of nucleation and subsequent growth.[64]

1.3.1.2 Sol-Gel Processing[65, 66]

Sol-gel processing is a wet chemical method for the synthesis of colloidal dispersions of inorganic and organic-inorganic hybrid materials, especially oxides and oxide-based hybrids. From these colloidal dispersions, powders, fibers, thin films and monoliths can be readily prepared. The sol-gel technique provides many advantages such as a low processing temperature and molecular level homogeneity.

. A typical sol-gel processing consists of hydrolysis and condensation of precursors. Precursors can be either metal alkoxides or inorganic and organic salts. Organic or aqueous solvents may be used to dissolve precursors, and catalysts are often added to promote hydrolysis and condensation reactions.

The interest in sol-gel processing can be traced back to the mid-1880s with the observation that the hydrolysis of tetraethyl orthosilicate (TEOS) under acidic conditions led to the formation of SiO_2 as fibers and monoliths. Sol-gel research has grown to be so important that it has been abundantly reviewed.[67-69] We will talk more about the sol-gel technique in Chapter II, i.e. the synthesis of $Bi_2Ti_2O_7$ nanotubes by the sol-gel technique.

1.3.1.3 Hydrothermal Technique[70]

In 1839, the German chemist Robert Bunsen reacted chemicals in aqueous solutions in thick-walled glass tubes at temperatures above 200 ℃ and at pressures above 100 bars. Crystals of barium carbonate and strontium carbonate that he grew under these conditions marked the first use of hydrothermal aqueous solvents as media.

Hydrothermal synthesis can be defined as a method of synthesizing single crystals which depends on the solubility of minerals in hot water under high pressure. In short, the synthesis method uses the solubility in water of almost all inorganic substances at elevated temperatures and pressures, and subsequent crystallization of the dissolved material from fluid. As suggested by the name of the process, water at elevated temperatures plays an essential role in precursor material transformation. Crystal growth is performed in an apparatus consisting of a steel pressure vessel called an autoclave, which contains thick-walled steel cylinders with a hermetic seal which can withstand high temperatures and pressures for prolonged periods of time. Furthermore, the autoclave material is inert with respect to the solvent.

Sometimes the synthesis method is also denoted as solvothermal, which means that water, but also other solvents are used, in accordance with the general principle of the method. It is also possible that additives can be employed to modify the initial properties of the pure hydrothermal water.

1.3.1.4 Molten Salt Synthesis (MSS)[71, 72]

The fundamental basis of molten salt reactions is the reliance on the use of inorganic molten salt as the reaction medium. Salt media used by other groups have ranged from the eutectic mixture of $AlCl_3$/NaCl/KCl with a relatively low melting point

of 89 ℃ to cryolite or Na_3AlF_6 with a particularly high melting point of 1003 ℃. Moreover, these salts often possess a host of favorable physicochemical properties such as a greater oxidizing potential, higher mass transfer, higher thermal conductivity, as well as relatively lower viscosities and densities, as compared with conventional solvents.

The MSS method is one of the simplest, most versatile, and highly cost-effective approaches available for obtaining crystalline, chemically pure, single-phase nanoscale materials at lower temperatures and often in overall shorter reaction times with little residual impurities as compared with conventional solid-state reactions. The intrinsic scalability, flexibility, and facility of this technique render it attractive for the fabrication of a range of materials. Our group has employed this technique and successfully produced various of materials—$BaTiO_3$, $SrTiO_3$,[73] $Ca_{1-x}Sr_xTiO_3$,[74] and $Bi_2Fe_4O_9$.[75] We will discuss this technique in detail in Chapter III, with respect to the synthesis of $BaZrO_3$ submicron sized particles by the molten salt method.

1.3.1.5 CVD (Chemical Vapor Deposition) Technique[76]

CVD is often used in the semiconductor industry to produce thin films. It is a chemical process used to fabricate high-purity, high-performance solid materials. In a typical synthesis, a substrate (usually a Si wafer) is placed in the center of the reaction chamber and exposed to one or more volatile precursors, which react with and/or decompose on the substrate surface to produce the desired deposit.

The CVD technique is also widely used to make 1D nanomaterials. The mechanism is known as the vapor-liquid-solid (VLS) process. A good example involves the synthesis of Ge nanowires by the catalysis of Au nanoparticles.[34]

1.3.1.6 Reverse Micellar Method[77]

Reverse micelles are water-in-oil droplets (contrary to oil-in-water droplets for micelles) stabilized by a surfactant. The polar head groups of the surfactant molecules organize themselves around small water pools. The surfactant most often used is sodium 2-bis(2-ethylhexyl) sulfosuccinate, Na(AOT). These droplets are displaced randomly and they exchange their water content. In a typical synthesis, two reactants are solubilized in two distinct micellar solutions respectively. On mixing, the reactants are in contact and react by an exchange process of the micelles. Thus, a wide range of chemical reactions, such as the hydrolysis of reactive precursors or precipitation reactions, can occur in micelles.

Advantages of this technique include the desired ability to make small nanoparticles and to control the size distribution. These can be achieved by choosing suitable surfactants, precursors, and molar ratios of water-to-surfactant.

1.3.2 Physical Methods

1.3.2.1 Lithography[78]

Lithography is a process of transferring a pattern (usually a mask) onto an underlying substrate (i.e. Si wafer). A typical process involves five steps. (1) Coating: a thin layer of resist material is applied on the substrate. (2) Exposure: the layer of resist with substrate underneath is exposed in an image-wise fashion through a mask, such that light (may also use other sources such as ion, electron: see next paragraph) strikes selected areas defined by the mask of the resist material. (3) Development: depending on the chemical nature of the resist material, the exposed areas may be rendered more soluble in some developing solvent than the unexposed areas, thereby producing a positive tone image of the mask. Conversely, the exposed areas may be rendered less soluble, producing a negative image of the mask. (4) Etching: The areas of resist that remain after the developing step can be used to mask the underlying substrate. The resist materials resist the etchant and prevent it from attacking the underlying substrates. (5) Stripping: Following the etching step, the resist is removed by stripping to produce a substrate with a positive or negative tone relief image.

Utilizing different radiation sources to induce the change of resist materials, many lithography techniques have been developed. Examples include photolithography, electron beam lithography, X-ray lithography, focused ion beam lithography and neutral atomic beam lithography. Despite their different names, they all share the same theory and are all based on similar fundamentals, as mentioned in the previous paragraph.

1.3.1.2 Soft Lithography[79, 80]

Soft lithography is a general term referring to a family of non-photolithographic techniques for microfabrication that are based on the printing of self assembled monolayers (SAMs) and molding of liquid precursors. It is called “soft’ because it uses elastomeric materials, most notably polydimethylsiloxane (PDMS). Soft lithography techniques include contact printing (μCP), micromolding in capillaries (MIMIC), microtransfer molding (μTM) and replica molding (REM).

As an alternative to the photolithographic technique, soft lithography offers several advantages: lower cost; suitability for applications in biotechnology and plastic electronics; suitability for applications involving large or nanoplanar surfaces; more pattern-transferring methods; and higher resolution.

These soft lithographic techniques were developed in the Whiteside group and have been summarized in excellent review articles and books.[81, 82]

1.3.1.3 Nanomanipulation

Nanomanipulation is based on scanning probe microscopy (SPM). It consists of two major tools: scanning tunneling microscopy (STM) and atomic force microscopy (AFM). SPM can not only image the surface of all kinds of solids but also be used as an effective tool in the fabrication and processing of nanostructures.

For instances, in an iconic experiment, a STM tip has been used to position 35 xenon atoms onto a nickel surface to form three letters "IBM".[83] An AFM tip has also been used to position Au nanoparticles on a mica surface.[84] Manipulation and fabrication by SPM offer great resolution and ability of in situ characterization and manipulation. However, it is also limited by the small scan area and slow scan rate. Also it requires tips of high quality, an extremely flat surface and a well-controlled fabrication environment.

1.3.1.4 Self Assembly

Self assembly is based on the fact that the final structure or assembly is close to or at a thermodynamic equilibrium. Thus it tends to form spontaneously. A lot of interactions have been exploited as the driving force: namely van der Waals, electrostatic and hydrophobic interactions, hydrogen bonding, capillary forces, gravitation and so on.

For example, the spontaneous formation of ordered 3-D arrays of iron oxide particles can be achieved when a drop of colloidal solution containing the particles is placed on a TEM grid and the solvent is allowed to evaporate.[85] Parallel and cross arrays of GaP, InP and Si nanowires can be achieved by passing a suspension of nanowires through fluidic channel structures formed between a PDMS mold and substrate.[86]

1.4 Unique properties of nanomaterials

Nanomaterials possess the structural features between those of atoms and the bulk materials. Although most microstructured materials have similar properties to their corresponding bulk analogues, the properties of materials at the nanometer scale are significantly different from those of atoms and bulk materials.

Why?

The nanometer sizes of materials render them with the following attributes:

(1) Large fraction of surface atoms: As a particle decreases in size, more atoms are found at the surface as compared with those inside. For example, a palladium cluster (Figure 1.3) measuring 7 nm in size possessed 35% of its atoms on its surface, at 5 nm, 45% of its atoms, and at 1.2 nm, 76% of its atoms. Hence nanomaterials have an extremely large surface area to volume ratio, resulting in more "surface"-dependent material properties. When the sizes of nanomaterials are comparable to the Debye length, the entire material will be affected by the surface properties of nanomaterials. Surface atoms are chemically more active as compared with interior atoms because they usually have fewer adjacent coordinate atoms and more unsaturated or dangling bonds. For example, metallic nanoparticles can be used as very active catalysts.

(2) Spatial confinement or quantum effect: A particle behaves as if it were free when the confining dimension is large as compared with the wavelength of the particle. The band gap remains at its original energy due to the continuous energy state. However, as the confining dimension decreases and reaches a certain limit, typically at the nanoscale, the energy levels become discrete. As a result, the band gap becomes size-dependent. This ultimately results in a blue shift in optical illumination as the size of the

particles decreases. For example, CdSe nanoparticles with different sizes possess different colors.

(3) Reduced imperfections: Nanostructures and nanomaterials favor a self-purification process in that the impurities and intrinsic material defects will move to near the surface upon thermal annealing. This increased materials' perfection affects the properties of nanomaterials. The chemical stability may be enhanced and the mechanical properties of nanomaterials will be better than that of the bulk material. For example, carbon nanotubes have been reported to have a Young's modulus of 1.8 ± 0.9 TPa, which is much higher than that of high-strength steel of ~ 200 GPa.[88]

1.5 Applications of nanomaterials

Applications of nanomaterials can be traced back to a long time ago. As mentioned earlier, colloidal gold and silver particles have served as pigments in stained glass church windows and ceramics since the 10^{th} century AD. Even Nature has taken advantage of the properties of nanostructures. Good examples include the capillary forces or the Lotus effect in plants.

Applications of nanostructures and nanomaterials are mainly based on (1) their peculiar physical properties, e.g. gold nanoparticles used as an inorganic dye and catalyst; (2) their huge surface area, e.g., mesoporous TiO_2 for DSSC (Dye Sensitized Solar Cell), and (3) the small size that offers additional possibilities for manipulation and room for accommodating multiple functionalities, e.g., nanomaterials for drug delivery.

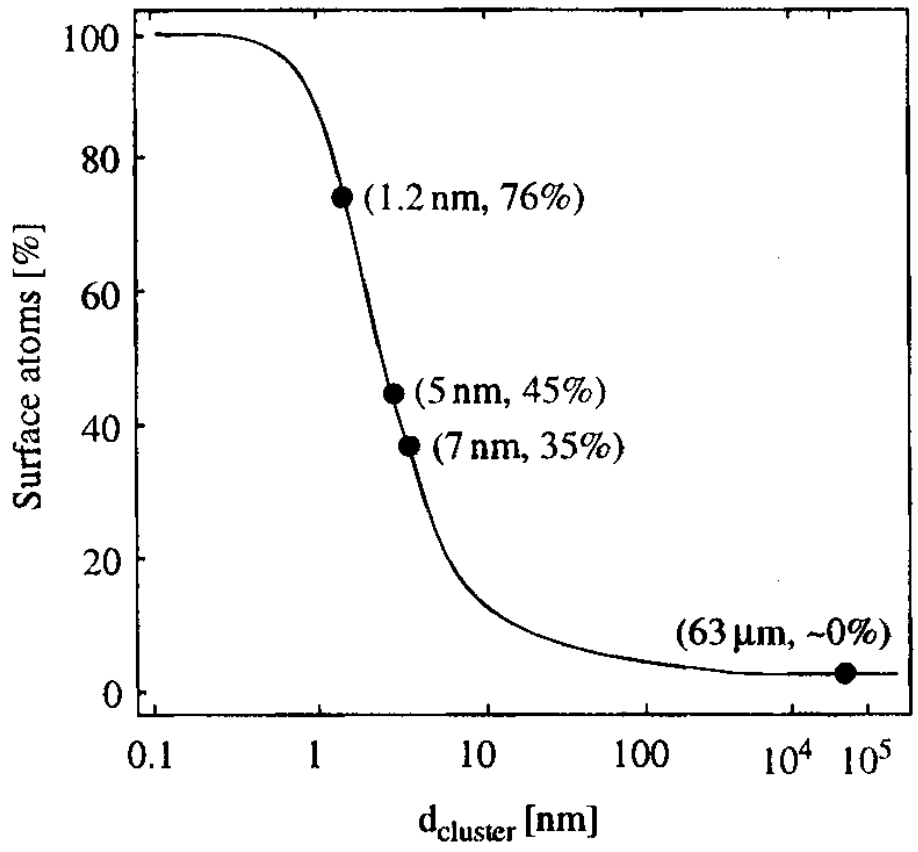

Figure 1.3 The percentage of surface atoms changes with the palladium cluster diameter.[87]

1.5.1 Nanoelectronics

Nanoelectronics refers to the use of nanotechnology for electronic components. Many nanoscale electronic devices have been produced, i.e. tunneling junctions,[89, 90] electrically configurable switches,[91, 92] carbon nanotube transistors,[93] and single molecular transistors.[94] These devices can also be connected together to form circuits.

Single-walled carbon nanotubes have been intensively studied for nanoelectronic devices. Their electrical conductivity depends on their diameter and the helicity of their graphene sheet. This special electrical property together with their extremely high tensile strength and mechanical flexibility renders CNTs as key elements for various nanoelectronic devices, such as single-electron transistors,[95] FETs,[96] sensors,[97] and circuits.[98]

Major obstacles preventing the development of such devices include the controlled spatial placement of nanometer-sized objects such as nanoparticles and molecules, molecular vibrations, robustness, and poor electrical conductivity.

1.5.2 Nanomechanics

Nanomechanics is a branch of nanoscience studying fundamental mechanical (elastic, thermal and kinetic) properties of physical systems at the nanometer scale.

In previous paragraphs, we introduced the applications of SPM to the field of imaging and measurement of local properties of the sample surface. SPM can also be used to make nanodevices. SPM is also a good example for the application of nanomechanics. When the surface of a cantilever or a tip is functionalized in such a way that either a chemically active or a chemically inactive surface is obtained, chemical or physical processes on the active cantilever surface can be observed using the temporal evolvement of the cantilever's response. Cantilevers can be used as a nanomechanical sensor device for detecting chemical interactions between binding partners on the cantilever surface and in its environment.

1.5.3 Solar Cells

Nanostructures are also desirable for solar cell devices for highly efficient conversion of light to electrical power due to their high surface area. For example, a dye sensitized solar cell (DSSC) developed by Grätzel et al,[99] in which a porous nanocrystalline TiO_2 film is used in conjunction with an efficient light absorbing dye, showed an impressive energy conversion efficiency of >10% at lower production costs than conventional Si solar cells. Other wide band gap semiconductors, like ZnO and SnO_2, were also studied for DSSCs. One-dimensional nanostructures, such as ZnO nanowire arrays and CdSe nanorods, have been studied to improve the energy conversion efficiency. [29, 100]

1.5.4 Catalysis

Catalytic activity often takes place at defects on surfaces, and on steps and kinks. They also allow for special bonding situations which are favorable for the breaking of and making of bonds. The irregular surface of nanoparticles offers a wonderful environment with a lot of such defects. In addition, atoms near the surfaces of small nanoparticles are much more flexible to move than in the large bulk, and thus surface reconstruction is much easier. The electronic property (e.g., Fermi level) of nanoparticles differs a lot from that of the bulk. All of these qualities render nanoparticles as better catalysts than their bulk counterparts.

Gold is a perfect example. Bulk gold is chemically inert and considered to be either inactive or unusable as a catalyst. However, gold nanoparticles have excellent calalytic properties. They are extremely active in the oxidation of carbon monoxide if deposited on oxide substrates, such as Fe_2O_3, NiO, and TiO_2. Other reactions include asymmetric dihydrolation, carboxylic ester cleavage, electrocatalytic reduction by anthraquinone functionalized gold particles, and particle-bound ring opening metathesis polymerization. Hutchings et al, have summarized gold catalysis in their well-written review.[101]

1.5.5 Photonic crystals

Photonic crystals are composed of periodic dielectric or metallo-dielectric nanostructures that affect the propagation of electromagnetic waves (EM) in the same way that the periodic potential in a semiconductor crystal affects electron motion by defining allowed and forbidden electronic energy bands. Essentially, photonic crystals contain regularly repeating internal regions of high and low dielectric constant. Photons (behaving as waves) propagate through this structure - or not - depending on their wavelength. Wavelengths of light that are allowed to travel are known as modes, and groups of allowed modes form bands. Disallowed bands of wavelengths are called photonic band gaps. This gives rise to distinctive optical phenomena such as the inhibition of spontaneous emission, high-reflecting omni-directional mirrors and low-loss waveguiding, amongst others. Since the basic physical phenomenon is based on diffraction, the periodicity of the photonic crystal structure has to be on the same length-scale as half the wavelength of EM waves i.e. ~200 nm (blue) to 350 nm (red) for photonic crystals operating in the visible part of the spectrum - repeating regions of high and low dielectric constants have to be of this dimension. This makes the fabrication of optical photonic crystals both cumbersome and complex.

A number of methods have been developed for the fabrication of photonic crystals. Examples include layer-by-layer stacking, CVD, electrochemical etching, and self-assembly of monodisperse spherical colloids. [102-105]

1.5.6 Applications in biotechnology

Nanobiotechnology is a rapidly evolving field of research at the crossroads of biotechnology and nanoscience, two interdiscriplinary areas, each of which combines advances in science and engineering.

Due to their small size or comparable size to that of a cell (10 -100 nm), virus (20 -450 nm), or protein (5 – 50 nm), nanoparticles offer attractive possibilities in biomedicine. They may be coated by organic groups to make them compatible with or bind to a biological entity of interest.

Ferromagnetic nanoparticles have been developed in view of the targeted delivery of therapeutic drugs. For example, Fe_3O_4 or γ-Fe_2O_3 nanoparticles are coated with a shell of SiO_2 and then with a biocompatible polymer which can also be functionalized to provide attachment points for the coupling of cytotoxic drugs or antibodies to the carrier complex.

Catabolism of tumors can be enhanced by artificially induced hyperthermia, which typically involves dispersing magnetic particles throughout the target issue and then applying an alternating magnetic field of sufficient strength and frequency to heat them up. If the temperature of the surrounding tissue can be kept above a therapeutic threshold of 42 ℃ for a certain amount of time, the cancer will be destroyed.[106]

Other applications include biocompatible inorganic devices (implant coatings, stents, seeds), microfluidics (lab-on-a-chip), luminescent quantum dots for biological labeling, contrast enhancment agents, and the fabrication of nanomaterials/nanostructures using biomolecules.[107]

1.6 Objectives of present work

The materials we are focused on study include nanoparticles (0D) and nanowires/rods/tubes (1D). Nanomaterials are of great scientific interest as they are an effective bridge between bulk materials and atomic or molecular structures. The properties of bulk materials are only dependent on their chemical composition. However at the nano-scale, the properties of materials are not only determined by chemical compositions, but also by sizes and shapes. Good examples involve quantum confinement effect in semiconductor nanoparticles, surface plasmon effects in metal nanoparticles, and superparamagnetism in magnetic nanoparticles. As compared to nanoparticles, the special one-dimensional structure along with size confinement of nanowires/rods/tubes renders them especially useful as bridges in nanoelectronics, as sensors and as carriers in drug delivery. Moreover, these 1D materials are good models to study the relationships between unique physical properties and dimensionality and size confinement.

Due to their unique physical properties and numerous applications, a tremendous amount of work has been accomplished in the field of 0D and 1D nanomaterials. However, there are still challenges ahead that we intend to address adequately in the thesis:

(1) Precise control of size, dimensionality, composition, crystal structure and assembly at the nanoscale.

(2) Development of an environmentally-friendly, energy effective synthesis method, (e.g. low temperature, use of water as a solvent instead of a toxic solvent)

(3) Rational design and fabrication of novel nanomaterials and nanocomposites.

(4) A deep understanding of the relationship between size, shape and physical properties.

Hence, the main focus of our work will be to develop low cost, low toxicity and facile synthesis techniques which yield adequate control over size, shape, dimensionality, purity and composition, so as to study the relationship between size, shape and physical properties, and to develop novel nanostructure materials via rational design and assembly.

As-synthesized materials that we will discuss in the thesis include ternary metal oxides ($Bi_2Ti_2O_7$, $BaZrO_3$, $MnWO_4$), binary metal oxides (ZnO, CuO, α-Fe_2O_3), metals (Ag, Au, Pt) and multifunctional nanostructures (SiO_2 nanotubes encapsulated with CdSe quantum dots and Fe_3O_4 nanoparticles). Synthesis techniques including the molten salt method, sol-gel processing, the template method and self-assembly have been applied. The shapes of as-prepared materials varied from nanocubes, nanospheres to one-dimensional nanowires and nanotubes. Their unique catalytic, magnetic, optical and electronic properties as compared with bulk materials have also been investigated.

1.6.1 Sol-gel synthesis of $Bi_2Ti_2O_7$ nanotubes and their photocatalytic properties – Chapter II

Bismuth titanate is a highly promising high-*k* dielectric material because of its high permittivity and low leakage current density. Despite the evident importance of $Bi_2Ti_2O_7$ as a functional material, very few reports of nanoscale structural motifs of these materials have appeared. Moreover, there have not been any reports about the 1D structures of this material. In our work, we address this issue by employing a template-based technique for the synthesis of $Bi_2Ti_2O_7$ nanotubes.[108] (Figure 1.4)

1.6.2 Shape and size control in the molten salt synthesis of submicron $BaZrO_3$ cubes and spheres – Chapter III

$BaZrO_3$, a cubic perovskite, has a number of applications including as a refractory material, as a reaction substrate in the synthesis of superconductors; and as high temperature microwave dielectrics. Although $BaZrO_3$ cubes are useful in piezoelectric applications, no report about this material structure has been reported on. In our work, we successfully created $BaZrO_3$ submicron sized cubes and spheres through a large-scale, environmentally friendly molten salt synthesis method.[109, 110] (Figure 1.5)

1.6.3 Template synthesis of 1D metal oxide nanostructures: ZnO, CuO and α-Fe_2O_3 - Chapter IV.

Transition metal oxides, like ZnO, CuO and α-Fe_2O_3, represent one of the most diverse classes of materials with important size-dependent optical, electronic, thermal, mechanical, chemical, and physical properties, with a wide range of correspondingly diverse applications, including as energy storage and sensing devices. In our work, we created ZnO nanowires, CuO nanowires and α-Fe_2O_3 nanotubes as well as their corresponding arrays via a low cost, generalizable, and simplistic template method.[111] (Figure 1.6)

1.6.4 Template synthesis of multiferroic $MnWO_4$ nanowires- Chapter V

$MnWO_4$ is a relatively lesser-known member of multiferroic materials, which show simultaneous ferromagnetic ordering and ferroelectric ordering. In our work, we synthesized $MnWO_4$ nanowires by a similar template method to 1D transition metal oxides, Also, we measured the magnetic behavior of $MnWO_4$ nanowires and compared that with bulk $MnWO_4$.[112] (Figure 1.7)

1.6.5 Template synthesis of 1D noble metals: Ag, Au and Pt – Chapter VI

Metallic nanostructures, including Ag, Au and Pt, have attracted significant attention due to their excellent optical, electrical, and thermal conductivity properties, which are highly relevant for diverse applications such as catalysis, optical imaging, optoelectronics, information storage, fuel-cell technology, and sensing. In our work, we synthesized Ag nanowires, Au nanowires and Pt nanowires and nanotubes. We also tested the electrocatalytic properties of these materials for the oxygen reduction reaction, which is believed to be the rate-limiting step in fuel cells.[113] (Figure 1.8)

1.6.6 Incorporation of nanoparticles into nanotubes – creation of multifunctional SiO_2 nanotubes – Chapter VII

CdSe quantum dots and Fe_3O_4 nanoprticles have been widely used in biotechnology due to their optical and magnetic properties respectively. CdSe quantum dots were applied in molecular imaging. Moreover, Fe_3O_4 nanoparticles have been used in magnetic separation, MRI contrast agents, drug delivery, and hyperthermia treatments. To protect these nanoparticles and render them biocompatible, a coating (i.e. silica or polymer) has normally been required. In our work, we generated a multifunctional silica nanostructure by incorporation of CdSe quantum dots and Fe_3O_4 nanoprticles inside a silica nanotube via a hydrophobic interaction (Figure 1.9). The resulting nanostructure has been attractive in terms of drug delivery applications.

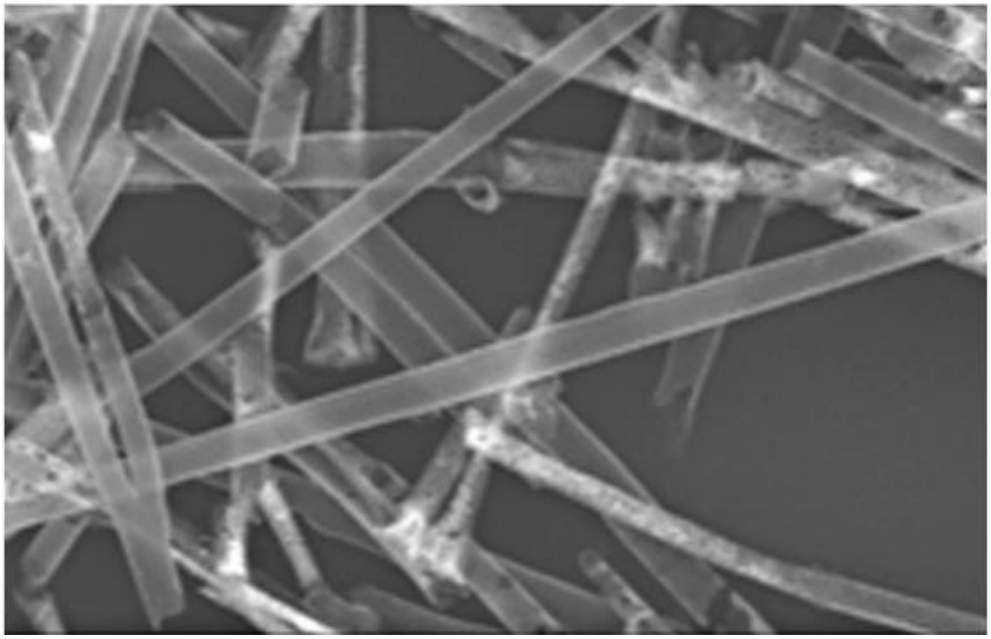

Figure 1.4 SEM image of as-prepared $Bi_2Ti_2O_7$ nanotubes by sol-gel processing.

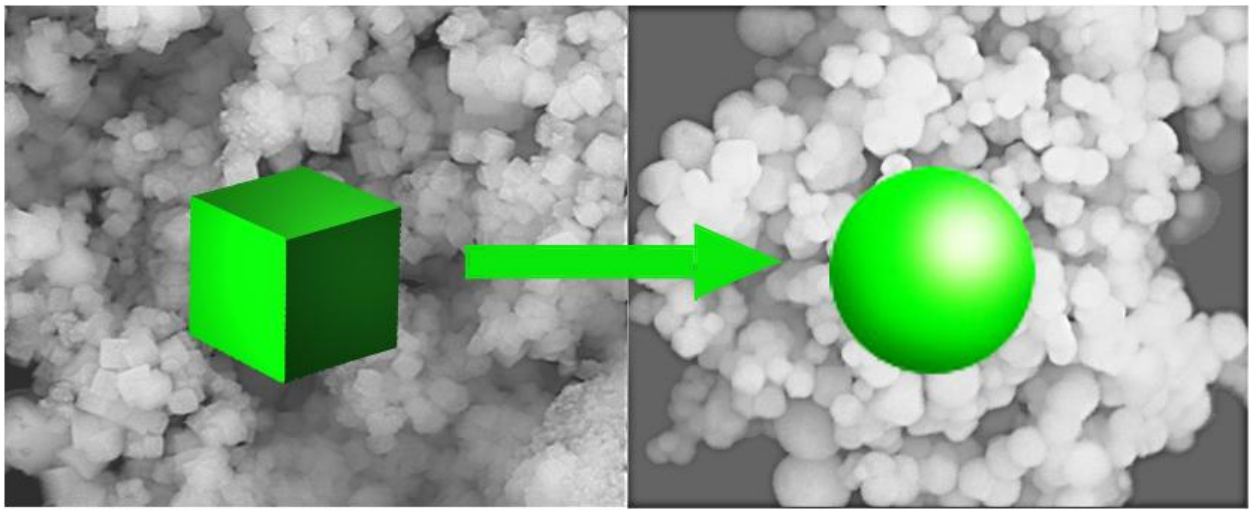

Figure 1.5. SEM images of as-prepared $BaZrO_3$ submicron sized cubes and spheres by molten salt method.

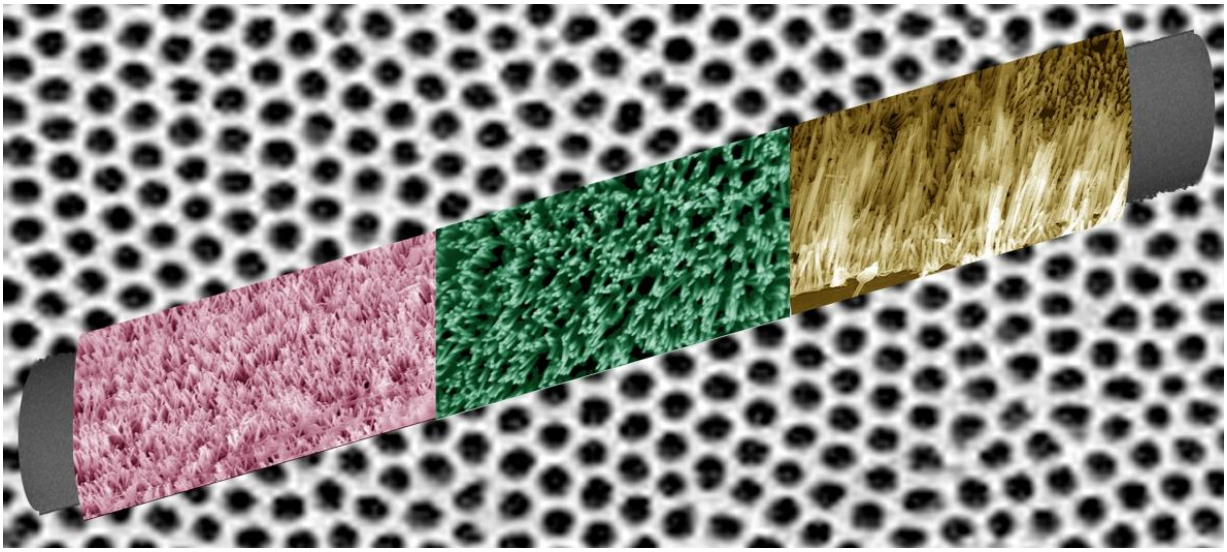

Figure 1.6. Schematic representation of the arrays of ZnO nanowires, CuO nanowires, and α-Fe_2O_3 nanotubes fabricated by template method.

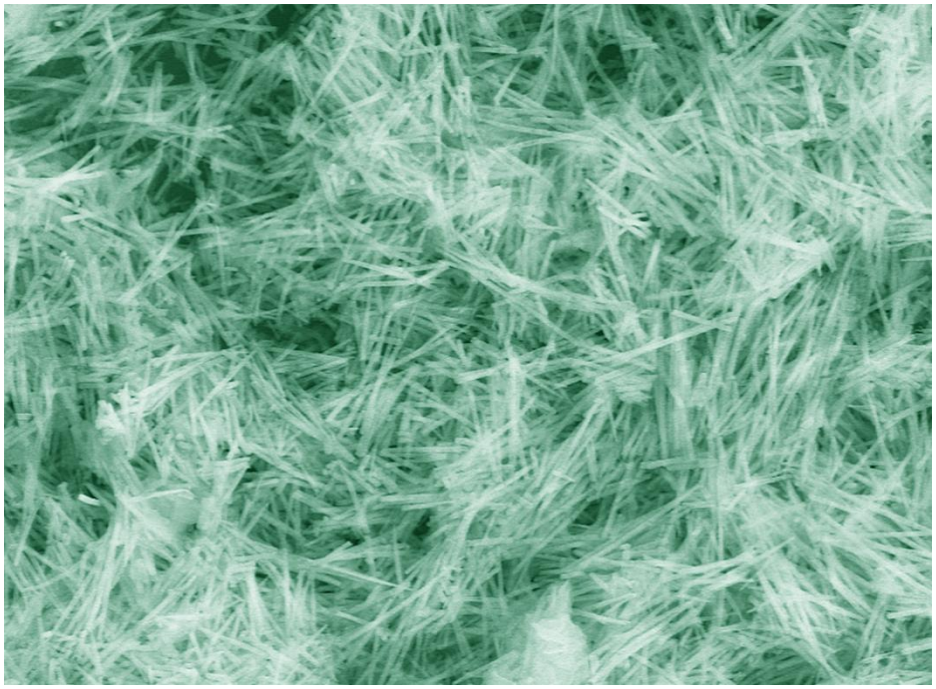

Figure 1.7. SEM image of as-prepared $MnWO_4$ nanowires by template synthesis.

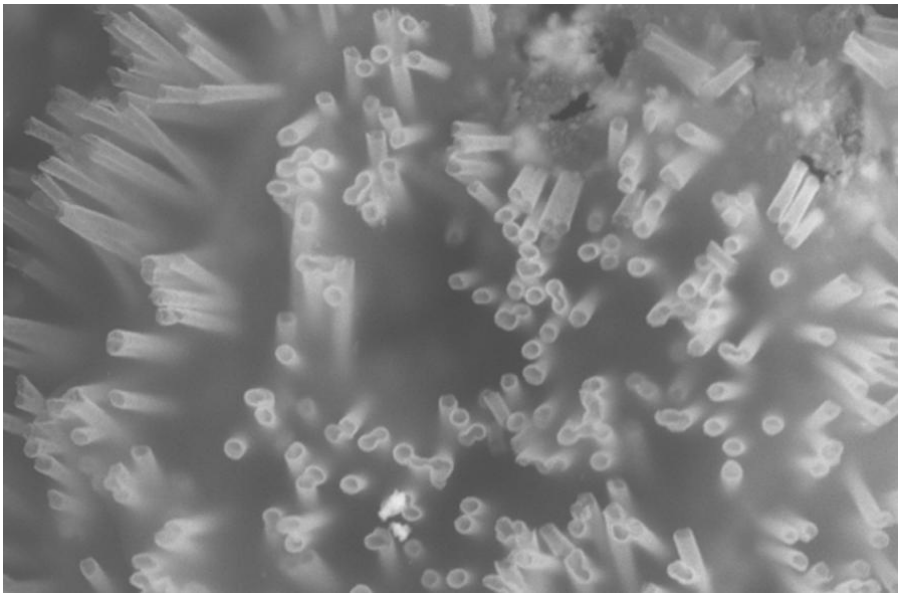

Figure 1.8. SEM image of as-prepared Pt nanostructures by template synthesis.

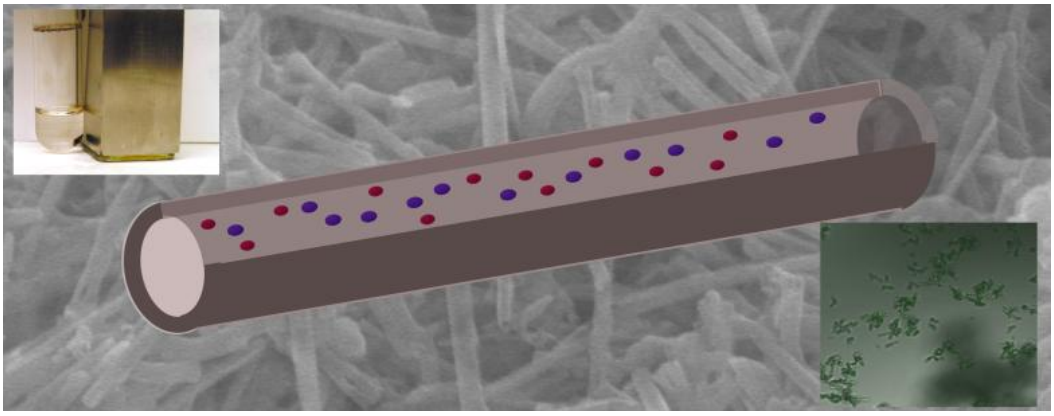

Figure 1.9. Schematic representation of multifunctional silica nanostructures.

1.7 Common characterization techniques used in our work

After preparation of these samples mentioned in Section 1.6, different characterization techniques have been applied to study their phase, size, morphology and physical properties. Some of these common techniques were applied to every or most of these systems. To avoid repeating same techniques in every chapter, we present them in this chapter.

1.7.1 X-ray Diffraction. Crystallographic information on samples was obtained on a Scintag diffractometer, operating in the Bragg configuration, using Cu Kα radiation (λ = 1.54 Å). Samples for analyses were obtained by grinding thoroughly in ethanol using a mortar and pestle, followed by loading onto glass slides and subsequent drying in air. Diffraction patterns were collected from 10 to 70 °at a scanning rate of 2 °per minute with a step size of 0.02 °. Parameters used for slit widths and accelerating voltages were identical for all samples.

1.7.2 Electron Microscopy. The particle size and morphology of the resulting products were initially characterized using a field emission SEM (FE-SEM Leo 1550) at accelerating voltages of 15 kV, which was equipped with EDS capabilities. Specifically, samples were deposited onto Si wafers as well as mounted onto conductive copper tapes, which were then attached to the surfaces of SEM brass stubs. These samples were then conductively coated with gold by sputtering them for 20 seconds so as to minimize charging effects under SEM imaging conditions.

For the creation of nanowire/nanotube arrays, membranes were initially attached to a piece of either double-sided conductive carbon tape or copper tape. The resulting aligned nanowire samples were created by immersion in either 1 M NaOH solution (for AAO membranes) for 0.5 h or in methylene chloride solution (for PC membranes) for 5 min so as to dissolve and remove the template. After washing steps with distilled water followed by air-drying, samples were subsequently mounted onto a variety of substrates for imaging.

Specimens for low magnification TEM and HRTEM were obtained by drying droplets of the samples from an ethanolic dispersion onto a 300 mesh Cu grid, coated with a lacey carbon film. TEM images were taken at an accelerating voltage of 120 kV on a Philips CM12 instrument. HRTEM images and SAED patterns were obtained on a JEOL 2010F HRTEM at an accelerating voltage of 200 kV. This instrument was equipped with an Oxford INCA EDS system with the potential of performing SAED to further characterize individual structures.

1.7.3 UV-Visible Spectroscopy. UV-visible spectra were obtained at high resolution on a Thermospectronics UV1 spectrometer using quartz cells with a 10-mm path length. Spectra were obtained for nanomaterials and for bulk samples, all of which had been sonicated in distilled water so as to yield homogenous dispersions. UV-visible absorption spectra were recorded using distilled water as a blank.

1.8 References

1. Booker, R.; Boysen, E., *Nanotechnology for Dummies*. Wiley Publishing, Inc.: NJ, **2005**
2. A report by the Interatency Working Group on Nanoscience, National Science and Technology Council, *Leading to the Next Industrial Revolution*; *National Nanotechnology Initiative*. **2000.**
3. Tait, H., *Five thousand years of glass*. The British Museum Press: London, **1991**.
4. Harden, D., *Glass of the Caesars*. The British Museum Press: London, **1988**.
5. Turkevich, J. *Gold. Bull.* **1985**, 18, 86.
6. Knoll, M.; Ruska, E. *Physik* **1932**, 12, 607.
7. Knoll, M.; Ruska, E. *Physik* **1932**, 12, 641.
8. Feynman, R. P. There's Plenty of Room at the Bottom, An Invitation to Enter a New Field of Physics. (http://www.zyvex.com/nanotech/feynman.html)
9. Kroto, H. W.; Heath, J. R.; O'Brien, S. C.; Curl, R. F.; Smalley, R. E. *Nature* **1985**, 318, 162.
10. Iijima, S. *Nature* **1991**, 354, 56.
11. Buzea, C.; Pacheco, I. I.; Robbie, K. *Biointerphases* **2007**, 2, MR17.
12. Rao, C. N. R.; Thomas, P. J.; Kulkarni, G. U., *Nanocrystals: Synthesis, Properties and Applications.* Springer: Heidelberg, **2007**.
13. Klimov, V. I., *Semiconductor and Metal Nanocrystals: Synthesis and Electronic and Optical Properties.* Marcel Dekker, Inc.: New York, **2003**.
14. Schmid, G., *Nanoparticles: From Theory to Application.* WILEY-VCH Weinheim, **2004**.
15. Snider, G. L.; Orlov, A. O.; Lent, C. S., Quantum dots in nanoelectronic devices. In *Nano and Molecular Electronics Handbook*, Lyshevski, S. E., Ed. CRC: **2007**, 8, 1-23.
16. Sargent, E. H. *Adv. Mater.* **2008**, 20, 3958.
17. Pagan, J. G.; Patel, K. N.; Barletta, P. T.; Burkhart, C. C.; Stokes, E. B. *ECS Trans.* **2006**, 3, 333.
18. Peng, Y.; Zhao, X.; Fu, G. *Nanoscience* **2007**, 12, 30.
19. Bertolini, G.; Paleari, L.; Catassi, A.; Roz, L.; Cesario, A.; Sozzi, G.; Russo, P. *Curr. Pharm. Anal.* **2008**, 4, 197.
20. Steigerwald, M. L.; Alivisatos, A. P.; Gibson, J. M.; Harris, T. D.; Kortan, R.; Muller, A. J.; Thayer, A. M.; Duncan, T. M.; Douglas, D. C.; L, E. B. *J. Am. Chem. Soc.* **1988**, 110, 3046.
21. Wang, Y.; Herron, N. *J. Phys. Chem.* **1987**, 91, 257.
22. Cushing, B. L.; Kolesnichenko, V. L.; O'Connor, C. J. *Chem. Rev.* **2004**, 104, 3893.
23. Kuo, C.-L.; Huang, M. H. *J. Phys.Chem. C* **2008**, 112, 11661.
24. Das, S.; Basu, S.; Majumdar, G.; Chakravorty, D.; Chaudhuri, S. *J. Nanosci. Nanotechnol.* **2007**, 7, 4402.
25. Jiang, Y.; Yang, D.; Zhang, L.; Li, L.; Sun, Q.; Zhang, Y.; Li, J.; Jiang, Z. *Dalton Trans.* **2008**, 31, 4165.
26. Hu, Y.; Afzaal, M.; Malik, M. A.; O'Brien, P. *J. Cryst. Growth* **2006**, 297, 61.
27. Kasai, S.; Asai, T. *Appl. Phys. Express* **2008**, 1, 083001/1.
28. Huang, M. H.; Mao, S.; Feick, H.; Yan, H.; Wu, Y.; Kind, H.; Webber, E.; Russo, R.; Yang, P. *Science* **2001**, 292, 1897.

29. Law, M.; Greene, L. E.; Hohnson, J. C.; Saykaly, R.; Yang, P. *Nat. Mater.* **2005**, 4, 455.
30. Lin, M. C.; Chu, C. J.; Tsai, L. C.; Lin, H. Y.; Wu, C. S.; Wu, Y. P.; Wu, Y. N.; Shieh, D. B.; Su, Y. W.; Chen, C. D. *Nano Letters* **2007**, 7, 3656.
31. Leao, C. R.; Fazzio, A.; Silva, A. J. R. d. *Nano Letters* **2007**, 7, 1172.
32. Kruyt, H. R.; Arkel, A. E. v. *Kolloid-Z* **1928**, 32, 29.
33. Furuta, N.; Ohasi, Y.; Itinose, H.; Igarashi, Y. *J. Appl. Phys.* **1975**, 14, 929.
34. Wu, Y.; Yang, P. *J. Am. Chem. Soc.* **2001**, 123, 3165.
35. Wu, Y.; Yang, P. *Chem. Mater* **2000**, 12, 605.
36. Chen, C. C.; Yeh, C. C. *Adv. Mater.* **2000**, 12, 738.
37. Duan, X.; Lieber, C. M. *Adv. Mater.* **2000**, 12, 298.
38. Martin, C. R. *Acc. Chem. Res.* **1995**, 28, 61.
39. T, M. W.; Jiang, J. S.; Searson, P. C.; Chien, C. L. *Science* **1993**, 261, 1316.
40. Yu, Y.-Y.; Chang, S. S.; Lee, C.-L.; Wang, C. R. C. *J. Phys. Chem. B* **1997**, 101, 6661.
41. He, R. R.; Law, M.; Fan, R.; F, K.; Yang, P. *Nano Letters* **2002**, 2, 1109.
42. Peng, X. G.; Manna, L.; Yang, W. D.; J, W.; Scher, E.; Kadavanich, A.; Alivatos, A. P. *Nature* **2000**, 404, 59.
43. Sun, Y.; Xia, Y. *Adv. Mater.* **2002**, 14, 833.
44. Lopes, W. A. *Phys. Rev. E* **2002**, 65, 031606.
45. Wilbur, J. L.; Kim, E.; Y, X.; Whitesides, G. M. *Adv. Mater.* **1997**, 7, 649.
46. Chesnel, K.; Fullerton, E. E.; Carey, M. J.; Kortright, J. B.; Kevan, S. D. *Phys. Rev. B: Condens. Matter Mater. Phys.* **2008**, 78, 132409/1.
47. Hale, R. L.; Lu, A. T.; Myers, D. J.; Rabinowitz, J. D.; Wensley, M. J. Thin-film drug delivery device. . 2007.
48. Kratschmer, W.; Lamb, L. D.; Fostiropoulos, K.; Huffman, D. R. *Nature* **1990**, 347, 354.
49. Dillon, A. C. *Nature* **1997**, 386, 377.
50. Gadd, G. E. *Science* **1997**, 277, 933.
51. Collins, P. G.; Zettl, A.; Bando, H.; Thess, A.; Smalley, R. E. *Science* **1997**, 278, 100.
52. Ghosh, S.; Sood, A. K.; Kumar, N. *Science* **2003,** 299, 1042.
53. Wagner, H. D.; Lourie, O.; Feldman, Y.; Tenne, R. *Appl. Phys. Lett.* **1998**, 72, 188.
54. Tanev, P. T.; Pinnavaia, T. J. *Science* **1995**, 267, 865.
55. Forster, S.; Antonietti, M. *Adv. Mater.* **1998**, 10, 195.
56. Cundy, C. S.; Cox, P. A. *Chem. Rev.* **2003**, 103, 663.
57. Jansen, J. C., In *Introduction to Zeolite Science and Pratice.*, Bekkum, H. v.; Flanigen, E. M.; Jacobs, P. A.; Jansen, J. C., Eds. Elsevier: Amsterdam, **2001**.
58. Avnir, D.; Levy, D.; Reisfeld, R. *J. Phys. Chem.* **1984**, 88, 5956.
59. Levy, D.; Einhorn, S.; Avnir, D. J. *J. Non-Cryst. Solids* **1989**, 113, 137.
60. Siegel, R. W.; Chang, S. K.; Ash, B. J.; Stone, J.; Ajayan, P. M.; Doremus, R. W.; Schadler, L. *Scripta Mater.* **2001**, 44, 2063.
61. Tu, J. P.; Wang, N. Y.; Yang, Y. Z.; Qi, W. X.; Liu, F.; Zhang, X. B.; Lu, H. M.; Liu, M. S. *Mater. Lett.* **2002**, 52, 452.
62. Haruta, M.; Delmon, B. *J. Chim. Phys.* **1986**, 83, 859.
63. Murray, C. B.; Norris, D. J.; Bawendi, M. G. *J. Am. Chem. Soc.* **1993**, 115, 8706.
64. Haruta, M.; Delmon, B. *J. Chim. Phys.* **1986**, 83, 859.

65. Hench, L. L.; West, J. K. *Chem. Rev.* **1990**, 90, 33.
66. Brinker, C. J.; Scherer, G. W., *Sol-Gel Science: The Physics and Chemistry of Sol-Gel Processing.* Academic Press, Inc.: San Diego, **1990**.
67. Brinker, C. J.; Scherer, G. W., *Sol-Gel Science.* Academic Press: New York, 1989.
68. Hench, L. L.; West, J. K. *Chem. Rev.* **1990**, 90, 33.
69. Klein, L. C., *Sol-Gel Technology for Thin Films, Fibers, Preforms, Electronics and Specialty Shapes.* Noyes Publications: Park Ridge, NJ, **1988**.
70. Byrappa, K.; Yoshimura, M., *Hydrothermal Technology for Crystal Growth (Materials and Processing Technology).* Noyes Publications Park Ridge, New Jersey, **2001**.
71. Blander, M., *Molten Salt Chemistry*. Interscience Publishers: New York, **1964**.
72. Bloom, H., *The chemistry of molten salts;an introduction to the physical and inorganic chemistry of molten salts and salt vapors.* W. A. Benjamin: New York, **1967**.
73. Mao, Y.; Banerjee, S.; Wong, S. S. *J. Am. Chem. Soc.* **2003**, 125, 15718.
74. Mao, Y.; Wong, S. S. *Adv. Mater.* **2005**, 17, 2194.
75. Park, T.-J.; Papaefthymiou, G. C.; Moodenbaugh, A. R.; Mao, Y.; Wong, S. S. *J. Mater. Chem.* **2005**, 15, 2099.
76. Jones, A. C.; Hitchman, M. L., *Chemical Vapour Deposition: Precursors, Processes and Applications.* Royal Society of Chemistry: Cambridge, **2009**.
77. Fanun, M., *Microemulsion:Properties and Applications*. CRC Press: London, **2008**.
78. Campbell, S. A., *The Science and Engineering of Microelectronic Fabrication.* Oxford University Press: Oxford, **2001**.
79. Xia, Y.; Whitesides, G. M. *Angew. Chem. Int. Ed.* **1998**, 37, 551.
80. Xia, Y.; Whitesides, G. M. *Annu. Rev. Mater. Sci.* **1998**, 28, 153.
81. Xia, Y.; Whitesides, G. M. *Annu. Rev. Mater. Sci.* **1998**, 28, 153.
82. Xia, Y. *Adv. Mater*, **2004**, 16 (special issue dedicated to George Whitesides).
83. Eigler, D. M.; Schweizer, E. K. *Nature* **1990**, 344, 524.
84. Baur, C.; Bugacov, A.; Koel, B. E.; Madhukar, A.; Montoya, N.; Ramachandran, T. R.; Requicha, A. A. G.; Resch, R.; Will, P. *Nanotechnology* **1998**, 9, 360.
85. Bentzon, M. D.; Tholen, A. *Ultramicroscopy* **1990**, 38, 105.
86. Huang, Y.; Duan, X.; Wei, Q.; Lieber, C. M. *Science* **2001**, 291, 630.
87. Niitzenadel, C.; Ziittel, A.; Chartouni, D.; Schmid, G.; Schlapbach, L. *Eur. Phys. J.* **2000**, 245, D8.
88. Robertson, D. H.; Brenner, D. W.; Mintmire, J. W. *Phys. Rev. B* **1992**, 45, 12592.
89. Reed, M. A.; Zhou, C.; Muller, C. J.; Burgin, T. P.; Tour, J. M. *Science* **1997**, 278, 252.
90. Cui, X. D.; Primak, A.; Zarate, X.; Tomfohr, J.; Sankey, O. F.; Moore, A. L.; Moore, T. A.; Gust, D.; Harris, G.; Lindsay, S. M. *Science* **2001**, 294, 571.
91. Collier, C. P.; Mattersteig, G.; Wong, E. W.; Luo, Y.; Beverly, K.; Sampaio, J.; Raymo, F. M.; Stoddart, J. F.; Heath, J. R. *Science* **2000**, 289, 1172.
92. Collier, C. P.; Wong, E. W.; Belohradsky, M.; Raymo, F. M.; Stoddart, J. F.; Kuekes, P. J.; Williams, R. S.; Heath, J. R. *Science* **1999**, 285, 391.
93. Tans, S. J.; Verschueren, A. R. M.; Dekker, C. *Nature* **1998**, 393, 49.
94. Liang, W.; Shores, M. P.; Bockrath, M.; Long, J. R.; Park, H. *Nature* **2002**, 417, 725.
95. Postma, H. W. C.; Peepen, T.; Yao, Z.; Grifoni, M.; Dekker, C. *Science* **2001**, 293, 76.
96. Liu, X.; Lee, C.; Zhou, C.; Han, J. *Appl. Phys. Lett.* **2001**, 79, 3329.

97. Kong, J.; Franklin, N. R.; Zhou, C.; Chapline, M. G.; Peng, S.; Cho, K.; Dai, H. *Science* **2000**, 287, 622.
98. Collins, P. G.; Arnold, M. S.; Avouris, P. *Science* **2001**, 292, 706.
99. O'Regan, B.; Grätzel, M. *Nature* **1991**, 353, 737.
100. Gur, I.; Fromer, N. A.; Geier, M. L.; Alivisatos, A. P. *Science* **2005**, 310, 462.
101. Hashmi, A. S. K.; Hutchings, G. J. *Angew. Chem. Int. Ed.* **2006**, 45, 7896.
102. Noda, S.; Tomoda, K.; Yamamoto, N.; Chutinan, A. *Science* **2000**, 289, 604.
103. Briner, A.; Wehrspohn, R. B.; Gosele, U.; Busch, K. *Adv. Mater.* **2001**, 13, 377.
104. Wanke, M. C.; Lehmann, O.; Muller, K.; Wen, Q. Z.; Stuke, M. *Science* **1997**, 275, 1284.
105. Xia, Y.; Gates, B.; Yin, Y.; Lu, Y. *Adv. Mater.* **2000**, 12, 693.
106. Pankhurst, Q. A.; Conolly, J.; Jones, S. K.; Dobson, J. *J. Phys. D: Appl. Phys.* **2003**, 36, R167.
107. Niemeyer, C. M.; Mirkin, C. A., *Nanobiotechnology: Concepts, Applications and Perspectives.* Wiley-VCH: Weinheim, **2004**.
108. Zhou, H.; Park, T.-J.; Wong, S. S. *J. Mater. Res.* **2006**, 21, 2941.
109. Zhou, H.; Mao, Y.; Wong, S. S. *J. Mater. Chem.* **2007**, 17, 1707.
110. Zhou, H.; Mao, Y.; Wong, S. S. *Chem. Mater.* **2007**, 19, 5238.
111. Zhou, H.; Wong, S. S. *ACS Nano* **2008**, 2, 944.
112. Zhou, H.; Yiu, Y.; Aronson, M. C.; Wong, S. S. *J. Solid State Chem.* **2008**, 181, 1539.
113. Zhou, H.; Zhou, W.-P.; Adzic, R. R.; Wong, S. S. *J. Phys. Chem. C* **2009**, 113, 5460.

Chapter II Sol-Gel synthesis of $Bi_2Ti_2O_7$ nanotubes and their photocatalytic properties

2.1 Introduction

2.1.1 Pyrochlore

Pyrochlore is the name of a solid solution $(Na,Ca)_2Nb_2O_6(OH,F)$. The name is derived from the Greek πῦρ, *fire*, and χλωρός, *green* because it typically turns green upon ignition in classic blowpipe analysis.

Pyrochlore is also a more generic term for the pyrochlore crystal structure (F*d3m*). The general formula is $A_2B_2O_7$. The structure can best be summarized as $A_2B_2O_6O'$, comprising two interpenetrating sublattices with the formulae of A_2O' and BO_6, in other words, a juxtaposition of two different types of cationic coordination (Figure 2.1). A number of materials belonging to this family of oxides have been successfully synthesized including $Cd_2V_2O_7$, $Cd_2Re_2O_7$, $Tl_2Ru_2O_7$, and $Zn_2Nb_2O_7$.[1-4]

The pyrochlore structure shows varied physical properties and ranges from serving as electronic insulators, ($La_2Zr_2O_7$), ionic conductors, ($Gd_{1.9}Ca_{0.1}Ti_2O_{6.9}$), metallic conductivity, ($Bi_2Ru_2O_{7-y}$), mixed ionic and electronic conductors, spin ice systems ($Dy_2Ti_2O_7$), spin glass systems ($Y_2Mo_2O_7$), to superconducting materials ($Cd_2Re_2O_7$).

2.1.2 $Bi_2Ti_2O_7$

$Bi_2Ti_2O_7$ is a particularly interesting pyrochlore oxide, characterized by the presence of Ti-O octahedral frameworks coupled with Bi-O tetrahedral units. The structure analysis of bismuth titanate ($Bi_2Ti_2O_7$) indicates that it possesses a face-centered cubic structure with F*d3m* symmetry (a = 20.68 Å).

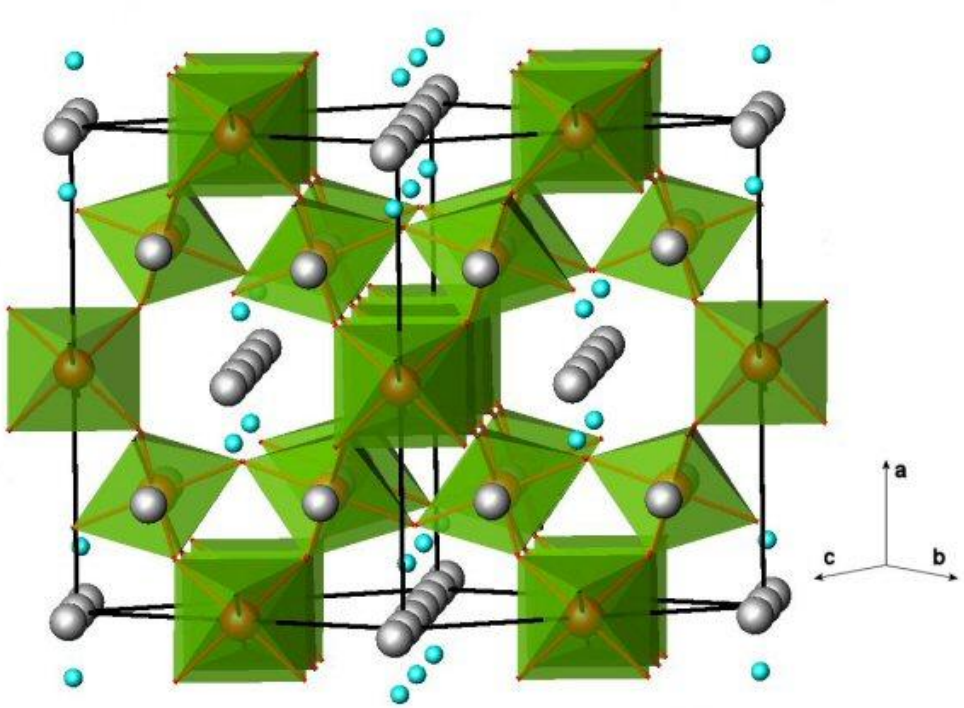

Figure 2.1 Structure of pyrochlore, showing rings of BO_6 octahedra in green, *A* cations in grey and non-polyhedral oxygens in cyan.

Bismuth titanate is interesting for a number of reasons. This material has been considered as a highly promising high-*k* dielectric material because of its high permittivity and low leakage current density. Specifically, because of its relatively high-*k* dielectric properties (dielectric constant, k = 110 -160), $Bi_2Ti_2O_7$ has attracted considerable attention as a useful component of (a) gate insulators in advanced metal-oxide semiconductor (MOS) transistors,[5-7] (b) storage capacitors in dynamic random access memory (DRAM) applications, and (c) buffer layers to improve the electrical properties of ferroelectrics such as $Pb(Zr_{0.5}Ti_{0.5})O_3$ (PZT) and $Bi_4Ti_3O_{12}$.[8-10] Moreover, it has recently been found that bismuth titanate can be used for oxidizing and thereby destroying environmentally harmful organic contaminants in water.[11]

2.1.3 Sol-gel processing

Interest in the sol-gel processing of inorganic ceramic and glass materials began in the mid-1800s when people found that the acid catalyzed hydrolysis of tetraethyl orthosilicate (TEOS), $Si(OC_2H_5)_4$, yields SiO_2 in the form of a "glass-like material".

Besides SiO_2, the controlled hydrolysis of alkoxides has also been used to produce submicrometer TiO_2, doped TiO_2, ZrO_2, and doped ZrO_2, doped SiO_2 and $SrTiO_3$.[12-16] Namely both glass and polycrystalline ceramic fibers have been prepared by using the sol-gel method including Al_2O_3, ZrO_2, ThO_2, MgO, TiO_2, $ZrSiO_4$, and $3Al_2O_3$ $2SiO_2$ fibers.[17-22] In addition, a variety of coatings and films have been developed by using the sol-gel method.[23, 24]

The advantages of sol-gel processing are higher purity, higher homogeneity, and lower processing temperatures as compared with traditional glass melting or ceramic powder methods.[24]

For example, consider the processing steps (Figure 2.2) involved are briefly summarized below. Take synthesis of SiO_2 by hydrolysis of alkoxide as example.[25]

Step 1: Mixing. A liquid alkoxide precursor, such as $Si(OR)_4$, where R is CH_3, C_2H_5, or C_3H_7, is hydrolyzed by mixing with water.

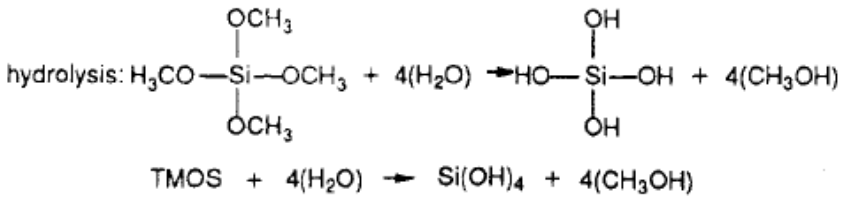

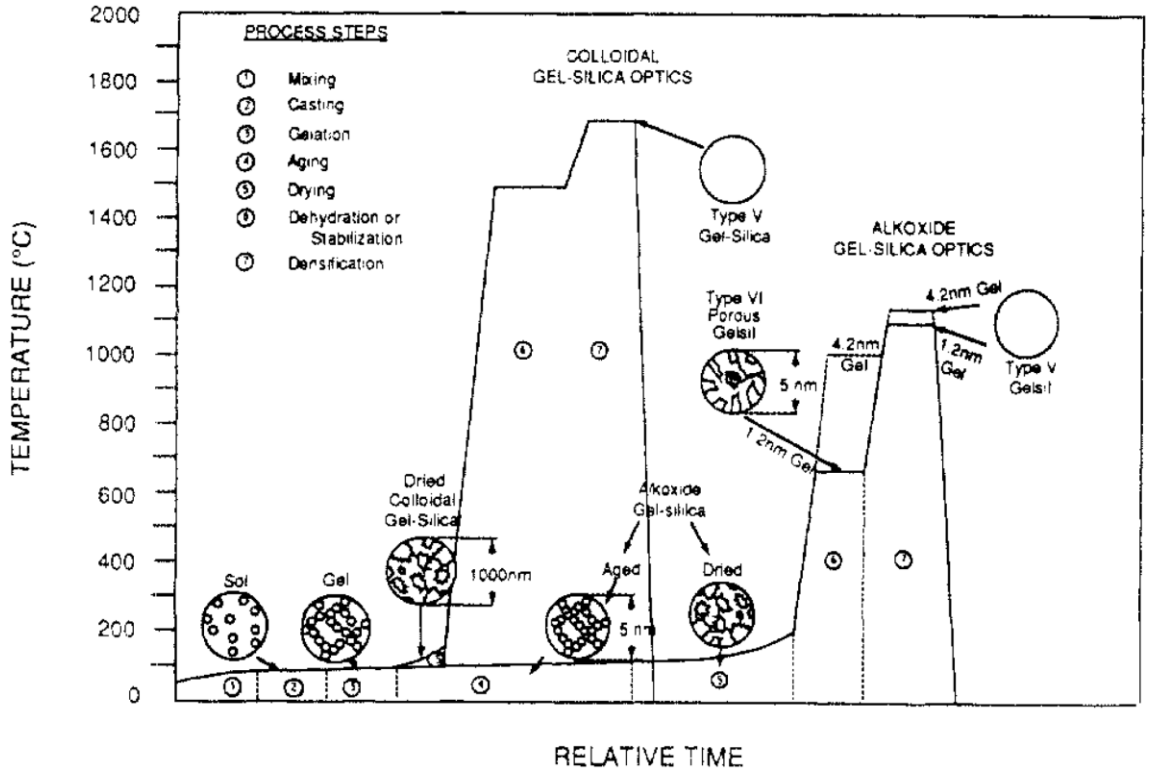

Figure 2.2 Gel-silica glass process sequence.[25]

The hydrated silica tetrahedral complex interacts in a condensation reaction, forming ΞSi-O-SiΞ bonds.

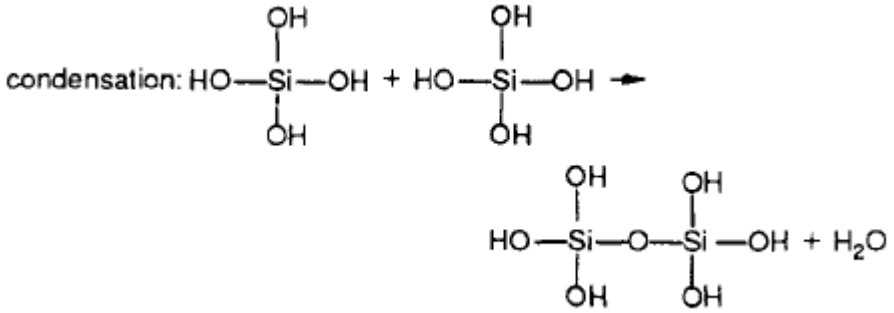

Then a polycondensation reaction results in a SiO_2 network. Both water and alcohol expelled from the reaction remains in the pores of the network. The size of the sol particles and the cross-linking within the particles depend upon the pH and ratio of water to alkoxide among other variables.

Step 2; Casting. The sol can be cast into a mold due to its low viscosity. The mold must be able to avoid adhesion of the gel.

Step 3: Gelation. The condensed silica species link together to become a three-dimensional network gradually. Upon gelation, the viscosity increases sharply, and a solid object assumes the shape of the mold. With appropriate control of the viscosity of the sol, fibers can be pulled apart or spun as gelation occurs.

Step 4: Aging. Aging of a gel, also called syneresis. During aging, the polycondensation process continues along with the localized solution and reprecipitation of the gel network, which increases the thickness of interparticle necks and decreases porosity.

Step 5: Drying. During drying, the liquid is removed from the interconnected pore network. If the liquid is removed as a gas phase from the gel network under hypercritical conditions (i.e. critical-point drying), the network does not collapse and a low density aerogel is produced. If the pore liquid is removed at or near ambient pressure by thermal evaporation and shrinkage occurs, the monolith is called an xerogel.

Step 6: Dehydration or Chemical Stabilization. A dried gel still contains a very large concentration of chemisorbed hydroxyls on the surface of the pores. The thermal treatment in the range of 500 – 800 ℃ desorbs the hydroxyls and thereby decreases the contact angle and the sensitivity of the gel to rehydration stresses, resulting in a stabilized gel.

Step 7: Densification. Heating the porous gel at high temperatures causes densification to occur. The pores are eliminated and the density ultimately becomes equivalent to that of fused quartz or fused silica. The porous gel is transformed to a dense glass when all pores are eliminated.

The advantages of sol-gel process are: (1) ease of preparation and cost effectiveness, (2) lower temperature calcinations, (3) ease of doping other elements in a homogeneous manner, (4) ease of preparation of composite with organic materials, (5) ease of structure control (i.e. nanoparticles, film, fiber, porous, etc.) with various additives, and (6) commercial availability of the starting materials, such as alkoxide, chloride, oxysulfate..

However, the disadvantages of this method include: (1) starting materials are often expensive, (2) removal of solvent and organic byproducts from gel is relatively difficult, and (3) volume shrinkage upon sol-gel transition is large.

2.1.4 Anodized aluminum oxide (AAO) templating

The AAO membranes can be synthesized by electrochemically anodizing a sheet of aluminum in a certain acid electrolyte under specific conditions. It has an almost perfectly regular ordered porous structure with controlled pore size and thickness, which is on a thin barrier layer alumina (BLA). It is suitable for a number of applications, such as DNA translocation, size-exclusive filtration, gas separation, and photonic crystals.[26-29] The uniformly arranged channels in AAO renders it key for another important application—i.e. as a template for the synthesis of 1D nanostrucutres. (Figure 2.3). A variety of materials have been examined for use with this template, with typical examples as diverse as metals, semiconductors, ceramics, and organic polymers. The only requirement seems to be that the material can be compatibly loaded into the pores using a method based on vapor-phase sputtering, liquid phase injection, or solution-phase chemical or electrochemical deposition. In our current work, we applied a sol-gel technique with the usage of an AAO template and we were able to obtain $Bi_2Ti_2O_7$ nanotubes.

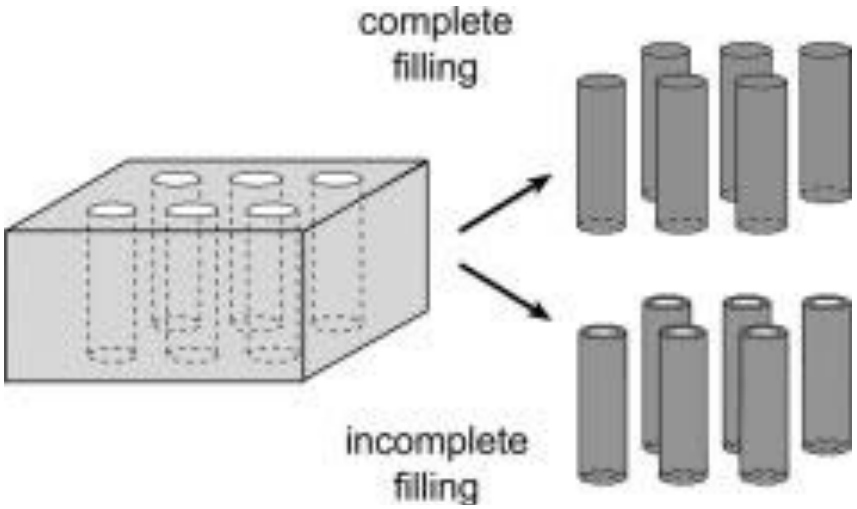

Figure 2.3 Schematic drawing showing the formation of nanowires and nanotubes by filling and partially filling of the pores within a porous membrane with the desired material or a precursor to this material.[30]

2.1.5 Current Work

Despite the evident importance of $Bi_2Ti_2O_7$ as a functional material, very few reports of nanoscale structural motifs of these materials have appeared. Furthermore, although the synthesis of a number of titania as well as hydrogen titanate, potassium hydrogen titanate, and sodium hydrogen titanate nanotubes has been readily achieved,[31-38] there have not been any viable syntheses of one-dimensional (1D) nanostructures of $Bi_2Ti_2O_7$ reported thus far. Indeed, 1D nanostructures are fundamentally interesting because they are the lowest dimensional anisotropic structures that can be used for the efficient transport of electrons and optical excitations.[30, 39] The importance of morphology-dependent properties has been previously highlighted, for example, with TiO_2 nanotubes and nanowires, which were reported to possess a higher photocatalytic activity as compared with TiO_2 nanoparticles.[40, 41] However, manipulation and property investigation of 1D nanostructures of metal oxides have been relatively hampered by difficulties associated with the reliable, reproducible fabrication of these structures with well-controlled size, dimension, morphology, phase purity, and chemical composition.

In the current work, we address these issues by employing a template-based technique towards the synthesis of $Bi_2Ti_2O_7$ nanotubes. The advantages of the methodology used include (a) the practicality of the sol-gel process, (b) the relative simplicity of the technique, and (c) the general versatility of the method in the preparation of high aspect ratio nanostructures.[42]

2.2 Experimental Section

2.2.1 Preparation

In a typical synthesis, $5x10^{-3}$ moles of bismuth nitrate pentahydrate, $Bi(NO_3)_3\ 5H_2O$, was initially dissolved in 5 mL of glacial acetic acid, and then an equimolar amount of titanium isopropoxide, $Ti(OC_3H_7)_4$, was added to the mixture with constant stirring. Approximately 0.5 to 25 ml of 2-methoxyethanol was subsequently added as a co-solvent to adjust the viscosity and surface tension of the as-prepared transparent sol. An AAO template (Whatman Anodisc®) containing channels with a pore size of 200 nm was soaked within the sol for 5 min and then, heated at 70 ℃ for 5 h to speed up the hydrolysis process. To remove residual organics, the template was heated at 400 ℃ for 30 min in a tube furnace with a slow heating rate of 5 ℃/min and further annealed at 600 ℃ for 1 h in air to obtain crystalline samples. $Bi_2Ti_2O_7$ nanotubes were isolated by dissolving the alumina template in a 6 M NaOH solution for 24 h. Purified nanotubes were collected via centrifugation after washing first with distilled water and then with ethanol for several times, respectively. A bulk sample was synthesized using an identical experimental procedure, but in the absence of an alumina (AAO) template.

2.2.2 Characterizaion

X-ray diffraction. See section 1.7.1.

Electron Microscopy. See section 1.7.2.

UV-visible Spectroscopy. See section 1.7.3.

Photocatalytic Activity. To test the photocatalytic efficiency of as-prepared bismuth titanate nanotubes, a solution mixture containing 10 mg/L methyl orange in the presence of 1 mg/L of $Bi_2Ti_2O_7$ nanotubes in water was prepared. Prior to irradiation, the suspensions were sonicated for 10 min and then magnetically stirred in the dark for 30 min to establish an adsorption/degradation equilibrium.[11] The suspension was subsequently irradiated under UV light (maximum emission wavelength at 365 nm) at a ~5 cm separation distance. Analogous control experiments were performed either without $Bi_2Ti_2O_7$ (blank) or in the presence of a bulk sample. Concentrations of methyl orange in the supernatant aliquots were subsequently analyzed by measuring the absorbance at 464 nm using a Thermospectronics UV1 spectrometer with 10-mm path length quartz cells.

2.3 Results and Discussion

The phase purity and crystallinity of both $Bi_2Ti_2O_7$ nanotubes and bulk powder were examined by XRD (Figure 2.4A-C). Essentially no impurity peaks were noted in the XRD pattern. As expected, the pattern could be well indexed to the cubic structure of $Bi_2Ti_2O_7$ (*Fd3m*, JCPDS #32-0118).[43] The lattice constant was calculated to be a = 20.69 Å, in good agreement with the literature value of a = 20.68 Å.

Figure 2.5A and B shows SEM images of $Bi_2Ti_2O_7$ nanotubes, prepared in an AAO template. The image of the corresponding bulk sample is shown in Figure 2.5C. These results suggest that as-synthesized nanotubes are straight and smooth and that they may occur as aggregated bundles. The outer diameters of these nanotubes range from 200 to 330 nm with lengths varying from 7 to 12 μm. The EDS pattern confirms the presence of Bi, Ti and O, as expected. The Al peak likely originates from a residual amount of Al_2O_3 derived from the template.

From TEM images (Figure 2.6A and inset to Figure 2.6A), one can gain insights into the morphology and diameter of $Bi_2Ti_2O_7$ nanotubes. The outer diameter measured is about 180 to 320 nm in agreement with SEM results; the wall thickness of these tubes measures about 6 nm. SAED data (inset to Figure 2.6B), taken from an individual $Bi_2Ti_2O_7$ nanotube, show ring patterns, characteristic of the presence of polycrystalline as well as amorphous domains in our as-prepared $Bi_2Ti_2O_7$ nanotubes. A typical HRTEM image (Figure 2.6B) further confirms the crystalline nature of our as-prepared nanotubes, showing the presence of a typical crystalline domain with an interplanar spacing of about 3.14 Å, which can be indexed to the (622) ring in the SAED spectrum.

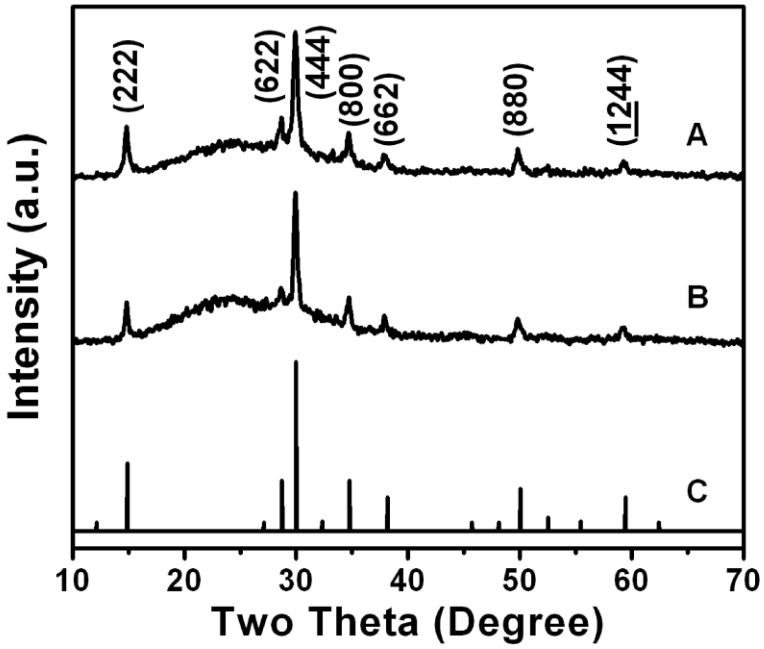

Figure 2.4 X-ray diffraction (XRD) patterns of (A) $Bi_2Ti_2O_7$ nanotubes; of (B) $Bi_2Ti_2O_7$ bulk; and of (C) a $Bi_2Ti_2O_7$ standard JCPDS No. 32-0118.

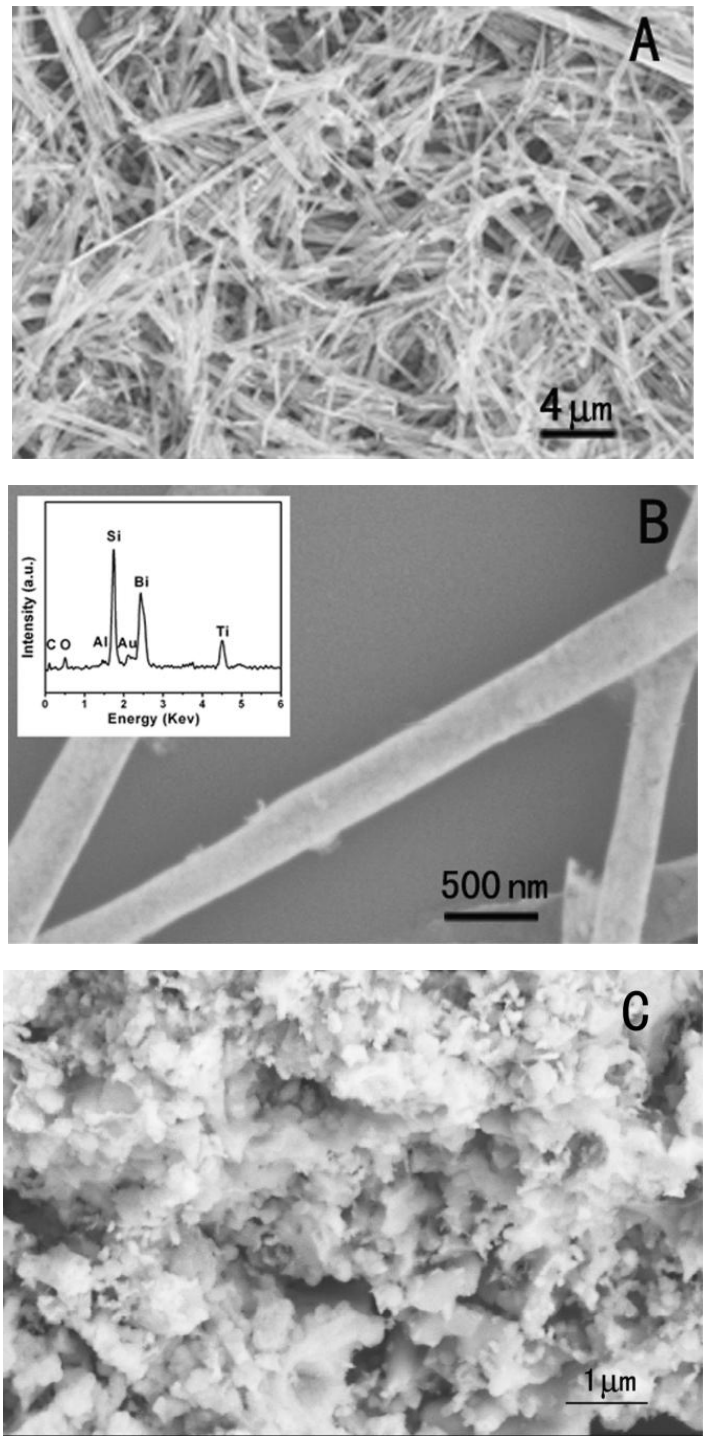

Figure 2.5. (A) and (B) Scanning-electron-microscopy (SEM) images of $Bi_2Ti_2O_7$ nanotubes. (A) and (B) are low and high-magnification SEM images, respectively, of bismuth titanate. Inset of (B) is an EDS pattern of $Bi_2Ti_2O_7$ nanotubes. The Si peak originates from the silicon substrate; Au can be attributed to the as-applied coating; (C) SEM image of a bulk $Bi_2Ti_2O_7$ sample.

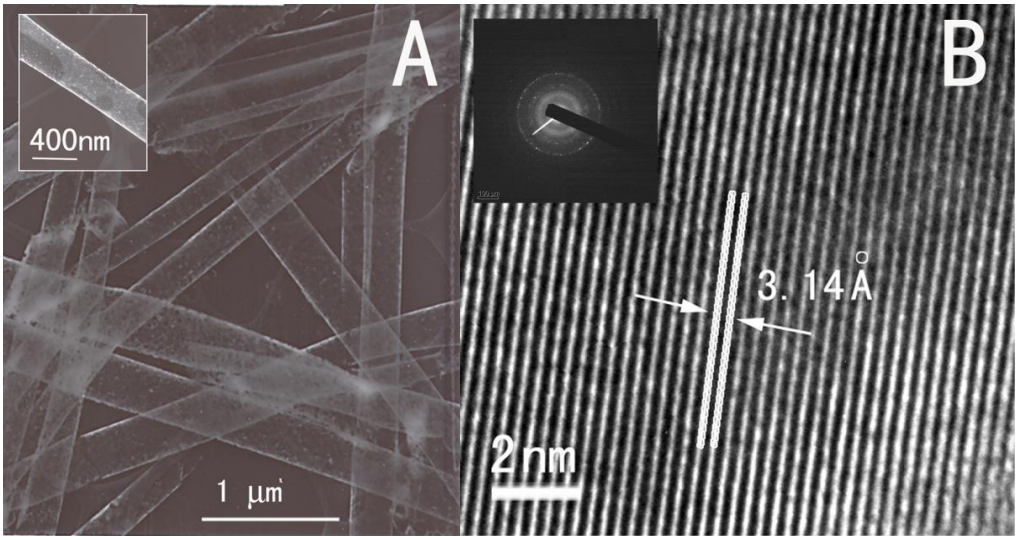

Figure 2.6 (A) TEM and (B) HRTEM images, respectively, of $Bi_2Ti_2O_7$ nanotubes. Inset of (A) is a high-magnification TEM image whereas inset of (b) is a SAED pattern of $Bi_2Ti_2O_7$ nanotubes.

UV-visible spectra of as-prepared $Bi_2Ti_2O_7$ nanotubes and bulk materials are shown in Figure 2.7. Both of these samples show signals typical of an indirect gap semiconductor with a broad band adsorption noted, likely due to an intrinsic band transition.[11] Moreover, we note that the peak of the adsorption band of the nanotubes (Figure 2.7A) is blue shifted relative to that of bulk sample (Figure 2.7B). This morphology–driven shift to higher energies has also been reported previously for TiO_2 nanowires and has been attributed to confinement effects.[41]

The photocatalytic activity of our as-prepared $Bi_2Ti_2O_7$ nanotubes was evaluated by measuring the degradation of methyl orange at 464 nm upon photoexcitation with UV light at 365 nm. Our data clearly show that both nanotubes and bulk sample are active photocatalysts, as illustrated in Figure 2.8 (top). In addition, the nanotube samples exhibit a higher photoactivity as compared with the bulk sample. This enhancement is most likely related to an increase in the surface area and crystallinity of the nanotubes. In addition, because the absorption spectrum of $Bi_2Ti_2O_7$ nanotubes is shifted to higher energies with respect to the bulk, the corresponding increase in sensitivity of these tubes towards that part of the optical spectrum may also account for the larger associated photoactivity noted.

The photocatalytic decolorization of methyl orange can be described as a pseudo-first-order reaction with the kinetics expressed by the equation, $\ln(C_0/C) = kt$, where C_0 is the initial concentration of aqueous methyl orange, C is the concentration of aqueous methyl orange at a given reaction time t, and k is the apparent reaction rate constant. We note that a linear relationship exists between concentration and absorbance measured.[11] From our data in Figure 2.8 (bottom), we were able to calculate apparent reaction rate constants of the nanotubes and of the corresponding bulk sample to be 6.88×10^{-3} min^{-1} and 3.62×10^{-3} min^{-1} respectively. Hence, quantitatively, these data support the higher photoactivity of $Bi_2Ti_2O_7$ nanotubes as compared with the bulk.

Bismuth nitrate and titanium alkoxide (e.g. butoxide or isopropoxide) are typically used as precursors in the synthesis of various bismuth titanates (including $Bi_2Ti_2O_7$ and $Bi_4Ti_3O_{12}$) using the sol-gel method.[44-46] Moreover, a typical solvent in these experiments is glacial acetic acid. Reports in the literature as well as our own experimental data suggest that in the absence of a stabilizing co-solvent, the sol is unstable and a white precipitate forms, in the absence of annealing, after about 20 h, an observation attributable to the reaction of Bi^{3+} and H_2O yielding $BiONO_3$. Polydisperse bismuth titanate particles can be obtained upon normal annealing to 600 ℃.

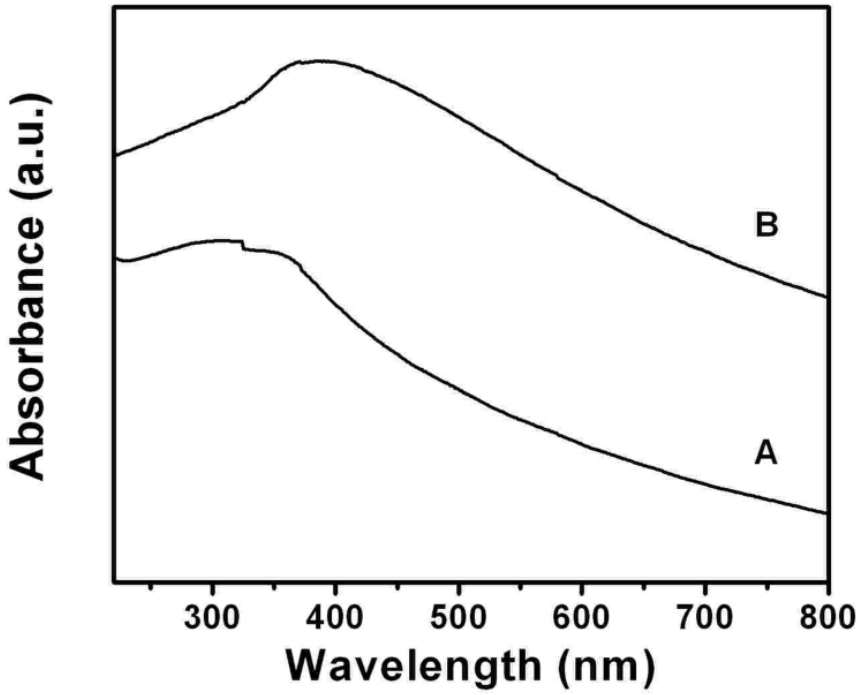

Figure 2.7. UV-Visible spectra of as-prepared (A) $Bi_2Ti_2O_7$ nanotubes and of (B) the corresponding $Bi_2Ti_2O_7$ bulk.

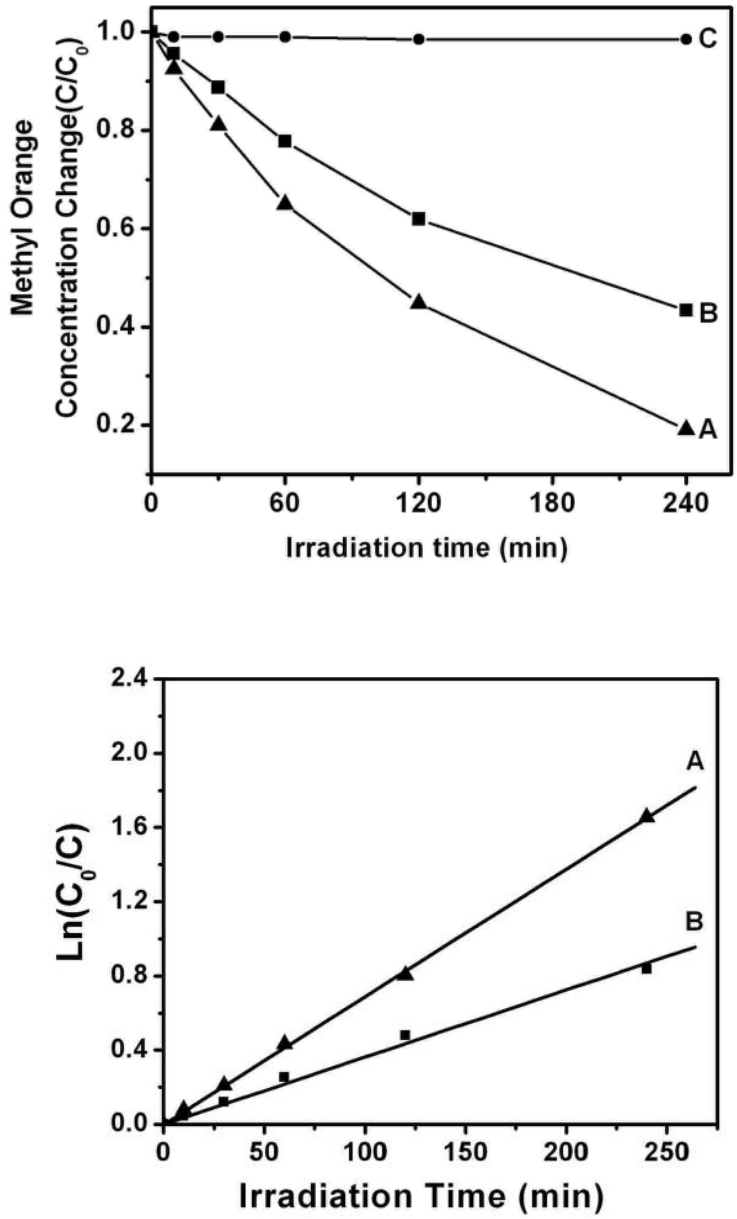

Figure 2.8 Top: Photodegradation of Methyl Orange in the presence of samples; bottom: Plot of the change in concentration of methyl orange as a function of irradiation time. (A) $Bi_2Ti_2O_7$ nanotubes; (B) $Bi_2Ti_2O_7$ bulk; and (C) blank control.

To adjust the viscosity and surface tension of the reaction solution as well as to prevent hydrolysis of bismuth nitrate, a number of additional co-solvents were independently added. For instance, several drops of ethanolamine were used to adjust the pH of the solution to a value between pH 2.5 and 4, whereas 2-methoxyethanol was added in varying volume ratios in order to stabilize the precursors. In our experiment, with 2-methoxyethanol, we were able to generate uniform, smooth $Bi_2Ti_2O_7$ nanotubes at volume ratios of alcohol to acid ranging from 5 : 10 to 50 : 10. Upon the addition of 2-methoxyethanol, the precursor sol was found to be stable for more than one month as compared with a sol left standing for 20 h without 2-methoxyethanol.

We performed additional experiments with different ratios of 2-methoxyethanol : glacial acetic acid (from 1 : 10 to 50 : 10 volume ratio mixtures) to fully investigate the solvent effect upon product morphology. Figure 2.8 clearly shows that with increasing amounts of 2-methoxyethanol, as-prepared tubes grow increasingly longer and possess noticeably smoother surfaces. In fact, if no 2-methoxyethanol is added (Figure 2.9A), as-prepared nanotubes are short (≤ 2 μm) and most of them appear fractured. Tubes synthesized with alcohol-to-acid volume ratios of 1:10 (Figure 2.9B) and 2:10 (Figure 2.9C) show similar behavior. Hence, we hypothesize that the addition of 2-methoxyethanol can significantly change the viscosity of the sol, and increase its wettability with respect to the inner pore surfaces of the AAO templates, thereby allowing for the generation of long, smooth nanotubes (Figure 2.9D-9F). We have additionally demonstrated that nanotubes can be generated in the total absence of glacial acetic acid (Figure 2.9G), though there is a fair amount of aggregation present.

We also studied the effect of changing the initial ratio of Bi precursor to Ti precursor. We found that if we changed the molar ratio of Bi to Ti from 1:1 to 2:1, we were still able to generate $Bi_2Ti_2O_7$. Increasing the annealing temperature from 650 to 750 ℃ made little difference in the resulting product. However, an additional temperature increase to 850 ℃ yielded the ferroelectric perovskite material, $Bi_4Ti_3O_{12}$ (Figure 2.10), in agreement with prior results concerning the phase transformation of $Bi_2Ti_2O_7$ to $Bi_4Ti_3O_{12}$ with increasing temperature.[47] We did note that after annealing at such a high temperature, the AAO template was more difficult to dissolve (even using a 10 M NaOH solution for one day had little effect), and hence, more challenging to separate from the actual nanotube sample.

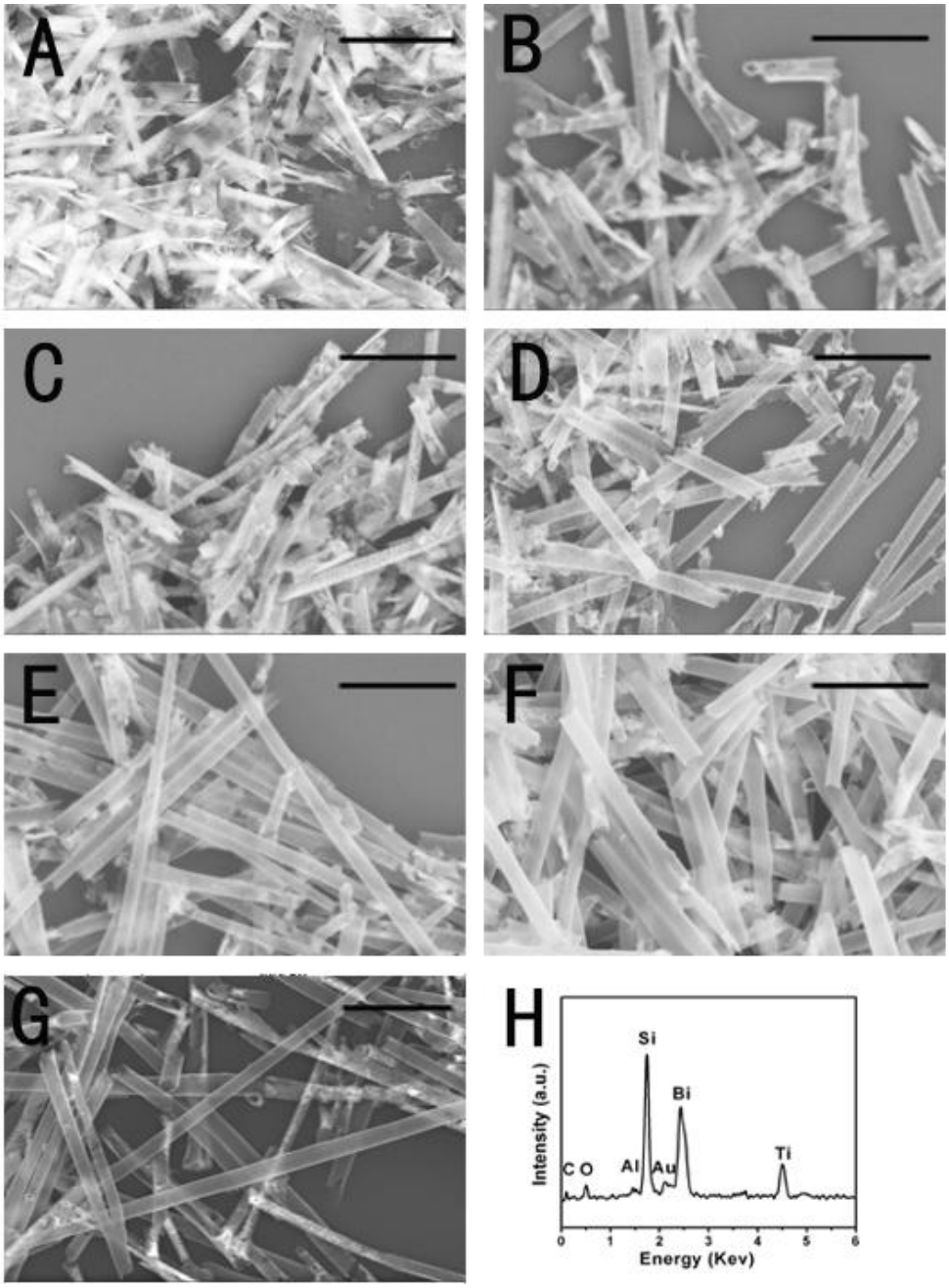

Figure 2.9 SEM images of $Bi_2Ti_2O_7$ nanotubes, synthesized in solvents containing varying volume ratios of 2-methoxyethanol to glacial acetic acid. (a) acetic acid alone; (b) 1:10; (c) 2:10; (d) 5:10; (e) 10:10; (f) 50:10; (g) 2-methoxyethanol alone; (h) typical EDS pattern. The Si peak originates from the silicon substrate; Au can be attributed to the as-applied coating. Scale bar represents 2 μm.

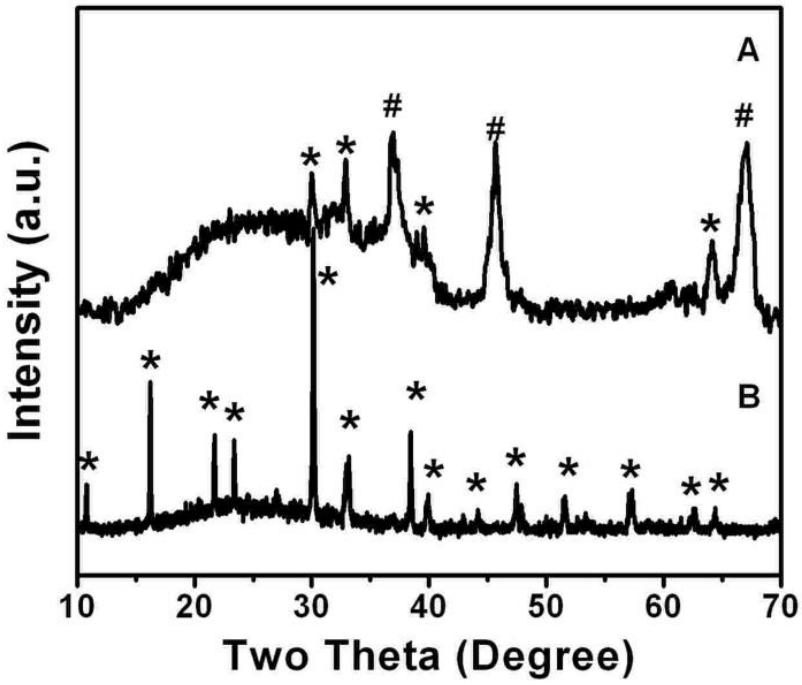

Figure 2.10 XRD patterns of (A) an as-prepared sample using an AAO template and of (B) a bulk sample upon annealing at 850 ℃. ★ and # represent signals associated with $Bi_4Ti_3O_{12}$ and Al_2O_3, respectively.

2.4 Conclusions

The current work describes the first synthesis of $Bi_2Ti_2O_7$ nanotubes, achieved using a sol-gel technique in the presence of an alumina template. The outer diameters of as-prepared bismuth titanate nanotubes range from 180 to 330 nm; the wall thickness is approximately 6 nm. The effects of solvent as well as of precursor ratio were also analyzed, with data suggesting a high degree of parameter control over the dimensions and morphology of bismuth titanate nanotubes. Results confirmed the presence of a phase transformation from $Bi_2Ti_2O_7$ to $Bi_4Ti_3O_{12}$ upon increasing annealing temperature. Kinetic studies on the photocatalytic decolorization of methyl orange suggested a higher photocatalytic efficiency of 1D nanoscale motifs of bismuth titanate as compared with the bulk material. Future research will focus on structure-property correlations as well as on dielectric measurements of these important high k dielectric, insulating materials.

2.5 References

1. Sleight, A. W. *Mater, Res. Bull.* **1974**, 9, 1185.
2. Longo, J. M.; Donohue, P. C.; Batson, D. A. *Inorg. Synth.* **1973**, 14, 146.
3. Wainer, E.; Wentworth, C. *J. Am. Ceram. Soc.* **1952**, 35, 207.
4. Lee, S.; Park, J.-G.; Adroja, D. T.; Khomskil, D.; Streltsov, S.; McEwen, K. A.; Sakai, H.; Yoshimura, K.; Anisimov, V. I.; Mori, D.; Kanno, R.; R, I. *Nat. Mater.* **2006**, 5, 471.
5. Hwang, G. W.; Kim, W. D.; Min, Y.-S.; Cho, Y. J.; Hwang., C. S. *J. Electrochem. Soc.* **2006**, 153, F20.
6. Yang, X. N.; Huang, B. B.; Wang, H. B.; Shang, S. X.; Yao, W. F.; Wei, J. Y. *J. Cryst. Growth* **2004**, 270, 98.
7. Wang, S. W.; Wang, H.; Wu, X.; Shang, S.; Wang, M.; Li, Z.; Lu, W. *J. Cryst. Growth* **2001**, 224, 323.
8. Wu, X. M.; Wang, S. W.; Wang, H.; Wang, Z.; Shang, S. X.; Wang, M. *Thin Solid Films* **2000**, 370, 30.
9. Wang, S. W.; Wang, H.; Shang, S. X.; Huang, J.; Wang, Z.; Wang, M. *J. Cryst. Growth* **2000**, 217.
10. Wu, W.; Fumoto, K.; Oishi, Y.; Okuyama, M.; Hamakawa, Y. *Jpn. J. Appl. Phys.* **1996**, 35, 1560.
11. Yao, W. F.; Wang, H.; Xu, X. H.; Zhou, J. T.; Yang, X. N.; Zhang, Y.; Shang, S. X. *Appl. Catal. A* **2004**, 259, 29.
12. Barringer, E. A.; Bowen, H. K. *J. Am. Ceram. Soc.* **1982**, 65, C199.
13. Fegley, B., Jr.; Barringer, E. A., In *Better Ceramics Through Chemistry*, Brinker, C. J.; Clark, D. E.; Ulrich, D. R., Eds. Elsevier: New York, **1984**.
14. Fegley, B., Jr.; White, P.; Bowen, H. K. *Am. Ceram. Soc. Bull.* **1985**, 64, 1115.
15. Hardy, A.; Gowda, G.; McMahan, T. J.; Riman, R. E.; E., R. W.; Bowen, H. K., In *Ultrastructure Processing of Advanced Ceramics.*, Mackenzie, J. D.; Ulrich, D. R., Eds. Wiley: New York, **1988**.
16. Fegley, B., Jr.; Barringer, E. A.; Bowen, H. K. *J. Am. Ceram. Soc.* **1984**, 67, C113.
17. Carroll-Porczynski, C. Z., *Advanced Materials*. Chemical Publishing Co.: New York, **1962**.

18. McCreight, L. R.; Rauch, H. W., Sr.; Sutton, W. H., *Ceramic Fibers and Fibrous Composite Materials.* Academic Press: New York, **1965**.
19. Rauch, H. W., Sr.; Sutton, W. H.; McCreight, L. R., *Ceramic Fibers and Fibrous Composite Materials.* Academic Press: New York, **1968**.
20. Seufert, L. E. US. Patent No. 3,808,015, **1974**.
21. Miyahara, K.; Nakayama, N. Process for Producing Polycrystalline Oxide Fibers. US. Patent 4,159,205, **1979**.
22. Leitheiser, M.; Snowman, H. G. Non-Fused Alumina Based Abrasive Material. . US. Patent Appl. 145,383, **1980**.
23. Schroeder, H. *Opt. Acta* **1962,** 9, 249.
24. Mackenzie, J. D. *J. Non-Cryst. Solids* **1982**, 41, 1.
25. Hench, L. L.; West, J. K. *Chem. Rev.* **1990**, 90, 33.
26. Rabin, Y.; Tanaka, M. *Phys. Rev. Lett.* **2005**, 94, 148103.
27. Sano, T.; Iguchi, N.; Iida, K.; Sakamoto, T.; Baba, M.; Kawaura, H. A. *Phys. Lett.* **2003**, 83, 4438.
28. Lira, H. D. L.; Paterson, R. *J. Membr. Sci.* **2002**, 206, 375.
29. Masuda, H.; Yamada, M.; Matsumoto, F.; Yokoyama, S.; Mashiko, S.; Nakao, M.; Nishio, K. *Adv. Mater.* **2006**, 18, 213.
30. Xia, Y.; Yang, P.; Sun, Y.; Wu, Y.; Mayers, B.; Gates, B.; Yin, Y.; Kim, F.; Yan, H. *Adv. Mater.* **2003**, 15, 353.
31. Zhu, H.; Gao, X.; Lan, Y.; Song, D.; Xi, Y.; Zhao, J. *J. Am. Chem. Soc.* **2004**, 126, 8380.
32. Armstrong, A. R.; Armstrong, G.; Canales, J.; Bruce, P. G. *Angew. Chem. Int. Ed.* **2004**, 43, 2286.
33. Tian, Z. R.; Voigt, J. A.; Liu, J.; Mckenzie, B.; Xu, H. *J. Am. Chem. Soc.* **2003**, 125, 12384.
34. Kasuga, T.; Hiramatsu, M.; Hoson, A.; Sekino, T.; Niihara, K. *Adv. Mater.* **1999**, 11, 1307.
35. Zhao, L.; Steinhart, M.; Yu, J.; Gosele, U. *J. Mater. Res.* **2006**, 21, 685.
36. Peng, H.; Li, G.; Zhang, Z. *Mater. Lett.* **2005**, 59, 1142.
37. Mao, Y.; Banerjee, S.; Wong, S. S. *Chem. Commun.* **2003**, 408.
38. Mao, Y.; Kanungo, M.; Hemraj-Benny, T.; Wong, S. S. *J. Phys. Chem. B* **2006**, 110, 702.
39. Patzke, G. R.; Krumeich, F.; Nesper, R. *Angew. Chem. Int. Ed.* **2002**, 41, 2446.
40. Lai, Y.; Sun, L.; Chen, Y.; Zhuang, H.; Lin, C.; Chin, J. W. *J. Electrochem. Soc.* **2006**, 153, D123.
41. Mao, Y.; Wong, S. S. *J. Am. Chem. Soc.* **2006**, 128, 8217.
42. Park, T.-J.; Mao, Y.; Wong, S. S. *Chem. Commun.* **2004**, 2708.
43. Hou, Y.; Huang, Z.; Xue, J.; Wu, Y.; Shen, X.; Chu, J. *Appl. Phys. Lett.* **2005**, 86, 112905.
44. Wang, Z.; Yang, C. H.; Sun, D. L.; Hu, J. F.; Wang, H.; Chen, H. C.; Fang, C. S. *Mater. Sci. Eng. B* **2003**, 102, 335.
45. Gu, H.; Dong, C.; Chen, P.; Bao, D.; Kuang, A.; Li, X. *J. Cryst. Growth.* **1998**, 186, 403.
46. Joshi, P. C.; Mansingh, A. *Appl. Phys. Lett.* **1991**, 59, 2389.
47. Su, W.-F.; Lu, Y.-T. *Mater. Chem. Phys.* **2003**, 80, 632.

Chapter III Shape and size control in the molten salt synthesis of submicron $BaZrO_3$ cubes and spheres.

3.1 Introduction

In Chapter II, we discussed the synthesis of ternary metal oxide $Bi_2Ti_2O_7$ nanotubes via a sol-gel technique using an AAO template. In this chapter, we will talk about the synthesis of another ternary metal oxide $BaZrO_3$ by a molten salt method, which is a common technique to synthesize metal oxides.

3.1.1 Perovskite

Perovskites are a large family of crystalline ceramics that derive their name from a specific mineral known as perovskite, first described in the 1830s by the geologist Gustav Rose, who named it after the famous Russian mineralogist Count Lev Aleksevich von Perovski. Perovskites are oxides having the same crystalline structure as the natural mineral $CaTiO_3$, which is usually expressed as ABO_3.

The structure of a perovskite is usually depicted in pseudocubic form, as shown in Figure 3.1. The structure contains two cation sites in the crystal lattice: the larger cation (A) resides on the corners of the unit cell, and the smaller cation (B) is located in the center of the unit cell. The oxygen ions (O) are on the centers of the faces, and the structure is formed via a network of corner-linked oxygen octahedra, with the larger cation (A) filling the dodecahedral holes and the smaller cation (B) filling the octahedral sites. Interestingly, and of technological importance, a variety of chemical compositions can crystallize in this structure. They are often subdivided into classes depending on the respective valences of the A- and B- site cations. Examples include $BaTiO_3$ ($A^{2+}B^{4+}O_3$); $NdAlO_3$ ($A^{3+}B^{3+}O_3$), and complex perovskites such as $Pb(Mg_{1/3}Nb_{2/3})O_3$.[1]

The perovskite structure possesses a very high degree of compositional flexibility, being able to tolerate a wide variety of cations on both the A and B sites. Variations in the relative size and charge of the A and B cations can be accommodated in a number of ways. Some involve distortions of the ideal cubic structure (normally via a tilting of the B-site octahedral), and others result from the introduction of face-sharing octahedra into the network of vertex-sharing octahedra. Both the A and B sites may be occupied by more than one cationic species in a particular compound (solid solution). In the case of B sites, this can involve cations of more than one element, or it may involve two oxidation states of the same element, The introduction of vacancies onto the anion sublattice is another method by which chemical reactivity can be varied.

Perovskites form a technologically important class of compounds which has wide applicability as multilayer capacitors ($BaTiO_3$),[3] piezoelectric transducers ($Pb(Zr,Ti)O_3$,[4]

thermistors ($BaTiO_3$),[5] switches ($LiNbO_3$),[6] actuators ($Pb(Mg,Nb)O_3$),[7] superconductors $YBa_2Cu_3O_{7-\delta}$,[8] and ferromagnets ($(Ca,La)MnO_3$).[9]

3.1.2 $BaZrO_3$

$BaZrO_3$, is a cubic perovskite with a unit cell edge length of 4.19 Å. $BaZrO_3$ exhibit a high protonic conductivity upon the addition of dopants, rendering it suitable for applications ranging from fuel cells to hydrogen sensors operated at high temperature.[10] Its high dielectric constant (30-40), its wide band gap (5.3 eV), and its correspondingly high breakdown strength make this oxide material appropriate for use in high voltage and high reliability capacitive applications, such as electro-optic devices and multilayer capacitors.[11-13] Moreover, its high melting point (2600 ℃) and its chemical stability at high temperatures render it suitable not only as a refractory material but also as a precursor in the production of high-quality, high T_c superconducting materials.[14] Finally, its sensitivity to humidity is useful for its application as a moisture sensor.[15] In addition to these favorable attributes, $BaZrO_3$ also finds applications as a refractory material, as a structural material in ceramic container crucibles, as components of thermal barrier coatings, as a substrate in the synthesis of superconductors, as pinning centers in superconducting cables, as gate insulator materials, and as high-temperature microwave dielectrics.[13, 16, 17]

3.1.3 Molten Salt Synthesis (MSS)

Molten salt, also known as a “fused salt”, refers to a salt that is in the liquid phase but normally exists as a solid at standard temperature and pressure (STP). The simplest idea of a molten salt would be to take sodium chloride and heat it to a temperature (greater than 801 ℃) where it would melt into a liquid. This liquid is stable, has a heat capacity similar to water (by volume), and flows much like water does. The major differences are the obvious higher temperatures attainable in the molten salt state and when the salt solidifies, it contracts, as opposed to expanding like water.

Molten salts have a variety of uses. Molten chloride salt mixtures are commonly used as baths for various alloy heat treatments, such as annealing and tempering of steel. Cyanide and chloride salt mixtures are used for the surface modification of alloys such as the carburizing and nitrocarburizing of steel. Cryolite is used as a flux in the production of aluminium. Fluoride, chloride, and hydroxide salts can be used as solvents in pyroprocessing of nuclear fuel. Molten salts can also be used as heat transfer fluids as well as for thermal storage in the solar industry.

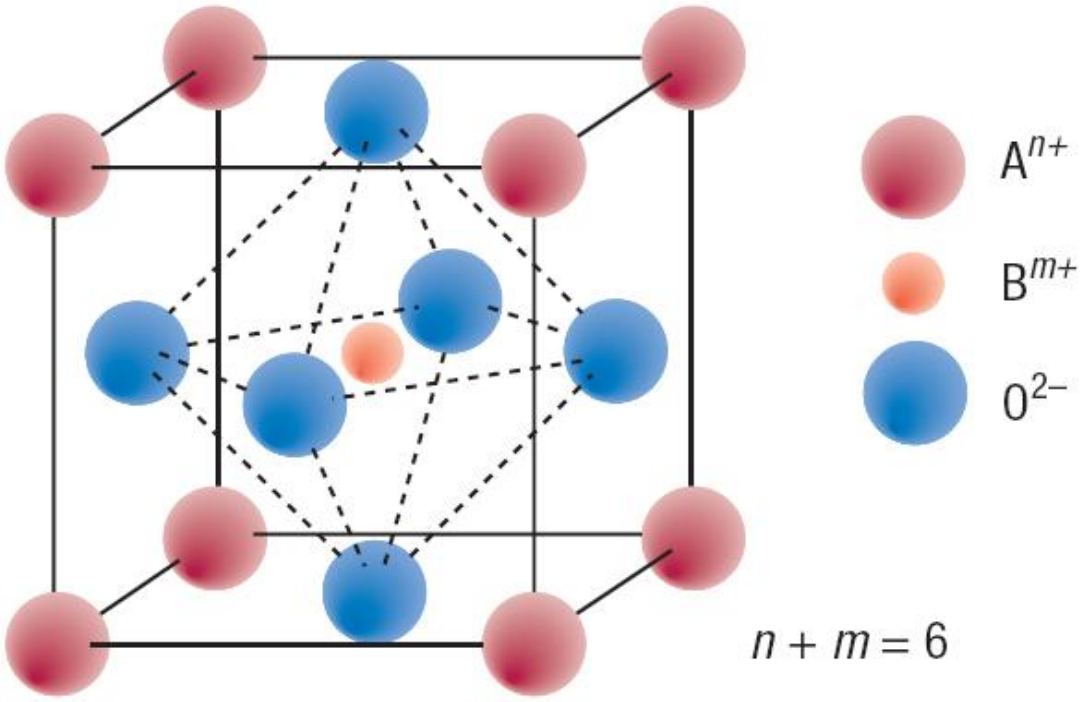

Figure 3.1 Unit cell of the ABO_3 perovskite structure. The A cations occupy the larger spaces in the 12-fold oxygen coordinated holes; the B cations occupy the much smaller octahedral holes (sixfold oordination). Full or partial substitution of the A or B cations with cations of different valence is possible. When the overall valence of the A-site and B-site cations (n+ m) adds up to less than 6, the missing charge is made up by introducing vacancies at the oxygen lattice sites.[2]

Besides these applications, molten salts have another important application, namely as a solvent in the synthesis process. The fundamental basis[18] of molten salt reactions is the reliance on the use of inorganic molten salt as the reaction medium. Salt media used by other groups have ranged from the eutectic mixture of $AlCl_3$/NaCl/KCl with a relatively low melting point of 89 ℃ to cryolite or Na_3AlF_6 with a particularly high melting point of 1003 ℃. Moreover, these salts often possess a host of favorable physicochemical properties such as a greater oxidizing potential, higher mass transfer, higher thermal conductivity , as well as relatively lower viscosities and densities, as compared with conventional solvents.[19] Due to their unique properties, MSS is one of the simplest, most versatile, and highly cost-effective approaches available for obtaining crystalline, chemically pure, single-phase nanoscale materials at lower temperatures and often in overall shorter reaction times with little residual impurities as compared to conventional solid-state reactions. The intrinsic scalability, flexibility, and facility of this technique render it attractive for the fabrication of a range of metal oxides. Our group has applied this technique into the synthesis of various ternary metal oxides such as $BaTiO_3$, $SrTiO_3$, $Ca_{1-x}Sr_xTiO_3$, and $Bi_2Fe_4O_9$ nanoparticles. [20-22]

Figure 3.2 shows the main processing stages of the MSS method with increasing temperature. There are a lot of important, controlled factors that will influence the resultant structural characteristics (purity, size, shape, and crystallinity) of as-prepared particles. These factors include the identity as well as the size of the anion associated with the salt, the nature of the solubility values as well as the dissolution rates of the constituent components within the molten salt itself, the precise melting point of either the salt or the complex salt mixture used, the heating temperature and duration, the unique morphological and chemical composition of the precursors involved, the cooling rate and the presence of surfactants.[18, 23, 24]

All of these experimental realities suggest, in theory, a high degree of tunability with respect to parameter selection for molten salt chemical reactions with the real possibility of generating large amounts of pure products with a predictable, reproducible morphology.[19, 24, 25] MSS is notable for its simplicity, large scale processing, lower reaction temperatures, and shorter reaction time. However, MSS is still not as well-understood as solution chemistry, partly because of difficulties in in-situ analysis. Moreover, shape and size control are also harder to achieve than in solution chemistry. Most of the stabilization agent, capping agent and surfactant are polymers and organic molecules, which normally all decompose at temperatures higher than 400 ℃. Although there are papers reporting that adding certain surfactants will favor the growth of unique shapes, the actual mechanism remains under investigation.

3.1.3 Current Work

A number of existing methods have been reported for the synthesis of nanoscale $BaZrO_3$ particulates. Apart from freeze-drying,[26] many reported studies have relied on liquid-phase reactions such as sol-gel,[27, 28] coprecipitation,[29] thermal decomposition,[30] and hydrothermal techniques[31-36] as well as conventional solid-state reactions[37, 38] in addition to combinations thereof. Many of these reactions often involved either an additional sintering[39] or sonication (e.g., nanoparticle formation probed as a function of ultrasonicator output power and time)[40] step. $BaZrO_3$ particles can also be formed by the

reaction[41] of very fine (70-90 nm) ZrO_2 powders and coarse (~1 μm) $BaCO_3$ powders in both dry as well as humid air using a temperature range of 900-1300 °C. Recently, the synthesis of nanoscale $BaZrO_3$ was initiated by urea-induced precipitation followed by a low-temperature thermal treatment.[42] A reported solvothermal method relied on the dissolution of either alkali or alkaline earth metals (e.g., Ba) in benzyl alcohol and a subsequent reaction with transition metal alkoxides (e.g., $Zr(O\textit{i}Pr)_4$ HO*i*Pr) at low-temperature ranges from 200 to 220 °C for 3 days.[43] A typical hydrothermal analogue to this reaction was associated with the reaction of $ZrOCl_2$ $8H_2O$, $Ba(OH)_2$, and KOH to create a slurry (pH 13), which was then heated in an autoclave at 130 °C for 1 day. In addition, $BaZrO_3$ nanoparticles have been prepared by a reverse micelle process in which (i) barium nitrate and zirconium dinitrate oxide were used as precursor materials, (ii) sodium hydroxide was utilized as the precipitating agent, and (iii) *n*-octane, 1-butanol, and cetyl trimethylammonium bromide were dispersed together to form the desired microemulsion.[44] Last, a microwave-assisted preparation, run under ambient conditions, has been reported in which $BaCl_2$ hydrate was initially dissolved in ethylene glycol, reacted with KOH, and ultimately microwave refluxed in the presence of $ZrOCl_2$ for 2 h, all under a static pressure of N_2, so as to generate particles measuring ~200 nm by 600 nm.[45]

Unlike bulk materials, the properties of nanoscale materials are not only dependent on composition, but also on size, dimensionality, and shape.[46] The only manuscript[32] to report the shape control of $BaZrO_3$ used a hydrothermal method under very high pH conditions to generate truncated rhombic dodecahedra and spheres with dimensions over 1 μm. Shape control was achieved by changing solvent polarity. In our work, we demonstrated shape control by molten salt method (see next section) through a rational dictation of annealing conditions, *i.e.* annealing temperature and time. As compared with conventional methods for shape control, which usually involve variations in parameters such as the addition of capping molecules, solvent changes, the rate of precursor molecule addition, and so forth,[47, 48] our protocol is relatively simple, easy to control, and reproducible. The primary shapes we have achieved include cubes and spheres. Cubic zirconates are useful in piezoelectric applications whereas spherical zirconates may find use in phosphors with high-luminescence efficiency. [32, 49]

In addition to achieving shape control synthesis of $BaZrO_3$ nanoparticles by MSS, we also investigated parameter control in MSS reactions for the production of ternary metal oxide perovskite structures with reliable shape and size control. We also expect our protocols to have relevance for the rational synthesis of other types of metal oxides.

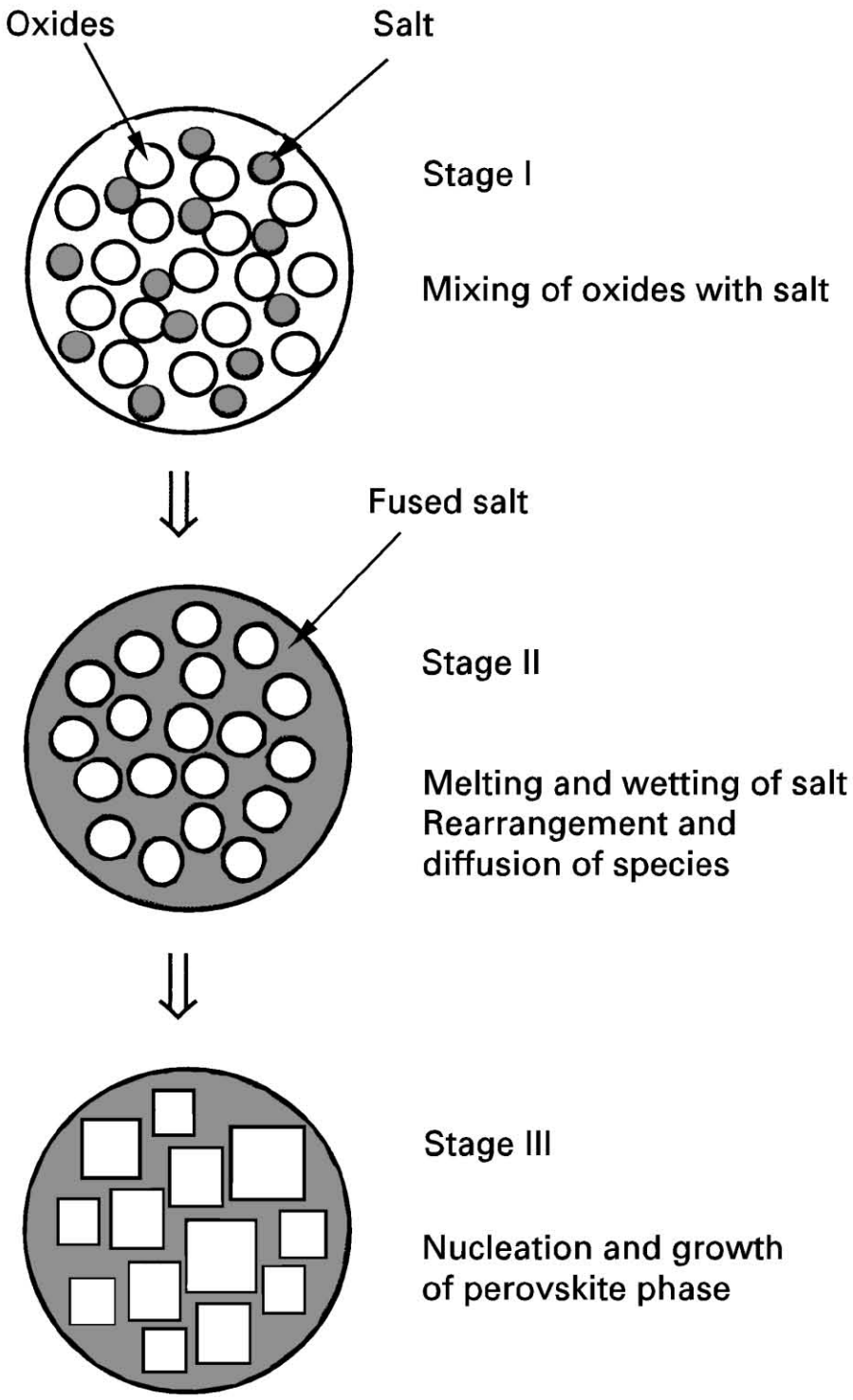

Figure 3.2 Schematic illustration of the MSS process with increasing temperature.[24]

3.2 Experimental Section

3.2.1 Synthesis

In a typical protocol, barium oxalate (Aldrich). ZrO_2 (Nanostructured & Amorphous Materials, Inc.; 40-50 nm), NaOH and KOH (Fisher) are mixed (molar ratio of 1 : 1 : 9.8 : 10.2) and ground for 10 min. The mixture is then placed in a ceramic crucible, inserted into a quartz tube, heated to 720 ℃ at rate of 5 ℃ min^{-1}, and isothermally annealed at this temperature. To achieve shape control, we made appropriate variations in annealing times, annealing temperature, overall reaction time, and cooling conditions. Samples were subsequently washed with distilled water, and dried at 80 ℃ overnight in an oven. Trivalent rare earth ions (Eu^{3+} in a 2% molar ratio) were introduced into the perovskite lattice by adding $Eu(NO_3)_3$ $6H_2O$ into the precursor mixture at the commencement of sample preparation.

3.2.2 Characterizaion

Qualitative X-Ray Diffraction See section 1.7.1.

Quantitative XRD (Q-XRD) The weight percentage of $BaZrO_3$ in as-prepared samples was obtained via Q-XRD. For precise quantitative analysis, the scan rate utilized was 0.2 ℃/min. Otherwise, parameters used for slit widths and accelerating voltages were identical for all samples. Quantitative analysis was achieved by employing a Rietveld refinement[50, 51] through the mediation of GSAS and EXPGUI software;[50, 52] this method is based on the fact that the intensity diffracted by a crystalline phase is essentially proportional to the quantity of the diffracting material. Hence, this protocol[51] relies on theoretically reconstructing the entire diffraction profile by gradual refinement of the relevant unit cell, structural parameters, and phase constituents. Structure models for various compounds used in the calculations including $BaCO_3$, ZrO_2, $BaZrO_3$, and $ZrSiO_4$ as well as crystallographic information files were obtained from the literature.[53-56] Calculated patterns were noted to fit reasonably well with measured data, from which precise weight percentages of the various chemical constituents could then be extracted.

For samples requiring a more accurate quantitative analysis of composition, a known quantity of zirconium silicate ($ZrSiO_4$, Acros, 99%), which was utilized as an internal standard,[57] was carefully combined with as-prepared samples. That is, the exact amount of internal standard used was set at 25% by careful rendering of the final weight ratio of the internal standard to that of the as-prepared sample as 1 : 3.

X-ray Photoelectron Spectroscopy (XPS). Elemental analysis was obtained by XPS. Pressed wafers or cut sections of the samples were attached to stainless steel sample holders using conductive double-sided carbon tape and installed in the vacuum chamber of a Model DS800 XPS surface analysis system (Kratos Analytical Plc of Manchester). The chamber was evacuated to a base pressure of ~5 x 10^{-9} Torr. A hemispherical energy analyzer was used for electron detection. XPS spectra were collected using a magnesium K_α X-ray source at an 80 eV pass energy and in 0.75 eV steps for each sample survey spectrum. Integration and analysis of elemental peak areas in high-resolution spectra

were used to generate estimates of the atomic and weight concentrations of the elements present in the samples.

Electron Microscopy. See section 1.7.2.

Photoluminescence (PL). PL data were obtained at 25 ℃ on a Jobin Yvon Spex Fluorolog 3 with a 1 s integration time. PL spectra for Eu^{3+}-doped samples were obtained at an excitation wavelength of 256 nm. 1 mg of Eu^{3+}-doped cube and sphere samples respectively were added to 10 ml distilled water. Prior to data collection, each solution was sonicated for approximately 30 s to obtain a visually non-scattering dispersion of the $BaZrO_3$ sample. Fluorescence data were taken immediately afterward. An identical procedure was performed for an aggregated bulk sample of $BaZrO_3$ prepared with a conventional solid state reaction method (*i.e.* heating of $BaCO_3$ and ZrO_2 powders at 1200 ℃). Data were normalized for concentration.

3.3 Results and Discussion

The purity and crystallinity of as-prepared cubic and spherical samples were examined using powder XRD (Figure 3.3). No obvious difference was noted between the results for cubic *vs*. spherical particles. All peaks can be readily indexed to the cubic phase (space group: P*m3m*) of $BaZrO_3$ (Figure 3.3A) with the calculated lattice constant of a = 0.4183 nm, in agreement with the literature (a = 0.4181 nm, JCPDS No. 74-1299, Figure 3.3B). No impurity peaks were detected.

The sizes and morphologies of as-prepared samples were examined by electron microscopy. In Figure 3.4A and 4B, it is evident that the sample mainly consists of cubes with an edge length of 120 ± 25 nm, when annealed at 720 ℃ for 30 min and immediately quenched to room temperature at an average rate of 100 ℃ min^{-1}. In Figure 3.4C and 4D, the sample is entirely composed of spherical particles with a diameter range of 320 ± 100 nm, upon annealing at 720 ℃ for 3.5 h and with gradual *in situ* furnace cooling to room temperature at an average rate of 3.5 ℃ min^{-1}. There is some degree of aggregation in both samples, which is consistent with our previous observations in these types of systems.[58, 59] Size distributions of observed cubes and spheres in both of these samples are shown in Figure 3.5. A nonuniform particle size distribution can be partially caused by an inhomogeneous distribution of precursors and reactive salt materials during the reaction process.[60]

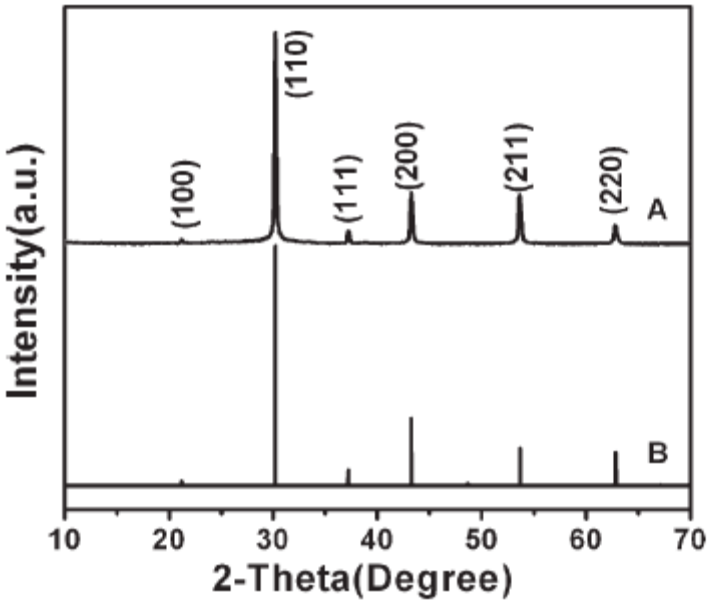

Figure 3.3 XRD pattern of $BaZrO_3$: (A) as-prepared samples (cubes and/or spheres); (B) standard from database (JCPDS No. 74-1299).

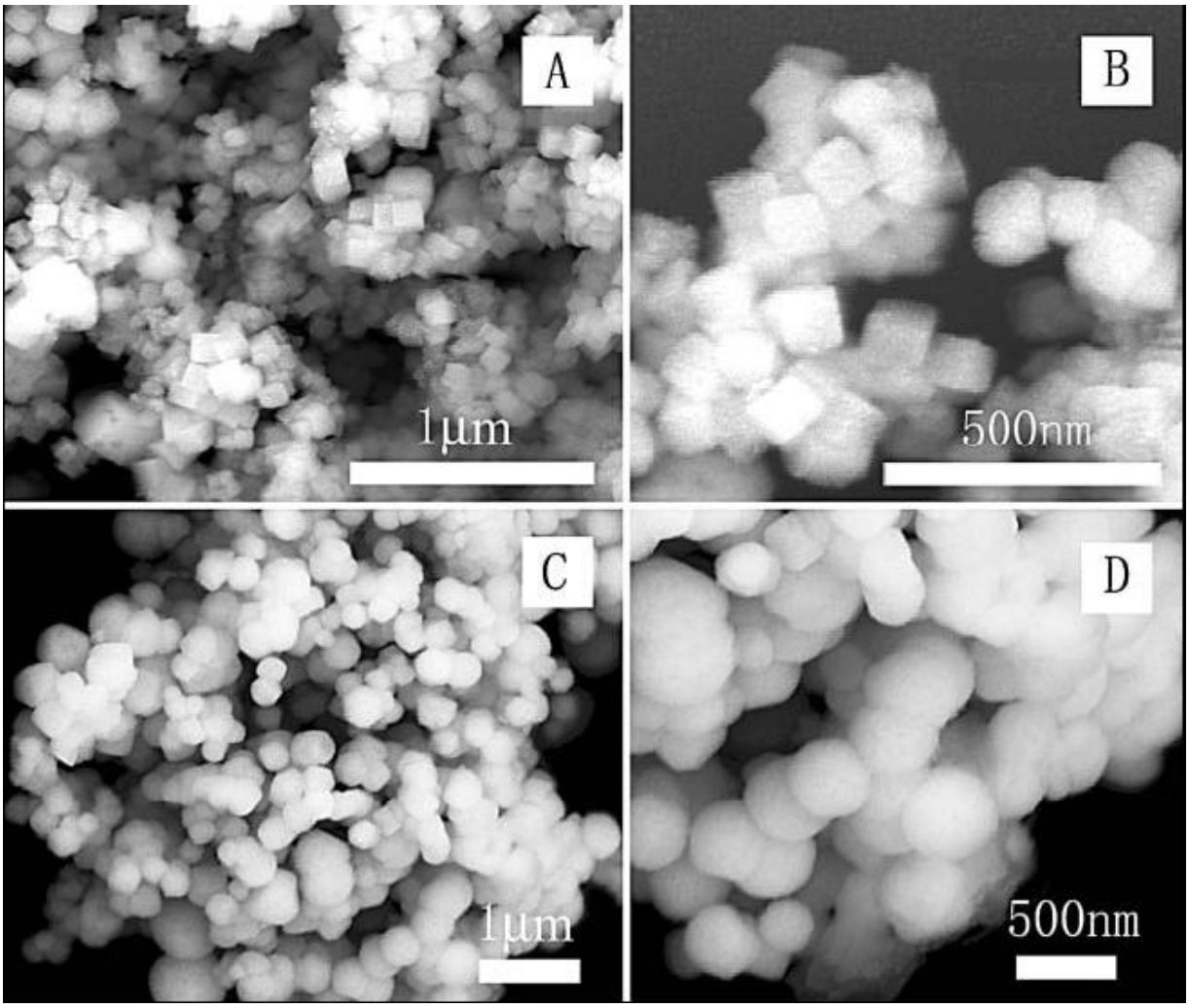

Figure 3.4 SEM images of as-prepared $BaZrO_3$ cubes (A and B) and spheres (C and D).

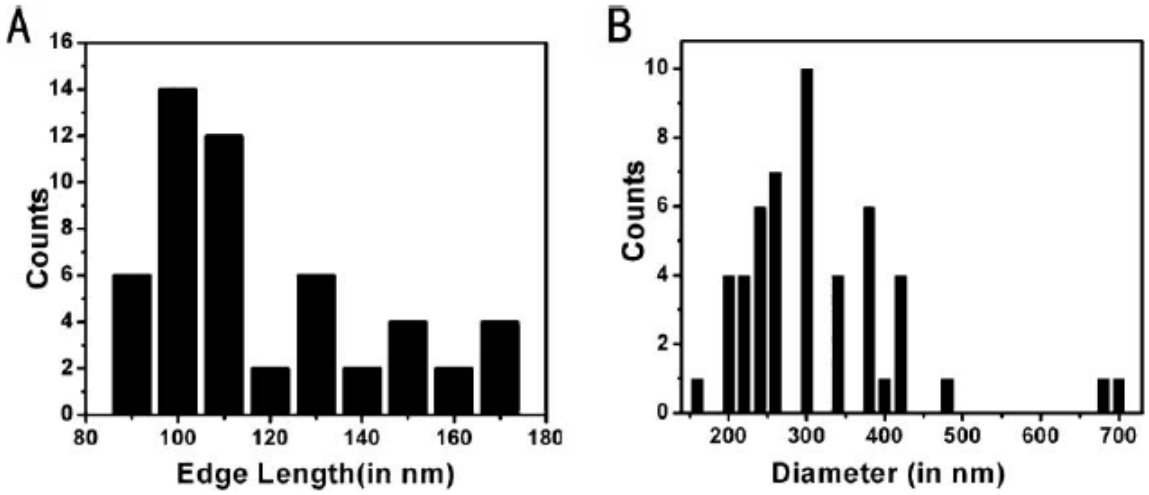

Figure 3.5 Size distributions of as-prepared $BaZrO_3$ particles. (A) cubes and (B) spheres.

The TEM data (Figure 3.6A) clearly show the cubic morphology of a typical individual particle. The HRTEM image obtained from the [001] projection (Figure 3.6B) suggests that the submicron-sized $BaZrO_3$ cubes are single-crystalline with no apparent defects and dislocations. The spacing of the observed lattice fringes has been deduced to be 0.29 nm, which can be associated with the {110} plane of the cubic phase of $BaZrO_3$. In addition, the corresponding SAED pattern (Figure 3.6C) can be indexed perfectly to the {110} diffraction planes, consistent with the HRTEM results and with the single crystalline nature of these as-prepared cubes. The corresponding EDS spectrum (Figure 3.6D) shows that the $BaZrO_3$ cubes are composed of the elements of Ba, Zr and O, as expected.

By comparison with $BaZrO_3$ cubes, $BaZrO_3$ spheres (Figure 3.7A) are also single-crystalline (Figure 3.7B) with no apparent defects and dislocations. The spacing of observed lattice fringes are 0.29 nm and 0.42 nm, respectively, and have been correspondingly indexed to the {011} and {100} planes of the cubic phase of $BaZrO_3$ in agreement with the SAED pattern (inset of Figure 3.7B). As expected, the EDS spectrum of our as-prepared spheres is essentially identical to that obtained for cubes.

XPS data were collected on representative samples. As shown in Figure 3.8A, signals corresponding to Ba, Zr, and O were noted; impurities, such as C, Na, K, and Si, were also present though. Specifically, on average, there was about 1.41 % Na and 2.28 % K in as-prepared samples. It is reasonable to ascribe the appearance of Na and K to residues from the salt mixture and the presence of Si to the reaction crucible itself. We cannot fully discount the possible formation of either sodium silicate or potassium silicate though it was likely to be insignificant. The use of either quartz or platinum crucibles in synthesis runs will likely solve this impurity problem. Any C observed would have resulted from contaminant sources such as CO_2 physisorbed on the surface of BaO.[58] Figure 3.8B shows a few high-resolution XPS spectra. The Ba $3d_{3/2}$ and $3d_{5/2}$ peaks are located at 794.4 eV and 779.11 eV, respectively, whereas the Zr $3d_{3/2}$ and $3d_{5/2}$ peaks are situated at 183.23 eV and 180.87 eV, respectively.[61, 62] These data are consistent with the oxidation states of Ba and Zr, as being +2 and +4, respectively, which are expected of $BaZrO_3$ formation.

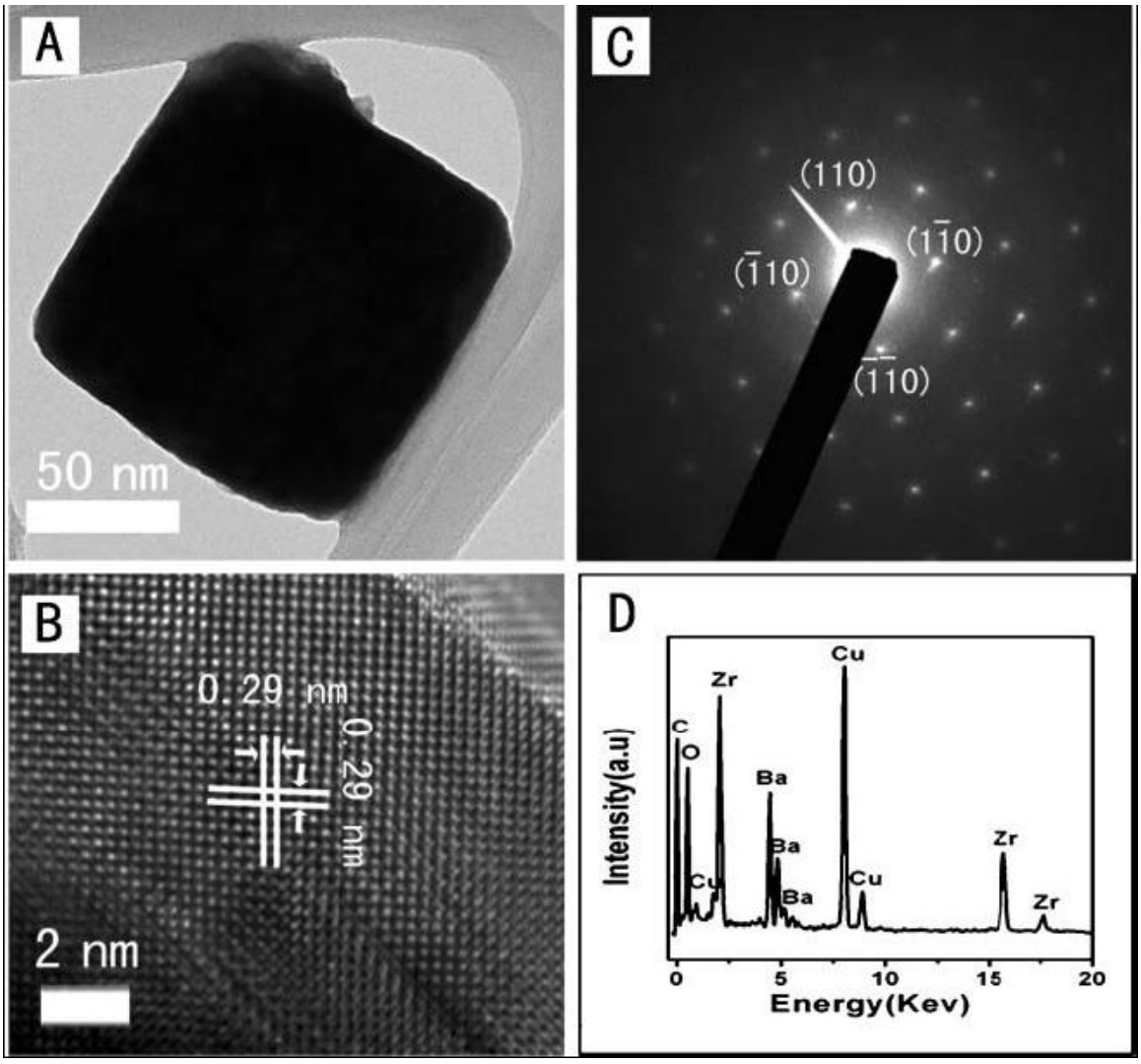

Figure 3.6 $BaZrO_3$ cubes: (A) Typical TEM image; (B) HRTEM image of a portion of the cube in (A) with zone axis corresponding to [001]; (C) SAED pattern of the cube sample; (D) EDS. The Cu and C peaks originate from the TEM grid.

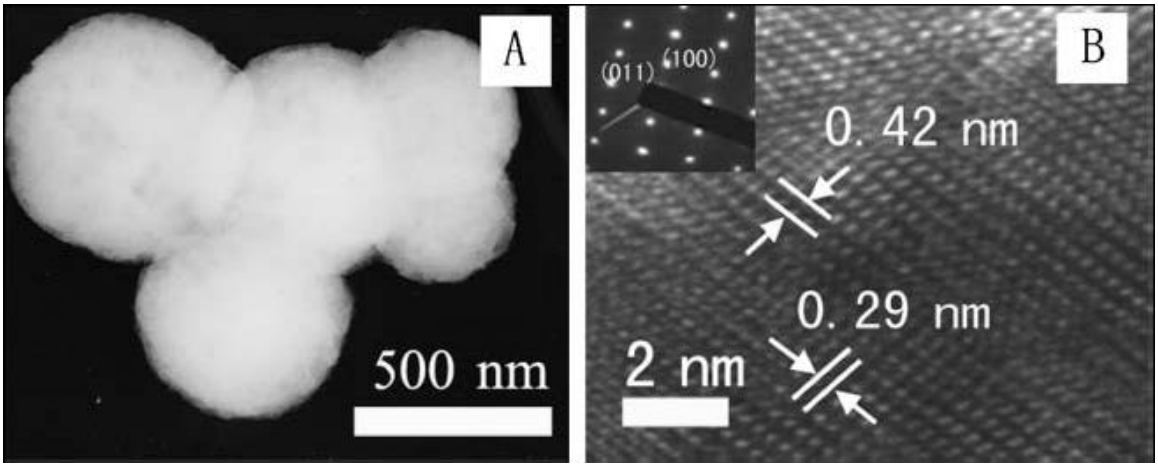

Figure 3.7 $BaZrO_3$ spheres: (A) typical TEM micrograph; (B) HRTEM image of a portion of one of the spheres in (A) corresponding to the zone axis of $[0\bar{1}1]$. Inset of (B) is the associated SAED pattern.

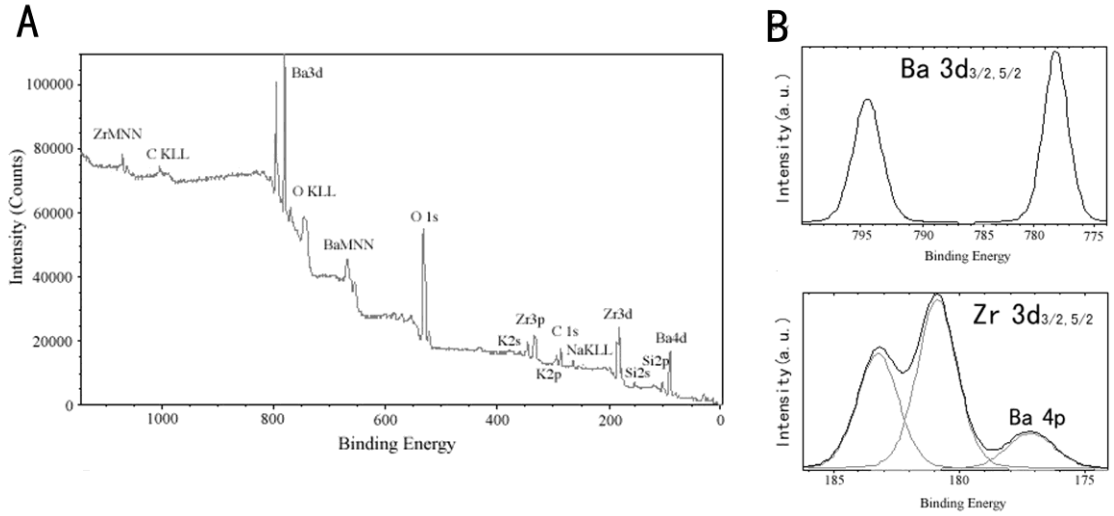

Figure 3.8 (A) Survey X-ray photoelectron spectrum of representative, as-prepared samples of barium zirconate. Binding energy units are in eV. (B) High-resolution X-ray photoelectron spectra of as-prepared samples of barium zirconate. Binding energy units are in eV. (top) Ba 3d spectrum. (bottom) Zr 3d spectrum.

Perovskite-type oxides can be used as host materials for rare earth photoluminescence. Thus, we doped $BaZrO_3$ samples with Eu ions in a simple modification of the above synthesis process. SEM observations indicate that the characteristic, expected morphology of the as-prepared samples did not alter upon doping. Figure 3.9 shows the room temperature PL emission spectra of the resulting doped zirconate samples. We note lines and features in the range of 570 to 660 nm, likely corresponding to emissions from the excited $^5D_0$ state level to lower lying ^7F_j (j = 0, 1, 2, 3, 4) levels of the $4f^6$ configuration of the Eu^{3+} ion.[32, 63, 64] The most prominent band localized at ~612 nm can be attributed to a $^5D_0$ to $^7F_2$ transition, which is expected based upon Judd-Ofelt selection rules.

We analyzed $BaZrO_3$ cubes and spheres as well as the corresponding bulk aggregate sample. For these particles, the data were found to possess similar spectral features though the bands did vary in intensity. As mentioned previously as a motivator for this work, zirconate spheres are expected to possess high luminescence efficiency. Not surprisingly, our results show that our as-prepared spherical particles possess the highest emission intensity, presumably because the intrinsic geometry of spherical particles minimizes scattering of light from the sample surface as compared with cubic particles and with other types of morphologies, even though the spherical particles maintained a larger average size than their cubic counterparts. By contrast, polyhedral samples, such as aggregated bulk zirconate particles (measuring ~50 – 100 μm), which are much less uniform and homogeneous, possess inherently more defects, surface cracks, and inter-particle elastic strains that will necessarily result in a reduced observable luminescence yield.[65] All of these results support the notion of morphology-dependent properties of $BaZrO_3$ samples and emphasize the importance of shape control.

To demonstrate the effect of different reaction parameters with respect to phase purity and particle morphology of $BaZrO_3$, we performed a series of systematic experiments, as delineated in Table 3.1. Experimental variables were carefully crafted so that the behavior of the subsets of samples could be reliably compared across individual discrete parameters, with all other parameters kept constant.

As an example, when examining samples annealed at different temperatures (samples G-I), even though the times required to attain the desired annealing temperatures were different, overall reaction times remained constant. We accomplished this feat partly by quenching samples to room temperature at a very high average rate of 100 ℃ min^{-1} to minimize the possible time differential resulting from cooling, starting from these various different annealing temperatures.

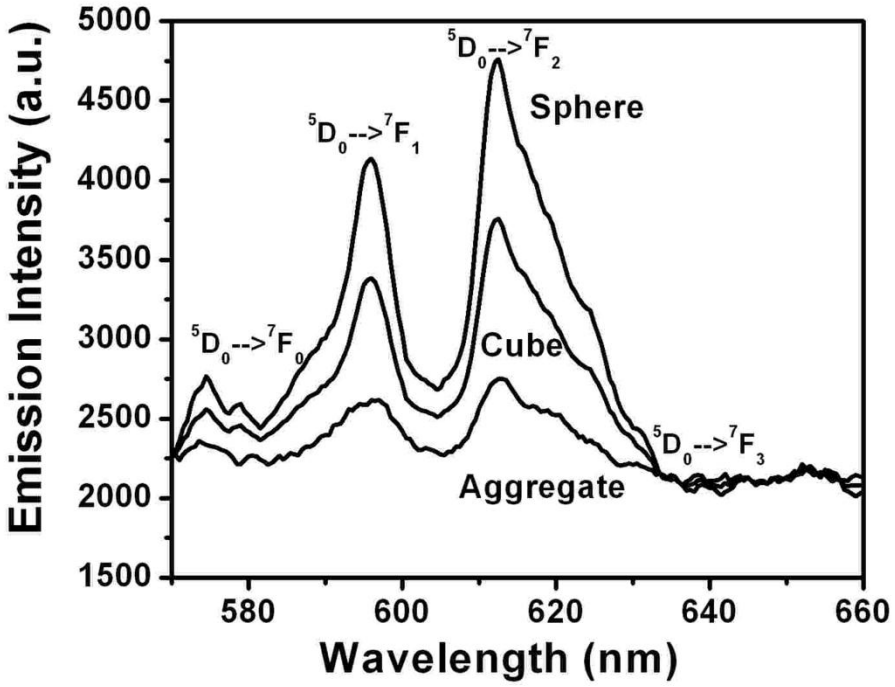

Figure 3.9 Room temperature PL emission (λ_{ex} = 256 nm) spectra of 2% Eu^{3+} doped $BaZrO_3$ samples possessing different morphologies.

Table 3.1. $BaZrO_3$ Samples Systematically Prepared with Different Processing Parameters at a Constant Heating Rate of 5 °C/Min[a]

parameter varied	sample	precursors	salt	annealing temp (°C)	time required to attain desired annealing temp (min)	time sample was maintained at desired annealing temp (min)	overall reaction time (min)	cooling rate (°C/min)	product description (obsd compound; percent purity; average particle size; morphology distribution)
salt	A	BaC_2O_4, ZrO_2	**no salt**	820	160	190	350	3.5	$BaZrO_3$ (69%; aggregates) with $BaCO_3$ and ZrO_2
	B	BaC_2O_4, ZrO_2	**NaOH/KOH**	720	140	210	350	3.5	$BaZrO_3$ (100%; ~320 nm; 100% spheres)
	C	BaC_2O_4, ZrO_2	**NaCl/KCl**	820	160	190	350	3.5	$BaZrO_3$ (93.9%; ~200 nm; cubes) with $BaCO_3$ and ZrO_2
	D	BaC_2O_4, ZrO_2	**NaCl**	820	160	190	350	3.5	$BaZrO_3$ (93.3%; ~200 nm; cubes) with $BaCO_3$ and ZrO_2
	E	BaC_2O_4, ZrO_2	**$NaNO_3$**	320	60	290	350	3.5	no $BaZrO_3$; impurities of $BaCO_3$ and ZrO_2
	F	BaC_2O_4, ZrO_2	**$NaNO_3$/NaCl**	320	60	290	350	3.5	no $BaZrO_3$; impurities of $BaCO_3$ and ZrO_2
annealing temp	G	BaC_2O_4, ZrO_2	NaOH/KOH	**520**	100	250	350	100	$BaZrO_3$ (84%; ~422 nm; 50% cubes/50% spheres) with $BaCO_3$ and ZrO_2
	H	BaC_2O_4, ZrO_2	NaOH/KOH	**620**	120	230	350	100	$BaZrO_3$ (95%; ~350 nm; 35% cubes/65% spheres) with $BaCO_3$ and ZrO_2
	I	BaC_2O_4, ZrO_2	NaOH/KOH	**720**	140	210	350	100	$BaZrO_3$ (100%; ~310 nm; 5% cubes/95% spheres)
annealing time	J	BaC_2O_4, ZrO_2	NaOH/KOH	720	140	30	**170**	100	$BaZrO_3$ (100%; ~120 nm; 100% cubes)
	K	BaC_2O_4, ZrO_2	NaOH/KOH	720	140	60	**200**	100	$BaZrO_3$ (100%; ~160 nm; 80% cubes/20% spheres)
	L	BaC_2O_4, ZrO_2	NaOH/KOH	720	140	120	**260**	100	$BaZrO_3$ (100%; ~265 nm; 30% cubes/70% spheres)
	I	BaC_2O_4, ZrO_2	NaOH/KOH	720	140	210	**350**	100	$BaZrO_3$ (100%; ~310 nm; 5% cubes/95% spheres)
	M	BaC_2O_4, ZrO_2	NaOH/KOH	520	100	70	**170**	100	$BaZrO_3$ (29%; ~211 nm; 90% cubes/10% spheres) with $BaCO_3$ and ZrO_2
	N	BaC_2O_4, ZrO_2	NaOH/KOH	520	100	100	**200**	100	$BaZrO_3$ (45%; ~222 nm; 85% cubes/15% spheres) with $BaCO_3$ and ZrO_2
	O	BaC_2O_4, ZrO_2	NaOH/KOH	520	100	160	**260**	100	$BaZrO_3$ (67%; ~297 nm; 75% cubes/25% spheres) with $BaCO_3$ and ZrO_2
	G	BaC_2O_4, ZrO_2	NaOH/KOH	520	100	250	**350**	100	$BaZrO_3$ (84%; ~422 nm; 50% cubes/50% spheres) with $BaCO_3$ and ZrO_2
influence of cooling rate	G	BaC_2O_4, ZrO_2	NaOH/KOH	520	100	250	350	**100**	$BaZrO_3$ (84%; ~422 nm; 50% cubes/50% spheres) with $BaCO_3$ and ZrO_2
	P	BaC_2O_4, ZrO_2	NaOH/KOH	520	100	250	350	**3.5**	$BaZrO_3$ (100%; ~450 nm; 40% cubes/60% spheres)
	J	BaC_2O_4, ZrO_2	NaOH/KOH	720	140	30	170	**100**	$BaZrO_3$ (100%; ~120 nm; 100% cubes)
	Q	BaC_2O_4, ZrO_2	NaOH/KOH	720	140	30	170	**3.5**	$BaZrO_3$ (100%; ~200 nm; 50% cubes/50% spheres)
	L	BaC_2O_4, ZrO_2	NaOH/KOH	720	140	120	260	**100**	$BaZrO_3$ (100%; ~265 nm; 30% cubes/70% spheres)
	R	BaC_2O_4, ZrO_2	NaOH/KOH	720	140	120	260	**3.5**	$BaZrO_3$ (100%; ~300 nm; 100% spheres)
nature of precursor	B	**BaC_2O_4, ZrO_2**	NaOH/KOH	720	140	210	350	3.5	$BaZrO_3$ (100%; ~320 nm; 100% spheres)
	S	**BaO, ZrO_2**	NaOH/KOH	720	140	210	350	3.5	$BaZrO_3$ (100%; ~490 nm; 100% spheres)
	T	**$BaCO_3$, ZrO_2**	NaOH/KOH	720	140	210	350	3.5	$BaZrO_3$ (100%; ~340 nm; 100% spheres)
	U	**$BaCl_2$, ZrO_2**	NaOH/KOH	720	140	210	350	3.5	$BaZrO_3$ (67%; aggregates) with $BaCO_3$ and ZrO_2
	V	**$Ba(NO_3)_2$, ZrO_2**	NaOH/KOH	720	140	210	350	3.5	$BaZrO_3$ (71%; aggregates) with $BaCO_3$ and ZrO_2
	W	**$Ba(OOCCH_3)_2$, ZrO_2**	NaOH/KOH	720	140	210	350	3.5	$BaZrO_3$ (75%; ~300 nm; 100% spheres) with $BaCO_3$ and ZrO_2
	X	**BaC_2O_4, $ZrOCl_2 \cdot 8H_2O$**	NaOH/KOH	720	140	210	350	3.5	$BaZrO_3$ (76%; aggregates) with $BaCO_3$ and ZrO_2

[a] Variables controllably altered in each series are in bold.

Selection of Salt As shown in Figure 3.10a, regardless of the overall reaction time, sample A. prepared in the absence of salt, contains not only $BaZaO_3$ but also impurity phases that can be attributed to $BaCO_3$ and ZrO_2. Although the decomposition temperature of $BaCO_3$ is expected to be around 821 ℃,[66] the appearance of $BaCO_3$ may arise from either the recombination of CO_2 and BaO during the cooling process or the incomplete decomposition of barium oxalate.

A number of samples were subsequently prepared by running molten salt reactions above the melting points of various salt media tried. Hence, we note that the weight percentage of $BaZrO_3$ increased from 69% (sample A, no salt used) to 93.3% (sample D) in the presence of NaCl (Fisher; mp 801 ℃) and to 93.9% (sample C) in a mixture of NaCl/KCl (50:50 mol % ratio; mp 658 ℃) at an annealing temperature of 820 ℃. In the presence of NaOH/KOH (49.2: 50.8 mol % ratio; mp 170 ℃) as the eutectic salt mixture, $BaZrO_3$ with a weight percentage of almost 100% could be generated at rather low temperatures (e.g., 720 ℃). Interestingly, this sample (sample B) remained compositionally stable even upon annealing to 820 ℃. It is noteworthy that in salt media such as $NaNO_3$ (J.T. Baker Chemical Co.; mp 310 ℃) and $NaNO_3$/NaCl (93.6:6.4 mol % ratio; mp 294.7 ℃), comprising samples E and F, from the XRD patterns, no $BaZrO_3$ was synthesized at all, even at the same overall reaction times as the other samples and even after annealing at 320 ℃. It should be noted that we did not proceed to higher annealing temperatures (such as 700-800 ℃) in these specific systems because salts such as $NaNO_3$ will decompose above 380 ℃. Nonetheless, overall, the apparent lack of $BaZrO_3$ particle formation using nitrate salts was a surprising result because there have been reports of perovskite particle aggregate formation in the presence of molten alkali metal oxonitrates.[67]

What is the effect of salt selection and of temperature? Molten salt solutions[68] can actually partake of several functions. They can either catalyze reactions,[69] participate in reactions themselves by consuming reagents,[70] or merely act as a non-interfering solvent for the reagents.[59] However, in every case, the intrinsic solubilities of individual precursor molecules within these particular solvents are critical.

Thus, although salts such as $NaNO_3$ and $NaNO_3$/NaCl possess relatively low melting temperatures (~200-300 ℃), few precursor molecules of the different reacting species will adequately dissolve and diffuse in these particular solvents under such conditions, meaning that the corresponding reaction rates are low. Therefore, little, if any, $BaZrO_3$ forms. By contrast, at high temperatures such as ~800 ℃, in the presence of NaCl, precursor molecules will more readily disperse, dissociate, rearrange, and then diffuse rapidly throughout the salt, forming a reasonably homogeneous solution that fosters rapid reaction. Higher temperatures therefore not only increase the flux and mobility of reactive components but also imply a lower viscosity within the reaction medium, all of which is consistent with a higher rate of reactivity.[25] Thus, overall, as compared with samples prepared in the absence of salt (e.g., sample A), it is evident that the presence of either a chloride or a hydroxide salt medium encouraged the formation of $BaZrO_3$ (e.g., samples B-D).

The effect of using a hydroxide salt can be summarized as follows. It turns out that the hydroxide ion can actively participate in the reaction itself. For instance, it has

been shown that molten hydroxide solutions[70] will not only react with metallic salts but also with metal oxides present. A plausible formation scheme (e.g., sample B) for $BaZrO_3$ is given in the presence of NaOH as the salt medium. KOH yields soluble K_2CO_3 as a byproduct, but otherwise the analysis is exactly the same as with NaOH alone.

$BaC_2O_4 + 2NaOH + ZrO_2 \rightarrow Na_2CO_3 + BaZrO_3 + H_2O + CO$ (1)

In the absence of hydroxide ion (e.g., sample E), a correspondingly viable reaction scheme is proposed as

$BaC_2O_4 + ZrO_2 \rightarrow BaZrO_3 + CO + CO_2$ (2)

We have calculated the thermodynamic Gibbs' free energies for each of these reactions at increasing annealing temperatures, as shown in Table 3.2.[66] There are two trends worth noting. First, as expected, as the temperature progresses from 520 to 720 ℃, the corresponding free energy values effectively double in magnitude, which is conducive to $BaZrO_3$ formation at higher temperatures. Second, the free energy values in the presence of hydroxide ion are ~100 kJ/mol more favorable for the reaction to occur; for instance, at 720 ℃, the free energy value for $BaZrO_3$ synthesis is approximately -439 kJ/mol in the presence of hydroxide ions, whereas in the absence of hydroxide ions, the corresponding free energy value is -341 kJ/mol. The large apparent difference in free energy of reaction coupled with the relatively high solubility and reactivity of metal species in hydroxide media can therefore explain the relative ease and overall completeness of $BaZrO_3$ formation that we have observed.

The nature of the salt medium also has an impact on the morphology of the as-prepared products. Ito et al. demonstrated this assertion in the synthesis of $PbTiO_3$ particles wherein cubic and rectangular particles were produced in the presence of KCl and LiF, respectively.[71, 72] A similar effect was observed in our own experiments, shown in Figure 3.10b-e. In the absence of salt, products aggregated as large agglomerates (Figure 3.10b). In chloride-containing media, cubic particles were obtained (Figure 3.10d, e), whereas spherical particles were more readily found in hydroxide-containing media (Figure 3.10c). The shape of a nanocrystal (i.e., the reason for the morphology difference) is often determined by the relative specific surface energies associated with the facets of the growing crystal. As supporting evidence, we note the presence of different crystalline surface planes formed, when we compare the TEM images of as-prepared $BaZrO_3$ cubes versus spheres in Figure 3.6B and 7B. Hence, it is likely that the preferential adsorption of molecules and ions, such as chloride versus hydroxide, to different crystal faces likely directs the growth of nanoparticles to their ultimate product morphology by controlling relative growth rates associated with the different crystal faces.[73-75] This effect is analogous to the use of surfactants in other synthetic systems to achieve shape control.[76, 77]

Another key point has been the dispersibility factor. Because of the relatively high viscosity of hydroxide,[70] as-prepared particles grown in hydroxide media tend to be more dispersed and isolated than those fabricated in chloride media. Thus, the use of different salt species not only has an impact on the ease of reaction but also correlates with the morphology of the as-prepared product. We should mention that since hydroxide media

tend to yield the best samples in terms of purity, morphology, and dispersion, the remainder of this chapter will primarily focus on samples prepared using this medium with careful and rational control over a number of other different variables.

Annealing Temperature. As we have previously noted, the solubility and reactivity of precursors increase with the increasing annealing/reaction temperature of the solvent medium itself. Moreover, it is known that the viscosity of the molten salt decreases rapidly with an increase of temperature, thereby greatly facilitating the diffusion of precursor species in the solvent itself.[25] These effects have been studied in the series of samples G-I, which had been annealed at 520, 620, and 720 ℃, respectively, with constant overall reaction times (350 min) and rapid cooling rates (100 ℃/min). Associated data are shown in Figure 3.11. From XRD data, we note that the weight percentage of $BaZrO_3$ in these samples correlates well with increasing annealing temperature, starting from 84% (sample G) to 95% (sample H). Essentially no impurity phase was detected at the highest temperature, 720 ℃ (sample I), implying higher rates of reactivity and essentially full conversion to $BaZrO_3$ at the highest annealing temperatures.

Another key issue has been product morphology. Whereas sample B, which had been slowly cooled to room temperature from an annealing temperature of 720 ℃, resulting in an effectively longer reaction time, consisted of ~100% spherical particles, samples G-I, which had been rapidly quenched, possessed varying percentages of cubes and spheres. In fact, the percentage of spheres increased from 50% in sample G to 65% in sample H and finally to 95% in sample I with increasing annealing temperature. Hence, these initial observations, which are consistent with our previous data,[78] suggest that higher annealing temperatures and longer overall reaction times are conducive to the production of relatively pure, spherically shaped $BaZrO_3$ samples.

Table 3.2. Gibbs' Free Energy of Formation Values for Reactions 1 and 2 Regarding $BaZrO_3$ Particle Formation

annealing temp (°C)	reaction 1 (presence of hydroxide ion in molten salt media) (kJ/mol)	reaction 2 (absence of hydroxide ion in molten salt media) (kJ/mol)
520	−263	−153
620	−320	−214
720	−379	−277
820	−439	−341

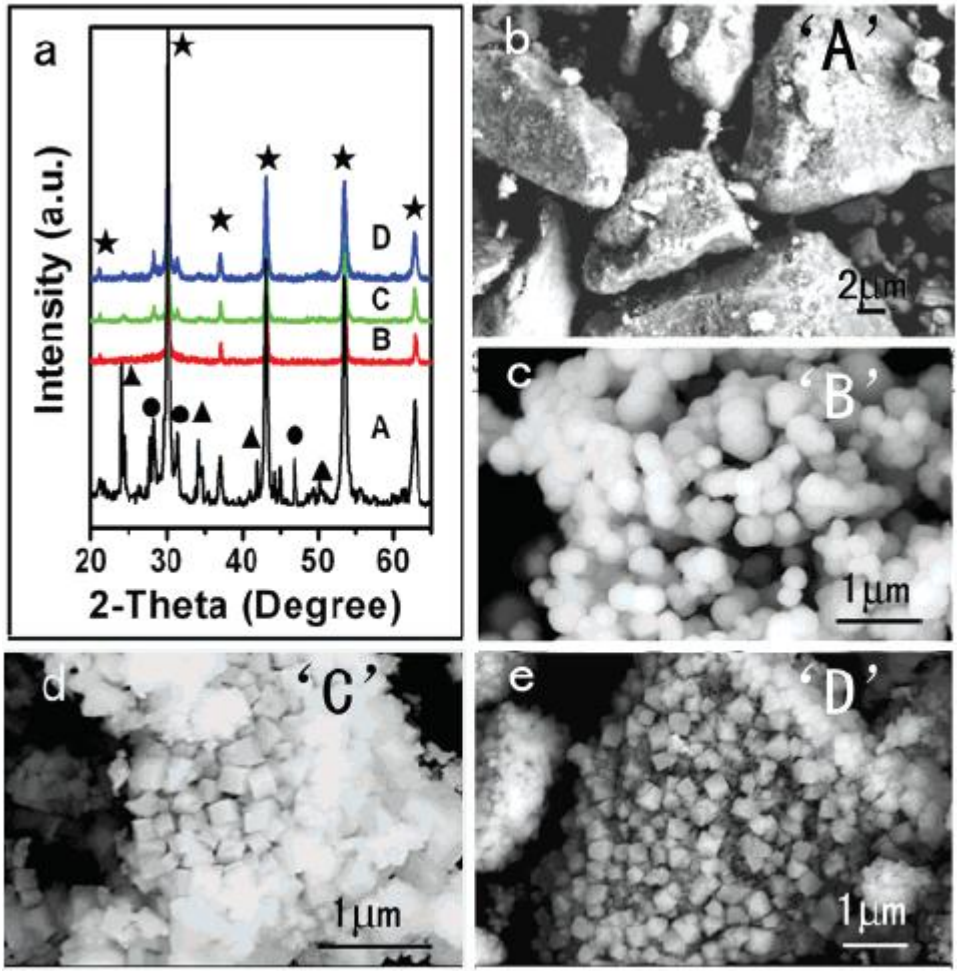

Figure 3.10 Selection of salt. (a) XRD patterns of samples A-D from Table 1, prepared using a molten medium containing no salt, NaOH/KOH, NaCl/KCl, and NaCl, respectively. (★, ▲, and ● represent reflection peaks associatd with $BaZrO_3$, $BaCO_3$, and ZrO_2, respectively). (b-e) Associated SEM images of samples A-D, respectively.

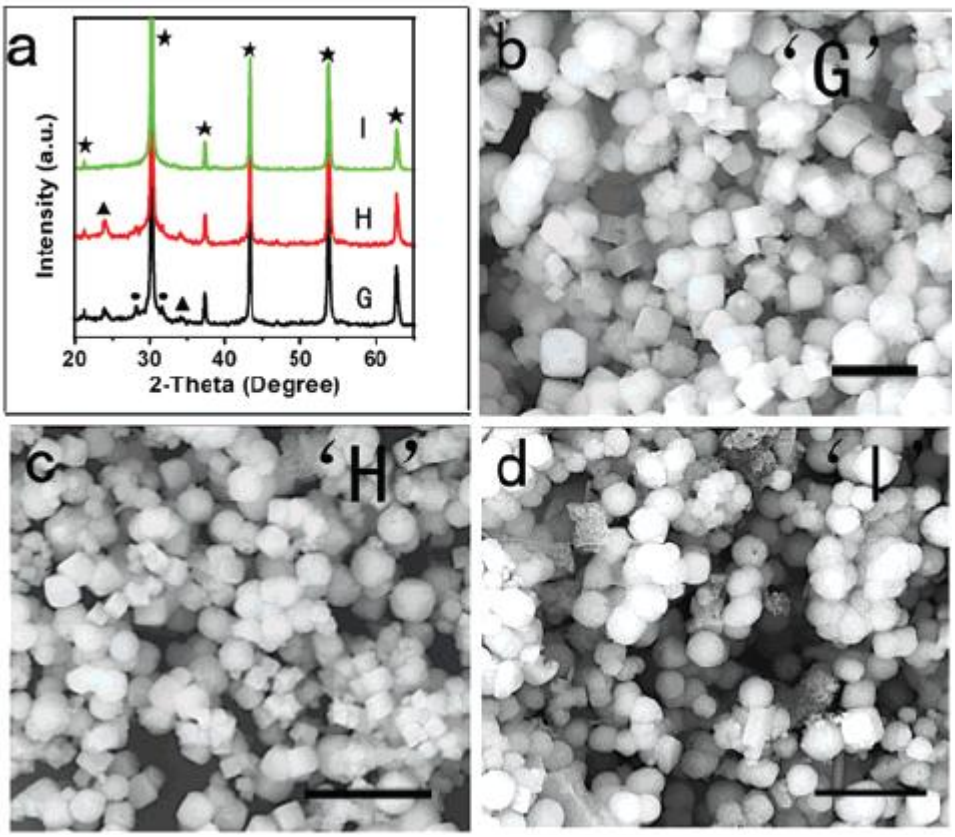

Figure 3.11 Annealing temperature. (a) XRD patterns of samples G, H, and I from Table 1. (★, ▲, and ● represent $BaZrO_3$, $BaCO_3$, and ZrO_2, respectively. (b-d) Corresponding SEM images of samples G, H, and I, respectively (i.e., in order of increasing annealing temperatures from 520 to 720 ℃). Scale bar = 1 μm.

Impact of Overall Reaction Time To explore the effect of overall reaction times more thoroughly, samples J-L and I were prepared at an identical temperature (i.e., 720 ℃) but with different annealing times and overall reaction times (e.g., ranging from 170 to 350 min). All of these samples contained ~100 wt % $BaZrO_3$ with no detectable impurity, on the basis of XRD analysis. In terms of morphology, as shown in Figure 3.12, sample J, synthesized with the least amount of reaction time (170 min), contained primarily cubes. As the overall annealing/reaction time was systematically increased, the percentage of spheres also increased from 20% in sample K (200 min of reaction time) to 70% in sample L (260 min of reaction time). Ultimately, in sample I, fabricated with a reaction time of 350 min, the proportion of spheres was ~95%. Simultaneously, the average diameter of particles increased accordingly from 120 nm for sample J, 160 nm for sample K, 265 nm for sample L, and finally to 310 nm for sample I. Hence, it was evident that with an increasing annealing time, the samples progressed from cubes to spheres with a corresponding, simultaneous increase in particle size.

A parallel sample series (e.g., G and M- O) was prepared by annealing at a lower temperature (520 ℃), while systematically varying overall reaction times from 170 to 350 min. The weight percentage of the $BaZrO_3$ phase increased from 29% in sample M, synthesized after reaction for 170 min, to as much as 84% in sample G, produced after 350 min of annealing. We also observed an analogous increase in diameter as well as in the percentage of spheres in samples that had undergone additional annealing. That is, we progressed from ~10% spheres in sample M to ~50% spheres in sample G, supportive of the assertion that the conversion rate from cubes to spheres is favored at higher annealing temperatures. [78] In this span of samples, average particle diameters increased from ~211 nm to as much as ~422 nm, suggesting that increasing annealing times favor particle growth.

Influence of Cooling Rates. In the vast majority of papers[58, 59, 79] dealing with MSS, either a slow cooling rate or an unimpeded furnace cooling is utilized. By contrast, in other techniques, such as coprecipitation, quenching (i.e., the idea of a very rapid cooling) is frequently used to control not only nucleation but also the subsequent growth, formation, and morphology of product particles.

Herein, we studied the effect of cooling rates in molten salt systems by comparing samples prepared by varying quenching rates. For instance, sample P (~450 nm) was synthesized under exactly the same conditions as sample G (~422 nm), with the exception that the former was cooled at a rate of 3.5 versus 100 ℃/min. However, sample P was essentially 100% pure, whereas sample G still possessed a detectable level of impurity. Thus, decreasing the cooling rate had the practical effect of increasing the overall reaction time, thereby allowing for improved sample quality.

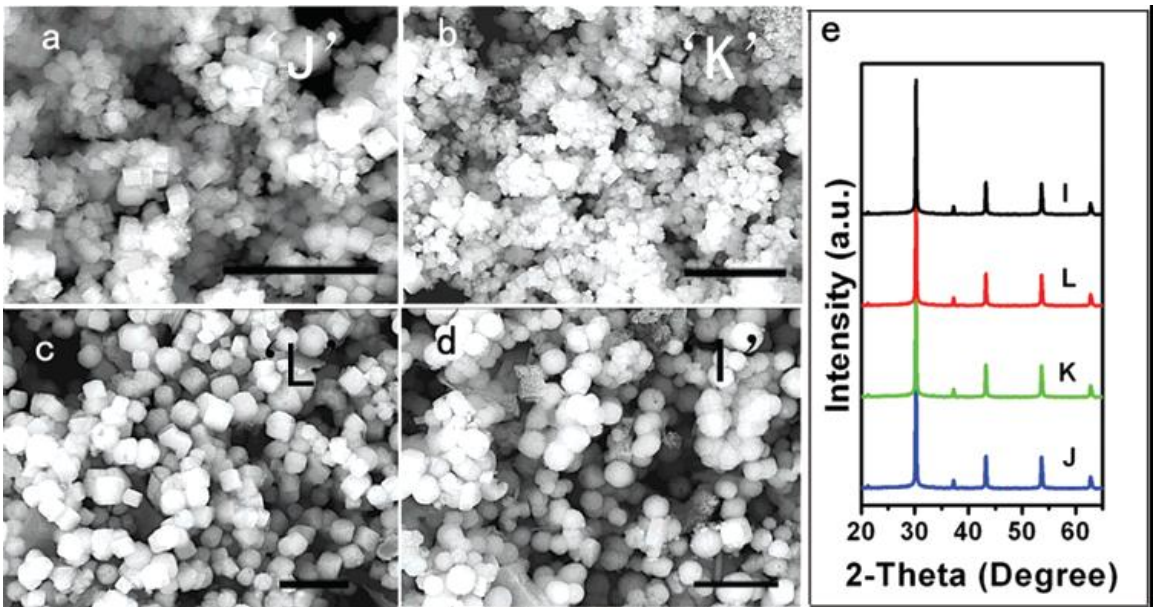

Figure 3.12. Impact of overall reaction time. Annealing performed at 720 ℃. (a-d) SEM images of samples J-L and I, described in Table 1 (i.e., in order of increasing overall reaction times from 170 to 350 min). Scale bar = 1 μm. (e) Corresponding XRD patterns of samples J-L and I.

As we noted earlier, an increased annealing time favored the formation of spheres in the products. The overall reaction time for the second pair of samples tested was 170 min. Hence, sample J (~120 nm), cooled at a rapid rate of 100 ℃/min embodied almost exclusively cubes, whereas sample Q (~200 nm), prepared identically but cooled at a slower rate of 3.5 ℃/min, contained a mixture of cubes and spheres (Figure 3.13). The overall reaction time for the third pair of samples tested was 260 min. Sample R (~300 nm) cooled at a rate of 3.5 ℃/min was characterized by spheres. By contrast, sample L (~265 nm), prepared identically but cooled at a rate of 100 ℃/min, was more heterogeneous with a noticeable quantity of cubes in addition to spheres.

In every case, samples that had been more slowly quenched at 3.5 ℃/min tended to possess larger particles on average than those samples that had been more rapidly quenched at 100 ℃/min. In addition, at any given annealing temperature, a slower cooling rate promotes the formation of spheres within the sample. Overall, these observations can be explained as follows. Both longer annealing times and higher annealing temperatures are conducive to the production of larger $BaZrO_3$ particles. Therefore, our results demonstrate that quenching in and of itself can be viably used in molten salt systems as a rational synthetic parameter not only to control particle growth but also to generate particles of a specific morphology, which could not otherwise be obtained under standard cooling conditions.[78]

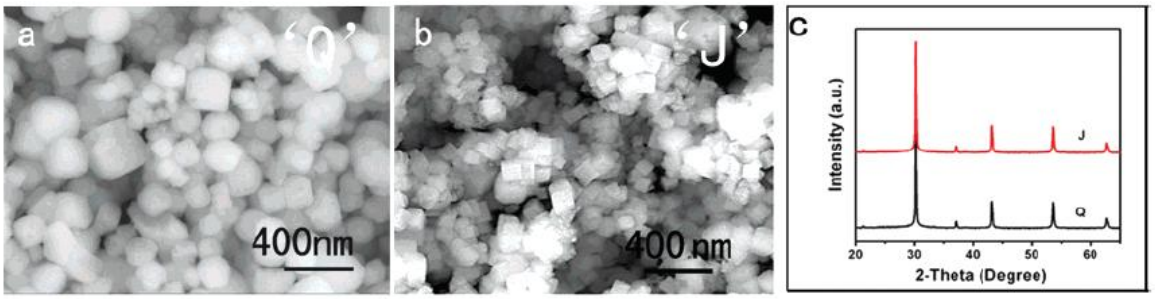

Figure 3.13 Influence of cooling rates. SEM images of samples (a) Q and (b) J, respectively. (c) Corresponding XRD patterns of samples Q and J, cooled at 3.5 and 100 ℃/min, respectively.

Choice of Precursors. From Figure 3.14, we noted that replacing barium oxalate (sample B) with either barium oxide (sample S) or barium carbonate (sample T) also yielded samples possessing a relatively high purity as well as a uniform monodisperse spherical morphology. Similarly, sample W, synthesized using barium acetate, is composed of a large proportion of spherical particles, as was the case with samples B, S, and T, but was observed to possess significant oxide impurities, such as $BaCO_3$ and ZrO_2. By contrast, samples synthesized with either chloride- or nitrate containing precursors of barium and of zirconium (samples U, V, and X) not only tended to be relatively impure with the presence of $BaCO_3$ and ZrO_2 but also were composed of large particle aggregates, measuring 1 to 2 μm.

What could explain this? Thermodynamically speaking, by altering the chemical identity of the precursors, we changed the values of the Gibbs' free energies of reactions in a corresponding fashion. For example, if we compare the precursor choice of $BaCl_2$, $Ba(NO_3)_2$, and barium oxalate at 720 °C, the corresponding Gibbs' free energies of reactions are computed to be -93, -80, and -379 kJ/mol, respectively. The large magnitude of the free energy parameter associated with barium oxalate clearly suggests that it is a highly favorable reaction, and the purity of our products supports that assertion. However, it should be noted that high quality $BaZrO_3$ particles were formed using BaO and $BaCO_3$ as precursors, even though the Gibbs' free energies for these reactions were -50 and -54 kJ/mol, respectively. Hence, it is expected that the reasons for the observed differences in purity and morphology as a function of precursor are not necessarily solely thermodynamic but rather are also dependent on a number of other factors including solubility, diffusion, and transport of reagent species within the reaction medium, all of which suggest a kinetic explanation for our observations.

Additional Factors. We have unpublished results demonstrating that a number of other factors likely play a role in morphology, purity, and composition. First, the addition of surfactant does not necessarily aid in enhancing product purity but in fact may simply assist in dispersing the product powder. Second, the amount of salt used in the reaction is also significant; the addition of excess salt can decrease impurity levels by favoring full dissolution and solubilization of precursors and subsequent precipitation of nuclei of the perovskite phase. In fact, perovskite particles have been noted to increase in size with increasing relative salt content.[24, 80] Third, we have previously shown[20] that the relative molar ratio of precursors either with or without surfactant could control the aspect ratio of as-prepared $Bi_2Fe_4O_9$ submicrometer- sized particles. That is, whereas the use of a 1:1 molar ratio of $Bi^{3+/}Fe^{3+}$ precursors generated smaller particles with cubic-like features, the highest molar ratio employed (i.e., 6:1 molar ratio of Bi^{3+}/Fe^{3+}) yielded larger structures with rod-like, rectangular shapes. Our preliminary results with $BaZrO_3$ are suggestive of a similar behavior in this system. Fourth, overly high heating rates will increase the quantity of impurities, likely because of nonoptimized reaction kinetics. Fifth, even the nature of the combustion boat may conceivably affect the purity of the product. For instance, we have noted that hydroxide media can potentially react with the porcelain boat itself.

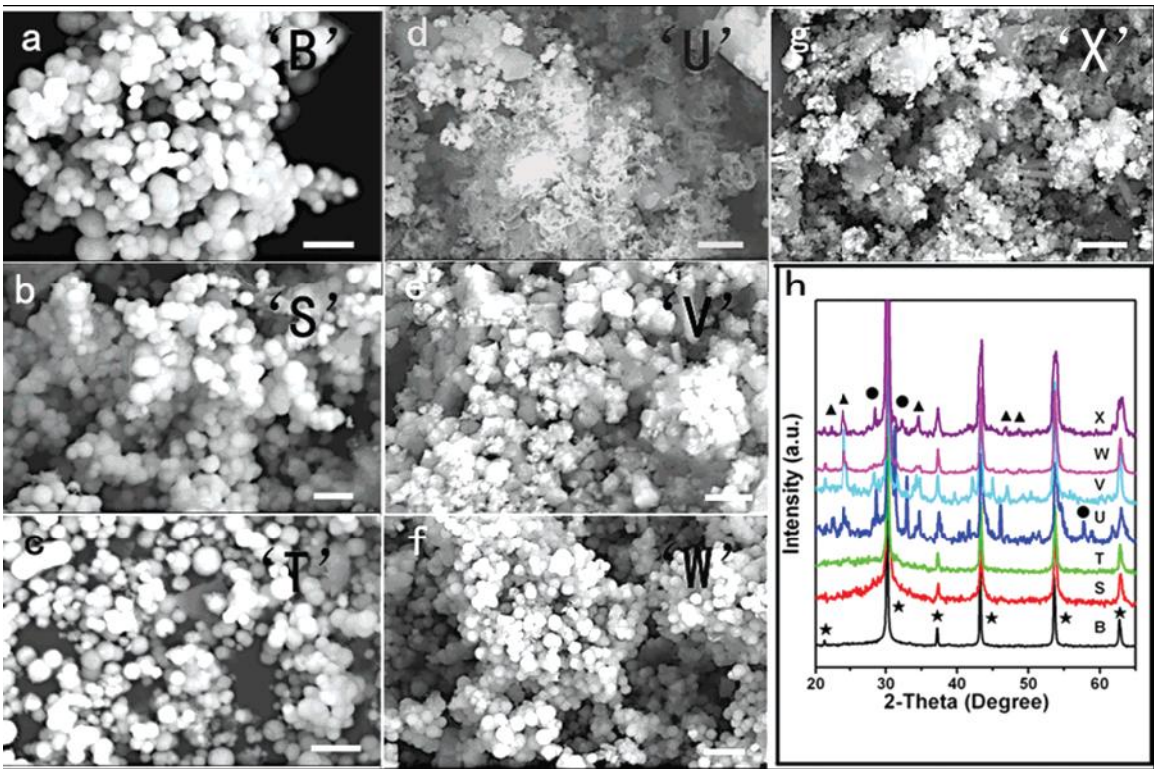

Figure 3.14 Choice of precursors. (a-g) SEM images of samples B and of S-X, respectively, prepared using a range of barium and zirconium precursors. Scale bar in each image = 1 μm. (h) Corresponding XRD patterns of these samples. Scale bar in microscopy images = 1 μm, ★, ▲, and ● represent reflection peaks associated with $BaZrO_3$, $BaCO_3$, and ZrO_2, respectively.

Mechanistic Insight. To gain insights into the mechanism of $BaZrO_3$ particle formation in the presence of NaOH/KOH, a series of samples (1-11) corresponding to successive temporal growth stages during the formation of sample I (which had been annealed at 720 ℃ for 210 min) was synthesized. Descriptions are shown in Figure 3.15a,b as well as in Table 3.3, with samples 8-11 in Table 3 corresponding to samples J, L and I from Table 1. Rod-like motifs, as shown by arrows in Figure 3.16a-d, initially appeared in samples 1-4, at reaction temperatures ranging from 220 to 420 ℃, and may be attributable to the formation of barium carbonate.[81] EDS analysis for all samples was consistent with the presence of Ba, Zr, O, and C peaks, as expected. It should be noted that the ratio of intensities of the Zr versus Ba signals ascribed to as-prepared rods was considerably lower than that for the corresponding, analogous particles, implying that these rods may have consisted of a mixture of ZrO_2, BaO, and $BaCO_3$.

Weight percentages of $BaZrO_3$ of these samples have been calculated, based on the XRD patterns shown in Figure 3.15c. Average particle sizes and percentages of spheres within samples were obtained from SEM images shown in Figure 3.16. Sample 1, quenched at 220 ℃, did not yield any crystalline $BaZrO_3$. Sample 2, quenched 10 min later at 270 ℃, consisted of 21.7% $BaZrO_3$; small cubic particles, measuring ~90 nm, were observed. From sample series 2-8, the weight percentage of $BaZrO_3$ increased dramatically from 21.7% associated with sample 2 (which had been prepared at 270 ℃ after 50 min of reaction time) to 96.1% associated with sample 7 (which had been synthesized at 720 ℃ after 140 min of reaction time). Overall data are summarized in Table 3.

Reaction at 720 ℃ yielded the best results in terms of sample purity. Over this particular sample set from 1 through 7, the observed particle size did not vary significantly (range of 90-100 nm), but the cube morphology predominated (Figure 3.15b). Increasing the overall reaction time further from 170 to 350 min (e.g., samples 8-11) not only increased the weight percentage of $BaZrO_3$ obtained to ~100% but also basically tripled the observed particle sizes from ~100 to >300 nm in diameter. Moreover, these latter samples possessed increasingly larger percentages of spherical particles.

All of these results agree well with the mechanism we proposed earlier for $BaZrO_3$ synthesis.[78] That is, upon heating of the initial mixture, the precursors dissolve into the resultant molten flux and gradually form $BaZrO_3$, which itself has a limited solubility. Upon attainment of a level of concentration supersaturation above the critical solubility (i.e., above the critical energy barrier) of $BaZrO_3$ required for the formation of nuclei, cubic particles are initially generated. Hence, increasing the annealing temperature has the practical effect of favoring the formation of $BaZrO_3$, thereby increasing its nucleation rate and generating a large quantity of initial cubic seed particles. This reasonable hypothesis (i.e., the formation of these seed particles) may explain why particles synthesized at higher temperatures at identical reaction times are actually smaller than those produced at lower temperatures (samples G-I). Moreover, because these initial cubic seed nuclei particles are likely to be below the critical particle size necessary for an in situ conversion, the implication is that particle transformation from cubes to spheres is not as favored at first.

That is, once nucleation begins, particle growth occurs simultaneously, as shown in Region A of Figure 3.17 (samples 2-8). The conversion of cubes to spheres also appears as a parallel process, upon attainment of a critical particle size for the cube precursors (Region B in Figure 3.17, samples 9-11). Overall, it is reasonable to assume that there is a critical threshold concentration required for the initial nucleation and formation of the cubes as well as a critical nucleus dimension for these cubes to acquire prior to their transformation into spheres. Growth and conversion trends converged for samples 9-11 with the formation of samples containing predominantly large spheres (>300 nm).

3.4 Conclusions

$BaZrO_3$ submicrometer-sized cubes and spheres were synthesized by a simple, large scale molten salt technique. Shape control was achieved by control of reaction temperature, time and cooling rate. On the basis of the MSS of $BaZrO_3$ submicrometer-sized particles, the effects of different parameters, such as salt, surfactant, reaction temperature, reaction time, precursor type, amount of salt, heating/cooling rate, and molar precursor ratio, on the resultant product purity, size, shape, and morphology have been discussed. Among these various parameters, the selection of salt is likely the most important one because solubility and reactivity effects associated with the salt can very significantly alter the synthesis process as well as the resultant particle size and shape.

In general, the production of relatively high-quality $BaZrO_3$ samples was favored by high annealing temperatures, slow cooling rates, and overall long reaction times. In terms of optimal overall reaction conditions, uniform, crystalline, well-dispersed, and chemically homogeneous $BaZrO_3$ submicrometer- sized particles were obtained using BaC_2O_4 and ZrO_2 as precursors, NaOH/KOH as the molten reaction medium, a molar ratio of BaC_2O_4/ZrO_2/salt corresponding to 1:1:20, a heating rate of 5 ℃/min, as well as a reaction temperature of 720 ℃. Shorter annealing times (e.g., 30 min) coupled with higher cooling rates (e.g., 100 ℃/min) favored the production of smaller-sized cubic particles. By contrast, longer annealing times (e.g., 60-210 min) and/or a slower cooling rate (5 ℃/min) induced particle conversion from cubes to spheres and usually resulted in a mixture of cube and sphere morphological motifs. Either increasing the annealing time or slowing the cooling rate resulted in the formation of larger spherical particles. Most importantly, we have shown that reliable size, shape, and composition control can be achieved in molten salt syntheses by judicious parameter selection.

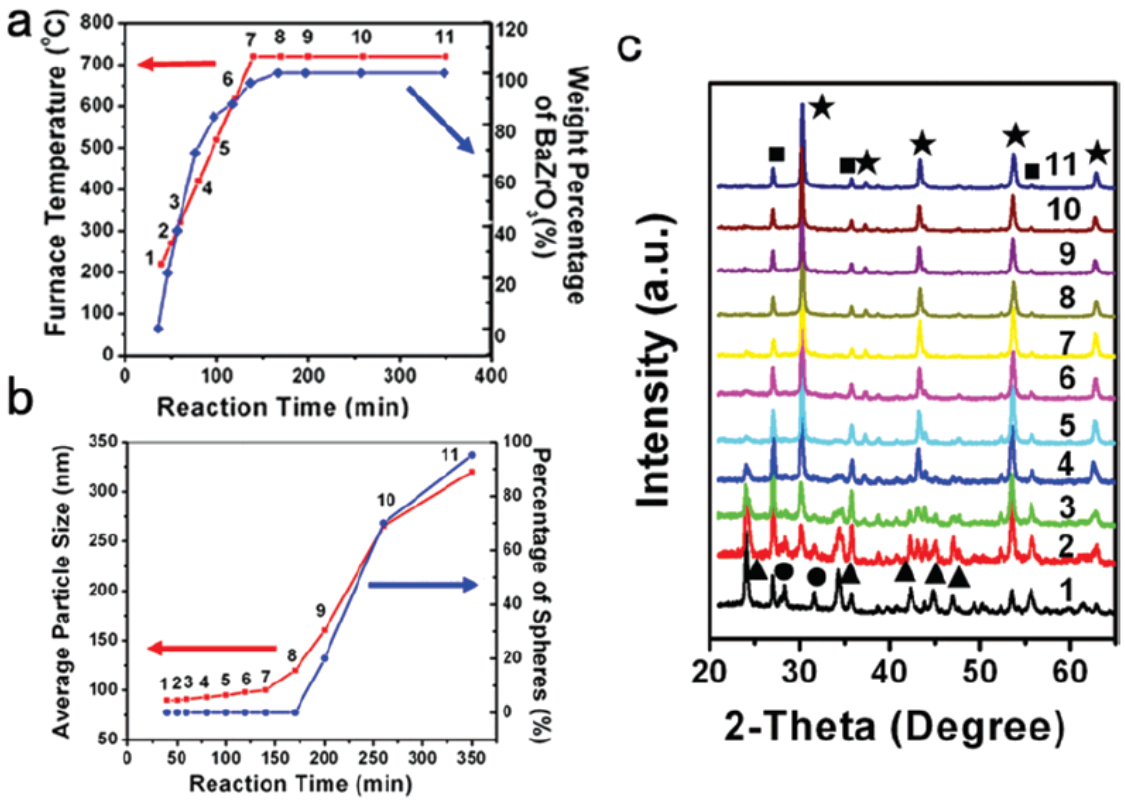

Figure 3.15 Time-dependent particle evolution. (a, b) Furnace temperature, wt% $BaZrO_3$, average particle size, and percentage of spheres of samples 1-11 plotted as a function of overall reaction time at a constant heating rate of 5 ℃/min. Lines connecting data points are intended for visual guidance only. (c) Corresponding XRD patterns of samples 1-11 upon mixing with a constant amount of $ZrSiO_4$ used as an internal standard. (★, ▲, ● and ■ represent $BaZrO_3$, $BaCO_3$, ZrO_2, and $ZrSiO_4$, respectively.)

Table 3.3. Samples Corresponding to Sequential Growth Stages of Sample I (Ultimately Annealed at 720 °C for 210 Min at a Constant Heating Rate of 5 °C/Min)[a]

sample	annealing temp (°C)	time required to reach desired annealing temp (min)	time sample was maintained at desired annealing temp (min)	overall reaction time (min)	average particle size (nm)	percentage of spheres	wt % $BaZrO_3$
1	220	40	0	40		0	~0
2	270	50	0	50	90	0	~21.7
3	320	60	0	60	91	0	~38.4
4	420	80	0	80	93	0	~68.8
5	520	100	0	100	95	0	~82.9
6	620	120	0	120	98	0	~87.9
7	720	140	0	140	100	0	~96.1
8	720	140	30	170	120	0	~100
9	720	140	60	200	160	20	~100
10	720	140	120	260	265	70	~100
11	720	140	210	350	320	95	~100

[a] For all samples, precursors used included BaC_2O_4 and ZrO_2 in the presence of a NaOH/KOH salt medium. The cooling rate was kept constant throughout at ~100 °C/min.

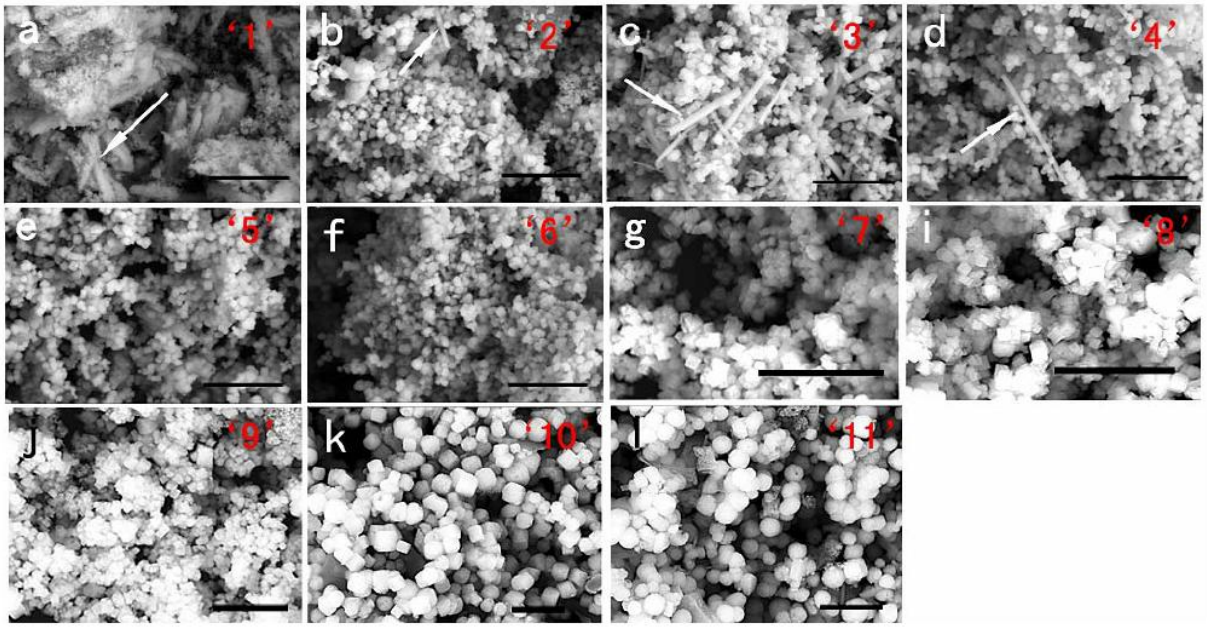

Figure 3.16 Time-dependent particle evolution. (a-l) SEM images of samples 1 to 11 respectively. Scale bar in each image = 1 μm.

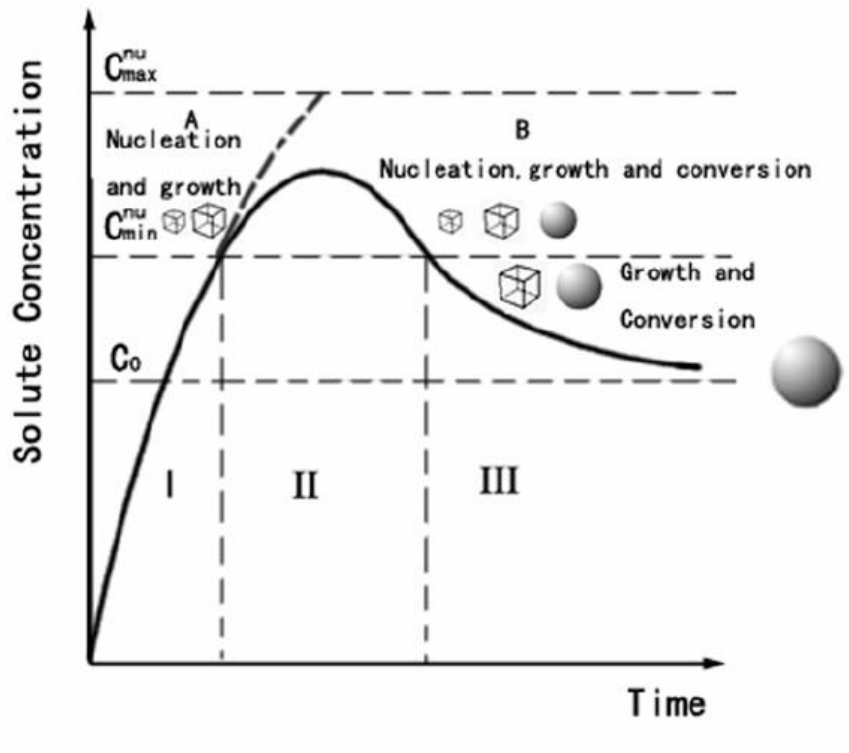

Figure 3.17 Schematic illustrating nucleation, growth and cube-to-sphere conversion processes for as-generated barium zirconate particles. C_o is the equilibrium solubility while C^{nu}_{max} and C^{nu}_{min} represent the maximum and minimum critical concentrations associated with nucleation. Region A is associated with dominant nucleation and growth processes, whereas region B includes the process of conversion of cubes to spheres as well. It should be noted that the dashed lines yield only general delineations amongst the various processes described.[82]

3.5 References

1. Schwartz, R. W. *Chem. Mater.* **1997**, 9, 2325.
2. Boukamp, B. A. *Nat. Mater.* **2003**, 2, 296.
3. Yang, G.; Yue, Z.; Gui, Z.; Li, L. *J. Appl. Phys.* **2008**, 104, 074115/1.
4. Hu, H.; Krupanidhi, S. B. *J. Mater. Res.* **1994**, 1484.
5. Li, X. *J. Mater. Sci.* **2008**, 19, 271.
6. Davydov, B. L.; Yagodkin, D. I. *Quantum Electronics* **2005**, 35, 1071.
7. Feng, Z.; Luo, H.; Yin, Z.; Guang, C.; Ling, N. *Appl. Phys. A* **2004**, 81, 1245.
8. Wu, M. K.; Ashburn, J. R.; Torng, C. J.; Hor, P. H.; Meng, R. L.; L. Gao; Huang, Z. J.; Wang, Y. Q.; Chu, C. W. *Phys. Rev. Lett.* **1987**, 58, 908.
9. Noue, J.; Maekawa, S. *Phys. C* **1994**, 235, 2199.
10. Yajima, T.; Suzuki, H.; Yogo, T.; Iwahara, H. *Solid State Ionics* **1992**, 51, 101.
11. Shende, R. V.; Krueger, D. S.; Rossetti, G. A.; Lombardo, S. J. *J. Am. Ceram. Soc. Bull.* **2001**, 84, 1648.
12. Macmanus-Driscoll, J. L.; Foltyn, S. R.; Jia, Q. X.; Wang, H.; Serquis, A.; Civale, L.; Maiorov, B.; Hawley, M. E.; Maley, M. P.; Peterson, D. E. *Nat. Mater.* **2004**, 3, 439.
13. Koenig, J.; Jaffe, B. *J. Am. Ceram. Soc.* **1964**, 47, 87.
14. Kang, S.; Leonard, K. J.; Martin, P. M.; Li, J.; Goyal, A. *Supercond. Sci. Technol.* **2007**, 20, 11.
15. Viviani, M.; Buscaglia, M. T.; Buscaglia, V.; Leoni, M.; Nanni, P. *J. Eur. Ceram. Soc.* **2001**, 21, 1981.
16. Erb, A.; Traulsen, T.; Muller-Vogt, G. *J. Cryst. Growth.* **1994**, 137, 487.
17. L.Macmanus-Driscoll, J.; Foltyn, S. R.; Jia, Q. X.; Wang, H.; Serquis, A.; Civale, L.; Maiorov, B.; Hawley, M. E.; Maley, M. P.; Peterson, D. E. *Nat. Mater.* **2004**, 3, 439.
18. Hayashi, Y.; Kimura, T.; Yamaguchi, T. *J. Mater. Sci.* **1986**, 21, 757.
19. Volkov, S. V. *Chem. Soc. Rev.* 1990, 19, 21.
20. Park, T.-J.; Papaefthymiou, G. C.; Moodenbaugh, A. R.; Mao, Y.; Wong, S. S. *J. Mater. Chem.* **2005**, 15, 2099.
21. Mao, Y.; Banerjee, S.; Wong, a. S. S. *J. Am. Chem. Soc.* **2003**, 125, 15718.
22. Mao, Y.; Wong, S. S. *Adv. Mater*, **2005**, 17, 2194.
23. Zboril, R.; Mashlan, M.; Petridis, D. *Chem. Mater.* **2002**, 14, 969.
24. Yoon, K. H.; Cho, Y. S.; Kang, D. H. *J. Mater. Sci.* **1998**, 33, 2977.
25. Bloom, H., *The Chemistry of Molten Salts.* W. A. Benjamin, Inc.: New York, **1967**.
26. Badica, P.; Aldica, G.; Iyo, A.; Bradea, I.; Jaklovszky, J. *Mater. Lett.* **2003**, 58, 250.
27. Ling, H.; Li, A.; Wu, D.; Tang, Y.; Liu, Z.; Ming, N. *Mater. Chem. Phys. C* **2002**, 75, 170.
28. Sin, A.; Montaser, B. E.; Odier, P.; Weiss, F. *J. Am. Ceram. Soc.* **2002**, 85, 1928.
29. Brzezinska-Miecznik, J.; Haberko, K.; Bucko, M. M. *Mater. Lett.* **2002**, 56, 273.
30. Kirby, N. M.; Van Riessen, A.; Buckley, C. E.; Wittorff, V. W. *J. Mater. Sci. Eng. B* **2005**, 40, 97.
31. Lencka, M. M.; Nielsen, E.; Anderko, A.; Riman, R. E. *Chem. Mater.* **1997**, 9, 1116.
32. Lu, Z.; Tang, Y.; Chen, L.; Li, Y. *J. Cryst. Growth* **2004**, 266, 539.
33. Kutty, T. R. N.; Vivekanandan, R.; Philip, S. *J. Mater. Sci.* **1990**, 25, 3649.
34. Vivekanadan, R.; Philip, S.; Kutty, T. R. N. *Mater. Res. Bull.* **1987**, 22, 99.
35. Millot, N.; Xin, B.; Pighini, C.; Aymes, D. *J. Eur. Ceram. Soc.* **2005**, 25, 2013.

36. Kolen'ko, Y. V.; Burukhin, A. A.; Churagulov, B. R.; Oleinikov, N. N.; Vanetsev, A. S. *Inorg. Mater.* **2002**, 38, 252.
37. Azad, A.; Subramaniam, S. *Mater. Res. Bull.* **2002**, 37, 85.
38. Yamanaka, S.; Hamaguchi, T.; Oyama, T.; Matsuda, T.; Kobayashi, S.; Kurosaki, K. *J. Alloys Compd.* **2003**, 359, 1.
39. Robertz, B.; Boschini, F.; Cloots, R.; Rulmont, A. *Int. J. Inorg. Mater.* **2001**, 3, 1185.
40. Athawale, A. A.; Bapat, M. *J. Metastable Nanocryst. Mater.* **2005**, 23, 3.
41. Ubaldini, A.; Buscaglia, V.; Uliana, C.; Costa, G.; Ferretti, M. *J. Am. Ceram. Soc.* **2003**, 86, 19.
42. Boschini, F.; Robertz, B.; Rulmont, A.; Cloots, R. *J. Eur. Ceram. Soc.* **2003**, 23, 3035.
43. Niederberger, M.; Pinna, N.; Polleux, J.; Antonietti, M. *Angew. Chem., Int. Ed.* **2004**, 43, 2270.
44. Leonard, K. J.; Sathyamurthy, S.; Paranthaman, M. P. *Chem. Mater.* **2005**, 17, 4010.
45. Palchik, O.; Zhu, J.; Gedanken, A. *J. Mater. Chem.* **2000**, 10, 1251.
46. El-Sayed, M. A. *Acc. Chem. Res.* **2004**, 37, 326.
47. Lee, S.-M.; Jun, Y.-W.; Cho, S.-N.; Cheon, J. *J. Am. Chem. Soc.* **2002**, 124, 11244.
48. Jun, Y.-W.; Choi, J.-S.; Cheon, J. *Angew. Chem., Int. Ed.* **2006**, 45, 3414.
49. Liu, X.; McCandlish, E. F.; McCandlish, L. E.; Mikulka-Bolen, K.; Ramesh, R.; Cosandey, F.; Jr., G. A. R.; Riman, R. E. *Langmuir* **2005**, 21, 3207.
50. Bish, D. L.; Howard, S. A. *J. Appl. Crystallogr.* **1988**, 21, 86.
51. Orlhac, X.; Fillet, C.; Deniard, P.; Dulac, A. M.; Brec, R. *J. Appl. Crystallogr.* **2001**, 34, 114.
52. Toby, B., H. *J. Appl. Crystallogr.* **2001**, 34, 210.
53. Smith, D. K.; Newkirk, W. *Acta Crystallogr.* **1965**, 18, 983.
54. Robinson, K.; Gibbs, G. V.; Ribbe, P. H. *Am. Miner.* **1971**, 56, 782.
55. De Villiers, J. P. R. *Am. Miner.* **1971**, 56, 758.
56. Levin, I.; Amos, T. G.; Bell, S. M.; Farber, L.; Vanderah, T. A.; Roth, R. S.; Toby, B., H. *J. Solid State Chem.* **2003**, 175, 170.
57. Eckert, J. O., Jr.; Huang-Houston, C. C.; Gersten, B. L.; Lencka, M. M.; Riman, R. E. *J. Am. Ceram. Soc.* **1996**, 79, 2929.
58. Mao, Y.; Wong, S. S. *Adv. Mater.* **2005**, 17, 2194.
59. Mao, Y.; Banerjee, S.; Wong, S. S. *J. Am. Chem. Soc.* **2003**, 125, 15718.
60. Park, J.-H.; Lee, D.-H.; Shin, H.-S.; Lee, B.-K. *J. Am. Ceram. Soc.* **1996**, 79, 1130.
61. Fuenzalida, V. M.; Pilleux, M. E. *J. Mater. Res.* **1995**, 10, 2749.
62. Lyapin, A.; Jeurgens, L. P. H.; Graat, P. C. J.; Mittemeijer, E. J. *Surf. Interface Anal.* **2004**, 36, 989.
63. Rao, B. V.; Rambabu, U.; Buddhudu, S. *Physica B.* **2006**, 382, 86.
64. Li, J.; Kuwabara, M. *Adv. Mater.* **2003**, 4, 143.
65. Gopolan, S.; Mehta, K.; Virkar, A. V. *J. Mater. Res.* **1996**, 11, 1863.
66. Barin, I.; knacke, O., *Thermochemical Properties of Inorganic Substances*. Springer-Verlag: New York, **1973**.
67. Deloume, J.-P.; Scharff, J.-P.; Marote, P.; Durand, B.; Abou-Jalil, A. *J. Mater. Chem.* **1999**, 9, 107.
68. Mamantov, G.; Braunstein, J., *AdVances in Molten Salt Chemistry*. Plenum Press: New York, **1973**.
69. Sundermeyer, W. *Chem. Ber.* **1964**, 97, 1069.

70. Liu, H.; Hu, C.; Wang, Z. L. *Nano Lett.* **2006**, 6, 1535.
71. Ito, Y.; Shimada, S.; Inagaki, M. *J. Am. Ceram. Soc.* **1995**, 78, 2695.
72. Ito, Y.; Jadidian, B.; Allahverdi, M.; Safari, A. In *Particle Shape Control of Molten Salt Synthesized Lead Titanate.*, Proceedings of the 2000 IEEE International Symposium on Applications of Ferroelectrics., Honolulu, HI, **2000**.
73. Murphy, C. J. *Science* **2002**, 298, 2139.
74. Puntes, V. F.; Krishnan, K. M.; Alivisatos, A. P. *Science* **2001**, 291, 2115.
75. Filankembo, A.; Giorgio, S.; Lisiecki, I.; Pileni, M. P. *J. Phys. Chem. B* **2003**, 107, 7492.
76. Xia, Y.; Yang, P.; Sun, Y.; Wu, Y.; Mayers, B.; Gates, B.; Yin, Y.; Kim, F.; Yan, H. *Adv. Mater.* **2003**, 15, 353.
77. Lee, S.-M.; Cho, S.-N.; Cheon, J. *Adv. Mater.* **2003**, 15, 441.
78. Zhou, H.; Mao, Y.; Wong, S. S. *J. Mater. Chem.* **2007**, 17, 1707.
79. Park, T.-J.; Wong, S. S. *Chem. Mater.* **2006**, 18, 5289.
80. Yoon, K. H.; Cho, Y. S.; Lee, D. H.; Kang, D. H. *J. Am. Ceram. Soc.* **1993**, 76, 1373.
81. Wang, L.; Zhu, Y. *Chem. Lett.* **2003**, 32, 594.
82. Haruta , M. and Delmon, B. *J. Chim. Phys. Phys.-Chim. Biol.* **1986**, 83, 859.

Chapter IV Template synthesis of 1D metal oxide nanostructures: ZnO, CuO and α-Fe_2O_3

4.1 Introduction

In previous chapters, we discussed the synthesis of ternary metal oxides ($Bi_2Ti_2O_7$ and $BaZrO_3$). In the current chapter, we will discuss a low-cost, simple way to synthesize one-dimensional binary metal oxides.

4.1.1 Template Method

As mentioned in chapter I and elucidated upon in chapter II, template-directed synthesis represents a straightforward route to one-dimensional nanostructures. It has been used in the fabrication of nanorods, nanowires and nanotubules of polymers, metals, semiconductors and oxides. Various templates with nanosized channels have been explored for the template growth of nanorods and nanotubules. The most commonly used and commercially available templates are anodized alumina membrane[1] and radiation track-etched polymer membranes[2]. Other membranes that have also been used as viable templates include nanochannel array glass,[3] radiation track-etched mica,[4] mesoporous materials,[5] porous silicon,[6] zeolites[7] and carbon nanotubes.[8, 9]

When choosing templates, certain requirements should be considered in addition to the pore size, morphology, size distribution and density of pores. First, the template materials must be chemically compatible with the processing conditions. For example, an electrical insulator is required for a template to be used in electrochemical deposition. A thermally stable template is required for use in vapor phase deposition. Secondly, the precursor materials or solution must be able to thoroughly wet the internal pore walls. Thirdly, the deposition should start from one end of the template channels and proceed both longitudinally and laterally for the synthesis of nanowires or nanorods. For example, in the synthesis of nanotubes, deposition should start from the pore wall and proceed inwards. Other considerations include the ease with which nanowires or nanorods are released from the templates and as well as handling conditions during the experiments.

4.1.1.1 Anodized Aluminum Oxide Template (AAO)

AAO, formed by the anodization of an Al sheet in appropriate acidic or basic electrolytic solutions,[10-12] possesses a honeycomb structure consisting of a close-packed array of columnar alumina units, each containing a central straight hole. The dimensions of the anodic porous alumina cells depend upon the anodizing conditions.[10, 11] The hole interval is determined by the applied voltage used for the anodization. The value of the constant of this interval divided by the applied voltage is approximately 2.5 nm/V. The actual hole size is dependent upon the electrolyte composition, temperature, period of anodization as well as the applied voltage.[12] The hole size is also controlled by a post-

anodizing process such as pore-widening treatment endendered by dipping the AAO in an appropriate acid solution after the anodization. The depth of the holes (i.e. thickness of the AAO template) has a good linear relationship with the period of the anodization.

Due to its ease of fabrication, thermal and chemical stability, and presence of a well-ordered pore structures with high aspect ratio, AAO has recently attracted much interest as a template material for the fabrication of several kinds of nanodevices. However, AAO can't be used under harsh condition, i.e. strong basic or acid solution, in which AAO will be dissolved. Moreover, after annealed at very high temperature (normally higher than 800 ℃), AAO will be very difficult to be destroyed.

4.1.1.2 Polycarbonate Membranes (PC)

Polycarbonate membranes are generated by bombarding a nonporous polycarbonate sheet, with a typical thickness ranging from 6 – 20 μm, with nuclear fission fragments to create damage tracks, and then chemically etching these tracks into pores.[2] In radiation track etched membranes, pores have a uniform size as small as 10 nm, which ore often randomly distributed. Pore densities can be as high as 10^9 pores/cm^2.

PC templates are not as thermally stable as AAO templates. They melt at a temperature above ~140 ℃ and decompose above 400 ℃. Hence they are not suitable for the synthesis which needs to proceed under high temperature conditions. One of their advantages is their ease of removal. Several minutes in methylene chloride or chloroform will destroy the template completely. Another advantage is that they can be used in acidic/basic conditions in which AAO cannot be used. This is also the reason why we used both of AAO and PC as templates in the synthesis of transition metal oxides nanostructures.

4.1.2 Transition Metal Oxides – ZnO, CuO and α-Fe_3O_4

4.1.2.1 ZnO

ZnO is a key, II-VI compound semiconductor, with particularly attractive properties such as a direct wide band gap (3.37 eV), a large exciton binding energy (60 meV at room temperature), and an exciton Bohr radius in the range of 1.4-3.5 nm.[13] Moreover, ZnO possesses a high breakdown voltage, good piezoelectric characteristics, biocompatibility, as well as high mechanical, thermal, and chemical stability. All of these favorable properties render this material highly versatile for a host of optoelectronic applications including room-temperature ultraviolet lasers,[14] photodetectors,[15, 16] dye sensitized solar cells,[17, 18] and field-effect transistors.[19-21] Moreover, the generation of high-quality, high aspect ratio, and high surface area ZnO nanowires as well as their corresponding assembly into functional arrays is expected to improve the luminescence efficiency of electro-optic devices and the sensitivity of chemical sensors. ZnO nanowire arrays have already been utilized as field emission sources as well as power generators for nanoscale devices.[22-24] ZnO nanowires and nanowire arrays have been previously synthesized *via* both vapor and solution phases. Typical approaches were based on metal_organic chemical vapor deposition (MOCVD),[25, 26] chemical vapor transport (CVT),[27, 28] and pulsed laser deposition (PLD).[29] These methods, while fully capable of

generating high-quality wires and arrays, do possess limitations. For instance, gas-phase methods tend to involve the use of high temperatures (*e.g.*, 450-900 ℃), potentially toxic precursors, and a very limited range of substrates in order to induce and direct the growth of ZnO nanowires. Moreover, PLD is not an inexpensive method of producing ZnO nanostructures. Solution-based methodologies also exist for ZnO formation.[30] As an illustrative example, layers of ZnO seed nanocrystals, measuring 5-10 nm in diameter, can be initially formed onto a Si substrate by thermally decomposing zinc acetate at 200-350 ℃, and this 50-200 nm film of crystal seeds can be subsequently grown into vertical nanowire arrays at 90 ℃.[31, 32] Recently, Wang *et al*.[23] extended this methodology to the growth of aligned ZnO nanowire arrays on a plastic film using Au nanocrystal seeds.

4.1.2.2 CuO

As a *p*-type semiconductor with a narrow band gap (1.2 eV), CuO is a candidate material for photothermal and photoconductive applications.[33, 34] Moreover, it is also an effective heterogeneous catalyst[35] for converting hydrocarbons completely into carbon dioxide and water. In addition, it is potentially a useful component in the fabrication of sensors, magnetic storage media, field emitters, lithium copper oxide electrochemical cells, cathode materials, and high *T*c-superconductors.[36, 37] CuO nanowires can, for instance, be synthesized merely by heating Cu substrates in air from 400 to 700 ℃,[33, 38] while 1D CuO nanostructures can be obtained by a high-temperature transformation of their 1D copper hydroxide nanoscale analogues.[39-43] Polycrystalline CuO nanofibers have been prepared through electrospinning.[44] Free standing CuO nanotube and nanowire arrays have been fabricated by depositing precursors of either a MOCVD process[45] or a sol-gel technique[46] into the uniform pores of alumina templates, followed by subsequent annealing.

4.1.2.3 α-Fe_2O_3

Because of its high stability, relatively low cost, and *n*-type semiconducting properties with a small band gap (2.1 eV), α-Fe_2O_3 has been associated with applications ranging from gas sensing, lithium-ion battery production, catalysis, water splitting, water purification, and solar energy conversion to pigmentation.[47-49] Nanobelts, nanowires, and arrays of hematite structures have been synthesized by different methods, such as (a) the direct thermal oxidation of a pure iron substrate in an oxidizing atmosphere with a temperature range of 500-800 ℃;[50, 51] (b) the vacuum pyrolysis of β-FeOOH nanowires in a pressure range of 10^{-2} to 10^{-3} atm;[52, 53] and (c) PLD using pressed Fe_3O_4 powder as a target.[54] Hematite nanotubes[49] and their corresponding arrays[55] have also been obtained by decomposing organometallic iron precursors, embedded within the pores of an alumina template, at high temperature. Moreover, hematite nanotubes have been synthesized by using carbon nanotubes as a structural template motif.[56]

4.1.3 Current Work

It is obvious based on all of the prior work that it would be desirable to develop a protocol that allows for an environmentally sound and cost-effective methodology of metal oxide nanoscale synthesis without the need to sacrifice on sample quality, crystallinity, monodispersity, and purity. That is, it would be a viable, complementary advance to develop a generalizable protocol aimed at ZnO, CuO, and α-Fe_2O_3 (hematite) nanowire/array formation with the goal of overcoming either the high temperatures, the need for expensive equipment, the use of potentially toxic precursors and byproducts, or the ultimate product polycrystallinity, characteristic of previous literature methods of metal oxide nanoscale synthesis.

In our group, we have modified and refined the conventional template-directed synthesis, popularized by Charles Martin's group,[57-59] to yield a relatively simple and versatile variation with which to prepare size controlled, one-dimensional nanostructures under ambient conditions in aqueous solution with reliable control over shape, dimensionality, and crystallinity. We have previously demonstrated[60] the room-temperature preparation of single-crystalline $BaWO_4$ and $BaCrO_4$ nanowires with different controllable sizes as well as the creation of arrays of these nanowires in the pores of an alumina membrane. We have subsequently extended this methodology to the production of BaF_2, CaF_2, and SrF_2, in addition to NH_4MnF_3 and $KMnF_3$ nanowire structures.[61] The gist of the method is that we initially mount conventional, commercially available membranes, composed of either alumina or polymer, between the two halves of a glass U-tube cell.[62, 63] The half-cells are then filled with equimolar solutions of precursor solutions. In effect, the pores in the membranes are used as the environment with which to confine and control the growth of our one-dimensional products. Moreover, these as-produced nanomaterials are chemically pure, are structurally well-defined, and can be generated in reasonable quantities.

The key point is that our method is generalizable and can be adapted to the production of binary metal oxides, which are the focus of our efforts herein. As an example of the potential of our strategy, we have used polycarbonate (PC) templates to synthesize ZnO nanowires and their corresponding arrays. By comparison with previous techniques discussed for ZnO nanostructure synthesis (for which similar arguments can be analogously made for CuO as well as for α-Fe_2O_3 nanostructures), the key attractive attributes of our methodology are (1) use of relatively low temperature (*i.e.*, room temperature to about 80 ℃); (2) short reaction time (about 30 min); (3) simplistic, inexpensive experimental setup, requiring the use of a homemade U-tube; (4) lack of either a toxic organic precursor or a toxic byproduct (in fact, we only utilized an inorganic metal salt solution along with sodium hydroxide in our synthesis); (5) relative ease of template removal by immersion in methylene chloride; (6) no need for either ZnO or metal nanocrystalline "nucleation seeds"; and finally, (7) substrate-less generation of ZnO nanowire arrays. What is highly significant is that the last point implies that ZnO (or frankly any other metal oxide such as CuO and α-Fe_2O_3) arrays can be theoretically transferred onto any type of substrate, be it curved, linear, rigid or pliant, upon template attachment to a conductive tape and subsequent template removal. This potential for highly flexible array generation will have relevance for applications as diverse as usage

in portable electronics, implantable biosensors, biodetectors, and self-powered electronic devices.[23]

4.2 Experimental Section

4.2.1 Preparation

Commercially available polycarbonate (PC) membranes (Millipore Co.) used in this study contained pore sizes of 50, 100, and 200 nm in diameter, respectively. These polycarbonate filters possess track-etched channels with pores randomly distributed across the filter membranes. Commercially available alumina (AAO) templates (Whatman Co., U.K.) used in this study maintained pore sizes of 200 nm in diameter.

To synthesize ZnO and CuO nanowires, a typical PC membrane was mounted between the two halves of a U-tube cell. The half-cells were then filled with equimolar solutions (0.1 M) of metal salt solutions (*e.g.*, $ZnCl_2$ (Aldrich) for ZnO and $Cu(NO_3)_2$ (Alfa Aesar) for CuO, respectively) and NaOH (Fisher) in water, respectively. The entire U-tube cell was subsequently placed in a water bath whose temperature was set at 80 ℃. It has been previously shown[40, 41, 64, 65] that under these experimental conditions, metal hydroxides (such as $Zn(OH)_2$ and $Cu(OH)_2$, in this example) initially form and then transform *via* a low temperature "dehydration" and subsequent crystallization process to ultimately yield their corresponding metal oxides (such as ZnO and CuO, in this case) upon low-temperature heating of the alkaline solution containing these species. Our results for CuO, in particular, visually confirmed this scenario as we were able to observe a change from the blue hue characteristic of $Cu(OH)_2$, initially generated at room temperature, to the coal black color associated with the CuO product in solution, upon heating to 80 ℃. After 30 min of reaction, the PC template was detached, thoroughly washed by distilled water, and ultimately removed by immersion in methylene chloride for 10 min. Isolated nanoscale metal oxide samples were then centrifuged, washed with ethanol and distilled water, and finally oven-dried at 80 ℃ for 24 h.

To synthesize α-Fe_2O_3 nanotubes, an AAO membrane was mounted, as opposed to a PC template, between the two halves of a U-tube cell. The half-cells were then filled with equimolar solutions (0.01 M) of $Fe_2(SO_4)_3$ (J.T. Baker) and ammonium hydroxide (Fisher) in water. The U-tube cell was maintained at room temperature. After 1 h of reaction to prepare $Fe(OH)_3$,[66] the AAO template containing the product was detached, thoroughly washed with distilled water, and oven-dried at 80 ℃ for 1 h. The AAO template was subsequently annealed at 600 ℃ for 60 min to ultimately generate α-Fe_2O_3 nanostructures. We note that we were unable to synthesize crystalline hematite, despite numerous experimental variations, without an annealing step. After annealing, the template was removed by immersion in 1 M NaOH for 1 h. Samples were then centrifuged, washed with distilled water until the pH of the solution attained a value of 7, and ultimately oven-dried at 80 ℃ for 24 h.

4.2.2 Characterization

X-ray Diffraction (XRD). See section 1.7.1.

Electron Microscopy. See section 1.7.2.

Photoluminescence (PL). Photoluminescence data were obtained at 25 ℃ on a Jobin Yvon Spex Fluorolog 3 with a 1 s integration time. PL spectra for ZnO nanowires in water solution were obtained at an excitation wavelength of 325 nm. Prior to data collection, the nanowire solution was sonicated for approximately 30 s to obtain a visually nonscattering dispersion. Fluorescence data were taken immediately afterward.

Ultraviolet-Visible Spectra (UV-vis). See section 1.7.3.

Infrared Spectroscopy (IR). Mid-infrared spectra were recorded by using a Nicolet Nexus 470 FTIR spectrometer with a resolution of 4 cm^{-1}. Solid samples were prepared using a potassium bromide (KBr) pellet.

Photocatalytic Activity. To test the photocatalytic efficiency of as prepared ZnO nanowires, a solution mixture of 10 mg/L methyl orange containing 1 g/L of ZnO nanowires in water was prepared. Prior to irradiation, the suspensions were sonicated for 10 min and then magnetically stirred in the dark for 30 min to establish an adsorption/degradation equilibrium. The suspension was subsequently irradiated under UV light (emission wavelength maximum at 366 nm) at a ~5 cm separation distance. Analogous control experiments were performed either without ZnO (blank) or in the presence of either a commercial bulk or a commercial nanoparticle (Nanostructured & Amorphous Materials, Inc., 20 nm) sample, normalized for identical metal oxide concentrations. Concentrations of methyl orange in the supernatant aliquots were subsequently analyzed by measuring the absorbance at 464 nm using a Thermospectronics UV1 spectrometer with 10-mm path length quartz cells.

For hematite nanotubes, a similar protocol was utilized with the exception that 4-chlorophenol (4-CP) was tested as opposed to methyl orange. Our source for 20-50 nm commercial hematite nanoparticles was Nanostructured & Amorphous Materials, Inc. The concentration of 4-CP utilized was 6 mg/L and the amount of catalyst loading was set at 50 mg/L. The process for testing the photocatalytic efficiency of hematite nanotubes was essentially identical to the one for ZnO nanowires with the exception that absorbance was measured at an emission wavelength maximum of 225 nm.

Degradation of Hydrogen Peroxide. To probe the ability of as prepared CuO nanowires to catalyze the degradation of H_2O_2, a 20 mL solution mixture containing 0.6 M H_2O_2 and 0.5 g/L CuO nanowires was initially prepared with rapid magnetic stirring. A 1 mL portion was removed every 30 min and the concentration of H_2O_2 in the subsequent pH-adjusted supernatant aliquots was then analyzed by titration with a solution of 0.02 M $KMnO_4$.[67] Analogous control experiments were performed either without CuO (blank) or in the presence of either a commercial bulk or a commercial nanoparticle (Nanostructured & Amorphous Materials, Inc., 30-50 nm) sample, normalized for identical metal oxide concentrations.

SQUID. Magnetization measurements were obtained using a Quantum Design magnetic property measurement system (MPMS) superconducting quantum interference device (SQUID) magnetometer, operated over a temperature range of 5-300 K, at an applied

field of 100 Oe. Magnetization *versus* applied field measurements were obtained using H values from -5000 to 5000 Oe. Powder samples of as-prepared products were pressed lightly, loaded into a gel cap, and then covered with silica wool. The sample was held within a uniform drinking straw, which was attached to the sample rod of the MPMS apparatus. Signals generated by measurements of an empty sample holder demonstrated that the holder assembly contributes 1% to the overall magnetic signal.

4.3 Results and Discussion

The purity and crystallinity of as-prepared metal oxide nanostructure samples were initially examined by powder XRD measurements (Figure 4.1). As shown in Table 4.1, all peaks of as-prepared samples can be readily indexed to pure phases of our desired materials. No detectable impurities were noted in any of the patterns. Thus, we were able to obtain hexagonal-phase ZnO and monoclinic-phase CuO crystals at 80 ℃ without the necessity of an additional annealing step at high temperature.

By contrast, for the production of rhombohedral phase Fe_2O_3, under identical experimental conditions (use of a polycarbonate (PC) template, at 80 ℃, same concentrations of precursors), the XRD pattern of the as-prepared sample was completely featureless. This diffraction result suggested that either little if any Fe_2O_3 crystals were produced or the as-prepared sample was effectively amorphous. Hence, we hypothesized that further annealing was likely needed to increase sample crystallinity. However, since the PC template could only be used below 140 ℃ beyond which it would either deform, melt, or even decompose, the use of an AAO template was substituted. Resultant samples (in AAO) were annealed at 600 ℃ for 1 h. An XRD pattern (Figure 4.1C, upper curve) showed that hematite (α-Fe_2O_3) crystals could therefore be obtained, as planned.

The morphology of as-synthesized one-dimensional samples was studied using FE-SEM and TEM. Figure 4.2A shows SEM images of as-prepared ZnO nanowires, isolated from a 200 nm PC template. Diameters of these ZnO nanowires are about 250 - 50 nm, whereas the associated lengths measure about 10 ± 1 μm. Additional images of ZnO nanowires, grown in templates with pore diameters measuring 50 and 100 nm, respectively, are presented in Figure 4.3. The diameters of these particular ZnO nanowires are 60 ± 10 and 120 ± 20 nm, respectively, consistent with the pore size dimensions of the originating templates themselves. Figure 4.2B shows an image of samples with the template partially removed and with individual, aligned ZnO nanowires protruding vertically from the inner surfaces of the template pores. In this architecture, nanowire arrays are structurally supported by the presence of the remnant PC template which thereby increased the overall strength of the composite structure. This is significant because it is known that the power-generating capability of polymer-supported ZnO nanowire arrays is higher than that of corresponding arrays lacking any such mechanical support.[23] In our experiments, arrays of ZnO nanowires appear to be structurally robust and well preserved, after careful and complete removal of the entire PC template by methylene chloride, as shown in Figure 4.2C (top view) and in Figure 4.2D,E (tilt view). The EDS spectrum (Figure 4.2F) shows the presence of Zn and O, as expected with the Si signal attributable to the underlying Si wafer used for imaging. By analogy to ZnO, SEM data on isolated CuO nanowires are shown in Figure 4.4A. Diameters and lengths are 250 ± 50 nm and 12 ± 2 μm, respectively. CuO nanowire

arrays were also prepared in an analogous fashion to that of ZnO, that is, upon removal of the PC template, as shown in Figure 4.4 panels B and C. The EDS spectrum (Figure 4.4D) confirms the existence of Cu and O with the presence of Si attributable to the underlying Si wafer used for microscopy imaging.

As opposed to nanowires, hollow α-Fe_2O_3 nanotubes were obtained using AAO as the reaction template (Figure 4.5A). Diameters and lengths of the as-obtained nanotubes measured approximately 260 ± 60 nm and 6 ± 3 μm, respectively. The existence of short nanotubes may arise from breakage of long nanotubes during the associated sonication process for TEM sample processing. Upon removal of a thin layer of AAO template, nanotubes can be clearly observed, growing within the pores of the template (Figure 4.5B). However, it is evident that the nanotubes themselves are not actually attached to the inner surfaces of the pores. Shrinkage of the tubes toward the pore centers may have resulted from a loss of water upon annealing of $Fe(OH)_3$ (generated in situ from the reaction of $Fe_2(SO_4)_3$ and ammonium hydroxide) at high temperature. Arrays of aligned iron oxide nanotubes are shown in Figure 4.5C after careful removal of the AAO template. The EDS spectrum (Figure 4.5D) is consistent with the existence of Fe and O, whereas the Al signal originates from the remaining AAO template and the Si signal emanates from the Si wafer used in the imaging process.

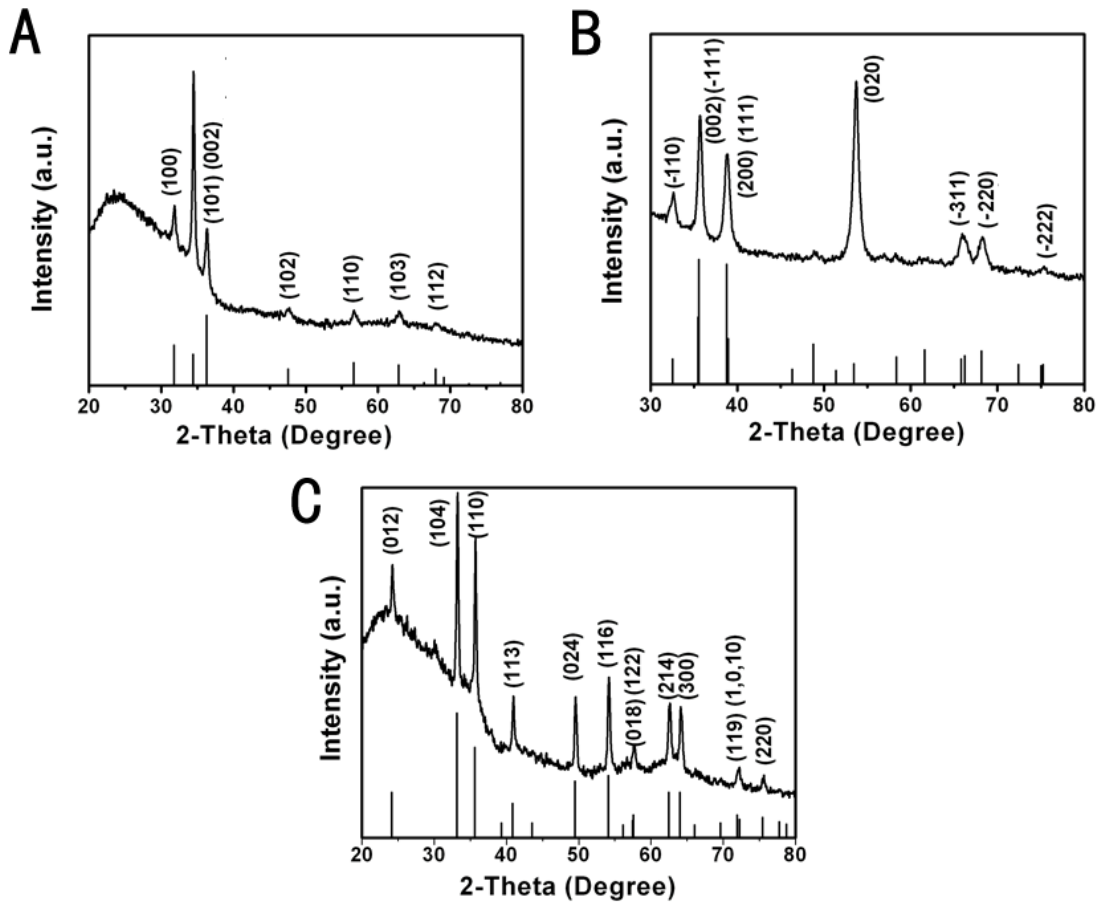

Figure 4.1 XRD patterns of as-prepared samples: (A) ZnO nanowires, (B) CuO nanowires, and (C) α-Fe_2O_3 nanotubes. Representative diffraction patterns (upper half) and corresponding standard JCPDS diffraction patterns (lower half) for each of the samples are shown in each figure part.

TABLE 4.1. Crystallographic Data of as-Prepared Samples and Comparisons with Expected Literature Values

sample	JCPDS database No.	phase (space group)	calculated constants	literature values
ZnO nanowires	36-1451	Hexagonal ($P63mc$)	$a = 0.3249$ nm	$a = 0.3249$ nm
			$c = 0.5206$ nm	$c = 0.5206$ nm
CuO nanowires	45-0937	Monoclinic ($C2/c$)	$a = 0.4685$ nm	$a = 0.4685$ nm
			$b = 0.3426$ nm	$b = 0.3425$ nm
			$c = 0.5130$ nm	$c = 0.5130$ nm
α-Fe_2O_3 nanotubes	33-0664	Rhombohedral ($R3c$)	$a = 0.5036$ nm	$a = 0.5035$ nm
			$c = 1.3749$ nm	$c = 1.3740$ nm

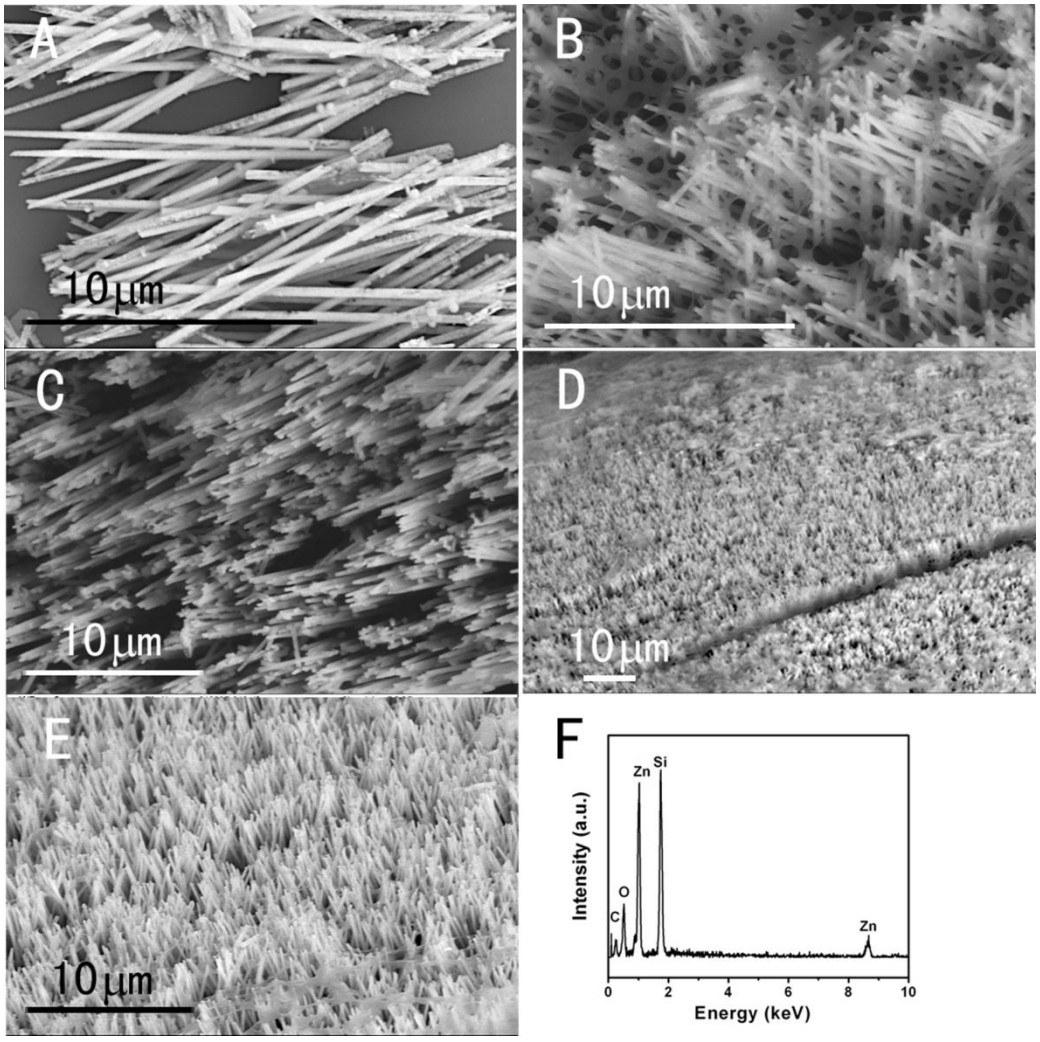

Figure 4.2 SEM images of (A) isolated ZnO nanowires and (B) ZnO nanowires embedded in the template; (C-E) additional SEM images of ZnO nanowire arrays after removal of the template; representative EDS pattern (F) of as-prepared ZnO nanowires and arrays.

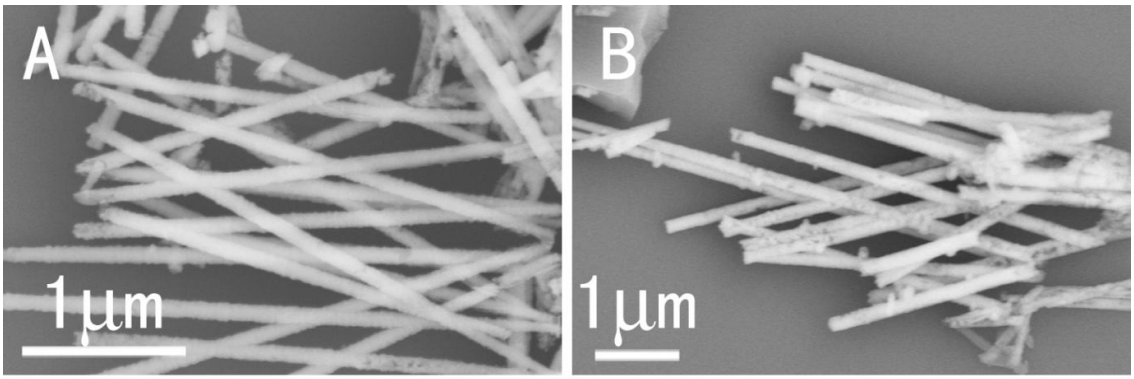

Figure 4.3 Collection of SEM images of ZnO nanowires prepared from a PC template possessing pore sizes of (A) 50 nm and (B) 100 nm, respectively.

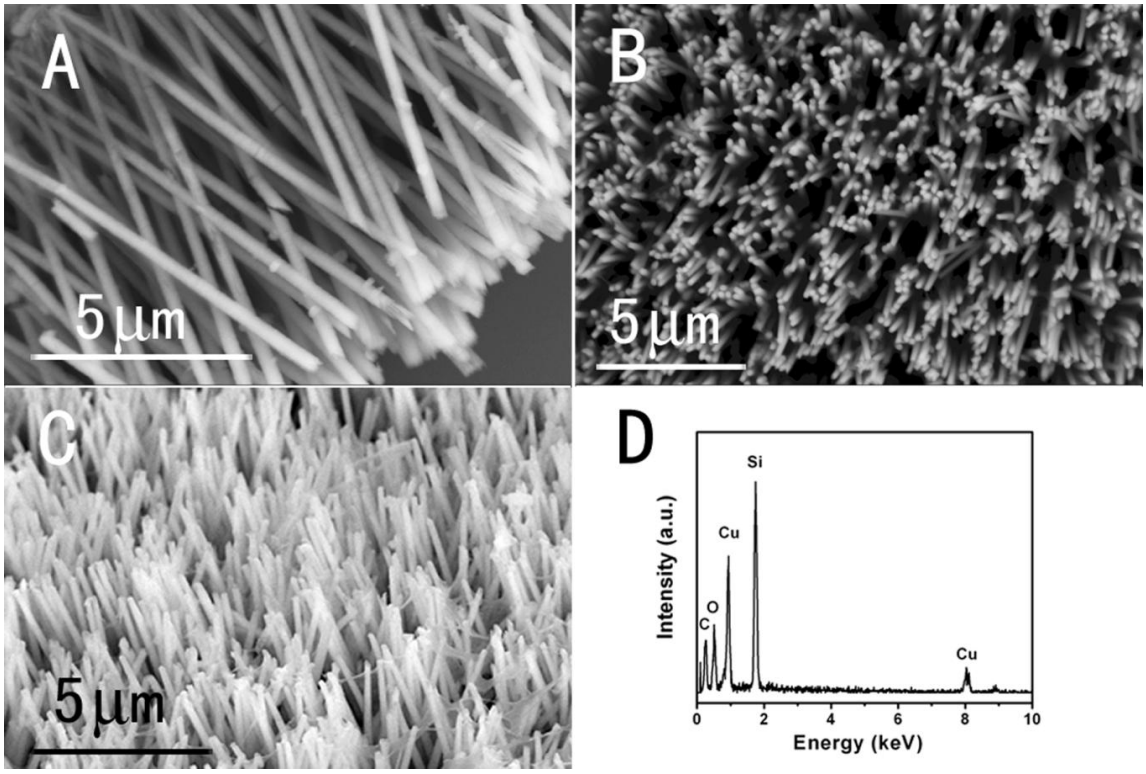

Figure 4.4 SEM image of (A) isolated CuO nanowires; (B, top-view; C, tilt-view) SEM images of arrays of CuO nanowires after template removal; representative EDS pattern (D) of as-prepared CuO nanowires and associated nanowire arrays.

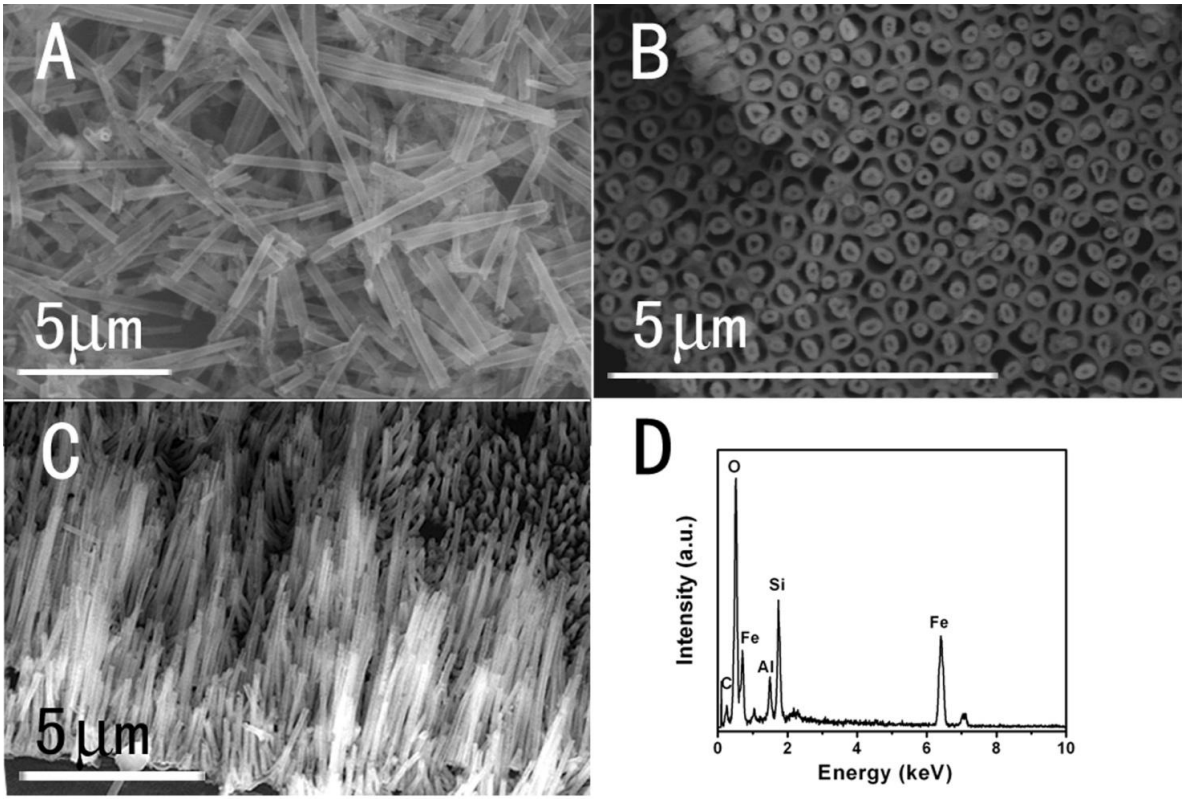

Figure 4.5 SEM image of (A) isolated α-Fe_2O_3 nanotubes; SEM images of arrays of α-Fe_2O_3 nanowires before (B, top-view) and after (C, tilt-view) template removal; representative EDS pattern (D) of as-prepared α-Fe_2O_3 nanotubes and arrays.

The morphology of all of the samples was also examined by low-magnification TEM as shown in Figure 4.6 panels A, C, and E. These images further confirm the range of sample diameters obtained from SEM data. All as-obtained nanowires and nanotubes are essentially uniform in terms of shape and morphology. A high resolution TEM image (Figure 4.6B) and associated SAED pattern (inset to Figure 4.6B) taken on an individual ZnO nanowire show the single crystalline nature of the sample. The lattice spacing can be indexed to the (100) plane. SAED patterns obtained at different spots along the same nanowire were effectively identical and confirm that each ZnO nanowire is essentially uniform in composition and relatively devoid of impurities. By contrast, although a similar procedure was used to generate CuO nanowires, the resulting product wasnot single crystalline. That is, a HRTEM image (Figure 4.6D) of a CuO nanowire shows the presence of different crystalline domains and SAED (inset to 4.6D) confirms that it is polycrystalline. The lattice spacing of the crystal domain indexed corresponds to (-111). Moreover, our as-generated α-Fe_2O_3 nanotubes consist of many small but misoriented single-crystalline nanocrystalline domains (Figure 4.6E and F), rendering the entire structure as polycrystalline in nature (inset in Figure 4.6F). The lattice spacing taken from one of these single-crystalline particles has been ascribed to the (110) plane. Considering that these iron oxide structures were prepared using an annealing step at high temperature, this result is not altogether surprising.

We were also able to generate array structures of our nanowire samples. Our protocol allows for the transference of any type of metal oxide array motifs onto a nonspecific substrate, nonlinear or otherwise, using double-sided, conductive tape. As a demonstration of principle of our ability to pattern metal oxide nanowire arrays over macroscopically relevant areas, we attached CuO arrays onto curved substrates of varying chemical composition. Figure 4.7 panels A and B are SEM images of CuO arrays immobilized using conductive carbon tape onto a plastic tip, measuring 1.5 mm in outer diameter. Figure 4.7B corresponds spatially to the white square designated in Figure 4.7A and highlights the feasibility of generating vertically aligned metal oxide arrays at room temperature. Figure 4.7C and 4.7D (magnified view corresponding spatially to the white square shown in 4.7C) show the presence of CuO arrays immobilized onto a silica glass rod, measuring 0.8 mm in outer diameter, as mediated by the presence of conductive, copper tape. By analogy, ZnO arrays were attached onto an identical silica glass rod, as shown in Figure 4.7E and 4.7F (magnified view corresponding spatially to the white square shown in 4.7E), using conductive, copper tape. We noted that array integrity was even more highly preserved in the case of ZnO and CuO nanowire arrays, partly because methylene chloride, used to remove the PC template, is not as corrosive to the intrinsic structure of copper tape as it is to carbon tape.

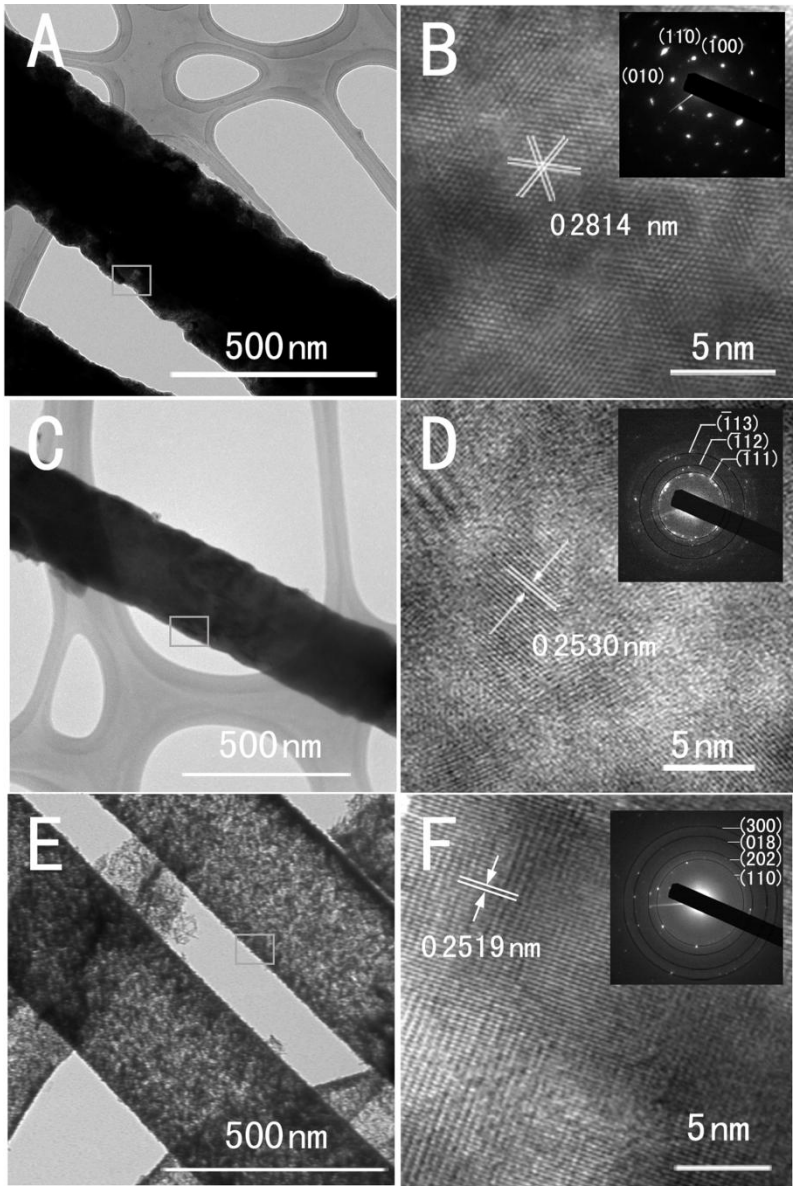

Figure 4.6 TEM (A, C, E) and HRTEM (B, D, F) images and corresponding SAED patterns (insets) of portions of ZnO nanowires (top), CuO nanowires (middle), and α-Fe_2O_3 nanotubes (bottom), respectively. Squares in panels A, C, and E highlight spatially specific locations on the various nanoscale oxide samples, where the HRTEM images were taken.

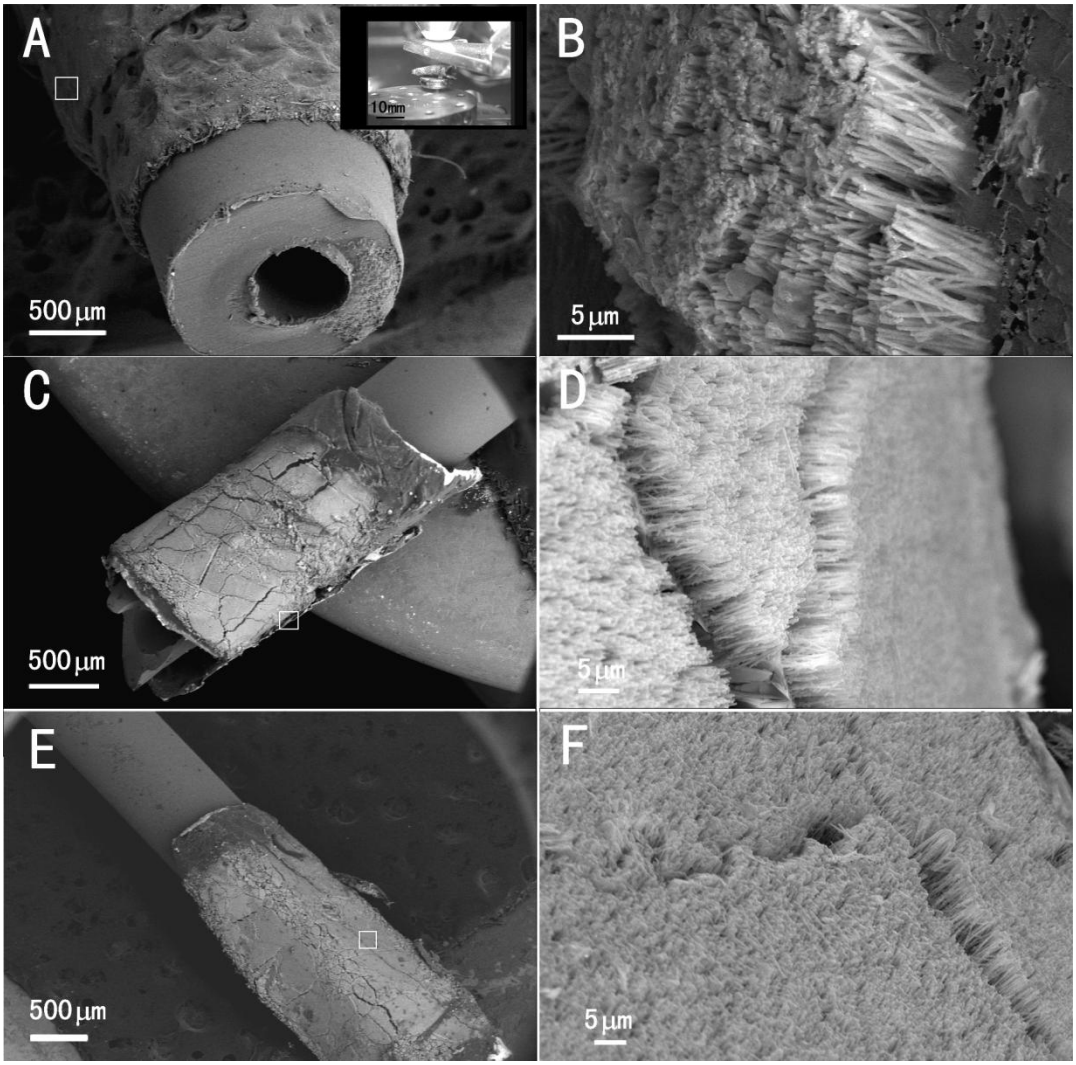

Figure 4.7 SEM images of CuO nanowire arrays immobilized onto (A and B) a plastic tip as well as onto (C and D) a curved glass rod. (E and F) Analogous SEM images of ZnO nanowire arrays immobilized onto a curved glass rod.

We emphasize that this technique, involving an initial nanoscale oxide nanowire formation inside a template followed by attachment to the desired substrate using conductive tape and subsequent template removal, is significant not only because this generalizable protocol can be performed under ambient conditions for essentially any type of material but also because this procedure can transfer arrays onto any type of substrate of any geometric configuration over a reasonably large macroscopic area, a capability which is technologically relevant. Moreover, the reported methodology is effectively independent of the mechanical deformability, melting behavior, and/or decomposition temperature of the substrate onto which the arrays are transferred, and furthermore, it does not necessitate the use of catalytic seed particles, all of which are important factors in conventional methods traditionally associated with array patterning. We even possess the potential of attaching chemically distinctive types of metal oxide arrays in spatially adjacent positions onto a given substrate using our simplistic technique.

Optical properties of as-prepared samples were also investigated. Figure 4.8 shows the UV-visible spectra of as-prepared samples. The absorption spectrum (Figure 4.8A) of the ZnO nanowires showed the presence of a maximum absorption peak at 364 nm, which blue-shifted relative to that of the corresponding signal for bulk ZnO, in agreement with prior work.[68, 69] By analogy, the maximum absorption peaks of CuO nanowires and of α-Fe_2O_3 nanotubes (Figure 4.8B and 4.8C) were noted at 205 and 208 nm, respectively, which also showed a blue-shift relative to that of their bulk counterparts, consistent with previous reports.[70, 71] Essentially, with decreasing sample size, the optical edge shifts to higher energy, a phenomenon attributable to quantum size and confinement effects.[72] Indeed, a size-dependent blue-shift has been observed in the absorption spectra of nanocrystalline motifs of many other bulk materials, such as TiO_2 nanowires.[73]

The room temperature photoluminescence (PL) spectrum of ZnO nanowires is shown in Figure 4.8D. A strong UV emission observed at ~380 nm most likely corresponds to near band-edge emission, while the presence of green emission at ~501 nm can be attributed to radiative recombination of photogenerated holes in the valence band with electrons in singly occupied oxygen vacancies.[31, 74, 75]

Moreover, evidence for the formation of metal oxides was provided by FT-IR spectra, shown in Figure 4.9. The broad absorption band around 500 cm^{-1} of the ZnO sample can be attributed to either the stretching mode of ZnO[68, 76] or an oxygen vacancy defect complex[77, 78] in that compound. By analogy, the maximum absorption band at around 520 cm^{-1} of the CuO sample corresponds to the broad stretching mode of CuO along the [101] direction.[79, 80] Finally, for the α-Fe_2O_3 sample, the presence of bands located at 580 cm^{-1} and 485 cm^{-1} is consistent with the presence of A_{2u}/E_u and E_u vibrations, respectively.[81-83]

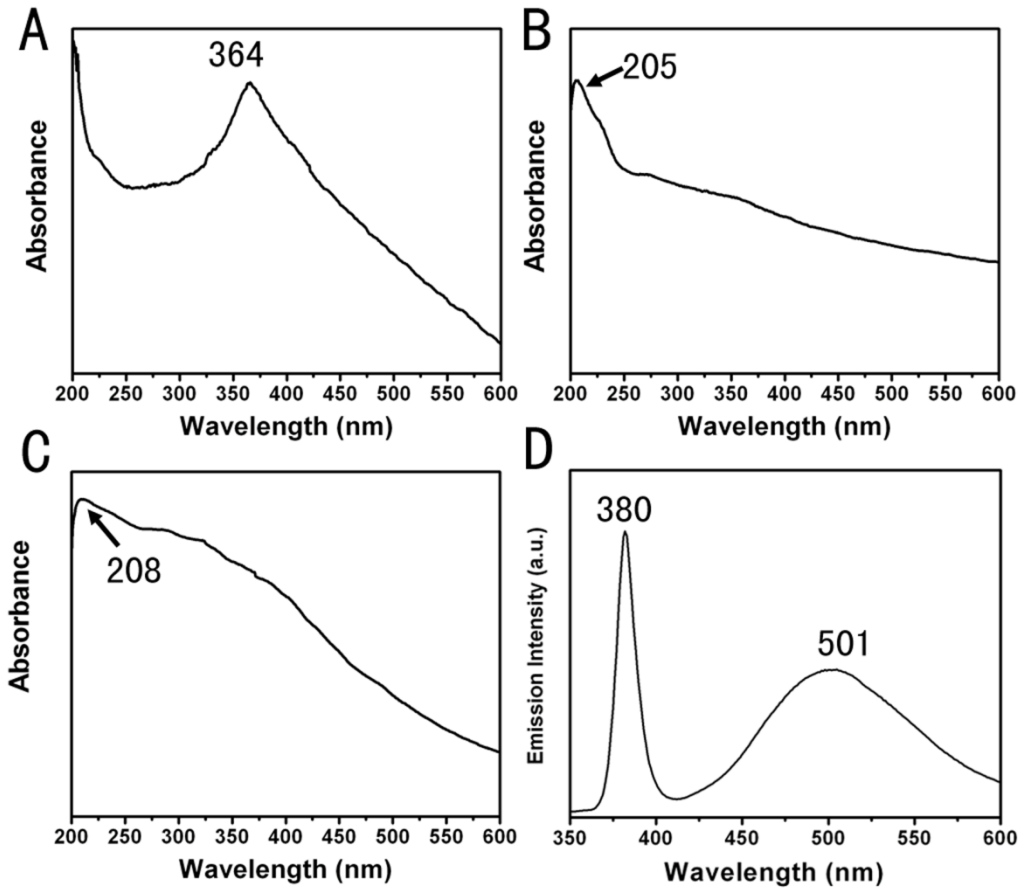

Figure 4.8 UV-visible spectra of as-prepared (A) ZnO nanowires, (B) CuO nanowires, and (C) α-Fe_2O_3 nanotubes; (D) photoluminescence spectrum of ZnO nanowires (excitation wavelength of 325 nm).

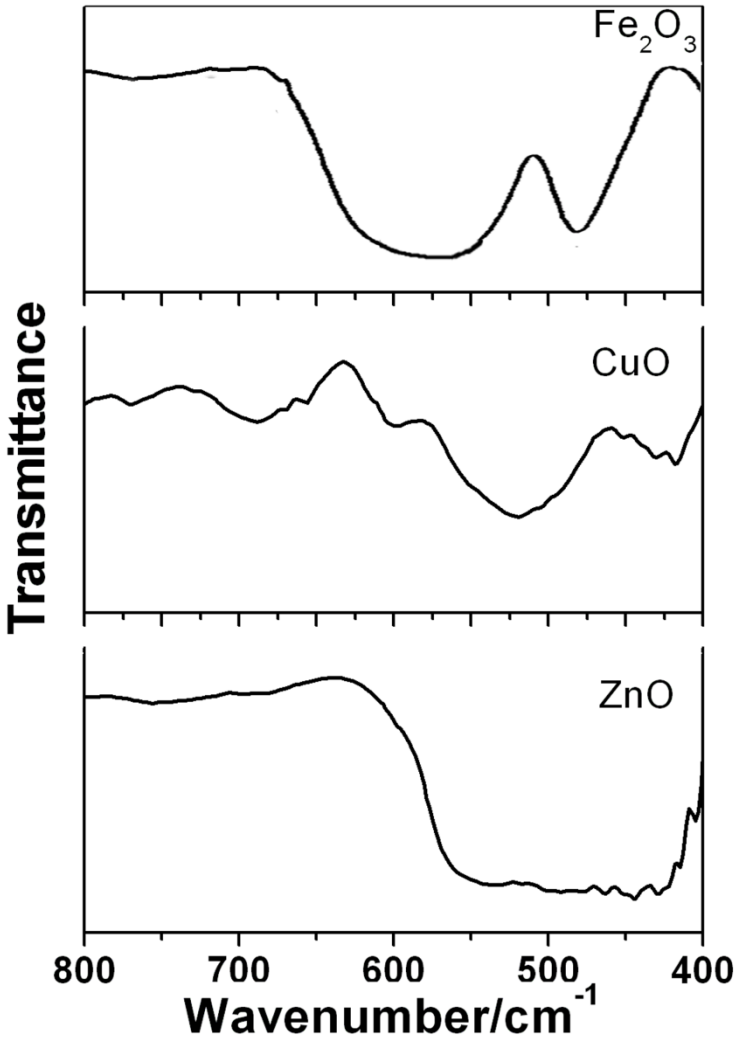

Figure 4.9 FT-IR spectra of as-prepared nanoscale samples of various metal oxides.

The magnetic behavior of as-prepared α-Fe_2O_3 nanotubes was investigated using SQUID analysis. Field-cooled and zero-field-cooled magnetization curves under 100 Oe are shown in Figure 4.10A. The magnetic phase transition from the canted ferromagnetic phase to another antiferromagnetically ordered state has been reported for bulk hematite samples to be around 260 K, characterized by a sharp decrease in the magnetization in the so-called Morin transition.[84] The magnetic behavior of our α-Fe_2O_3 nanotubes was different though. Our results are in agreement with analogous data observed for a hydrothermally prepared α-Fe_2O_3 nanotube sample,[85] as well as for spherical α-Fe_2O_3 nanoparticles.[86] For instance, for our template-prepared nanotubes, we observed a hysteresis loop at 5 K (Figure 4.10B), indicative of the presence of a coercive field at 245 Oe, characteristic of a soft magnet; by analogy, hydrothermally prepared nanotubes yielded a coercive field of 280 Oe.[85]

These results are suggestive of a long-range magnetic ordering, suppressing the Morin transition. Moreover, it can be observed that our α-Fe_2O_3 nanotubes show a well-defined peak at 65 K, below which the magnetic moments of particles are frozen or blocked; by analogy, for spherical α-Fe_2O_3 nanoparticles, that blocking temperature was 45 K.[86] Our FC curve above the blocking temperature does not follow standard Curie-Weiss behavior, suggesting the presence of strong intertube interactions. As we cannot ascribe these behaviors to any magnetic impurities in our samples, our overall observations herein can potentially be assigned to structural disorder, such as the presence of small crystalline particulate regions, an assertion supported by the polycrystalline nature of our iron oxide tubes, as evidenced by the TEM/HRTEM images in Figure 4.6E, F. In addition, morphology, finite size, and surface effects are additionally important factors, since hematite nanocubes[70] also behave magnetically distinctively as compared with the bulk.

Semiconductor-assisted photocatalysis and photo-oxidation of organic contaminants, as exemplified by model organic systems, remain as reasonable methodologies for converting pollutants into relatively harmless byproducts. The photocatalytic potential of as-prepared ZnO nanowires was evaluated by measuring the absorption intensity of methyl orange at 464 nm upon photoexcitation with UV light at 366 nm. Our data clearly show that nanowires and nanoparticles as well as the bulk sample of ZnO are active photocatalysts, as illustrated in Figure 4.11A. Our nanowire samples exhibited a slightly higher photoactivity as compared with that of both bulk and nanoparticle samples and that observed enhancement of photocatalytic activity is most likely related to a relative increase in the purity and crystallinity of our nanowires. Moreover, because the absorption spectrum of ZnO nanowires is shifted to higher energy with respect to that of the bulk as well as of commercial nanoparticles, the corresponding increase in sensitivity of our nanowires toward that part of the optical spectrum may also account for the larger amount of associated photoactivity noted.[72] Similar morphology dependent trends in photocatalytic behavior have been previously reported for anatase TiO_2.[73] A similar enhancement of photocatalytic activity was also observed for as-prepared α-Fe_2O_3 nanotubes as compared with that of the nanoparticles and bulk in the decomposition reaction[87] of 4-chlorophenol (4-CP) to CO_2, H_2O, and HCl on the basis of changes in the intensity of the 4-CP absorption peak at 225 nm (Figure 4.11B).

We determined that both of these photodegradation reactions were pseudo-first-order reactions. We calculated apparent reaction rate constants of methyl orange degradation for ZnO nanowires, nanoparticles, and the corresponding bulk samples to be 2.77 X 10^{-2}, 2.13 X 10^{-2}, and 1.92 X10^{-2} min^{-1}, respectively. By analogy, rate constants for the photocatalytic degradation reaction of 4-chlorophenol by α-Fe_2O_3 nanotubes, nanoparticles, and the corresponding bulk samples were deduced to be 3.60 X 10^{-3}, 2.49 X 10^{-3}, and 1.86 X 10^{-3} min^{-1}, respectively.

Metal oxides are known to effectively catalyze the degradation of H_2O_2, a model compound for the degradation of organic species. [88] The effect of CuO in catalyzing the degradation of H_2O_2 through a heterogeneous process is shown in Figure 4.11C. It was found that the concentration of H_2O_2 decreased much more quickly in the presence of CuO nanowires and nanoparticles as compared with that of the CuO bulk. In fact, after 3 h of reaction, we noted an approximate 35% and 19% loss of H_2O_2 with CuO nanowires and nanoparticles, respectively, as compared with only a 10% reduction of hydrogen peroxide in the presence of bulk CuO. The small, observed enhancement of photocatalytic activity of our nanowires, relative to that of both commercial bulk and nanoparticle samples, may be related to a rise in CuO crystallinity and chemical purity, characteristic of our as-prepared nanostructures.

Finally, we want to address another question: Why did ZnO and CuO form as wires whereas α-Fe_2O_3 was primarily produced in tubular form? In the experimental setup in these experiments, the contents of each solution in either half of the U-tube are allowed to diffuse toward each other across a wetted template membrane physically separating the two halves (Figure 4.12). Hence, metal cations and hydroxide anions will meet at the interface, react in a hydrolysis process, and nucleate the formation of the corresponding hydroxides. These insoluble hydroxides will begin to precipitate from solution, once the supersaturation value, which is rather low based on the magnitudes of the solubility product constants of these materials, shown in Table 4.2, for their production has been exceeded. We offer a plausible scenario (Figure 4.13) for the initial metal hydroxide nanostructure formation observed herein.

If the interactions between reagent molecules are stronger than those between the reagent molecules and the pore walls, the nucleation process and accompanying product formation will tend to happen within the voluminous confines of the pores themselves in a homogeneous-type process. That is, single crystals of nanoscale metal hydroxides therefore derive from isolated, disparate nucleation sites, which then grow by extension throughout the porous network. Continued growth then occurs at the particle surface at a rate limited by ion availability, until the crystal impinges on the template surface itself, which ultimately limits further particle growth. Within the cylindrical confines of the template pores, as-formed particles in this scenario essentially self-assemble with each other into either *wire-like or rod-like motifs*.

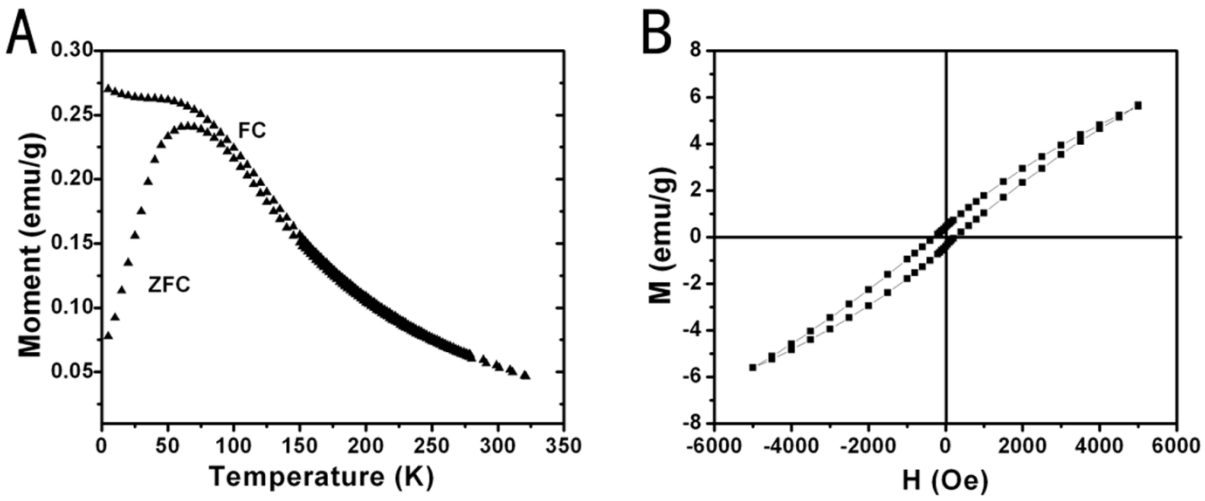

Figure 4.10 (A) Temperature dependence of the magnetic susceptibility for α-Fe_2O_3 nanotubes, showing zero field cooling (ZFC) and field cooling (FC) curves, with an applied magnetic field set at 100 Oe; (B) hysteresis loop at 5 K revealing the coercivity of as-prepared hematite nanotubes.

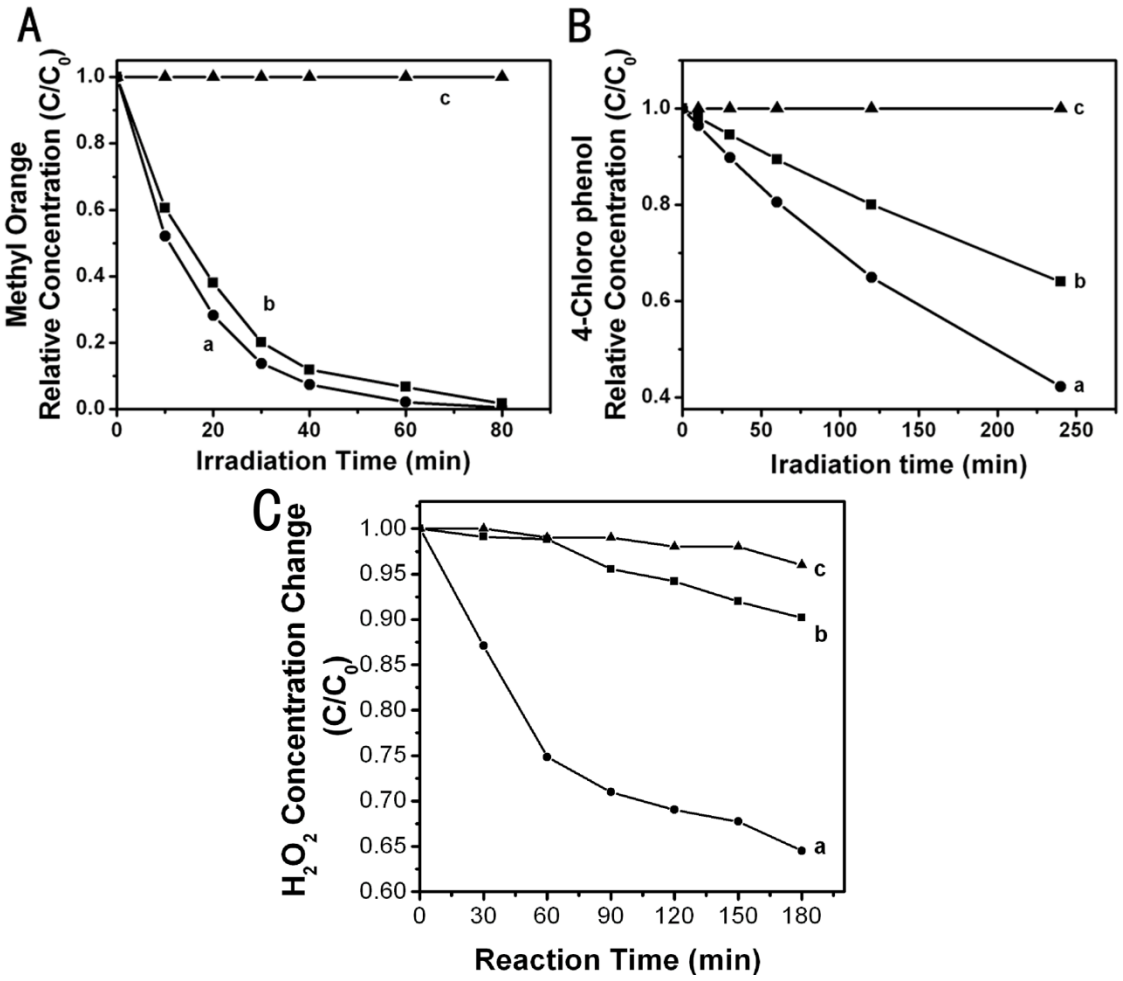

Figure 4.11 (A) Photodegradation of methyl orange in the presence of (a) ZnO nanowires, (b) ZnO nanoparticles, (c) ZnO bulk, and (d) a blank control. (B) Photodegradation of 4-chlorophenol in the presence of (a) α-Fe_2O_3 nanotubes, (b) α-Fe_2O_3 nanoparticles, (c) α-Fe_2O_3 bulk, and (d) a blank control. (C) Degradation of H_2O_2 in the presence of (a) CuO nanowires, (b) CuO nanoparticles, (c) CuO bulk, and (d) a blank control.

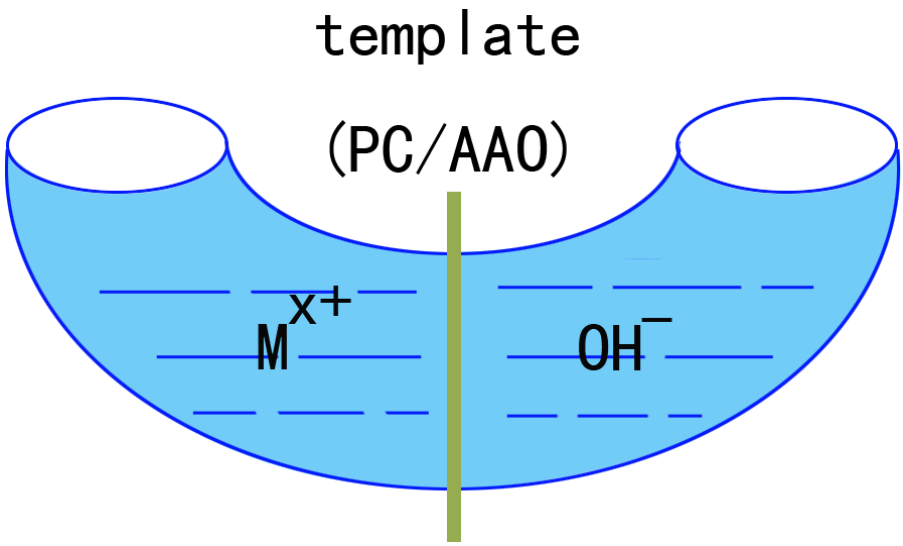

Figure 4.12 Schematic of the U-tube experimental setup used to synthesize metal oxide nanostructures.

Table 4.2 Solubility product constant (K_{sp}) values at 25 ℃ for as-generated metal hydroxides

Hydroxide	K_{sp}
$Cu(OH)_2$	$4.8 \cdot 10^{-20}$
$Fe(OH)_3$	$2.79 \cdot 10^{-39}$
$Zn(OH)_2$	$3 \cdot 10^{-17}$

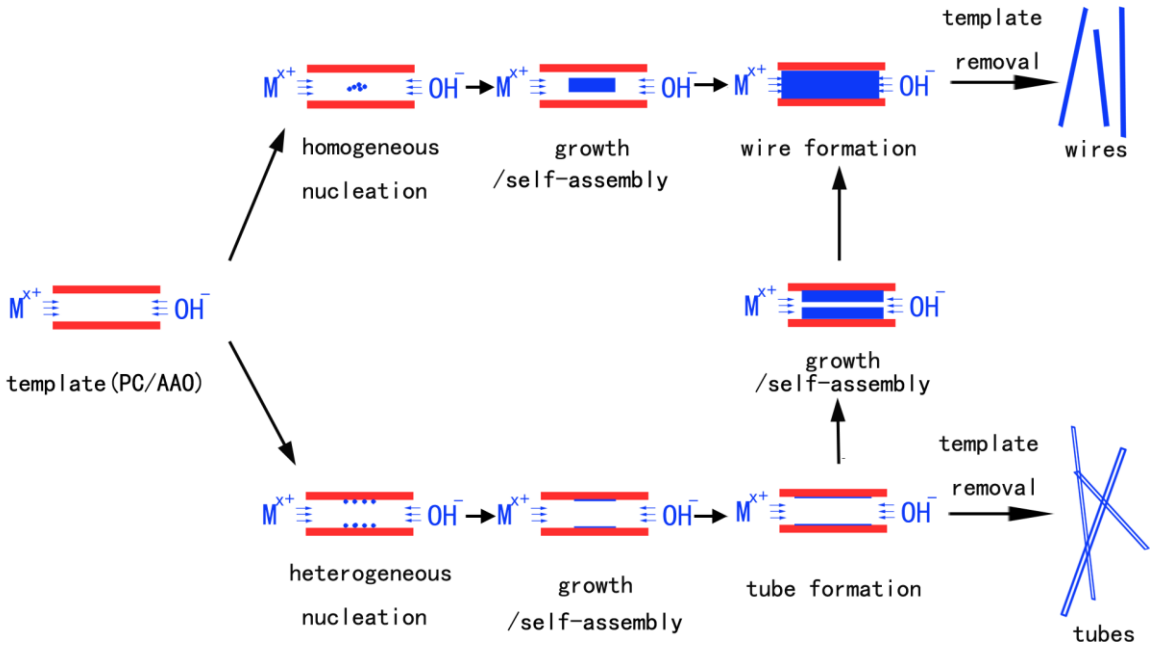

Figure 4.13 Postulated mechanism for synthesizing nanowires and nanotubes from template pores, based on plausible explanations using heterogeneous and homogeneous processes.

On the other hand, if the interactions between the reagent molecules are weaker than those between the reagent molecules and the pore walls, the nucleation and accompanying growth processes may tend to be localized at the surfaces of the pore walls in a heterogeneous-type process. Such a process may occur, for instance, if the pore wall is positively charged while the reagent particles are negatively charged. This preferential confinement of growth to the inherent geometry of the pore walls can therefore lead to the generation of primarily *tube-like motifs* upon the elongation and assembly of the as-formed particles. Such a scenario has been previously noted in the case of polymeric microtubules formed in templates, wherein nascent polymer chains initially adsorbed to the pore walls yielding a thin polymer "skin", that became thicker with time until it was quenched with water.[62] With continued reaction, nanowire formation can be visualized as a lateral thickening of the tubular structure, which, as further supply of precursors to the inside is blocked by the ever-growing tube thickness coupled with an ever-decreasing inner tube diameter, eventually constricts the entire porous interior of the template, filling it completely. In other words, continued growth of the nanotubes is limited only by reagent ion availability and diffusivity as well as by intrinsic geometrical constraints imposed by the template channels.

Hence, nanowires are considered as the ultimate limit of nanotube growth, at least in terms of its width. This hollow nanotube-to-solid nanowire transformative mechanism has been previously proposed with respect to the synthesis of TiO_2 nanotubes and nanowires within alumina (AAO) templates.[89] It should be noted that concentration and temperature are also expected to govern the morphologies of the resulting nanotubes and nanowires with lower concentrations and temperatures expected to favor short, hollow nanotubes, while high concentrations and temperatures are expected to lead to the growth of longer, thicker wires. In support of this mechanism, we have performed a systematic series of experiments (Table 4.3) to probe the effect of parameters such as (a) temperature and (b) concentration on the resulting nanostructure morphology.

The importance of temperature cannot be minimized. In fact, chemically pure, crystalline nanoscale ZnO and CuO samples (*e.g.*, samples A and B from Table 4.1) upon template removal, were obtained only when the U-tube experimental setup itself was heated to 80 ℃. It is plausible to assume that a higher temperature accelerates ion diffusion rates across the template. Hence, we ran our U-tube experiments at room temperature as a comparison. In terms of the concentration parameter, we varied the concentration of OH^-, necessary to induce precipitation, in our experiments from 0.01 to 0.1 M with higher concentrations (and therefore fluxes) of hydroxide ion expected to foster particle nucleation as well as nanostructure longation. It should be noted though that the effect of changing this variable is slightly more nuanced as local, dynamic concentrations of hydroxide within the template environment are dependent on diffusion rates as well. According to our mechanistic discussion, a higher temperature and/or a higher base concentration should promote high diffusion rates and correspondingly high local concentrations of interacting reagent ions. These conditions should therefore lead to initial particle formation followed by subsequent aggregation, coalescence, and self assembly of these constituent particles to yield either nanowires or nanotubes.

This prediction is borne out by the production of sample C, created at the highest temperature and base concentration used, wherein the ZnO and CuO generated consisted solely of nanowires. Conversely, upon reduction of either base concentration (sample D) or temperature (sample E), shorter nanowires (a few micrometers in length *versus* tens of micrometers in length for sample C) were obtained and in some cases, isolated particles were also generated in addition to the wire-like motifs. Simultaneous decreases in both temperature and base concentration yielded only small, discrete particles of likely either $Zn(OH)_2$ or $Cu(OH)_2$, measuring tens of nanometers (sample F and G), irrespective of the template used (*e.g.*, PC or alumina), suggesting that for these two materials in particular, the nucleation and growth processes were essentially homogeneous in nature.

The case of iron oxide nanostructure formation in the presence of an alumina template is clearly different as heterogeneous processes likely predominate. That is, the reagent particle-pore wall interaction was comparatively strong and nucleated particles assembled primarily into tubular motifs. For instance, even under the mildest of experimental conditions, for example at very low concentrations of ammonium hydroxide (0.01 M) and at room temperature, 1D iron-containing nanotubes (likely $Fe(OH)_3$) were synthesized, as shown in sample H. The fact that under similar conditions, we could not generate 1D nanostructures of either zinc hydroxide or copper hydroxide suggests that the significantly smaller *K*sp value ($\sim 10^{-40}$; Table 4.2) of $Fe(OH)_3$, as compared with the relatively higher *K*sp values ($\sim 10^{-20}$; Table 4.2) for $Cu(OH)_2$ and $Zn(OH)_2$, was highly conducive to iron hydroxide nanostructure formation. Increasing the concentration of ammonium hydroxide to 0.1 M while maintaining the reaction temperature constant (sample I) led to the generation of longer $Fe(OH)_3$ nanotubes, which might have arisen owing to higher local concentrations of reactive reagent ions, which is again consistent with our mechanism; in fact, it was only with an additional annealing step to 600 ℃ that one could successfully synthesize hematite nanotubes (sample J). By contrast, increasing both the reaction temperature (to 80 ℃) and hydroxide concentration (to 0.1 M) as well as reverting to a PC template (sample K) resulted in the formation of iron-containing, nonhematite nanowires. The presence of the filled nanowire structures within the PC template reflected the more favorable reagent particle-particle *versus* particle-pore wall interaction in this pore environment. Hence, iron oxide nanowire growth in PC templates is analogous to the homogeneous processes described for Zn and Cu. Such an assertion was further confirmed by the formation of sample L, prepared under low-temperature and low concentration conditions. As with sample F by analogy, only small, discrete particles, measuring about 100 nm in diameter and likely consisting of either amorphous hematite or more likely, iron hydroxide, were obtained.

TABLE 4.3. Effect of Parameter Selection on Preparation of Metal Oxide 1-D Nanostructures at a Constant Overall Reaction Time of 1 h. Measured 1-D Nanostructure Widths (*W*) Are Dependent on Corresponding Pore Dimensions of Templates Used

sample	metal salts used	basic solution	concn of base (M)	temp (°C)	template	observed product morphology (width, *W*; length, *L*; diameter, *D*)
A	Zn^{2+}	NaOH	0.1	80	polycarbonate	ZnO nanowires. *W*: 60 ± 10 nm. *L*: 2−4 μ*m*
B	Zn^{2+}	NaOH	0.1	80	polycarbonate	ZnO nanowires. *W*: 120 ± 20 nm. *L*: 2.5−5 μ*m*
C	Zn^{2+}/Cu^{2+}	NaOH	0.1	80	polycarbonate	ZnO/CuO nanowires. *W*: 250 ± 50 nm. *L*: 10−15 μ*m*
D	Zn^{2+}/Cu^{2+}	NaOH	0.01	80	polycarbonate	ZnO/CuO nanowires. *W*: 250 ± 50 nm. *L*: 1−2 μ*m* ZnO/CuO nanoparticles. *D*: 90 ± 30 nm
E	Zn^{2+}/Cu^{2+}	NaOH	0.1	room temp	polycarbonate	$Zn(OH)_2/Cu(OH)_2$ nanowires. *W*: 250 ± 50 nm. *L*: 4−8 μm
F	Zn^{2+}/Cu^{2+}	$NH_3 \cdot H_2O$	0.01	room temp	polycarbonate	$Zn(OH)_2/Cu(OH)_2$ nanoparticles. *D*: 90 ± 30 nm
G	Zn^{2+}/Cu^{2+}	$NH_3 \cdot H_2O$	0.01	room temp	alumina	$Zn(OH)_2/Cu(OH)_2$ nanoparticles. *D*: 90 ± 30 nm
H	Fe^{3+}	$NH_3 \cdot H_2O$	0.01	room temp	alumina	$Fe(OH)_3$ nanotubes. *W*: 300 ± 50 nm. *L*: 3−9 μm
I	Fe^{3+}	$NH_3 \cdot H_2O$	0.1	room temp	alumina	$Fe(OH)_3$ nanotubes. *W*: 300 ± 50 nm. *L*: 4−12 μm
J	Fe^{3+}	$NH_3 \cdot H_2O$	0.01	(a) room temp; (b) annealing to 600 °C	alumina	α-Fe_2O_3 nanotubes. *W*: 260 ± 6 nm. *L*: 3−9 μm
K	Fe^{3+}	NaOH	0.1	80	polycarbonate	amorphous Fe_2O_3 (or β-FeOOH) nanowires. *W*: 250 ± 50 nm: *L*: 4−5 μm
L	Fe^{3+}	$NH_3 \cdot H_2O$	0.01	room temp	polycarbonate	$Fe(OH)_3$ nanoparticles. *D*: 100 ± 20 nm

4.4 Conclusions

The modified template technique we have developed allows for reasonably short reactions to be run under mild, ambient conditions in aqueous solution with reliable control over shape, dimensionality, and crystallinity, originating from the spatial geometry of the confining porous template environment. We have highlighted the potential of the technique herein to the reliable and reproducible synthesis of not only isolated structures (measuring 50-200 nm in diameter and several micrometers in length) but also of arrays of ZnO, CuO, and α-Fe_2O_3 over spatially relevant, macroscopic (cm^2) areas of various types of substrates (*i.e.*, not only flat silicon surfaces but also curved glass rods). In addition, size- and shape-dependent optical, magnetic, and catalytic properties of these as-prepared 1D metal oxides were investigated and noted to be mainly comparable with or better than the associated properties of the corresponding bulk oxides.

Moreover, we have also proposed plausible explanations for the formation of nanotube and nanowire formulations of the same material under different sets of experimental conditions. That is, it is possible to control morphology by tuning the nature of the physicochemical interactions between reagent molecules and the pore walls, for instance, either (i) by chemically modifying the hydrophilicity, hydrophobicity, and surface charge of the internal pore sidewalls or (ii) by physically altering reagent concentrations, reaction pH, reaction temperatures, and reaction times. This is a particularly advantageous strategy when the metal oxide nanoscale material is difficult to generate by other conventional means.

4.5 References

1. Furneaux, R. C.; Rigby, W. R.; P.Davidson, A. *Nature* **1989**, 337, 147.
2. Fleisher, R. L.; Price, P. B.; Walker, R. M., *Nuclear Tracks in Solids.* University of California Press: Berkeley, CA, **1975**.
3. Tonucci, R. J.; Justus, B. L.; Campillo, A. J.; Ford, C. E. *Science* **1992**, 258, 783.
4. Possin, G. E. *Rev. Sci. Instrum.* **1970**, 41, 772.
5. Wu, C.; Bein, T. *Science* **1994**, 264, 1757.
6. Fan, S.; Chapline, M. G.; Franklin, N. R.; Tombler, T. W.; Cassell, A. M.; Dai, H. *Science* **1999**, 283, 512.
7. Enzel, P.; Zoller, J. J.; Bein, T. *Chem. Commun.* **1992**, 633.
8. Guerret-Piecourt, C.; Bouar, Y. L.; Loiseau, A.; Pascard, H. *Nature* **1994**, 375, 564.
9. Ajayan, P. M.; Stephan, O.; Redlich, P.; Colliex, C. *Nature* **1995**, 375, 564.
10. Keller, F.; Hunter, M.; Robinson, D. L. *J. Electrochem. Soc.* **1953**, 100, 411.
11. J.P.O'Sullivan; Wood, G. C. *Proc. R. Soc. Lond., Ser. A* **1970**, 317, 511.
12. Ebihara, K.; Takahashi, H.; Nagayama, M. *J. Surf. Fin. Soc. Jpn.* **1983**, 34, 548.
13. Reynolds, D. C.; Look, D. C.; Jogai, B.; Litton, C. W.; Collins, T. C.; Harsch, W.; Cantwell, G. *Phys. Rev. B* **1998**, 57, 12151.
14. Huang, M. H.; Mao, S.; Feick, H.; Yan, H.; Wu, Y.; Kind, H.; Webber, E.; Russo, R.; Yang, P. *Science* **2001**, 292, 1897.
15. Kind, H.; Yan, H.; Messer, B.; Law, M.; Yang, P. *Adv. Mater,* **2002**, 14, 158.

16. Soci, C.; Zhang, A.; Xiang, B.; Dayeh, S. A.; Aplin, D. P. R.; Park, J.; Bao, X. Y.; Lo, Y. H.; Wang, D. *Nano Lett.* **2007**, 7, 1003.
17. Law, M.; Greene, L. E.; Johnson, J. C.; Saykally, R.; Yang, P. *Nat. Mater.* **2005**, 4, 455.
18. Suh, D.-I.; Lee, S.-Y.; Kim, T.-H.; Chun, J.-M.; Suh, E.-K.; Yang, O.-B.; Lee, S.-K. *Chem. Phys. Lett.* **2007**, 442, 348.
19. Goldberger, J.; Sirbuly, D. J.; Law, M.; Yang, P. *J. Phys. Chem. B* **2005**, 109, 9.
20. Noh, Y.-Y.; Cheng, X.; Sirringhaus, H.; Sohn, J. I.; Welland, M. E.; Kang, D. J. *Appl. Phys. Lett.* **2007**, 91, 043109-1.
21. Wang, X.; Zhou, J.; Lao, C.; Song, J.; Xu, N.; Wang, Z. L. *Adv. Mater*, **2007**, 19, 1627.
22. Wang, Z. L.; Song, J. *Science* **2006**, 312, 242.
23. Gao, P. X.; Song, J.; Liu, J.; Wang, Z. L. *Adv. Mater*, **2007**, 19, 67.
24. Wang, X.; Liu, J.; Song, J.; Wang, Z. L. *Nano Lett.* **2007**, 7, 2475.
25. Park, W. I.; Yi, G.-C.; Kim, M.; Pennycook, S. J. *Adv. Mater*, **2002**, 14, 1841.
26. Jeong, M.-C.; Oh, B.-Y.; Nam, O.-H.; Kim, T.; Myoung, J.-M. *Nanotechnology* **2006**, 17, 526.
27. Yang, P.; Han, H.; Mao, S.; Russo, R.; Johnson, J.; Saykally, R.; Morris, N.; Pham, J.; He, R.; Choi, H.-J. *Adv. Funct. Mater.* **2002**, 12, 323.
28. Umar, A.; Kim, B.-K.; Kim, J.-J.; Hahn, Y. B. *Nanotechnology* **2007**, 18, 175606-1.
29. Sun, Y.; Fuge, G. M.; Ashfold, M. N. R. *Chem. Phys. Lett.* **2004**, 396, 21.
30. Vayssieres, L. *Adv. Mater*, **2003**, 15, 464.
31. Greene, L. E.; Law, M.; Goldberger, J.; Kim, F.; Johnson, J. C.; Zhang, Y.; Saykally, R. J.; Yang, P. *Angew. Chem. Int. Ed.* **2003**, 42, 3031.
32. Greene, L. E.; Law, M.; Tan, D. H.; Montano, M.; Goldberger, J.; Somorjai, G.; Yang, P. *Nano Lett.* **2005**, 5, 1231.
33. Jiang, X.; Herricks, T.; Xia, Y. *Nano Lett.* **2002**, 2, 1333.
34. Musa, A. O.; Akomolafe, T.; Carter, M. J. *Sol. Energy Mater. Sol. Cells* **1998**, 51, 305.
35. Reitz, J. B.; Solomon, E. I. *J. Am. Chem. Soc.* **1998**, 120, 11467.
36. Lanza, F.; Feduzi, R.; Fuger, J. *J. Mater. Res.* **1990**, 5, 1739.
37. Podhajecky, P.; Zabransky, Z.; Novak, P.; Dobiasova, Z.; Eerny, R.; Valvoda, V. *Electrochim. Acta* **1990**, 35, 245.
38. Cheng, C.-L.; Ma, Y.-R.; Chou, M. H.; Huang, C. Y.; Yeh, V.; Wu, S. Y. *Nanotechnology* **2007**, 18, 245604-1.
39. Cao, M.; Hu, C.; Wang, Y.; Guo, Y.; Guo, C.; Wang, E. *Chem. Commun.* **2003**, 1884.
40. Wen, X.; Xie, Y.; Choi, C. L.; Wan, K. C.; Li, X.-Y.; Yang, S. *Langmuir* **2005**, 21, 4729.
41. Du, G. H.; Tendeloo, G. V. *Chem. Phys. Lett.* **2004**, 393, 64.
42. Lu, C.; Qi, L.; Yang, J.; Zhang, D.; Wu, N.; Ma, J. *J. Phys. Chem. B* **2004**, 108, 17825.
43. Zhang, W.; Ding, S.; Yang, Z.; Liu, A.; Qian, Y.; Tang, S.; Yang, S. *J. Cryst. Growth* **2006**, 291, 479.
44. Wu, H.; Lin, D.; Pan, W. *Appl. Phys. Lett.* **2006**, 89, 133125-1.
45. Malandrino, G.; Finocchiaro, S. T.; Nigro, R. L.; Bongiorno, C.; Spinella, C.; Fragala, I. L. *Chem. Mater.* **2004**, 16, 5559.

46. Yi-Kun, S.; Cheng-Min, S.; Hai-Tao, Y.; Hu-Lin, L.; Hong-Jun, G. *Trans. Nonferrous Met. SOC. China* **2007**, 17, 783.
47. Gondal, M. A.; Hameed, A.; Yamani, Z. H.; Suwaiyan, A. *Chem. Phys. Lett.* **2004**, 385, 111.
48. Ohmori, T.; Takahashi, H.; Mametsuka, H.; Suzuki, E. *Phys. Chem. Chem. Phys.* **2000**, 2, 3519.
49. Chen, J.; Xu, L.; Li, W.; Gou, X. *Adv. Mater.* **2005**, 17, 582.
50. Fu, Y. Y.; Wang, R. M.; Xu, J.; Chen, J.; Yan, Y.; Narlikar, A. V.; Zhang, H. *Chem. Phys. Lett.* **2003**, 379, 373.
51. Wen, X.; Wang, S.; Ding, Y.; Wang, Z. L.; Yang, S. *J. Phys. Chem. B* **2005**, 109, 215.
52. Wang, X.; Chen, X.; Gao, L.; Zheng, H.; Ji, M.; Tang, C.; Shen, T.; Zhang, Z. *J. Mater. Chem.* **2004**, 14, 905.
53. Xiong, Y.; Li, Z.; Li, X.; Hu, B.; Xie, Y. *Inorg. Chem.* **2004**, 43, 6540.
54. Morber, J. R.; Ding, Y.; Haluska, M. S.; Li, Y.; Liu, J. P.; Wang, Z. L.; Snyder, R. L. *J. Phys. Chem. B* **2006**, 110, 21672.
55. Shen, X.-P.; Liu, H.-J.; Pan, L.; Chen, K.-M.; Hong, J.-M.; Xu, Z. *Chem. Lett.* **2004**, 33, 1128.
56. Sun, Z.; Yuan, H.; Liu, Z.; Han, B.; Zhang, X. *Adv. Mater.* **2005**, 17, 2993.
57. Hulteen, J. C.; Martin, C. R. *J. Mater. Chem.* **1997**, 7, 1075.
58. Martin, C. R. *Science* **1994**, 266, 1961.
59. Martin, C. R. *Chem. Mater.* **1996**, 8, 1739.
60. Mao, Y.; Wong, S. S. *J. Am. Chem. Soc.* **2004**, 126, 15245.
61. Mao, Y.; Zhang, F.; Wong, S. S. *Adv. Mater.* **2006**, 18, 1895.
62. Martin, C. R.; Dyke, L. S. V.; Cai, Z.; Liang, W. *J. Am. Chem. Soc.* **1990**, 112, 8976.
63. Liang, W.; Martin, C. R. *Chem. Mater.* **1991**, 3, 390.
64. Uekawa, N.; Iahii, S.; Kojima, T.; Kakegawa, K. *Mater. Lett.* **2007**, 61, 1729.
65. Ullah, M. H.; Kim, I.; Ha, C.-S. *J. Mater. Sci.* **2006**, 41, 3263.
66. Nashaat, N., N.; Maen, M., H. *Langmuir* **2007**, 23, 13093.
67. Klassen, N. V.; Marchington, D.; Mcgowan, H. C. E. *Anal. Chem.* **1994**, 66, 2921.
68. Prasad, V. D.; Souza, C.; Yadav, D.; Shaikh, A. J.; Vigneshwaran, N. *Spectrochim. Acta, Part A* **2006**, 65, 173.
69. Snitka, V.; Jankauskas, V.; Zunda, A.; Mizariene, V. *Mater. Lett.* **2007**, 61, 1763.
70. Wang, S.-B.; Min, Y.-L.; Yu, S.-H. *J. Phys. Chem. C* **2007**, 111, 3551.
71. Kaur, M.; Muthe, K. P.; Despande, S. K.; Choudhury, S.; Singh, J. B.; Verma, N.; Gupta, S. K.; Yakhmi, J. V. *J. Cryst. Growth* **2006**, 289, 670.
72. Zhou, H.; Park, T.-J.; Wong, S. S. *J. Mater. Res.* **2006**, 21, 2941.
73. Mao, Y.; Wong, S. S. *J. Am. Chem. Soc.* **2006**, 128, 8217.
74. Huang, M. H.; Wu, Y.; Feick, H.; Tran, N.; Weber, E.; Yang, P. *Adv. Mater.* **2001**, 13, 113.
75. Vanheusden, K.; Warren, W. L.; Seager, C. H.; Tallant, D. R.; Voigt, J. A.; Gnade, B. E. *J. Appl. Phys.* **1996**, 79, 7983.
76. Maensiri, S.; Laokul, P.; Promarak, V. *J. Cryst. Growth* **2006**, 289, 102.
77. Xiong, G.; Pal, U.; Serrano, J. G. *J. Appl. Phys.* **2007**, 101, 024317-1.
78. Kaschner, A.; Haboeck, U.; Strassburg, M.; Strassburg, M.; Kaczmarczyk, G.; Hoffmann, A.; Thomsen, C.; Zeuner, A. H. R.; Alves, D. M. H.; Meyer, B. K. *Appl. Phys. Lett.* **2002**, 80, 1909.

79. Amores, J. M. G.; Escribano, V. S.; Busca, G.; Lorenzelli, V. *J. Mater. Chem.* **1994**, 4, 965.
80. Borgohain, K.; Singh, J. B.; Rao, M. V. R.; Shripathi, T.; Mahamuni, S. *Phys. Rev. B* **2000**, 61, 11093.
81. Wang, Y.; Muramatsu, A.; Sugimoto, T. *Colloids Surf., A* **1998**, 134, 281.
82. Music, S.; Czako-Nagy, I.; Salaj-Obelic, I.; Ljubesvic, N. *Mater. Lett.* **1997**, 32, 301.
83. Chernyshova, I. V.; Hochella, M. F.; Madden, A. S. *Phys. Chem. Chem. Phys.* **2007**, 9, 1736.
84. Morin, F. J. *Phys. Rev.* **1950**, 78, 819.
85. Liu, L.; Kou, H.-Z.; Mo, W.; Liu, H.; Wang, Y. *J. Phys. Chem. B* **2006**, 110, 15218.
86. Zysler, R. D.; Winkler, E.; Mansilla, M. V.; Fiorani, D. *Physica B.* **2006**, 384, 277.
87. Bandara, J.; Klehm, U.; Kiwi, J. *Appl. Catal. B* **2007**, 76, 73.
88. Drijvers, D.; Langenhove, H. V.; Beckers, M. *Water Res.* **1999**, 33, 1187.
89. Cochran, R. E.; Shyue, J.-J.; Padture, N. P. *Acta Mater.* **2007**, 55, 3007.

Chapter V Template synthesis of multiferroic $MnWO_4$ nanowires

5.1 Introduction

In Chapter IV, we presented the synthesis of 1D binary metal oxide using a modified template method. The resulting insoluble materials were first formed as hydroxides via reaction of metal ions and hydroxide ions. The hydroxides then transformed into metal oxides by a "dehydration" step. Theoretically, this technique can be used to make not only binary metal oxides, but any materials that have low solubilities and that readily precipitate in the solution. In this chapter, we created 1D ternary metal oxides by the same technique. The model material we chose was $MnWO_4$, an important multiferroic material.

5.1.1 Multiferroic Materials

Multiferroic materials refer to materials that show simultaneous ferromagnetic order (or any other kind of magnetic) and ferroelectric ordering. The search for these materials has been driven by the prospect of controlling charges by applied magnetic fields and spins by applied voltages, and using this capability to construct new forms of multifunctional devices. Much of the early work on multiferroics was directed towards bringing ferroelectricity and magnetism together in one material,[1, 2] which has proven to be a very difficult problem, as these two contrasting order parameters turned out to be mutually exclusive.[3-7] Most ferroelctrics are transition metal oxides, in which transition ions have empty d shells. The collective shift of cations and anions inside a periodic crystal induces bulk electric polarization. Magnetism, on the contrary, requires transition metal ions with partially filled d shells, as the spins of electrons occupying completely filled shells add to zero and do not participate in magnetic ordering.[8] Furthermore, it was found that the simultaneous presence of electric and magnetic dipoles does not guarantee strong coupling between the two, as microscopic mechanisms of ferroelectricity and magnetism are quite different and do not strongly interfere with each other.[9, 10]

For ferroelectricity and magnetism to coexist in a single phase, therefore, the atoms that move off centre to form the electric dipole moment should be different from those that carry the magnetic moment. In the magnetic perovskite-structure oxides and related materials, multiferroism is most commonly achieved by making use of the stereochemical activity of the lone pair on the large cation to provide ferroelectricity, while keeping the small cation magnetic. This is the mechanism for Bi-based magnetic ferroelectrics. A typical example is bismuth ferrite, $BiFeO_3$.[11] A second route to multiferroism is provided by geometrically driven ferroelectricity, which is compatible with the coexistence of magnetism. $YMnO_3$[12, 13] and $BaNiF_4$[14] fall into this class. The third route would involve a ferroelectricity induced by the formation of a symmetry-lowering magnetic ground state that lacks inversion symmetry.[15] An example of this is

$TbMnO_3$. Finally, certain non-centrosymmetric charge-ordering arrangements can cause ferroelectricity in magnetic materials, like $LuFe_2O_4$.[16, 17]

5.1.2 $MnWO_4$

$MnWO_4$, otherwise known as hűbnerite, is a relatively lesser known member of this class of materials and possesses spontaneous electric polarization manifested in a spiral magnetically ordered state.[18-22] $MnWO_4$ belongs to the monoclinic *P2/c* space group, characterized by alternating layers of transition metal and tungsten atoms parallel to the (100) plane, as shown in Figure 5.1[22, 23]. Specifically, each Mn and W atom is in an approximately octahedral coordination surrounded by six nearest neighbor oxygen atom sites.[23] In addition to its relatively low melting point as well as desirable magnetic and multiferroic properties, the electrical conductivity of $MnWO_4$ is also sensitive to changes in humidity, thereby making it useful as a humidity sensor with potential applications ranging from medicine, meteorology, to agriculture.[24]

5.1.3 Current Work

Conventional preparatory methods for bulk $MnWO_4$ production are diverse, ranging from chemical reaction in molten salt media,[25] mechanical grinding in a vibrating mill,[26] to high temperature decomposition of complex precursors.[27] Conversely, $MnWO_4$ nanocrystals have been synthesized by a solvothermal route, using an autoclave, in which hydrated $MnCl_2$ and Na_2WO_4 were annealed at 180 ℃ in a pH range of 5–11 in the presence of homologous surfactants (such as ethylene glycol (EG), polyethylene glycol (PEG)-400, and PEG 10 000).[28] Similarly, single-crystalline $MnWO_4$ nanoplates have been produced by hydrothermally annealing hydrated $MnSO_4$ and Na_2WO_4 in the presence of DMF at 160 ℃ for 10 days in an autoclave.[29] In addition, the sol–gel method has previously been used to generate $MnWO_4$ films.[24]

Nonetheless, the motivation to generate one-dimensional (1D) nanostructures of these materials is high. Indeed, 1D nanostructures are fundamentally interesting because they are the lowest dimensional anisotropic structures that can be used for the efficient transport of electrons and optical excitations.[30, 31] Nanofibers and nanowires of $MnWO_4$ have primarily been fabricated by complexation–precipitation methods, associated with hydrothermal treatments of Na_2WO_4 and $MnCl_2$ (or $MnSO_4$) precursors either in the presence [23, 28] or absence of[32] surfactant (such as cetyltrimethylammonium bromide, ethylene glycol, and polyethylene glycol) at temperatures ranging from 100 to 180 ℃ for periods of 4–24 h. All of these methods, however, necessitate a relatively high temperature of reaction (>100 ℃) as well as precise pH control in order to achieve the desired morphology.

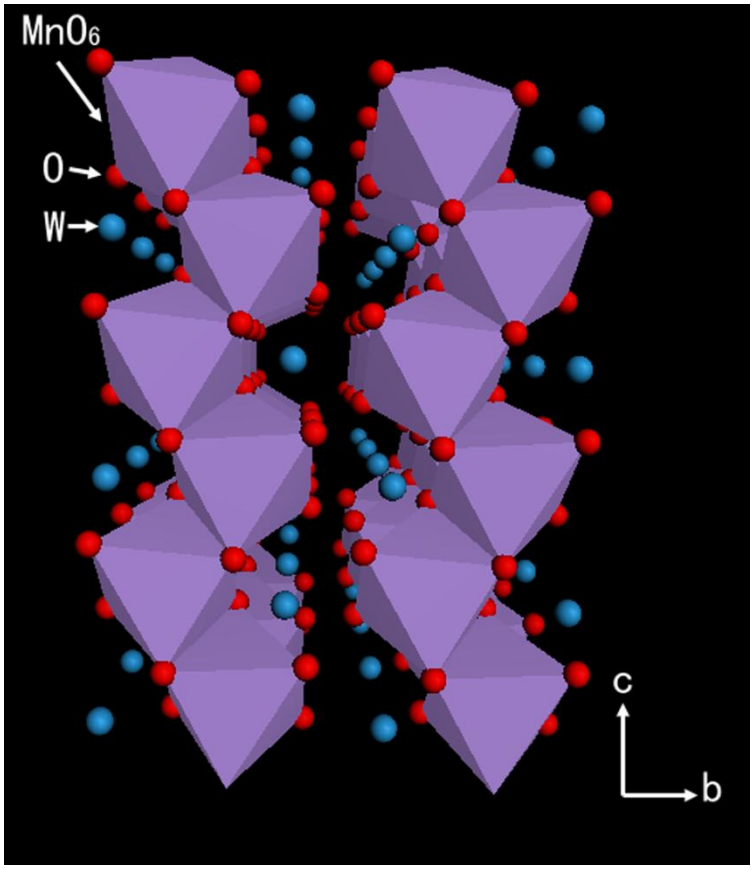

Figure 5.1 Crystal structure of $MnWO_4$.

In this chapter, we have generalized a convenient, room temperature method, previously described in Chapter IV to synthesize polycrystalline $MnWO_4$ nanowires and nanowire arrays through the mediation of a polycarbonate (PC) template. With this protocol, which operates under ambient conditions in aqueous solution with reliable control over shape, dimensionality, and crystallinity, we were able to make $MnWO_4$ nanowires and nanowire arrays under ambient conditions without the use of either surfactant or any high-temperature annealing treatment. Others have referred to this process as a precipitation metathesis reaction.[33] We also analyzed our $MnWO_4$ nanoscale samples using microscopy, spectroscopy, and magnetic measurements.

5.2 Experimental Section

5.2.1 Preparation

Commercially available PC membranes (Millipore Co. USA) used in this study possessed an average diameter of 50, 100 and 200 nm, respectively. These filter membranes contained track etched channels with pores randomly distributed across their surface.

In a typical synthesis of $MnWO_4$ nanowires, a PC membrane was mounted between the two halves of a U-tube cell. The half cells were then filled with 0.1M solutions of Na_2WO_4 and $MnCl_2$ in water, respectively. After 12 h, the PC template was detached, thoroughly washed with distilled water, and ultimately removed by immersion in methylene chloride for 10 min. Isolated $MnWO_4$ nanowires were then obtained by initial centrifugation, followed by washing with ethanol and distilled water, and finally oven drying at 80 ℃ for 24 h. Bulk $MnWO_4$ samples were prepared in a similar way without the use of a template membrane. Specifically, 0.1M aqueous solutions of Na_2WO_4 and $MnCl_2$ were mixed directly. The precipitates ultimately isolated were washed with distilled water and finally dried at 80 ℃ for 24 h.

5.2.2 Characterizaion

X-ray diffraction (XRD) See section 1.7.1.

Electron microscopy See section 1.7.2.

Ultraviolet–visible spectra (UV–visible) See section 1.7.3.

Infrared (IR) spectroscopy Mid-IR spectra were recorded by using a Nicolet NexusTM 470 FTIR spectrometer with a resolution of 4 cm^{-1}. Solid samples were prepared for analysis using a potassium bromide (KBr) pellet.

SQUID The field and temperature dependences of a bulk powder of $MnWO_4$ as well as a powder of MnWO4 nanowires with an average diameter of 200 nm were measured. The experiments were carried out using a Quantum Designs Magnetic Phenomena Measurement System (MPMS) for temperatures ranging from 1.8 to 300 K, and in fields as large as 5 T. The nanoparticles were suspended in paraffin prior to measurement, and we have normalized their magnetization to that of the bulk powder at room temperature

throughout. The bulk powder was compressed into a hard compact specimen weighing 0.009 g.

5.3 Results and Discussion

The purity and crystallinity of as-prepared $MnWO_4$ samples were examined by powder XRD measurements (Figure 5.2). All peaks can be readily indexed to a pure monoclinic phase (space group: *P2/c*) of $MnWO_4$ with calculated lattice constants of a = 0.4813 nm, b = 0. 5783 nm, and c = 0.5008 nm, which are in good agreement with database literature values (a = 0.4829 nm, b = 0. 5759 nm, and c = 0.4998 nm, JCPDS no. 13-0434, lower curve of Figure. 5.2).

The morphology of as-synthesized one-dimensional samples, derived from a 200nm PC template, was studied using FE-SEM and TEM. Figure 5.3 shows SEM images of as-prepared $MnWO_4$ nanowires, isolated from a PC template, possessing 200 nm pore sizes. Diameters of $MnWO_4$ nanowires were noted to be ~260 ± 40 nm, whereas their associated lengths measured ~5.4 ± 1.2 μm. Figure 5.3B (top view) and 5.3C (tilt view) show images of as-generated MnWO4 arrays upon removal of the PC template. The EDS spectrum (Figure 5.3D) confirms the existence of Mn, W, and O, as expected. Sample morphology of the samples was also characterized using low-magnification TEM as shown in Figure 5.4A. These images further confirm the dimensional range of as-prepared nanowires, calculated from SEM data. It should also be mentioned that as-obtained nanowires were noted to be relatively uniform in terms of shape and morphology. A HRTEM image (Figure 5.4B) and associated FFT image (inset to Figure 5.4B) taken on an individual $MnWO_4$ nanowire show the polycrystalline nature of the sample. The lattice spacing measured in the image can be indexed to the (-111) plane. Additional SEM images of $MnWO_4$ nanowires, prepared using templates with pore diameters measuring 50 and 100 nm, respectively, are presented in Figure 5.5. The diameters of these particular $MnWO_4$ nanowires are 55 ± 10 and 100 ± 20 nm, respectively, consistent with the pore size dimensions of the originating templates themselves with associated lengths of 2.0 ± 0.5 and 3.0 ± 1.1 μm, respectively. The morphology of bulk samples was also investigated using FE-SEM as shown in Figure 5.6. The bulk samples essentially consisted of uniform particulate structures with diameters in the range of 1.5 ± 0.1 μm. EDS patterns showed the presence of peaks associated with Mn, W and O, respectively.

Optical properties of as-prepared 200 nm nanowire samples were also investigated from the UV to IR range. The IR spectrum (Figure 5.7A) of $MnWO_4$ nanowires shows a number of absorption bands (located at 579, 669, 757, 810, 875, and 912 cm^{-1}) in the range of 500–1000 cm^{-1} which are similar to that of the bulk IR pattern previously reported for $MnWO_4$ H_2O, wherein the inorganic modes lie at the low-wavenumber end of the spectra.[34] Many of these infrared bands can be assigned to internal stretching modes, i.e. $v_3(A_u)$ and $v_3(E_u)$ transitions.[35] The UV–visible (Figure 5.7B) spectrum showed a similarity in the absorption profile between that of the 200 nm nanowires and of the bulk.

The magnetic behavior of our as-prepared 200 nm $MnWO_4$ nanowires was investigated using SQUID analysis. $MnWO_4$ has been considered as a moderately

frustrated antiferromagnetic spin system.[20] Bulk $MnWO_4$ has been found to undergo successive magnetic phase transitions at ~13.5 K (T_N), ~12.7 K (T_2), and ~7.6 K (T_1), corresponding to three long-wavelength magnetic ordering states: AF3, AF2, and AF1.[18, 36] The ground state, AF1 ($T<T_1$), is a commensurate collinear antiferromagnetic phase; the magnetic moments are aligned collinearly along the 'easy' axis of magnetization, which is within the ac plane at an angle of 35–37 ° from the a-axis. By contrast, AF2 ($T_1<T<T_2$) consists of an incommensurate elliptically modulated spiral spin structure. Finally, the AF3 ($T_2<T<T_N$) phase denotes an incommensurate, sinusoidal collinear AFM structure with magnetic moments lying along the x-axis.[18, 20] Prior investigations of the magnetic properties of $MnWO_4$ were mainly performed on bulk samples so it was important to note the comparable behavior of $MnWO_4$ nanowires.

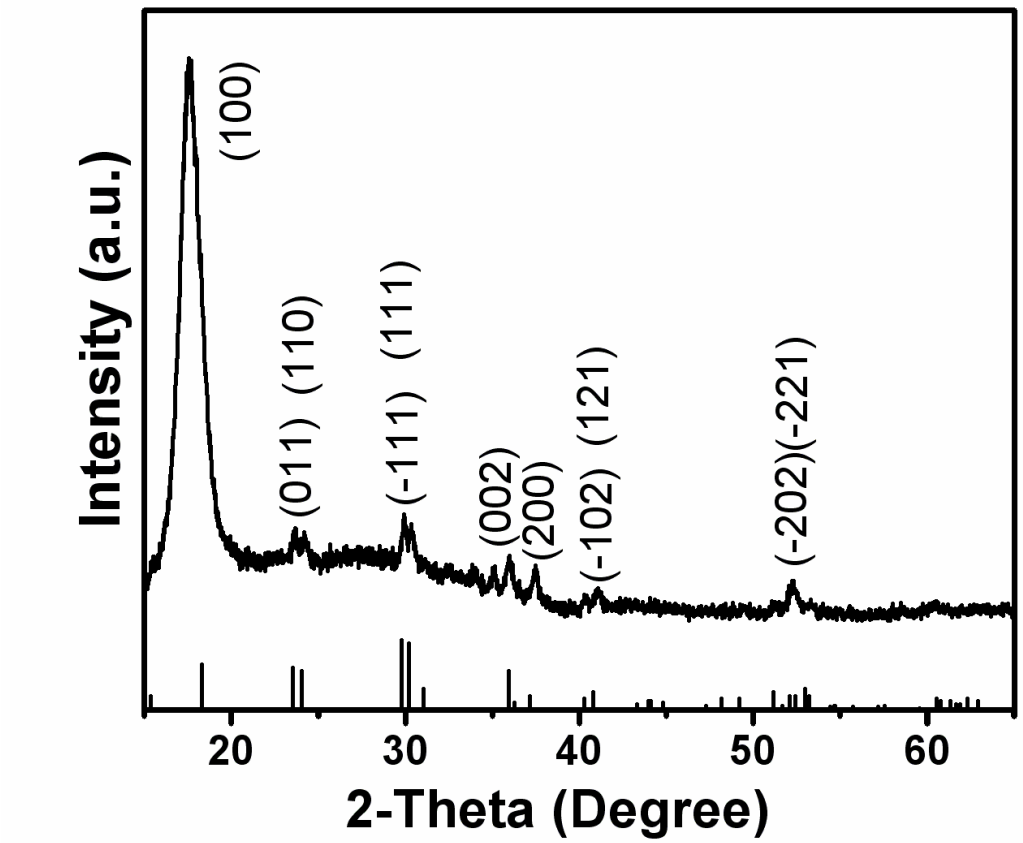

Figure 5.2 XRD patterns of as-prepared samples (upper half) and of the corresponding database standard (JCPDS #13-0434, lower half).

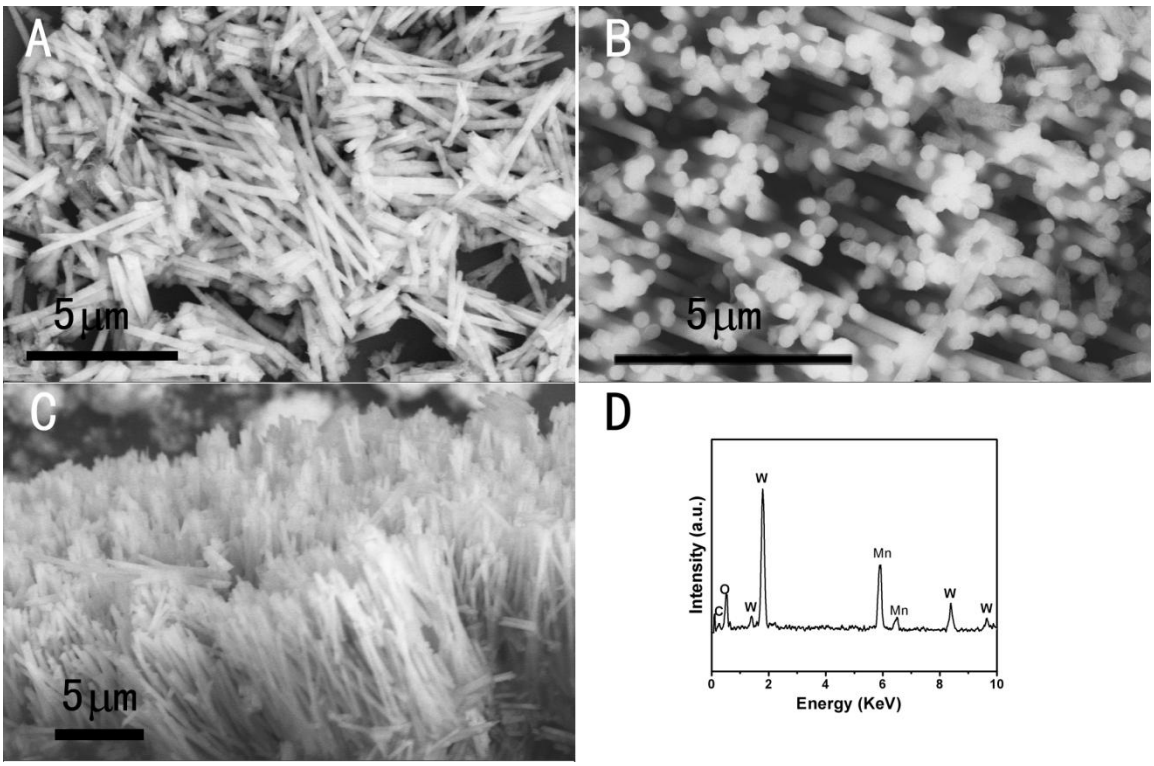

Figure 5.3 SEM images of (A) isolated $MnWO_4$ nanowires, (B) MnWO4 arrays (top view), (C) $MnWO_4$ arrays (side view) and (D) Representative EDS pattern of as-prepared $MnWO_4$ nanowires and nanowire arrays.

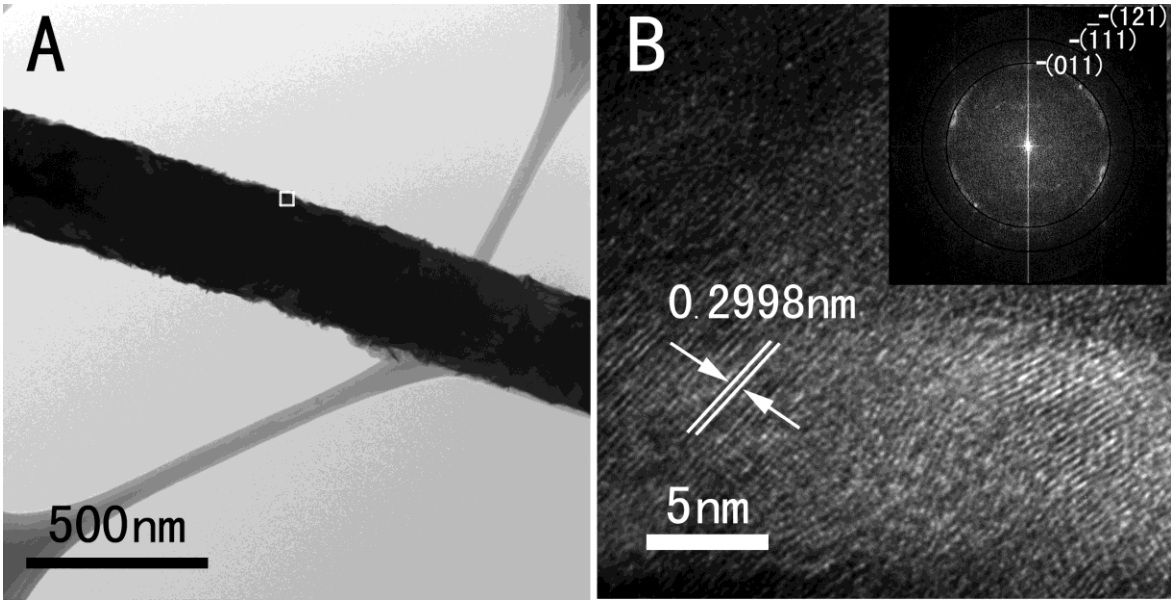

Figure 5.4 TEM (A) and HRTEM (B) images as well as the corresponding FFT pattern (inset) of $MnWO_4$ nanowires.

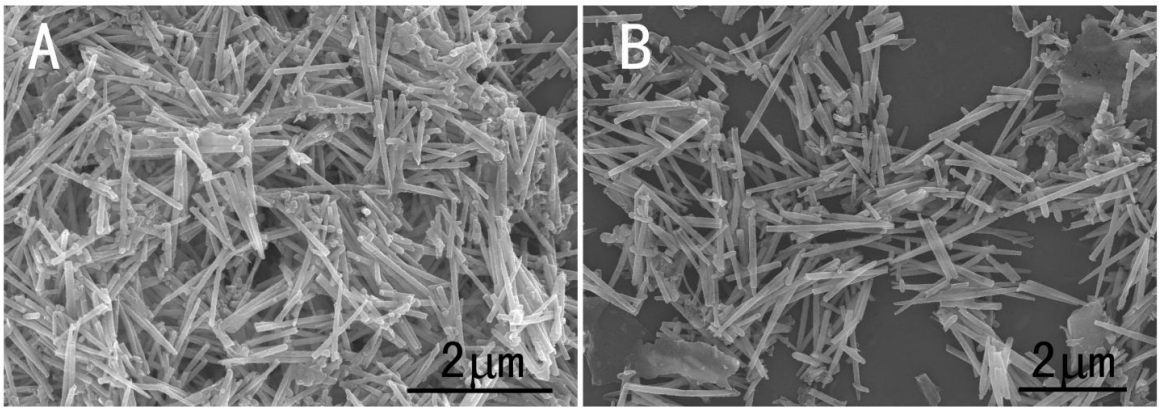

Figure 5.5 SEM images of isolated $MnWO_4$ nanowires prepared from (A) a 50 nm PC template and (B) a 100 nm PC template.

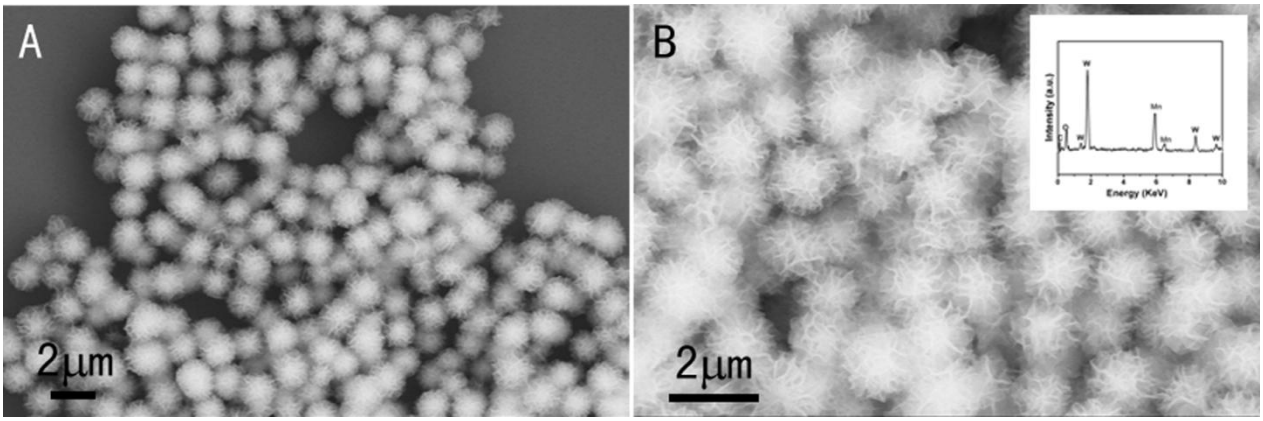

Figure 5.6 SEM images as well as an EDS pattern (inset to B) of bulk $MnWO_4$.

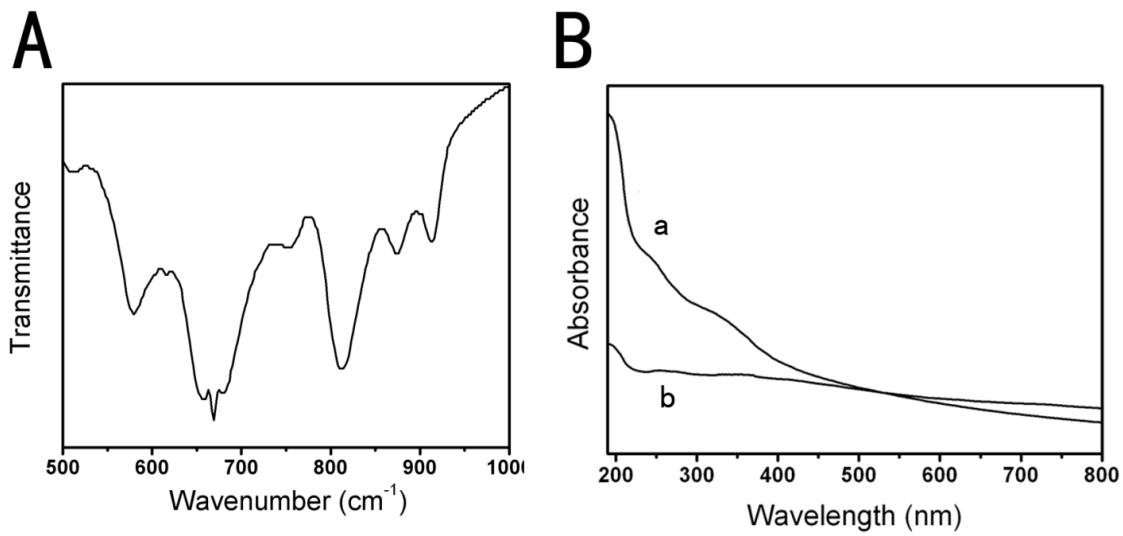

Figure 5.7 IR spectrum (A) and UV-visible spectrum (B) of $MnWO_4$ ((a) bulk and (b) nanowires).

The temperature dependence of the magnetic susceptibility, measured in a field of 0.1 T, has been compared for the two samples in Figure 5.8A and B, measured after cooling in zero field (ZFC) and in a field of 5 T (FC). In all cases, the susceptibility increases with decreasing temperature, reaching a single broad maximum near 7 K. Figure 5.9 shows that the susceptibility is well described by the Curie–Weiss law for temperatures from 10 to 300 K, indicating that it arises from a conventional paramagnetic state involving independent fluctuations of independent Mn moments. The Weiss temperature, θ = -25 K, implies a net antiferromagnetic interaction among the Mn moments, with a magnitude in reasonable agreement with the value of θ = -15 K found for bulk powdered $MnWO_4$.

The maximum in the susceptibility signals the onset of magnetic order at ~7.5 K, presumably antiferromagnetic order, although the breadth of the maximum and also the separation of the FC and ZFC data below this ordering temperature suggests an appreciable level of magnetic frustration and perhaps short range order. In principle, this might result in the nanoparticle samples experiencing a superparamagnetic effect caused by uncompensated surface moments. However, the results found for the bulk powder are very similar and we conclude that disorder is a more likely explanation. That is, while the presence of chemical impurity might normally account for the slight anomaly observed, we did not detect any such magnetic impurity in our samples. Hence, these observations can potentially be assigned to structural disorder in the sample, such as the presence of small-crystalline particulate regions, an assertion supported by the polycrystalline nature of our metal tungstate nanowires, as evidenced by the TEM/HRTEM images in Figure 5.4A and B. Indeed, the susceptibility peak in both of our samples is much broader and occurs at a lower temperature than that previously reported for a $MnWO_4$ powder[22] and a single crystal.[18] What is more, is that no features are found in the temperature derivative of the susceptibility, which might correspond to the three thermodynamic transitions found in heat capacity measurements.[22]

The field dependences of the magnetization for both the bulk and nanoparticle samples are presented in Figure 5.10A and B. The magnetization is always linear in field, showing that the magnetic response is dominated by that of the individual moments, both above and below the antiferromagnetic ordering temperature. The rapid reduction in the slope of the magnetization curves with increased temperature is wholly congruent with the overall Curie–Weiss susceptibility. Accordingly, we have plotted the ZFC susceptibility data, x = M/H, measured for both samples as a function of H/T in Figure 5.11, to confirm that the magnetization sweeps taken at temperatures from 3 to 80 K all collapse onto universal curves, presumed to be approximated by Brillouin functions. This collapse shows that the magnetization is dominated by fluctuations of individual Mn moments, and not by critical fluctuations or other collective effects.

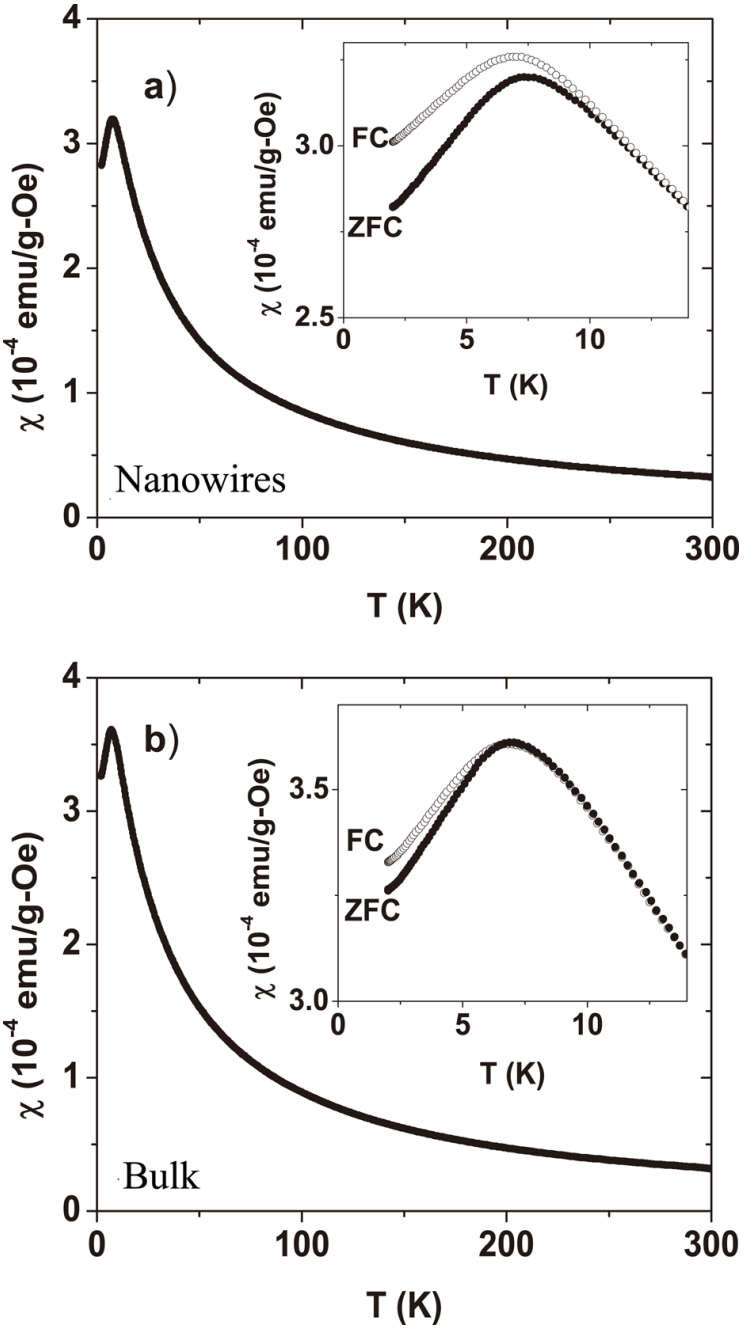

Figure 5.8 (a) Magnetic susceptibility χ of powder of 200 nm nanowires, measured in a field of 0.1 T. The inset shows a modest hysteresis between data taken under zero field cooled (ZFC) and data taken after cooling in a 5 T field (FC). (b) Same, but for a bulk powder sample of $MnWO_4$.

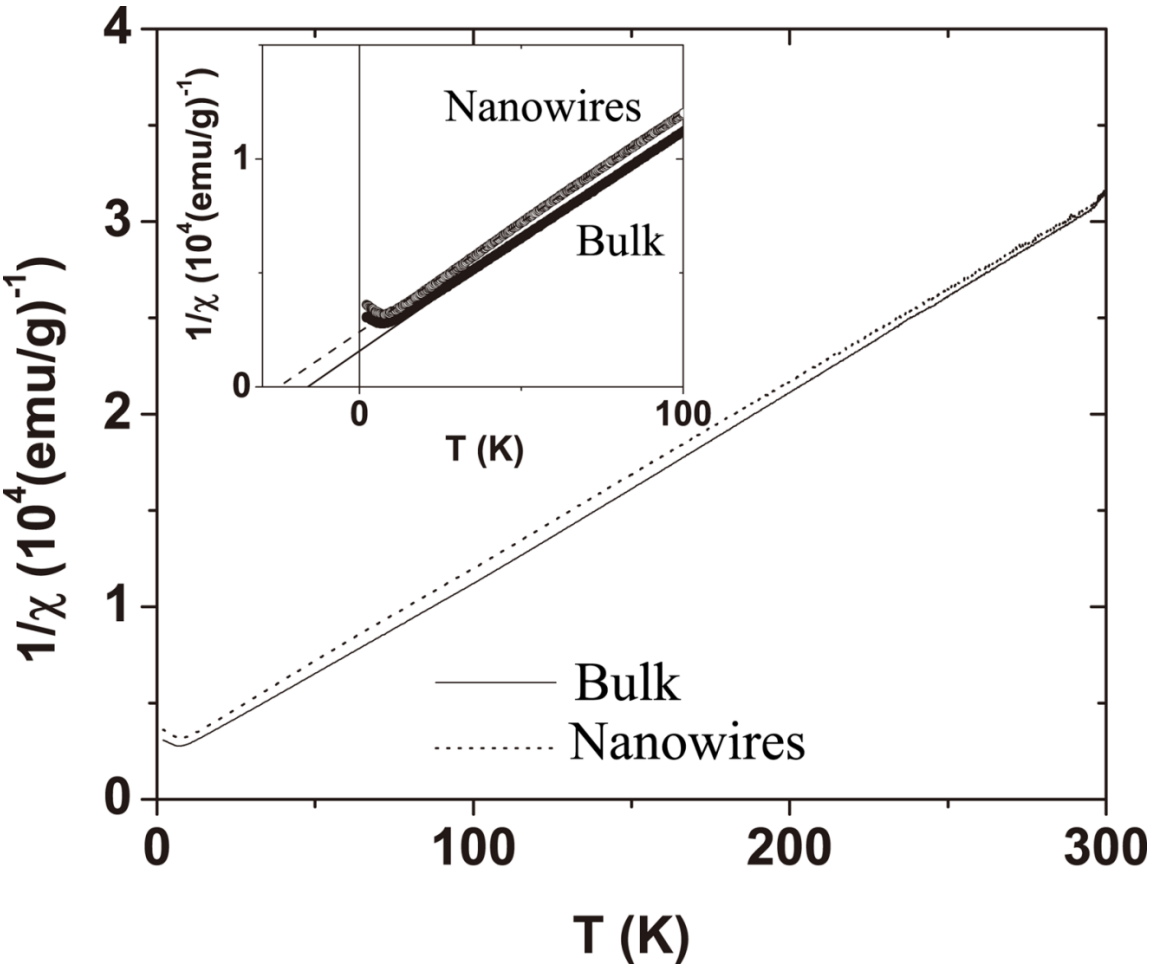

Figure 5.9 Temperature dependence of the inverse susceptibility χ^{-1} for bulk (solid line) and 200 nm nanowire (dashed line) samples. Inset compares linear fits (solid line (bulk), dashed line (nanowires)), indicating that the Curie-Weiss law is valid for temperatures from ~15 K to 300 K.

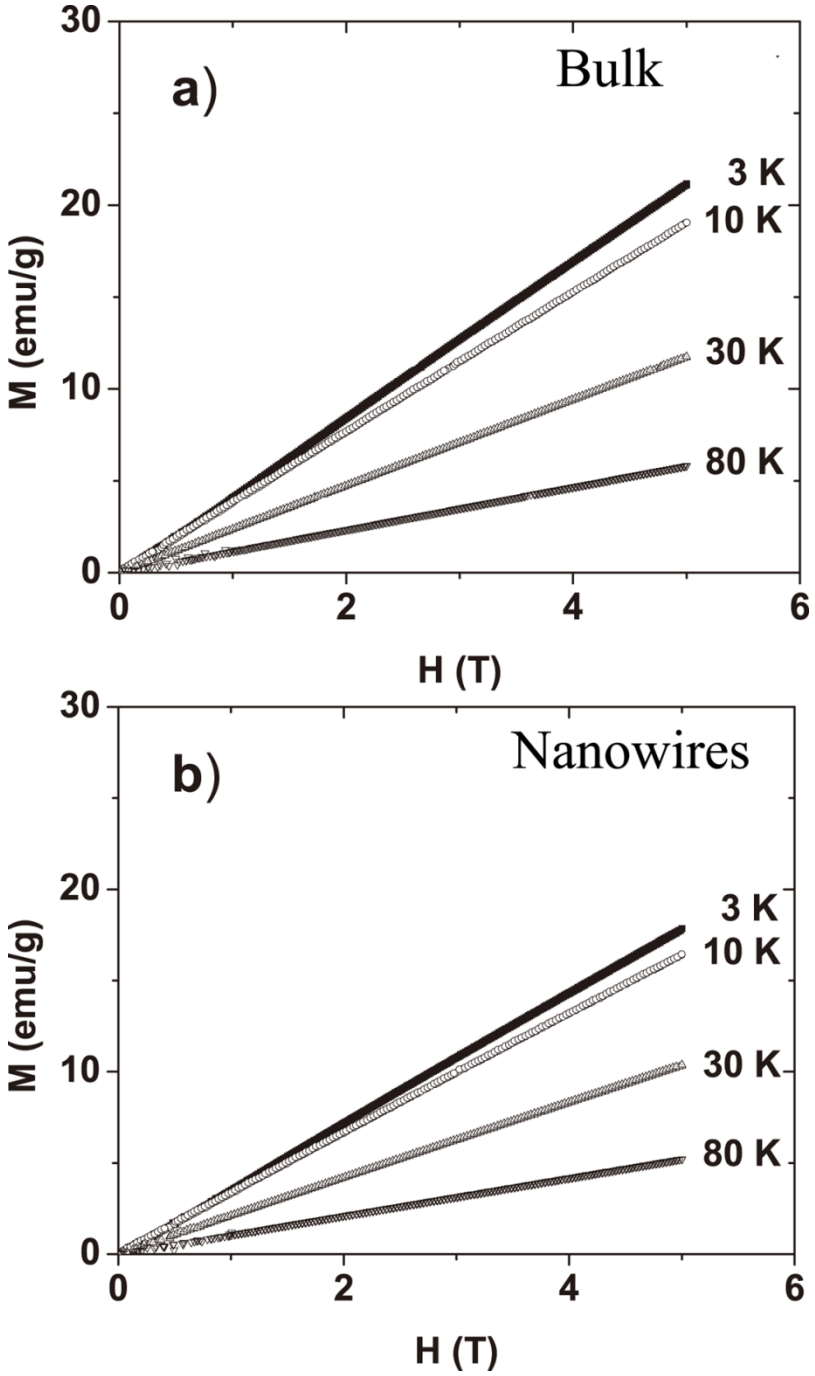

Figure 5.10 Field dependences of the magnetization M, at different fixed temperatures for the bulk $MnWO_4$ powder (a) and 200 nm nanowires (b).

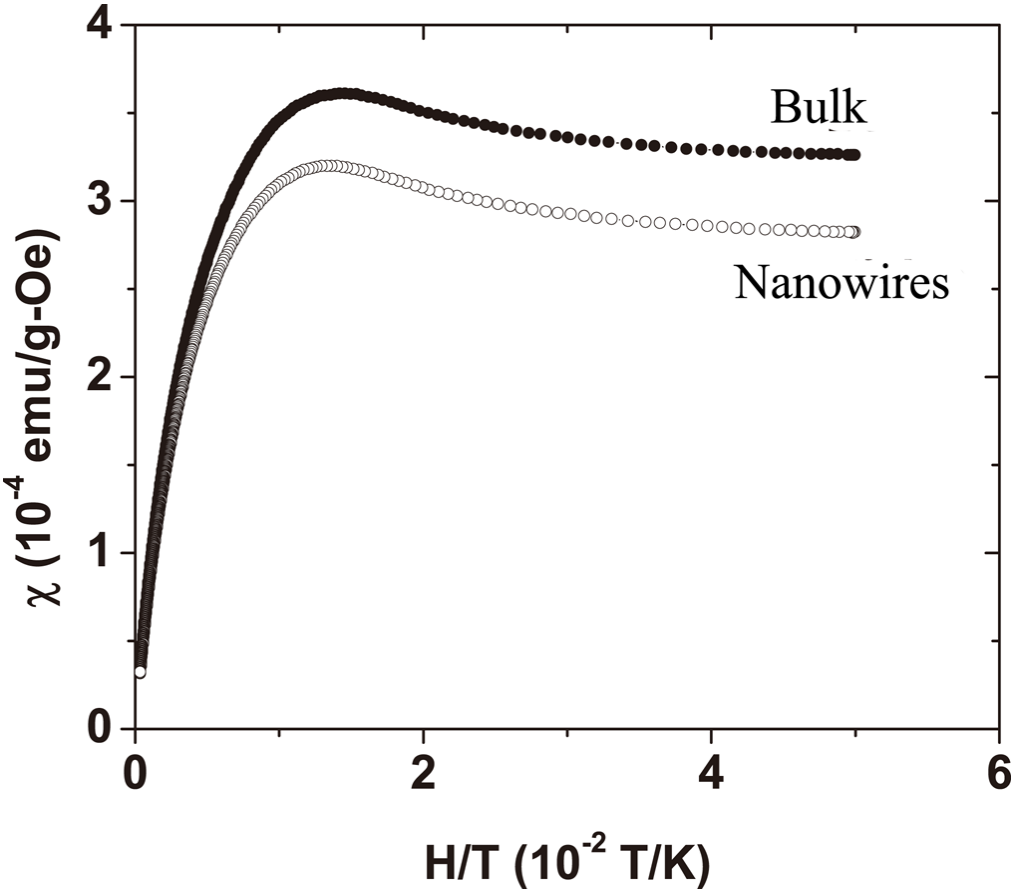

Figure 5.11 Field-temperature scaling behavior of the susceptibility $\chi = M/H$ is measured for both the bulk powder and the 200 nm nanowire samples.

Taken together, these magnetic measurements reveal a system in which antiferromagnetic short-range order is established, although the development of these correlations is sluggish and coexists with a predominantly paramagnetic response both above and below the transition. No evidence for finite size effects due to particle size was found in these nanowire samples, which show almost the same properties as that of the bulk powder of $MnWO_4$.

As described previously in other papers,[37-40] in the current experiment, we use the pores of PC membranes as the physical environment in which to control the growth of well-defined morphologies of crystals of our manganese tungstate structures. The membranes used are thin, and are mounted in a double diffusion setup, which enables the continuous flow of ions into the membrane pores but prevents their overly rapid mixing. Thus, in the experimental setup used in these experiments, the contents of each solution in either half of the U-tube are allowed to diffuse towards each other across a wetted template membrane physically separating the two halves. Manganese cations and tungstate anions meet at the interface, react in a precipitation/ metathesis process, and nucleate the formation of the corresponding metal tungstates. These insoluble tungstates will begin to precipitate from solution, once the supersaturation value for their production has been exceeded.

If the interactions between reagent molecules are stronger than those between the reagent molecules and the pore walls, the nucleation process and accompanying product formation will tend to happen within the voluminous confines of the pores themselves in a homogeneous-type process. That is, crystals of nanoscale metal tungstates therefore derive from isolated, disparate nucleation sites, which then grow by extension throughout the porous network. Continued growth then occurs at the particle surface at a rate limited by ion availability, until the crystal impinges upon the relatively inert template surface itself, which ultimately limits further particle growth. Within the cylindrical confines of the template pores, as-formed particles in this scenario essentially self-assemble with each other into either wire-like or rod-like motifs.

Conversely, if the interactions between the reagent molecules are weaker than those between the reagent molecules and the pore walls, the nucleation and accompanying growth processes may tend to be localized at the surfaces of the pore walls in a heterogeneous-type process. Such a process may occur, for instance, if the pore wall is positively charged while the reagent particles are negatively charged. This preferential confinement of growth to the inherent geometry of the pore walls can therefore lead to the generation of primarily tube-like motifs upon the elongation and assembly of the as-formed particles. With continued reaction, nanowire formation can be viewed as a lateral thickening of the tubular structure, which, as further supply of precursors to the inside is blocked by the ever-growing tube thickness coupled with an ever-decreasing inner tube diameter, eventually constricts the entire porous interior of the template, filling it completely. In other words, continued growth of the nanotubes is limited only by reagent ion availability and diffusivity as well as by intrinsic geometrical constraints imposed by the template channels. Hence, nanowires can be considered as the ultimate limit of nanotube growth, at least in terms of its width.

5.4 Conclusions

$MnWO_4$ nanowires and nanowire arrays have been synthesized by a simple, room-temperature method with the aid of a PC template. These reactions have been run under simplistic, ambient conditions in aqueous solutions with reproducibility in terms of morphology and chemical composition. We have also used this protocol not only to generate isolated structures but also to produce arrays of these ternary metal oxides. As-synthesized nanowires measured 260 ± 40nm in diameter and 5.4 ± 1.2 μm in length, isolated from a 200 nm PC template. Those generated from templates with pore diameters of 50 and 100 nm measured 55 ± 10 and 100 ± 20 nm, respectively, with accompanying lengths in the microns. Optical and magnetic properties of $MnWO_4$ nanowires have been investigated, suggestive of subtle differences in behavior between bulk and nanoscale manifestations of an identical material. The fact that the nanowires were polycrystalline did not obviously appear to adversely affect the performance metrics of these materials. However, it is obvious that for many systems, the ability to generate pure, single-crystalline motifs is crucial to relevant structure–property correlations. Hence, in terms of future work, we will likely explore other methods of nanoscale $MnWO_4$ preparation, including using catanionic reverse micelles.[41-44]

5.5 References

1. Smolenskii, G. A.; Chupis, I. E. *Usp. Fiz. Nauk* **1982**, 137, 415.
2. Smolenskii, G. A.; Chupis, I. E. *Sov. Phys. Usp.* **1982**, 25, 475.
3. Jona, F.; Shirane, G., *Ferroelectric Crystals*. Dover: New York, **1993**.
4. Schmid, H. *Ferroelectrics* **1994**, 162, 317.
5. Hill, N. A. *J. Phys. Chem. B* **2000**, 104, 6694.
6. Lines, M. E.; Glass, A. M., *Principles and Applications of Ferroelectrics and Related Materials*. Oxford Univeristy Press: Oxford, **2001**.
7. Khomskii, D. I. *Bull. Am. Phys. Soc. C* **2001**, 21.002.
8. Cheong, S.-W.; Mostovoy, M. *Nat. Mater.* **2007**, 6, 13.
9. Katsufuji, T.; Mori, S.; Masaki, M.; Moritomo, Y.; Yamamoto, N.; Tagaki, H. *Phys. Rev. B* **2001**, 64, 104419.
10. Kimura, T.; Kawamoto, S.; Yamada, I.; Azuma, M.; Takano, M.; Tokura, Y. *Phys. Rev. B* **2003**, 67, 180401.
11. Wang, J.; Neaton, J. B.; Zheng, H.; Nagarajan, V.; Ogale, S. B.; Liy, B.; Viehland, D.; Vaithyanathan, V.; Schlom, D. G.; Waghmare, U. V.; Spaldin, N. A.; Rabe, K. M.; Wutting, M.; Ramesh, R. *Science* **2003**, 299, 1719.
12. van Aken, B. B.; Palstra, T. T. M.; Filippetti, A.; Spaldin, N. A. *Nat. Mater.* **2004**, 3, 164.
13. Fennie, C. J.; Rabe, K. M. *Phys. Rev. B* **2005**, 72, 100103(R).
14. Ederer, C.; Spaldin, N. A. *Phys. Rev. B* **2006**, 74, 1.
15. Kimura, T.; Goto, T.; Shintani, H.; Ishizaka, K.; Arima, T.; Tokura, Y. *Nature* **2003**, 426, 55.
16. Subramanian, M. A.; He, T.; Chen, J.; Rogado, N. S.; Calvarese, T. G.; Sleight, A. W. *Adv. Mater*, **2006**, 18, 1737.

17. Ikeda, N.; Ohsumi, H.; Ohwada, K.; Ishii, K.; Inami, T.; Kakurai, K.; Murakami, Y.; Yoshii, K.; Mori, S.; Horibe, Y.; Kito, H. *Nature* **2005**, 436, 1136.
18. Taniguchi, K.; Abe, N.; Takenobu, T.; Iwasa, Y.; Arima, T. *Phys. Rev. Lett.* **2006**, 97, 097201.
19. Ehrenberg, H.; H.Weitzel; Heid, C.; Fuess, H.; Wltschek, G.; Kroener, T.; Tol, J. V.; Bonnet, M. *J. Phys.: Condens. Matter* **1997**, 9, 3189.
20. Arkenbout, A. H.; Palstra, T. T. M.; Siegrist, T.; Kimura, T. *Phys. Rev. B* **2006**, 74, 184431-1.
21. Heyer, O.; Hollmann, N.; Klassen, I.; Jodlauk, S.; Bohaty, L.; Becker, P.; Mydosh, J. A.; Lorenz, T.; Khomskii., D. *J. Phys.: Condens. Matter* **2006**, 18, L471.
22. Lautenschlager, G.; Weitzel, H.; Vogt, T.; Hock, R.; Bohm, A.; Bonnet, M.; Fuess, H. *Phys. Rev. B* **1993**, 48, 6087.
23. Lei, S.; Tang, K.; Fang, Z.; Huang, Y.; Zheng., H. *Nanotechnology* **2005**, 16, 2407.
24. Qu, W.; Wlodarski, W.; Meyer, J.-U. *Sensors Actuators B* **2000**, 64, 76.
25. Schultze, V. D.; Wilke, K. T.; Waligora, C. *Z. Anorg. Allg. Chem.* **1967**, 352, 184.
26. Alvrecht, V. R.; Mobius, R. *Anorg. Allg. Chem.* **1972**, 392, 62.
27. Jang, M.; Weakley, T. J. R.; Doxsee, K. M. *Chem. Mater.* **2001**, 13, 519.
28. Chen, S.-J.; Chen, X.-T.; Xue, Z.; Zhou, J.-H.; Li, J.; Hong, J.-M.; You, X.-Z. *J. Mater. Chem.* **2003**, 13, 1132.
29. Zhang, L.; Lu, C.; Wang, Y.; Cheng, Y. *Mater. Chem. Phys.* **2007**, 103, 433.
30. Xia, Y.; Yang, P.; Sun, Y.; Wu, Y.; Mayers, B.; Gates, B.; Yin, Y.; Kim, F.; Yan, H. *Adv. Mater.* **2003**, 15, 353.
31. Patzke, G. R.; Krumeich, F.; Nesper, R. *Angew. Chem. Int. Ed. Engl.* **2002**, 41, 2446.
32. Yu, S.-H.; Liu, B.; Mo, M.-S.; Huang, J.-H.; Liu, X.-M.; Y.-T. Qian. *Adv. Funct. Mater.* **2003**, 13, 639.
33. Jung, J.-S.; Ren, L.; O'Connor, C. J. *J. Mater. Chem.* **1992**, 2, 829.
34. Ingham, B.; Chong, S. V.; Tallon, J. L. *Curr. Appl. Phys.* **2006**, 6, 553.
35. Tarte, P.; Liegeois-Duyckaerts, M. *Spectrochim. Acta—Part A* **1972**, 28A, 2029.
36. Ehrenberg, H.; Weitzel, H.; Fuess, H. *Physica B.* **1997**, 560, 234.
37. Mao, Y.; Wong, S. S. *J. Am. Chem. Soc.* **2004**, 126, 15245.
38. Mao, Y.; Zhang, F.; Wong, S. S. *Adv. Mater.* **2006**, 18, 1895.
39. Mao, Y.; Park, T.-J.; Zhang, F.; Zhou, H.; Wong, S. S. *Small* **2007**, 3, 1122.
40. Zhang, F.; Mao, Y.; Park, T.-J.; Wong, S. S. *Adv. Funct. Mater.* **2008**, 18, 112.
41. Shi, H.; Qi, L.; Ma, J.; Cheng, H. *J. Am. Chem. Soc.* **2003**, 125, 3450.
42. Shi, H.; Qi, L.; Ma, J.; Cheng, H.; Zhu, B. *Adv. Mater.* **2003**, 15, 1647.
43. Shi, H.; Qi, L.; Ma, J.; Wu, N. *Adv. Funct. Mater.* **2005**, 15, 442.
44. Shi, H.; Wang, X.; Zhao, N.; Qi, L.; Ma, J. *J. Phys. Chem. B* **2006**, 110, 748.

Chapter VI Template synthesis of 1D noble metals: Ag, Au and Pt

6.1 Introduction

In previous chapters (Chapter IV and V), we have demonstrated the successful synthesis of 1D binary and ternary metal oxides by a simple, low-cost template method. All of these materials were prepared based on precipitation reactions confined in the pores of templates. Because hydroxides and tungstates have limited solubilities in water, they readily precipitated from the water once metal ions mixed with hydroxide ions or tungstate ions. In this chapter, we extend this idea to an oxidation-reduction reaction instead of a precipitation reaction. The materials we have chosen are noble metals, which can be readily reduced by a reducing agent such as $NaBH_4$, citric acid, ascorbic acid, ethylene glycol and so on.

6.1.1 Noble Metals

Metallic nanostructures, including Au, Ag, and Pt, have attracted significant attention due to their excellent optical, electrical, and thermal conductivity properties, which are highly relevant for diverse applications such as catalysis, optical imaging, optoelectronics, information storage, fuel-cell technology, and sensing.[1-8] Specifically, they strongly absorb and scatter light in the visible region and are relatively stable to oxidation.[9] For instance, gold nanowire arrays have been used as sensors for mercury[10] and organothiol[11] detection in addition to as biosensors for enzyme[12] and disease detection.[13] Moreover, gold nanotube membranes have been reported as highly selective molecular sieves.[14] Ordered silver nanowires have been developed as infrared polarizers[15] as well as platforms for surface-enhanced Raman scattering.[16] Platinum nanotubes have been developed as electrodes in ferroelectric semiconductor memory applications due to their chemical stability and low leakage,[17] while their nanowire analogues have been considered as components of high-frequency electrochemical resonators.[18]

As compared with bulk and zero-dimensional nanoparticles, one-dimensional (1-D) analogues of metallic nanostructures have become even more fundamentally and practically important in recent years. In a long metallic nanowire, electron confinement effects are present not only along the radial direction, but also along the axial direction. Metal nanowires and their corresponding nanowire arrays have been previously prepared using a number of different methodologies. One of most popular wet chemical protocols involves the initial preparation of small sized 3-4 nm spherical (e.g. citrate-capped Au) nanoparticles followed by growth of these seed particles in a rod-like micellar environment[19-22] under ambient conditions. Specifically, gold nanorods can be prepared via the reduction, in the presence of ascorbic acid, of $HAuCl_4$ in a surfactant (i.e. cetyltrimethylammonium bromide, CTAB)-based solution[23] with the gold seed-to-salt

ratio determining the resulting aspect ratios. Recently, specially designed small organothiols have been used to replace CTAB as means of obtaining biocompatible, less cytotoxic Au nanorods.[24] By analogy, uniform Ag nanowires, measuring 30 to 50 nm in diameter with lengths up to 50 μm, can be routinely produced using a 'self-seeding' process in which $AgNO_3$ and poly(vinyl pyrrolidone) solutions are simultaneously injected into refluxed ethylene glycol, serving as both solvent and reducing agent, using a two-channel syringe pump in the presence of either Pt or Ag seeds.[25, 26] In a similar fashion, Pt(II) species have initially been formed by reducing H_2PtCl_6 with ethylene glycol at 110 ℃ in the presence of poly(vinyl pyrrolidone) (PVP); this polyol process was mediated by the addition of either $FeCl_3$, $FeCl_2$, or even $NaBH_4$, which enabled the reduction of Pt(II) to Pt atoms which subsequently nucleated and grew into uniform, high-aspect-ratio nanowires.[27, 28]

6.1.2 Oxygen Reduction Reaction (ORR)

The oxygen reduction reaction (ORR) is a key cathodic reaction in electrochemical energy conversion processes (e.g. in fuel cells and batteries). It is a multielectron reaction that may include a number of elementary steps involving different reaction intermediates. Below is a scheme that appears to be the most effective one for describing the complicated reaction pathway by which O_2 is reduced at metal surfaces:[29]

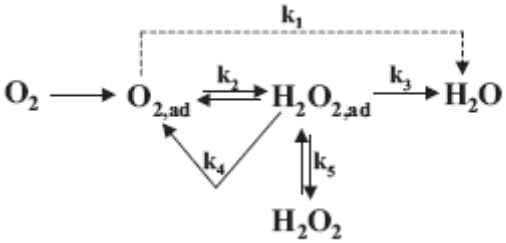

Based on this scheme, O_2 can be electrochemically reduced either directly to water with a rate constant k_1 without the intermediate formation of $H_2O_{2,ad}$ (direct $4e^-$ reduction) or to $H_2O_{2,ad}$ with a rate constant k_2 (series $2e^-$ reduction). The $H_2O_{2,ad}$ can then be electrochemically reduced to water with the rate constant k_3 (series $4e^-$ pathway), decomposed on the electrode surface (k_4), or desorbed into the solution (k_5).

Platinum metal and platinum alloys are the best available electrocatalysts for the ORR so far. However, the extremely high cost of platinum metal is the biggest problem for commercial application. Recently, many attempts have been made by researchers and fuel cell developers to create a non-Pt catalyst for low temperature air cathodes. Examples include ruthenium,[30] cobalt-nickel,[31] and carbon nanotubes.[32]

6.1.3 Current Work

The key element of our recent synthesis work has been on designing reasonably green approaches to nanoscale production. We have shown some related work in previous chapters (binary and ternary metal oxides). In the current chapter, we have expanded this body of work to encompass highly significant one-dimensional nanostructures of gold, silver, and platinum. In this particular context, the specific

advantages of our protocol are that we do not necessitate either the use of surfactant or catalyst seed particles, which are commonly used in the synthesis of metal nanomaterials. Hence, we are able to avoid laborious and repetitive washing steps using either strong acid/base or organic solvent in order to remove surfactant or catalytic metal. This is important because remnant, exposed surfactant as well as the presence of even small percentages of extraneous metal can often be seriously detrimental to the catalytic and optoelectronic performance of these materials.[33] Moreover, our technique is facile, involves no heating step, does not require the use of expensive experimentation, and is relatively rapid, taking only 30 to 60 minutes in order to generate pure, crystalline samples. In fact, we merely used a home-made U-tube cell whose two halves were separated by a polycarbonate template (PC); the reaction used to generate our nanorods and arrays of those materials was based on the one-step reduction of metal ions in ethanol solution in the presence of sodium borohydride. We believe this method should also be applicable to the fabrication of other interesting 1-D elemental metallic nanostructures including Co, Ni, and Fe.

As compared with a large volume of papers describing applications, including sensing and imaging,[34-36] of 1-D metallic nanostructures based on their intrinsically interesting optical properties, there are comparatively fewer papers that detail the catalytic properties of 1-D metallic nanostructures in spite of the fact that Pt, Au and Ag are all excellent catalysts in bulk. Hence, to better understand the shape-dependent catalytic properties of our as-prepared materials, we therefore studied a model electrocatalytic oxygen reduction reaction (ORR) (discussed in the 6.1.2) involving one-dimensional Pt, Au, and Ag nanostructures respectively, which is generally important for the development of effective fuel cell catalysts. Indeed, the last decade has seen considerable advances made in fuel cell electrocatalysis, yielding improved electrocatalysts and increasing our understanding of the kinetics of an ORR. However, further improvements with respect to catalysts for the ORR are necessary, because of a limited efficiency of energy conversion in fuel cells caused by the reaction's associated slow kinetics.

In general terms, the approaches used to increase ORR electrocatalytic activity involve: (i) decreasing the particle size and (ii) alloying of Pt so as to synthesize bi-metallic catalysts. Since the highest surface-to-volume ratio, and utilization of Pt can be achieved with nanoparticles, they are the preferred form of most catalysts, including those for the ORR. It is generally accepted that the oxidation of small nanoparticles renders them less active for the ORR on the basis of real surface area (specific activity) as compared with bulk Pt. Higher coordination of Pt surface atoms in solid samples makes them less susceptible to oxidation than those on the surfaces of nanoparticles. Yan et al.[37] reported the synthesis and characterization of support-less platinum nanotubes and platinum-alloy nanotubes for fuel cell cathode catalysts. However, current synthetic methods produce metallic tubes with wall diameters of 4-7 nm. As a result, a large proportion of platinum group metals (PGM), either within the tube wall or the internal tube surface area, cannot participate in the ORR reaction. Herein, we will explore the activity of larger Pt 1-D nanostructures that do not suffer from the above shortcomings.

6.2 Experimental Section

6.2.1 Preparation

Commercially available polycarbonate (PC) membranes (Millipore Co., USA) used in this study contained pore sizes of 200 nm in diameter. These PC filters possess track-etched channels with 10^{12} pores randomly distributed across the filter membranes. To synthesize one-dimensional Ag, Au, and Pt nanostructures, a typical PC membrane was mounted between the two halves of a U-tube cell. One half-cell was then filled with solutions (0.1 M) of metal salts (e.g., $AgNO_3$ (Alfa Aesar) for Ag, $HAuCl_4$ (Sigma Aldrich) for Au, and H_2PtCl_6 (Sigma Aldrich) for Pt); the other half-cell was immersed with a 0.5 M solution of $NaBH_4$ (Acros) in ethanol. After 30 to 60 minutes of reaction at room temperature, the PC template was detached, thoroughly washed with distilled water, and ultimately removed by immersion in methylene chloride for 10 min.

6.2.2 Characterizaion

X-Ray diffraction See section1.7.1.

Electron Microscopy See section 1.7.2.

UV-visible Spectroscopy absorption measurements were obtained using a Thermospectronics UV1 spectrometer with a quartz cell possessing a 10-mm path length. For these data, metal nanowire sol samples were prepared, according to a protocol, previously outlined by the Martin group.[38] Specifically, template membranes containing the metal nanowires were immersed into $CHCl_3$ and manually shaken for ~10 s to dissolve the membrane. This resulted in a dispersion of freed nanowires into the solvent medium, thereby facilitating sol formation. The intensity of the absorption band depends on the aspect ratio and diameter of the nanowires as well as on the quantity of metal suspended.[38]

ORR reaction Studies of the kinetics of the ORR on both 1-D nanowire and 0-D nanoparticle catalysts have been performed using the thin-layer rotating disk electrode (RDE) method. In this method, the relevant catalysts are dispersed in water and sonicated for 30 min so as to create a uniform suspension. Subsequently, a 15-μL aliquot of this suspension was placed onto a glassy carbon substrate (RDE, Pine Instruments) and dried in air. Then, the catalyst layer was covered with 5 μL of a 4 μg/10 μL Nafion solution, which was diluted with water from an initial 5% Nafion stock solution supplied by Aldrich. A reference electrode (Ag/AgCl, 3M Cl^-) was used using a double-junction chamber (Cypress). All of the potentials recorded in this paper are given with respect to a reversible hydrogen electrode (RHE). A platinum foil was used as the counter electrode. By means of comparison with our 1-D nanostructures, Pt nanoparticles with an average particle size of 8 nm were purchased from TKK (Tokyo, Japan). Perchloric acid was obtained from Fisher, while KOH was purchased from Alfa Aesar. Solutions were prepared using MilliQ UV-plus water (Millipore). All of the current densities were normalized to the geometric area of the rotating disk electrode, whereas the electrochemical measurements were carried out at room temperature.

6.3 Results and Discussions

The purity and crystallinity of as-prepared, one-dimensional Ag, Au, and Pt nanostructures were examined by means of powder XRD measurements (Figure 6.1). All peaks of as-prepared samples could be readily indexed to pure phases of our desired materials and no detectable impurities were noted in any of our patterns. In fact, our results suggest that we were able to obtain the cubic phases of Ag (F*m3m*, JCPDS No. 04-0783), Au (F*m3m*, JCPDS No. 04-0784), and Pt (F*m3m*, JCPDS No. 04-0802), respectively, at room temperature.

The morphology of as-synthesized one-dimensional samples was studied using FE-SEM and TEM (Figure 6.2). Parts a and b of Figure 6.2 delineate SEM images of as-prepared Ag nanowires isolated from a 200 nm PC template. Diameters of these isolated Ag nanowires, bereft of nanoparticles, were 220 ± 30 nm, with associated lengths in the range of about 2 ± 1 μm. Arrays of Ag nanowires were also obtained by careful and complete removal of the entire PC template using methylene chloride, as shown in Figure 6.2c. The EDS spectrum (Figure 6.2d) highlights the presence of Ag, as expected, with the Si signal emanating from the underlying Si wafer used for imaging. The rigid nanowire morphology was further examined using low magnification TEM, as shown in Figure 6.2e. The HRTEM image (Figure 6.2f) and SAED pattern (inset to Figure 6.2f) revealed that the as-prepared nanowire samples were likely to be polycrystalline. Nonetheless, measured *d* spacings could be indexed to the (111) plane.

By analogy, the morphologies of as-prepared, one-dimensional Au (diameter, 220 ± 25 nm; length, 4.5 ± 1 μm) and Pt (diameter, 200 ± 20 nm; length, 3.5 ± 1.5 μm) nanostructure samples are shown in Figures 6.3 and 6.4, respectively. The overall diameters of these samples are in agreement with those of the template pore size, implying diameter control of these materials is achievable merely by using templates of the appropriate pore dimension.

Figure 6.3a shows the presence of isolated Au nanowires, whereas parts b and c of Figure 6.3 highlight top and tilt views of the corresponding arrays, obtained after removal of the PC template, on a double-sided carbon tape surface, immobilized onto a SEM stub. The EDS spectrum (Figure 6.3d) on dispersed, isolated nanowire samples denotes the presence of Au, as expected, with the Si signal emanating from the underlying Si wafer used for imaging. The TEM (Figure 6.3e) and HRTEM image (Figure 6.3f) with its associated SAED pattern (inset to Figure 6.3f) revealed that the as-prepared nanowire samples were likely polycrystalline. Diffraction spots could be indexed to the (111), (220), (222), and (420) planes, and the measured *d* spacing of 0.230 nm could be assigned to the (111) plane.

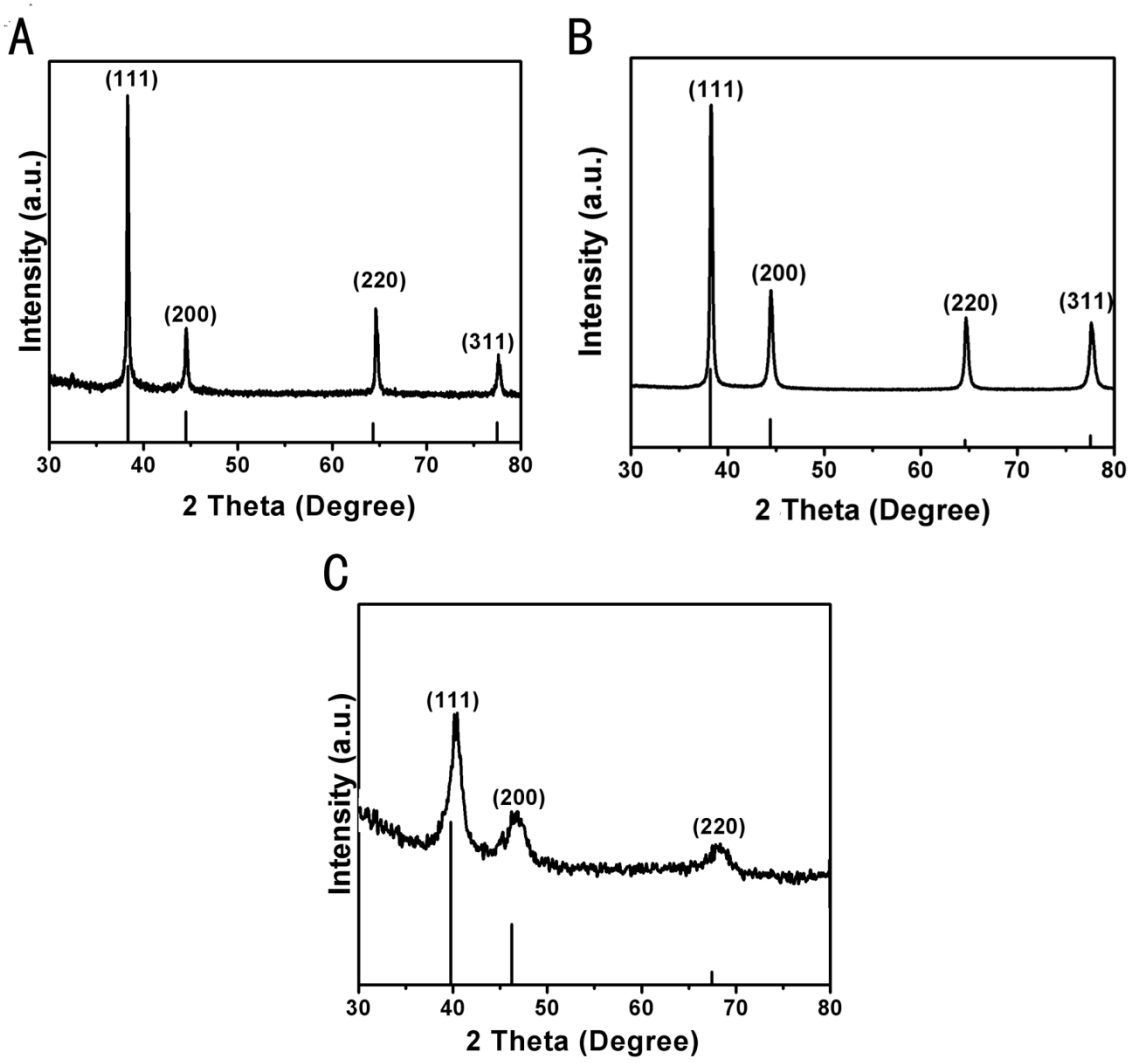

Figure 6.1 XRD patterns of as-prepared samples: (a) Ag nanowires, (b) Au nanowires, and (c) Pt 1-D nanostructures. Representative diffraction patterns (upper half) and the corresponding standard JCPDS diffraction patterns (lower half) for each of the samples are shown in each part.

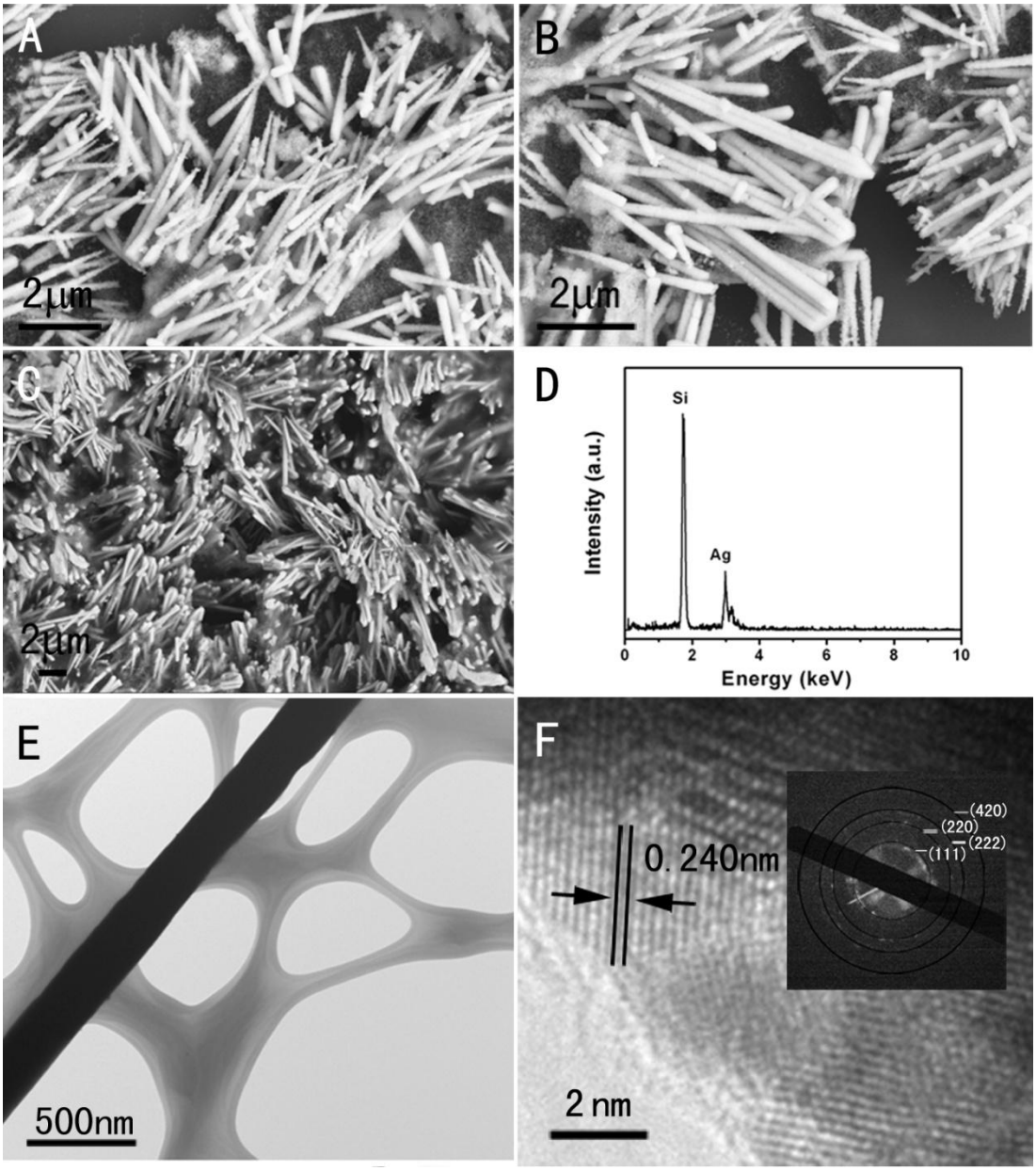

Figure 6.2 SEM images of (a-b) isolated Ag nanowires and of (c) Ag nanowire arrays upon removal of the template. Representative EDS pattern (d) of as-prepared Ag nanowires and arrays. Corresponding TEM (e) and HRTEM (f) images as well as associated SAED pattern (inset) of Ag nanowires.

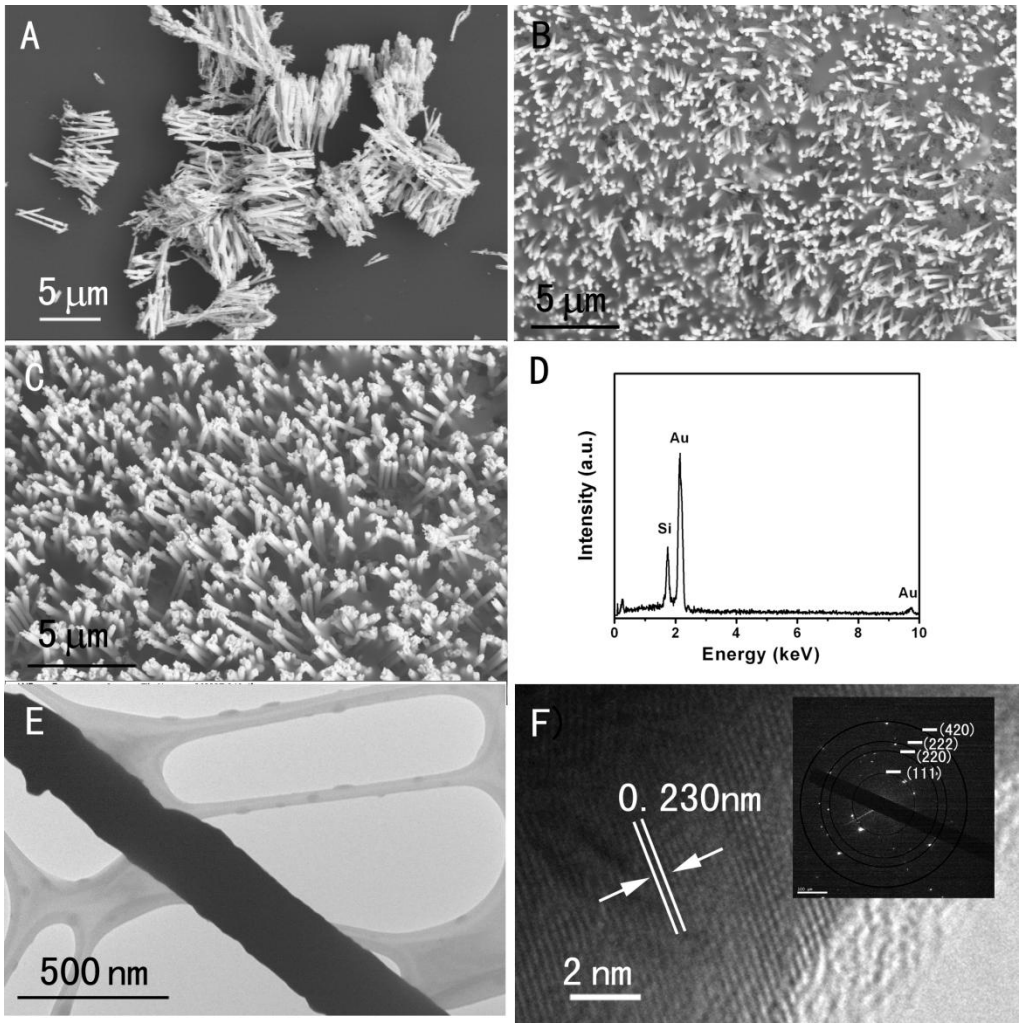

Figure 6.3 SEM images of (a) isolated Au nanowires and of (b-c) Au nanowire arrays after removal of the template. Representative EDS pattern (d) of as-prepared Au nanowires and arrays. Corresponding TEM (e) and HRTEM (f) images as well as associated SAED pattern (inset) of Au nanowires.

Although a similar procedure was used to generate all three noble metal nanostructures, at times, a mixture of Pt nanotubes and nanowires was obtained, by contrast with what we observed with Ag and Au. While Figure 6.4a clearly depicts individual nanostructures, the SEM images of parts b and c of Figure 6.4, representing tilt and top views of as-prepared arrays, are consistent with the presence of hollow tubes with a wall thickness of 30 ± 3 nm. The EDS spectrum (Figure 6.4d) indicates the presence of Pt, as expected, with the Si signal emanating from the underlying Si wafer used for imaging. By contrast, the low-magnification TEM image in Figure 6.4e is suggestive of the formation of Pt nanowires. The coexistence of both hollow and solid filled structures has also been observed in Pt samples generated from 50 nm pore-sized PC templates. In effect, both nanotubes and nanowires, representing different stages of Pt nanostructure growth, were observed and are denoted by the red and blue arrows, respectively, in Figure 6.5. We also measured a diameter range for these nanostructures of around 60 ± 10 nm, confirming our assertion that size control can be easily achieved merely by using templates with desired pore sizes. Finally, the HRTEM image (Figure 6.4f) with its associated SAED pattern (inset to Figure 6.4f) on an individual nanowire motif revealed that the as-prepared nanostructure samples were likely polycrystalline in nature. Diffraction spots could be indexed to the (111), (220), (311), and (331) planes, and the measured *d* spacing could be assigned to the (111) plane.

Why the presence of tubes? Tube formation has been previously explained elsewhere.[39] Essentially, it is believed that this observation is a result of stronger interactions between reagent molecules and the template pore walls in the case of Pt vs between the reagent molecules themselves as in the case of Ag and Au, resulting in different nucleation steps (i.e., heterogeneous vs homogeneous, yielding hollow tubes vs filled rods) for the corresponding processes. This preferential confinement of growth to the inherent geometry of the pore walls can therefore lead to the generation of primarily tubelike motifs. It should be mentioned, though, that with continued reaction, nanowire formation can be obtained as simply a lateral thickening of the tubular structure, which, as further supply of precursors to the inside is blocked by the ever-growing tube thickness coupled with an ever-decreasing inner tube diameter, eventually constricts the entire porous interior of the template, filling it completely. Hence, Pt nanowires would be considered as the ultimate extension of nanotube growth, at least in terms of its width. We have confirmed the validity of this hypothesis by additional experiments in which we have shown that independent increases in either Pt precursor concentration (from 0.05 to 0.2 M) or reaction temperature (from 0 to 50 °C) will increasingly favor nanowire production.

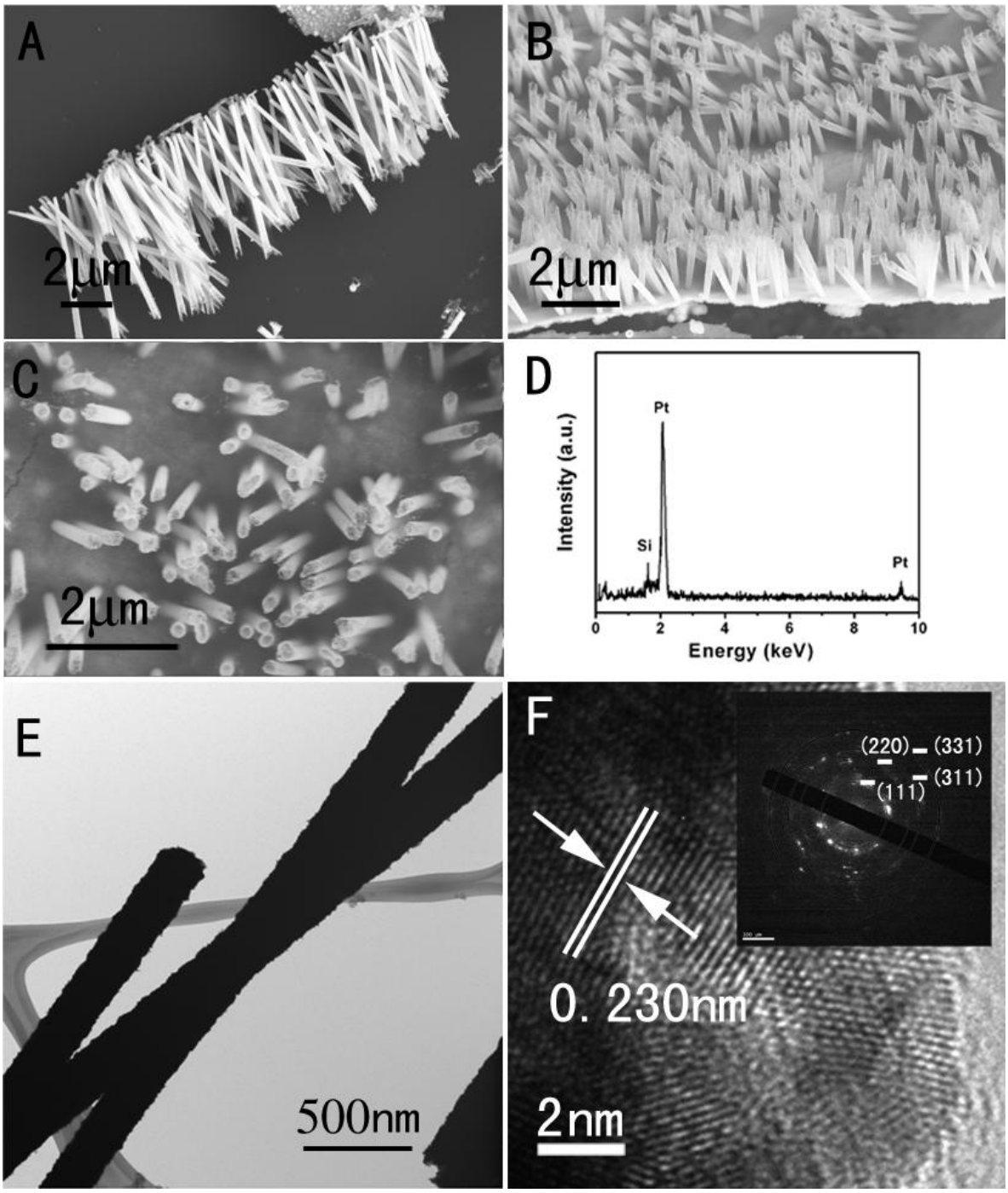

Figure 6.4 SEM images of (a) isolated Pt nanotubes and (b-c) Pt nanotube arrays after removal of the template. Representative EDS pattern (d) of as-prepared Pt nanowires and arrays. Corresponding TEM (e) and HRTEM (f) images and associated SAED pattern (inset) of Pt nanowires.

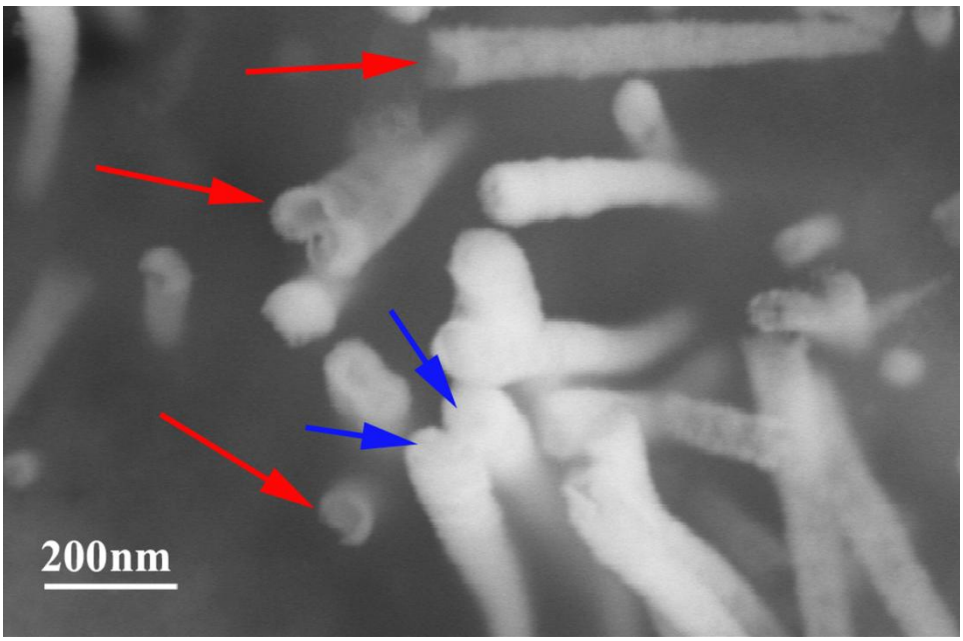

Figure 6.5 SEM images of both isolated Pt nanotubes (red arrows) and Pt nanowires (blue arrows), measuring ~60 nm in diameter, after removal of the template.

There is precedence for this explanation in the concurrent synthesis of TiO_2 nanotubes and nanowires within AAO templates.[40] Moreover, a similar explanation[41] has been advocated for the electrochemical production of highly ordered Pt nanotube arrays within a porous anodic alumina template, where it was postulated that the presence of a higher concentration of $[PtCl_6]^{2-}$ and therefore a correspondingly increased growth rate of Pt along the surfaces of the pore walls led to the observed structural motif; in this scenario, a longer reaction time ultimately led to the production of wires.

The UV-visible spectra of metal nanowire sols collected in $CHCl_3$ are shown in Figure 6.6. The optical properties of metal nanostructures are dominated by surface plasmon resonances due to collective oscillations of electrons in the conduction band that are excited by light of appropriate frequencies.[34] The measured resonance wavelength is dependent on a number of factors including particle shape, the nature of the surrounding medium, particle size, as well as interparticle interactions.[38, 42] Representative absorption spectra for Ag and Au are shown in parts a and b of Figure 6.6 and agree with a previous report on these systems[38] in terms of the broadness and asymmetry of the as-obtained profiles, which has been partially attributed to sample polydispersity. The λ_{max} values for our Ag and Au nanowires herein are 413 and 570 nm, respectively, which are somewhat red-shifted as compared with prior results[38] on metal nanowires with similar aspect ratios but with smaller diameters (i.e., 40 and 90 nm). Nonetheless, this observed red shift has been previously ascribed to the presence of aggregation and coalescence[43-46] in addition to intrinsic size effects.[42] The absorption spectrum of Pt nanoscale samples (Figure 5c) is relatively featureless and weak in the 300-900 nm region presented in agreement with literature[47] but can be explained by the fact that the surface plasmon excitation of Pt is expected at around 270 nm.

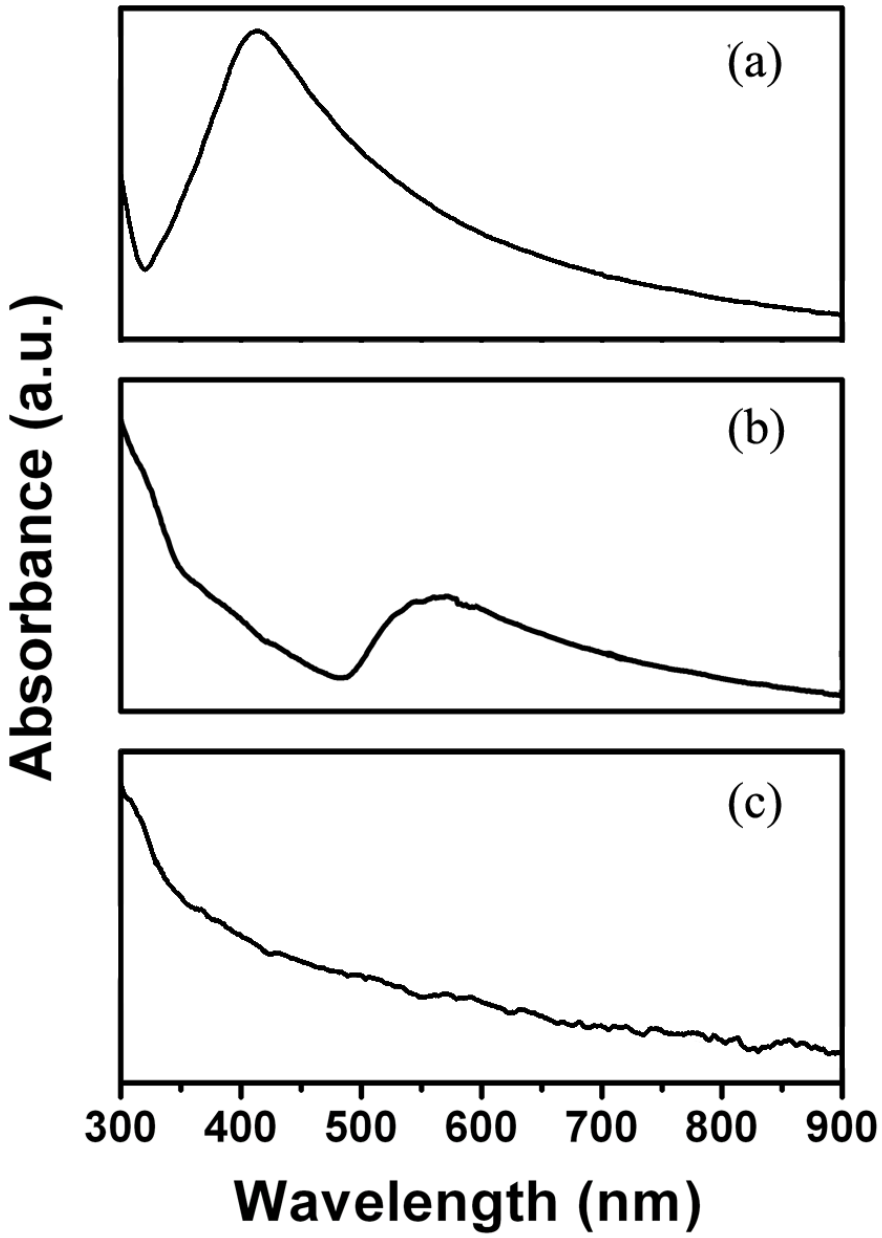

Figure 6.6 UV-visible absorption spectra of 1-D (a) Ag, (b) Au, and (c) Pt nanostructured samples.

Platinum metal and platinum alloys are the best available electrocatalysts for the ORR, which is a key cathodic reaction in electrochemical energy conversion processes (e.g., in fuel cells and batteries). Figure 6 shows the cyclic voltammetry and ORR activity for 1-D Pt nanostructures loaded on a RDE in 0.1 M $HClO_4$ solution. Results for Pt nanoparticles (8 nm) that were obtained under identical conditions are also shown in Figure 6.6 for comparison. To adequately evaluate the intrinsic ORR activity of our Pt catalysts, the measured kinetic currents were normalized to the real surface areas (19.5 and 6.5 cm^2 for our Pt nanoparticles and 1-D nanostructures, respectively) of our catalysts. On the basis of this analysis, the bar graph (inset to Figure 6.7) clearly shows that the Pt 1-D nanostructures possess a higher ORR specific surface area activity as compared with that of the Pt nanoparticles alone. In fact, the observed enhancement is a factor of 2. The enhanced ORR catalytic activity on Pt 1-D nanostructures with respect to nanoparticles could be due to a host of factors including changes in structural geometry, the presence of lower surface defects, the preferential exposure of certain crystal facets,[48] as well as to the differing surface electronic properties of these nanomaterial motifs, specifically with respect to the large fraction of surface atoms with a high degree of coordination in the 1-D structure. As a consequence, oxidation of this surface is shifted positively by comparison with nanoparticles, thereby facilitating faster kinetics of the ORR.[49, 50] Our results reported herein are in strong agreement with a prior report.[48]

Because the specific activity for the ORR on Pt is highly structure sensitive, we should note that it is approximately an order of magnitude lower for 2 nm particles as compared with that on either a Pt(111) electrode or a Pt monolayer on a Pd(111) surface.[51] Atomically smooth Pt surfaces, with a small number of low-coordination atoms, are more active than surfaces with a high concentration of such sites because of the reduced interaction with OH and O species at high potentials, which block the O_2 reduction reaction.[51, 52] Figure 6.8 shows the corresponding cyclic voltammetry data and ORR activity for Au and Ag nanowires in the presence of 0.1 M KOH. Silver and gold can be useful catalysts for the ORR in alkaline solutions. For example, Adzic et al.[53] have shown that the ORR activity on Au single crystal surfaces is highly structure dependent. Specifically, the Au(100) surface was found to be the most active electrode in alkaline media. In our case, the Au nanowires showed quite good ORR activity, although it maintained predominantly the (111) structure, suggestive again of the unique surface electronic properties of the 1-D metallic nanostructures.

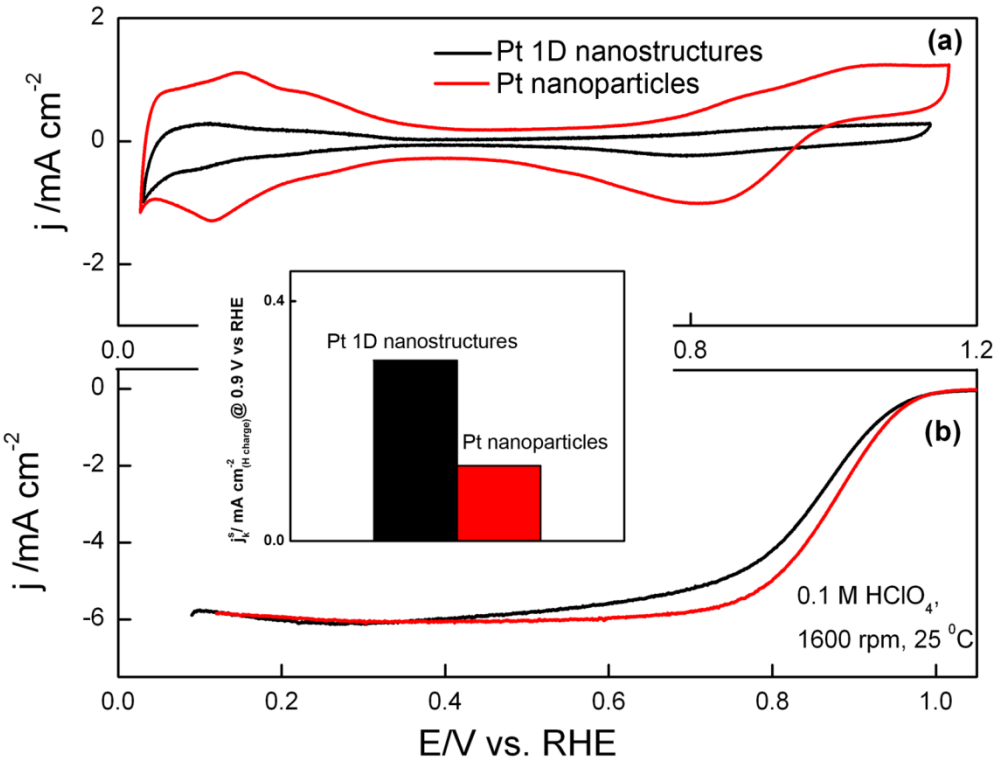

Figure 6.7 (a) Cyclic voltammograms for Pt nanoparticles (8 nm in diameter) and Pt 1-D nanostructures in the presence of 0.1 M $HClO_4$ with a scan rate of 50 mV/s. (b) Polarization curves of Pt nanoparticles (8 nm) and Pt 1-D nanostructures in the presence of 0.1 M $HClO_4$ at room temperature. Rotating speed, 1600 rpm; scan rate, 10 mV/s. Inset: A comparison of ORR specific activities in RDE measurements for these two samples in the presence of 0.1 M $HClO_4$ at room temperature. The kinetic current densities at 0.9 V were normalized to real surface areas derived from the H charge.

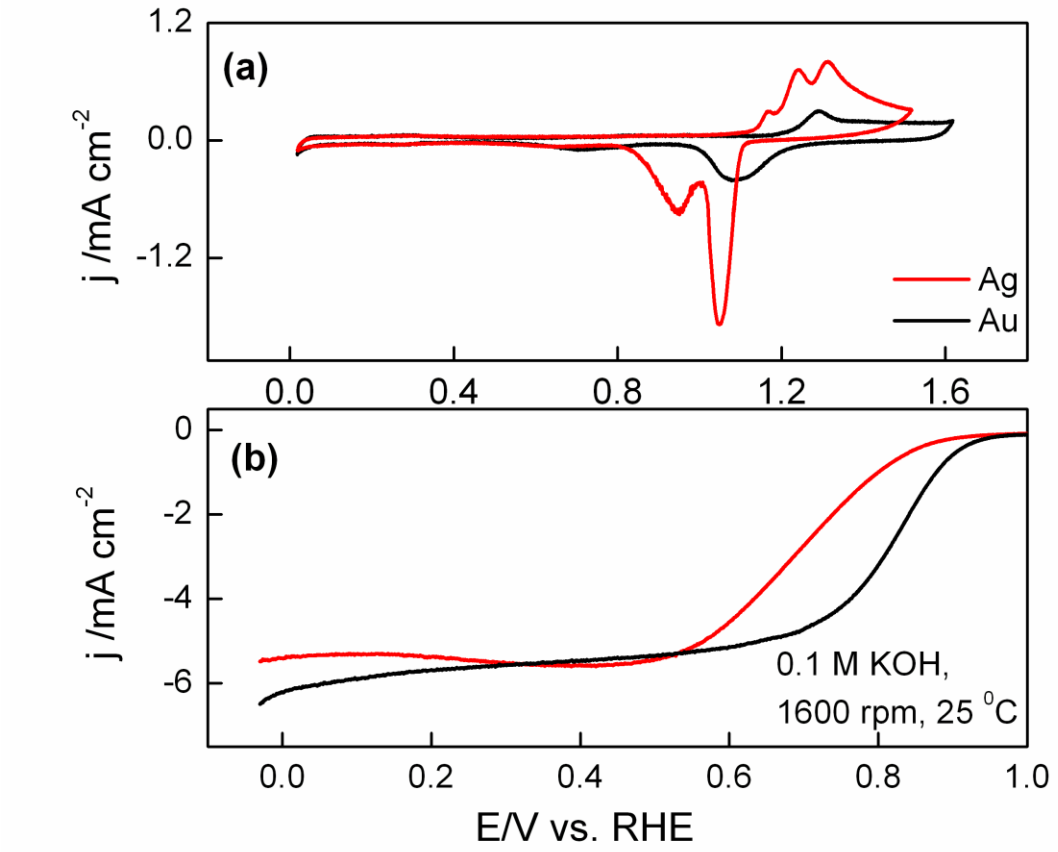

Figure 6.8 (a) Cyclic voltammograms for Au (black line) and Ag (red line) nanowires in 0.1 M KOH with a scan rate of 50 mV/s. (b) Polarization curves of Au (black line) and Ag (red line) nanowires in 0.1 M KOH at room temperature. Rotating speed, 1600 rpm; scan rate, 10 mV/s.

6.4 Conclusions

In conclusion, crystalline one-dimensional metal nanowires and arrays of controllable morphology, shape, size, and composition have been generated using an ambient, surfactantless synthesis technique. As-prepared samples have been tested as electrocatalysts for the ORR. Pt 1-D nanostructures were found to possess a higher ORR specific surface area activity as compared with that of the Pt nanoparticles alone. Ag and Au nanowires also evinced reasonable ORR activity in alkaline solution. Our results are expected to assist in designing better electrode materials for fuel cell applications. The synthesis technique is likely generalizable to the fabrication of other 1-D metallic nanomaterials, such as Pd, Rh, and Ru, and will therefore benefit research into the shape-dependent properties of metallic nanomaterials.

6.5 References

1. Cheng, S.-F.; Chau, L.-K. *Anal. Chem.* **2003**, 75, 16.
2. Gates, A. T.; Fakayode, S. O.; Lowry, M.; Ganea, G. M.; Murugeshu, A.; Robinson, J. W.; Strongin, R. M.; Warner, I. M. *Langmuir* **2008**, 24, 4107.
3. Hunyadi, S. E.; Murphy, C. J. *J. Mater. Chem.* **2006**, 16, 3929.
4. Leong, W. L.; Lee, P. S.; Mhaisalkar, S. G.; Chen, T. P.; Dodabalapur, A. *Appl. Phys. Lett.* **2007**, 90, 042906-1.
5. Mitsudome, T.; Mikami, Y.; Funai, H.; Mizugaki, T.; Jitsukawa, K.; Kaneda, K. *Agew. Chem.* **2008**, 47, 138.
6. Thomas, J. M. *Pure Appl. Chem.* **1988**, 60, 1517.
7. Zhang, J.; Sakaki, K.; Sutter, E.; Zdzic, R. R. *Science* **2007**, 315, 220.
8. Pina, C. D.; Falletta, E.; Rossi, M. *Nanopart. Catal.* **2008**, 427.
9. Murphy, C. J.; Gole, A. M.; Hunyadi, S. E.; Orendorff, C. J. *Inorg. Chem.* **2006**, 45, 7544.
10. Keebaugh, S.; Kalkan, A. K.; Nam, W. J.; Fonash, S. J. *Electrochem. Solid-State. Lett.* **2006**, 9, H88.
11. Liu, Z.; Searson, P. C. *J. Phys. Chem. B* **2006**, 110, 4318.
12. Cusmà, A.; Curulli, A.; Zane, D.; Kaciulis, S.; Padeletti, G. *Mater. Sci. Engin. C* **2007**, 27, 1158.
13. Basu, M.; Seggerson, S.; Henshaw, J.; Jiang, J.; Cordona, R. d. A.; Lefave, C.; Boyle, P. J.; Miller, A.; Pugia, M.; Basu, S. *(GNWA). Glycoconj. J.* **2004**, 21, 487.
14. Wirtz, M.; Yu, S.; Martin, C. R. *Analyst* **2002**, 127, 871.
15. Pang, Y. T.; Meng, G. W.; Fang, Q.; Zhang, L. D. *Nanotechnology* **2003**, 14, 20.
16. Jeong, D. H.; Zhang, Y. X.; Moskovits, M. *J. Phys. Chem. B* **2004**, 108, 12724.
17. Seo, B. I.; Shaislamov, U. A.; Kim, S.-W.; Kim, H.-K.; Hong, S. K.; Yang, B. *Physica E* **2007**, 37, 279.
18. Husain, A.; Hone, J.; Postma, H. W. C.; Huang, X. M. H.; Drake, T.; Barbic, M.; Scherer, A.; Roukes, M. L. *Appl. Phys. Lett.* **2003**, 83, 1240.
19. Jana, N. R.; Gearhart, L.; Murphy, C. J. *Adv. Mater.* **2001**, 13, 1389.
20. Jana, N. R.; Gearhart, L.; Murphy, C. J. *J. Phys. Chem. B* **2001**, 105, 4065.
21. Jana, N. R.; Gearhart, L.; Murphy, C. J. *Chem. Commun.* **2001**, 617.
22. Jana, N. R.; Gearhart, L.; Murphy, C. J. *Chem. Mater.* **2001**, 13, 2313.

23. Gai, P. L.; Harmer, M. A. *Nano Lett.* **2002**, 2, 771.
24. Xu, C.; Varghese, L.; Irudayaraj, J. *Langmuir* **2007**, 23, 9114.
25. Sun, Y.; Gates, B.; Mayers, B.; Xia, Y. *Nano Lett.* **2002**, 2, 165.
26. Sun, Y.; Xia, Y. *Adv. Mater.* **2002**, 14, 833.
27. Shen, Z.; Yamada, M.; Miyake, M. *Chem. Commun.* **2007**, 245.
28. Lee, E. P.; Peng, Z.; Cate, D. M.; Yang, H.; Campbell, C. T.; Xia, Y. *J. Am. Chem. Soc.* **2007**, 129, 10634.
29. Wroblowa, H.; Pan, Y. C.; Razumney, J. *J. Electroanal. Chem.* **1976**, 69, 1465.
30. Lee, J.-W.; Popov, B. N. *J. Solid State Electrochem.* **2007**, 11, 1355.
31. Garcıa-Contreras, M. A.; Fernandez-Valverde, S. M.; Vargas-Garcıa, J. R. *J. Alloys Compd.* **2007**, 434-435, 522.
32. Gong, K.; Du, F.; Xia, Z.; Durstock, M.; Dai, L. *Science* **2009**, 323, 760.
33. Waszczuk, P.; Barnard, T. M.; Rice, C.; Masel, R. I.; Wieckowski, A. *Electrochem. Commun.* **2002**, 4, 599.
34. Murphy, C. J.; Gole, A. M.; Hunyadi, S. E.; Stone, J. W.; Sisco, P. N.; Alkilany, A.; Kinard, B. E.; Hankins, P. *Chem. Commun.* **2008**, 544.
35. Chattopadhyay, S.; Shi, S. C.; Lan, Z. H.; Chen, C. F.; Chen, K.-H.; Chen, L.-C. *J. Am. Chem. Soc.* **2005**, 127, 2821.
36. Rex, M.; Hernandez, F. E.; Campiglia, A. D. *Anal. Chem.* **2006**, 78, (445-451).
37. Chen, Z.; Waje, M.; Li, W.; Yan, Y. *Angew. Chem. Int. Ed.* **2007**, 46, 4060.
38. Cepak, V. M.; Martin, C. R. *J. Phys. Chem. B* **1998**, 102, 9985.
39. Zhou, H.; Wong, S. S. *ACS Nano* **2008**, 2, 944.
40. Cochran, R. E.; Shyue, J.-J.; Padture, N. P. *Acta Mater.* **2007**, 55, 3007.
41. Zhao, Y.; Guo, Y.-G.; Zhang, Y.-L.; Jiao, K. *Phys. Chem. Chem. Phys.* **2004**, 6, 1766.
42. Liz-Marz án, L. M. *Langmuir* **2006**, 22, 32.
43. Garrell, R. L.; Schultz, R. H. *J. Colloid Interface Sci.* **1985**, 105, 483.
44. Antonietti, M.; Thunemann, A.; Wenz, E. *Colloid Polym. Sci.* **1996**, 274, 795.
45. Wang, W.; Efrima, S.; Regev, O. *Langmuir* **1998**, 14, 602.
46. Satoh, N.; Hasegawa, H.; Tsujii, K.; Kimura, K. *J. Phys. Chem.* **1994**, 98, 2143.
47. Fu, X.; Wang, Y.; Wu, N.; Gui, L.; Tang, Y. *J. Mater. Chem.* **2003**, 13, 1192.
48. Sun, S.; Jaouen, F.; Dodelet, J.-P. *Adv. Mater.* **2008**, 20, 3900.
49. Mayrhofer, K. J. J.; Strmcnik, D.; Blizanac, B. B.; Stamenkovic, V.; Arenz, M.; Markovic, N. M. *Electrochimica Acta* **2008**, 53, 3181.
50. Takasu, Y.; Ohashi, N.; Zhang, X. G.; Murakami, Y.; Minagawa, H.; Sato, S.; Yahikozawa, K. *Electrochimica Acta* **1996**, 41, 2595.
51. Zhang, J. L.; Vukmirovic, M. B.; Xu, Y.; Mavrikakis, M.; Adzic, R. R. *Angew. Chem. Intl. Ed.* **2005**, 44, 2132.
52. Wang, J. X.; Zhang, J.; Adzic, R. R. *J. Phys. Chem. A* **2007**, 111, 12702.
53. Adzic, R. R.; Strbac, S.; Anastasijevic, N. *Mater. Chem. Phys.* **1989**, 22, 349-375.

Chapter VII Incorporation of nanoparticles into nanotubes – creation of multifunctional SiO_2 nanotubes

7.1 Introduction

In the previous chapter, materials we synthesized were all single component materials. In this chapter, we will discuss a multifunctional nanostructure created by incorporation of CdSe quantum dots and Fe_3O_4 nanoparticles into a SiO_2 nanotubes matrix. The resulting nanostructure maintains all functionality of its constituent components.

7.1.1 Application of semiconductor QDs in biology

There are many points of intersection between nanoscience, nanotechnology and the biological sciences. Sensing and imaging the biological systems by inorganic nanomaterials, mainly semiconductors and metals, is one of them.[1]

Advances in synthesis and biofunctionalization of colloidal semiconductor nanocrystals during the past decade have generated an increasingly widespread interest among investigators in the fields of biology and medicine.[2-5] These nanometer-sized semiconductorsare also called quantum dots. A typical example is CdSe quantum dots.

CdSe quantum dots exhibit distinctive size-dependent energy levels. As the size increases, the energy gap decreases. Extensive optical tunability, from ultraviolet to infrared,[6] can be achieved by varying the size and the composition of QDs, enabling simultaneous examination of multiple molecules and events.

As Compared with organic fluorophores, the most commonly used probes in cell biology, QDs have several advantages. First, organic dyes typically have narrow absorption spectra, meaning a relatively narrow window of excitation wavelengths. Moreover, they maintain asymmetric emission spectra broadened by a red-tail. By contrast, QDs have a broad absorption spectra enabling excitation by a wide range of wavelengths. Furthermore, their emission spectra are symmetric and narrow. Secondly, QDs are also very stable light emitters due to their inorganic composition, which makes them less susceptible to photobleaching than organic dye molecules.[3, 6] Thirdly, the two-photon cross-section of QDs is significantly higher than that of organic dyes, making them well suited for examination of thick specimens and in vivo imaging.[7-9] Their last advantage is associated with the fluorescence lifetime of 10 to 40 ns of QDs, compared with the order of a few nanoseconds for organic dyes.[3, 10, 11] This can greatly reduce levels of background noise for an image by using QD labels combined with pulsed laser and time-gated detection.

In the past six years, there has been tremendous progress in the synthesis and optimization of QDs for biological environments which have opened the doors to an expanding variety of diverse biological applications, such as serving as specific markers for cellular structures, and molecules, tracing cell lineage, monitoring physiological events in live cells, measuring cell motility, as well as tracking cells in vivo.

7.1.2 Application of magnetic nanoparticles in biology

Magnetic nanoparticles have been synthesized with a number of different compositions and phases, including iron oxides,[12-14] such as Fe_3O_4, and γ-Fe_2O_3, pure metals,[15, 16] such as Fe and Co, spinel-type ferromagnets,[17, 18] such as $MgFe_2O_4$, $MnFe_2O_4$, and $CoFe_2O_4$, as well as alloys[19, 20] such as $CoPt_3$ and FePt.

In terms of biotechnology and biomedicine, magnetic separation can be used as a quick and simple method for the efficient and reliable capture of specific proteins or other biomolecules. Most particles used for this purpose are superparamagnetic, when their size is small enough that each of them is a single magnetic domain, meaning that they can magnetized with an external magnetic field and immediately redispersed when the magnet is removed. For example, magnetic iron oxide nanoparticles functionalized with dopamine have been used for protein separation.[21]

Magnetic nanoparticles can also be used as drug carriers in drug delivery. This is also refered to as "magnetic drug delivery".[22] In the presence of magnetic nanoparticles, drug molecules can be guided to a chosen site under the localized magnetic field gradients, held there until the therapy is complete, and then removed. The strategy has the potential to carry a large dose of drug to achieve high local concentrations, and hence to avoid toxicity and other adverse side effects arising from high drug doses in other parts of the organism.

Another interesting application of magnetic nanoparticles is in hyperthermia treatment which is considered as a supplementary treatment to chemotherapy, radiotherapy, and surgery in cancer therapy.[23, 24] Once magnetic nanoparticles are exposed to a varying magnetic field, heat is generated by mass of magnetic hysteresis loss, Néel-relaxation, and Brown-relaxation mechanisms.[25]

Magnetic iron oxide nanoparticles have also been extensively studied and used as magnetic resonance imaging (MRI) contrast agents. The basic principle of MRI is based on nuclear magnetic resonance (NMR) together with the relaxation of proton spins in a magnetic field. [26] A strong magnetic field is first applied to align the spins, wherein the process is subjected to a specified frequency. When a "resonance" frequency in the radio-frequency (RF) range is introduced to the nuclei, the protons absorb energy and are excited to another state. After the disappearance of the RF pulse, the excited nuclei relax to their initial, lower-energy state. There are two different relaxation pathways, called longitudinal (T_1) relaxation and transverse (T_2) relaxation respectively. Commercially available T1 contrast agents are usually paramagnetic complexes. T_2 contrast agents are based on iron oxide nanoparticles, which are the most representative nanoparticulate agents. They can effectively shorten T_2* relaxation times in the liver, spleen, and bone marrow by means of selective uptake and accumulation.[27]

7.1.3 Silica nanotubes

Hollow inorganic nanotubes are attracting a great deal of attention due to their fundamental significance and potential applications in bioanalysis and catalysis.[28] Among them, silica nanotubes have attracted special interest because of their ease of fabraication, hydrophilic nature, ease of colloidal suspension formation, and surface functionalization accessibility for both outer and inner walls.[29]

Recently, modified silica nanotubes have shown potential applications in the biological field. For example, Lee et al. created magnetic nanotubes by forming a layer of magnetite nanoparticles on the inner surface of silica nanotubes.[30] These nanotubes can be used for magnetic-field-assisted bioseparation, biointeraction, and drug delivery. Martin et al. created smart nanotubes for bioseparations and biocatalysis by differentially functionalizing silica nanotubes.[31]

7.1.4 Current work

Due to their relatively comparable size to biological systems, biologically functionalized nanoparticles have been widely used for a host of biomedical applications such as biolabeling, imaging, tumor targeting, diagnostics, optical sensing, biosensors, protein detection, drug delivery, and contrast enhancement in MRI. [32-37] However, to achieve adequate control over size, composition, and crystal structure, the synthesis of these nanoparticles frequently occurred under non-aqueous reaction conditions. Hence, the as-prepared nanoparticles are often coated with a monolayer of hydrophobic surfactant molecules.[38-40] This makes it difficult to use bare nanoparticles for *in vivo* biomedical applications.

To be biologically active, nanoparticles need to be surface functionalized not only to be water-soluble and buffer-stable, but also to provide sites for subsequent functional conjugation with biological moieties. Among many methods to achieve this objective (i.e., ligand exchange and cross-coupling reactions), the use of a silica shell coating has become one of the more popular strategies.

Recently, a lot of papers have reported multifunctional silica composite fornation. Silica beads were often used as outer shell materials or the substrate. Moreover, these functional materials usually involved both magnetic and luminescent materials. These materials initially consisted of mostly organic complexes, such as Prussian Blue (magnetic) and lanthanide Tb(III)/Sm(III) (luminescent).[41] Soon inorganic nanoparticles found use in this field because of their unique size and shape dependent properties. For example, magnetic properties, such as blocking temperature, coercivities, and magnetization values in magnetite NPs, have been found to depend on size.[42] As compared with organic dyes, QDs offer high photostability, good fluorescence efficiency, broad excitation spectra, narrow emission band-widths with emission wavelengths directly correlated with particle sizes, and finally, a large two-photon absorption cross-section.

As compared with a vast amount of reports for the production of multifunctional silica beads, reports of their 1D analogues have been significantly lower. As discussed in

7.1.3, silica nanotubes are ideal for biological applications. Silica is relatively nontoxic and biocompatible. Nanotubes possess inner voids that can be filled in with a variety of species ranging in size from large proteins to small molecules. Their inner and outer surfaces can be differentially functionalized. Moreover, the diameter of tubes can be precisely controlled by the template technique.

In the current work, we inserted pre-formed, monodisperse magnetic Fe_3O_4 NPs and luminescent CdSe QDs into the inner surface, preferentially functionalized by a hydrophobic coating, of a silica nanotube template through non-covalent interactions. This 'insertion' reaction did not involve either ligand exchange, strong acid/strong base, or high-temperature steps. Our as-created 1D silica nanocomposite possessed not only the distinctive magnetic profile of Fe_3O_4 but also the desirable optical signature of CdSe. Furthermore, the structural integrity of these functional nanoparticles was preserved and retained within the silica nanotube's outer shell, thereby offering a protective layer against local environmental influences. What is even more intriguing is that the outer silica surface could itself act as a reactive platform with which to graft an additional moieties, such as biomolecules. Finally, our silica nanotube constructs are reasonably monodisperse in size and shape, which is sometimes difficult to achieve in the synthesis of as-prepared magnetic, luminescent silica beads.

7.2 Experimental Section

7.2.1 Preparation

The synthesis route is depicted in Figure 7.1. The SiO_2 nanotubes were prepared by a previously described sol-gel template method.[43] Briefly, AAO membranes possessing uniform, cylindrical 200 nm diameter pores were used as templates for the fabrication of our 1D nanomaterials. An initial silica sol solution was produced by mixing TEOS, H_2O, ethanol, and HCl in a molar ratio of 1:4:20:0.03. The AAO membrane was then immersed in the sol for 1 hour. After drying at room temperature for 1 day, the silica gel-containing template was annealed at 400 ℃ for 24 h so as to finally yield silica nanotubes within the AAO pores. This annealing step at 400 ℃ cannot be neglected. It is very important in selectively removing the AAO template in subsequent steps. To functionalize the interior walls of the silica nanotubes with a hydrophobic surface, the silica nanotube-alumina membrane composite was immersed for 30 min in a 5% n-octadecyltrichlorosilane (OTS) solution (vol/vol) in hexane.[44] In this process, silane molecules would primarily attach to the inner silica tube surface, due to steric reasons. The external silica wall was itself in direct contact with the alumina pore channel as determined by sol-gel processing. This presence of a hydrophobically tuned interior was thereafter necessary in order to facilitate the incorporation of a significantly higher percentage of subsequently added nanoparticles than otherwise would have been expected by taking advantage of the capillary effect alone.

In our current synthesis, CdSe QDs and Fe_3O_4 NPs were synthesized following a previous protocal.[45, 46] Both CdSe and Fe_3O_4 as-prepared nanoparticles were precipitated by ethanol and re-dispersed in cyclohexane, a lower boiling point solvent, which could be more easily be removed compared with 1-octadecene, solvent used in the synthesis of

CdSe QDs and Fe_3O_4 NPs. TEM images of them are shown in Figure 7.2. Sizes are 3-4 nm for CdSe and 12-15 nm for Fe_3O_4, respectively.

Upon washing in hexane in order to remove excess OTS, our as-formed silica nanotube-alumina membrane composite was initially immersed into a cyclohexane solution containing CdSe QDs (10 mM) for 1 day. Then after washing with cyclohexane to remove unbound CdSe QDs, the membrane composite was immersed into a cyclohexane solution containing NPs (100 mM) for 24 h. The precise sequence of immersion for the silica nanotube-alumina template composite with respect to the individual solutions containing the QDs and NPs could be interexchanged, without significant alteration in the resultant product. Finally, the composite was washed with cyclohexane and dried at room temperature for 1 day, prior to removal of the alumina template itself.

AAO can be etched in either strong acidic or strong basic solution. However, Fe_3O_4 NPs incorporated in the silica pores would also dissolve in acidic solution. Moreover, the high pH solution would attack not only AAO but also the silica nanotubes themselves. Hence, we did several experiments varying, annealing temperature, concentration of NaOH solution and immersion time. The best conditions consisted of annealing at 400 ℃ followed by immersion in 1.25 M NaOH for 1.5 h. The resistance of silica nanotubes to NaOH removal was increased by annealing at 400 ℃ so that silica nanotubes were barely attacked by NaOH even after 1.5 h immersion in NaOH solution. Meanwhile, the AAO template itself was almost removed by NaOH solution. Hence our nanotube samples were obtained by selectively removing the template.

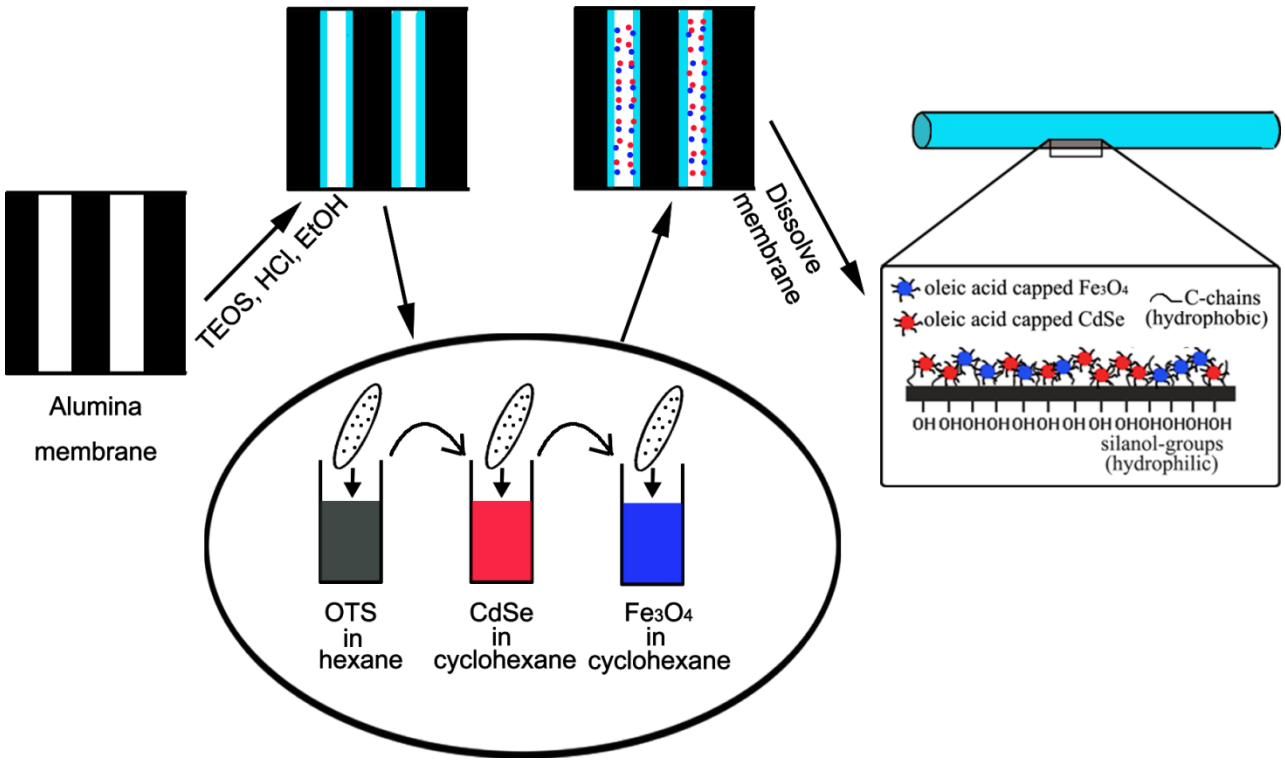

Figure 7.1 Synthesis route for the creation of multifunctional silica-encapsulated composite nanostructures

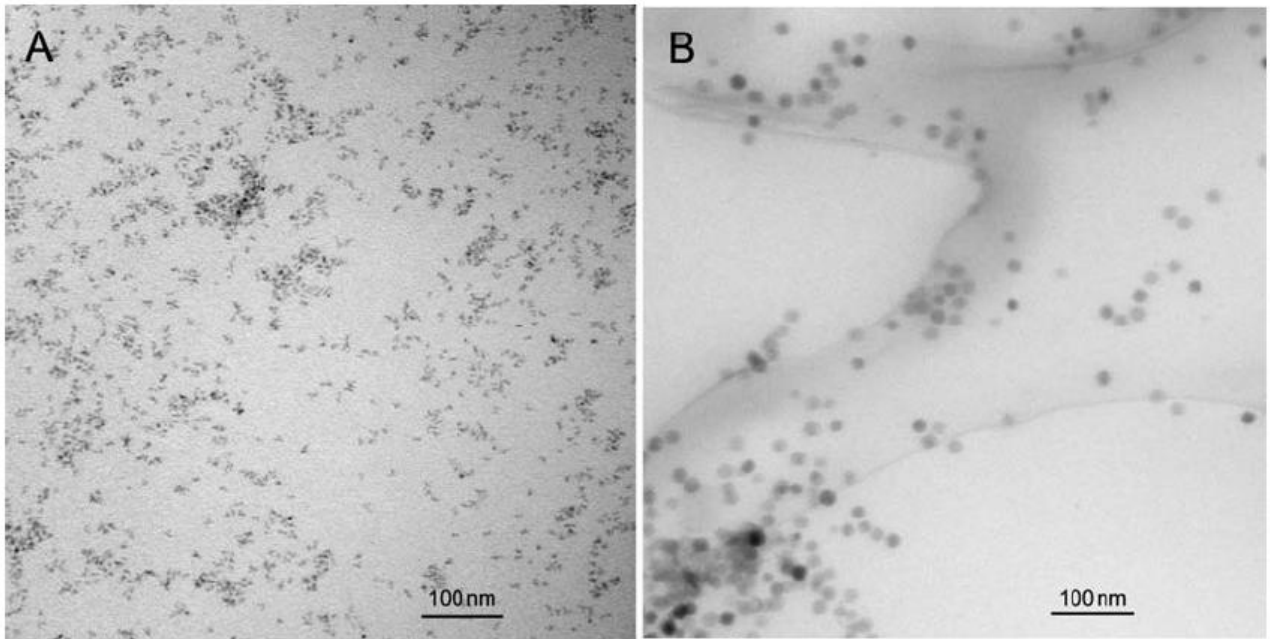

Figure 7.2 TEM images of as-prepared (A) CdSe QDs and (B) Fe_3O_4 NPs.

Silica-encapsulated composite samples were collected either by centrifugation or through a combination of magnetic separation, washing, and drying steps. Figure 3 highlights the importance of the OTS treatment of the silica nanotube-AAO membrane composite. In the derivatized analogues, we have a clear visual confirmation of nanoparticle inclusion upon immersion of the composite into the colored nanoparticle solutions. Conversely, use of an unmodified silica-encapsulated composite yields results that resemble control experiments, wherein little discoloration (and therefore nanoparticle incorporation) of the sample is observed.

7.2.2 Characterizaion

X-Ray diffraction See section 1.7.1.

Electron Microscopy See section 1.7.2 for SEM and low magnification TEM. High-resolution TEM (HRTEM) images and selected area electron diffraction (SAED) patterns were obtained on a JEOL 2010F instrument, equipped with a Gatan high-angle annular dark field detector (HAADF) for performing incoherent HAADF or Z-contrast imaging in scanning TEM mode at accelerating voltages of 200 kV.

UV-visible Spectra See section 1.7.3.

Photoluminescence Samples for photoluminescence (PL) spectra were dispersed in deionized water and sonicated for 1 min. Fluorescence data were subsequently obtained at 25 ℃ on a Jobin Yvon Spex Fluorolog 3 with a 1 sec integration time, using an excitation wavelength of 488 nm. For the CdSe QD sample, cyclohexane was used as the solvent. Conversely, for silica-encapsulated CdSe, silica-encapsulated Fe_3O_4, and silica nanotubes incorporating CdSe and Fe_3O_4 nanocrystals, water was utilized as the dispersing medium.

Cell culture HeLa cells were cultured in a minimal essential medium (MEM, Giboco) solution. This treatment was supplemented however with 10% (v/v) heat-inactivated fetal bovine serum (FBS) as well as with 1 % (v/v) penicillin and streptomycin (P/S) at 37 ℃ in a humidified atmosphere in the presence of 5% CO_2. Cells were trypsinized, and reseeded onto a lysine-coated 35-mm bottom glass dish (MatTek Corp.) at a concentration of 1×10^5 cells/mL overnight for further use.

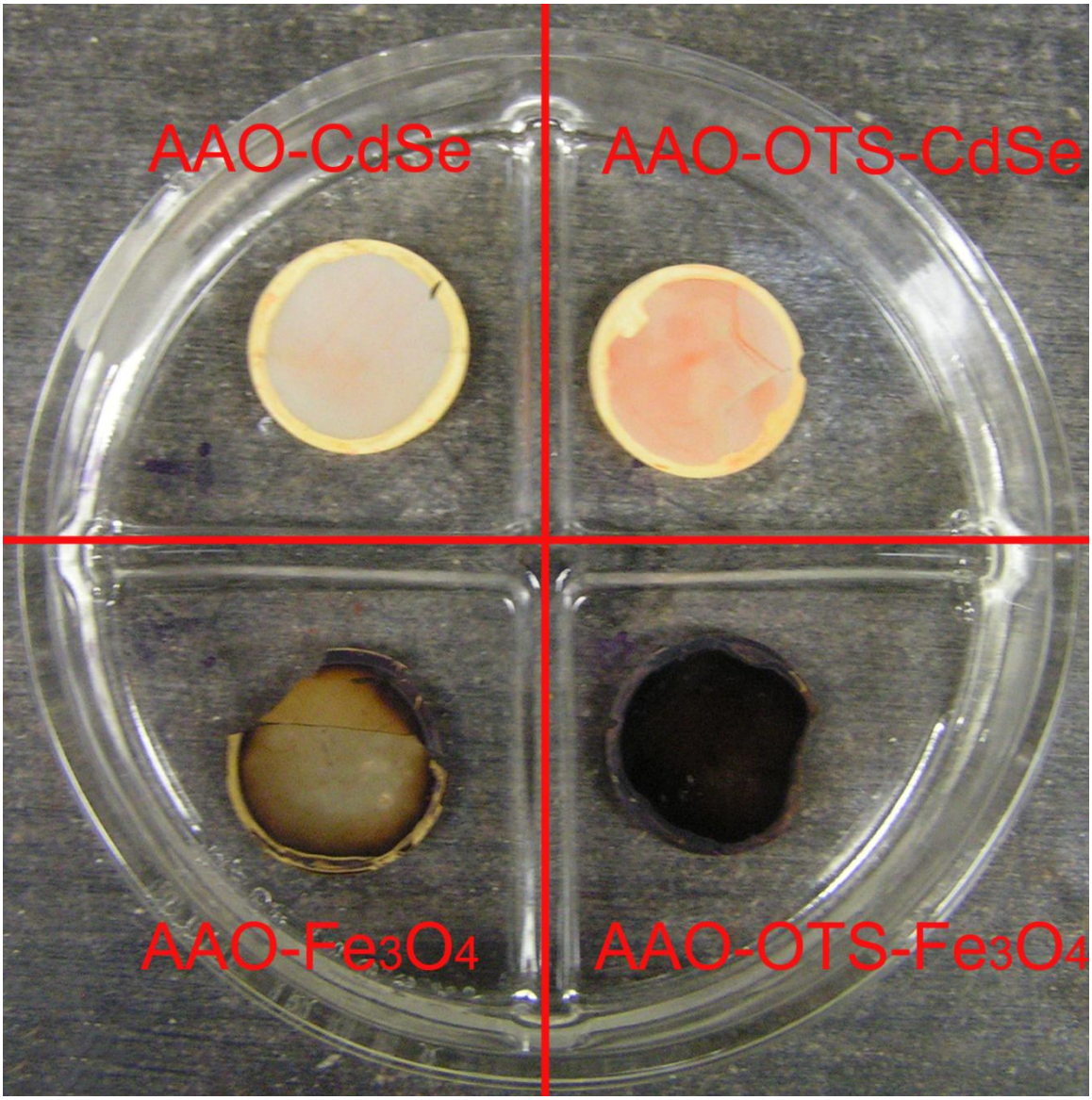

Figure 7.3 Top-view optical image showing clear visual differences between unmodified AAO (left half of image) and OTS-modified AAO (right half of image) after immersion into solutions containing either CdSe QDs or Fe_3O_4 NPs.

Confocal microscopy imaging For nanomaterials only, a diluted sample was dropped onto a 36-mm uncoated bottom glass dish (MatTek Corp.) for imaging. For cell experiments, the nanomaterial sample was additionally incubated with cells in a lysine-coated glass dish overnight. Cells were then washed with phosphate buffered saline (PBS) twice to remove excess nanomaterials. Cell membranes were then stained with the Texas Red®-X conjugate of wheat germ agglutinin (TR-WGA, Invitrogen). Confocal microscopy experiments were subsequently performed using a Zeiss LSM 510 META NLO two-photon laser scanning confocal microscope system. For green fluorescence, the system was operated using a 488 nm excitation wavelength; we detected emission wavelengths of 527 ± 23 nm using a 500-550 nm bandpass filter. For red fluorescence, the system was operated using a 543 nm excitation wavelength; we detected emission at 615 ± 20 nm using a 560 nm longpass filter. Images were captured using a C-Apochromat $63\times/1.2$ Water (corr.) objective or a Plan-Apochromat $100\times/1.45$ oil objective. Acquired data were analyzed using LSM 510 META software.

Magnetic Measurements The field and temperature dependences of as-prepared magnetite nanocrystals and of silica nanotube composites encapsulating both Fe_3O_4 and CdSe nanocrystals were measured. The magnetization measurements of the silica encapsulated CdSe/Fe_3O_4 composite structure and of the control sample of Fe_3O_4 nanoparticles were carried out in a Quantum Design Magnetic Measurement System (MPMS) at 30 and 300 K, in applied magnetic fields ranging from -50 to 50 kOe. The dried powders were dispersed in 50 μL of paraffin and contained in a gelatin capsule fastened in a plastic straw for immersion into the magnetometer. No subtraction of the diamagnetic signal from the sample container was made for the magnetization data.

7.3 Results and Discussion

The crystallographic phase of our resulting silica-encapsulated nanocomposite was examined by XRD and shown in Figure 7.4A. We have also examined our constituent nanostructures, namely as-prepared CdSe QDs (JCPDS #19-0191) and Fe_3O_4 NPs (JCPDS #19-0629). Peaks for all materials appeared to be broadened, as would be expected of small nanomaterials by comparison with their bulk analogues. Although the magnetite peaks are prominent, there is no peak that can be ascribed to silica and CdSe in the resulting pattern of the composite. The absence of the silica peak is due to the amorphous nature of the silica nanotube creasted by sol-gel template synthesis.[47, 48] The absence of the CdSe peak may be attributed to the limited amount of CdSe QDs imcorporated into the silica nanotubes. To ensure biocompatibililty, we had intentionally lowered the concentration of CdSe QDs versus that of Fe_3O_4 NPs in the final composite, because of the potential issue of CdSe toxicity. In the final product, the concentration of CdSe QDs was optimized to ensure detection under normal fluorescence conditions.

The optical UV-visible absorption spectra of as-prepared samples are shown in Figure 7.4B. In agreement with prior data on silica nanotubes,[49] there is a peak for silica nanotubes located in the region of 300 to 800 nm. CdSe QDs possess a strong absorption peak at around 550 nm, which corresponds to a mean size of 3 nm, in expected agreement with our synthetic protocol.[50] Also, due to its low concentration, it was not obviously present in the composite spectrum. The broad, featureless signal due to Fe_3O_4 can be ascribed to the fact that it is an indirect band gap semiconductor.[51] A weak shoulder in

the silica composite spectrum at 470 nm is in agreement with prior observations on analogous nanocomposites.[52-54]

Figure 7.5 shows the PL spectra of isolated CdSe QDs, silica-encapsulated CdSe, silica-encapsulated Fe_3O_4, and silica nanotubes containing both CdSe and Fe_3O_4 nanocrystals, respectively. The presence of an emission peak of pristine CdSe QDs in cyclohexane solution was noted at around 590 nm, in general agreement with what has been previously reported.[50, 52] The weakness of the peak intensity however has been ascribed to the exposure of surface defects associated with the nature and composition of the dispersing medium.[55] Also, as expected, there was no peak in the silica-encapsulated Fe_3O_4 sample. The peak at around 570 nm in water was noted not only for silica-encapsulated CdSe but also for silica nanotubes containing both CdSe and Fe_3O_4 nanocrystals. Though the emission peak remained symmetric without a red tail, the signal was clearly blue-shifted and broadened as compared with that of bare CdSe, an observation that has been noted with analogous silica-encapsulated systems.[56-58] One possible reason suggested is that the quantum dots may have undergone ligand removal and surface 'corrosion' during the encapsulation process leaving the QDs unprotected.[59] Our observation of emission peaks in all silica nanotube samples incorporating CdSe suggests that the optical properties of CdSe QDs remained intact even after insertion into silica, thereby rendering these composite structures as legitimate luminescent imaging probes.

Sample morphology was examined by electron microscopy measurements on Au-coated samples (Figure 7.6). The diameter of as-prepared silica nanotubes were in the range of ~ 220 ± 40 nm with lengths of ~ 4.5 ± 1.5 μm. As is apparent from the data, there was no obvious change in silica nanotube morphology, even after incorporation of discrete functional nanoparticles. The EDS of the silica nanotube alone evinced the presence of Si in addition to Al and O signals originating from the Al template residue. By contrast, the silica-encapsulated composite showed an expected Si signal as well as a number of Fe peaks, though no peaks clearly attributable to Cd and Se were observed. This absence of Cd and Se peaks was likely due to the relatively low concentration of CdSe as compared with Fe_3O_4 in addition to inherently poor instrumental sensitivity.

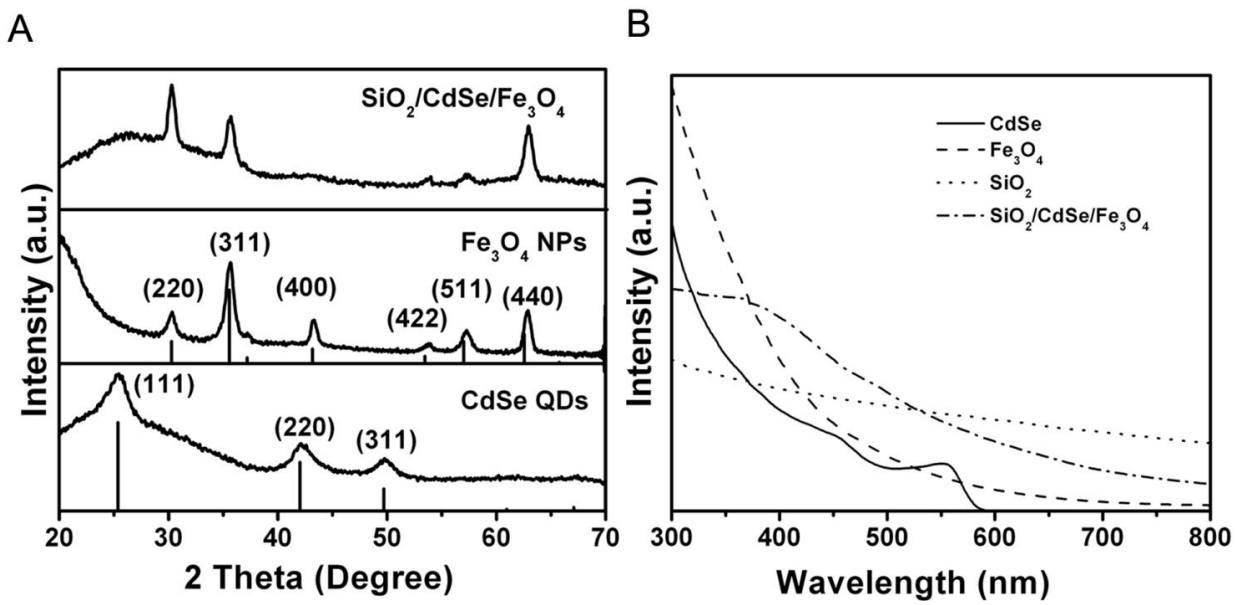

Figure 7.4 XRD patterns (A) of CdSe QDs, Fe_3O_4 NPs, and silica-encapsulated composites, respectively. (B) Corresponding UV-visible spectra of CdSe QDs, Fe_3O_4 NPs, silica nanotubes, and silica-encapsulated composites, respectively.

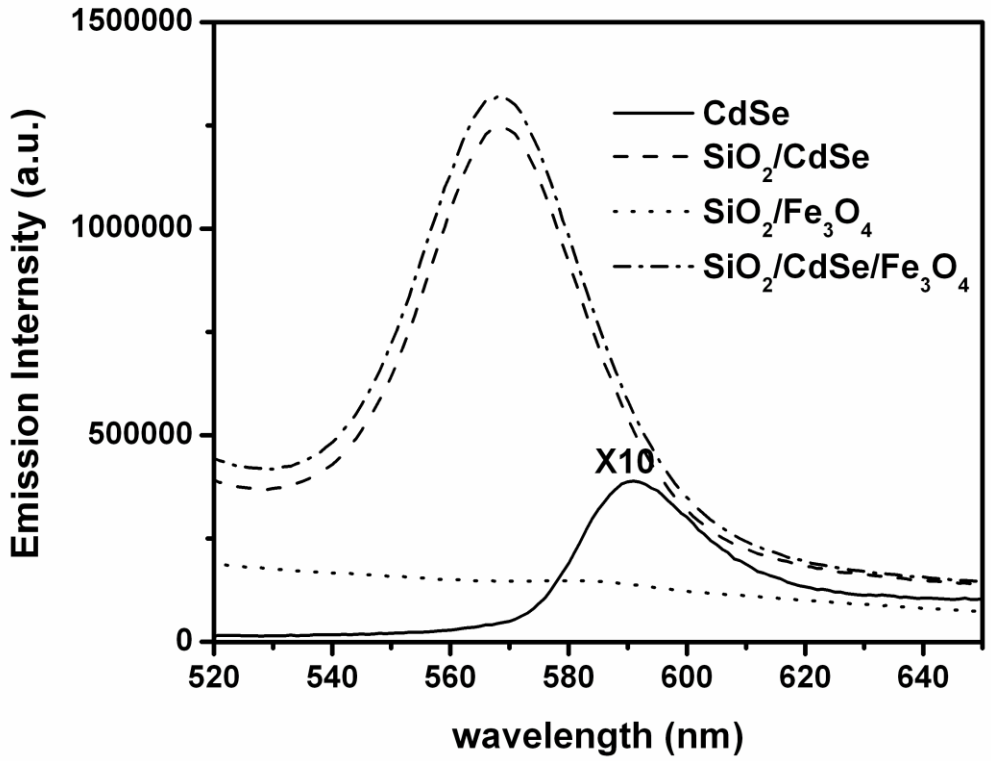

Figure 7.5 Room-temperature PL emission spectra (λ_{ex}=488 nm) of bare CdSe QDs as well as of silica-encapsulated CdSe, silica-encapsulated Fe_3O_4 NPs, and silica nanotube composites incorporating both CdSe and Fe_3O_4 nanocrystals.

Analytical HRTEM techniques were utilized to obtained further structural insights into the nature of our samples. An isolated silica nanotube control sample, in the absence of Fe_3O_4 and CdSe, is shown in Figure 7.7A and B. This material is clearly opened at its end and its surface texture is morphologically distinctive from that of our product nanocomposites. Bright field (BF) and high-angle annular dark field (HAADF) STEM images are presented in Figure 7.7C and D and magnified in Figure 7.7E and F. As expected, it is apparent from these data that there is a discernible contrast amongst the nanotubes and the two differently-sized nanoparticles, reflective of variations in chemical composition (Z-atomic number) of these materials. Localized EDS spectra at specific nanoparticles sites on the silica nanotube surface were obtained using a 0.2 nm beam in STEM mode and the corresponding data are shown in Figure 7.7G. Briefly, the presence of Cd was noted with the smaller nanoparticles (blue curve), whereas the signal was associated with the larger nanoparticles (red curve), confirming the presence of CdSe QDs and Fe_3O_4 NPs associated with this silica nanotube matrix. The determination of lattice dimensions obtained from the HRTEM image (Figure 7.7H) further supports this assertion. Specifically, measured *d*-spacings, taken from adjacent nanocrystalline structures, can be attributed to the (220) planes of CdSe (0.210 nm) and Fe_3O_4 (0.300 nm), respectively.

We should mention that these zero-dimensional nanostructures were solidly bound to our silica 1-D matrix, even after extensive washing without evident property dilution. Based on our microscopy analysis, the loading density of our nanoparticles was noted to be ~24 Fe_3O_4 NPs and ~4 CdSe QDs per 100 nm of silica nanotube surface, though these values could be altered by rational manipulation of particle concentrations. In the Supplementary Information section (Figures 7.8 and 7.9), we have demonstrated that we can independently vary the amounts and ratios of CdSe and/or Fe_3O_4 NPs incorporated into our silica nanotube by judiciously controlling either the immersion time (up to 24 h) or actual NP concentration (up to 100 mM). As such, we found that if needed, we could load as much as 3% of CdSe and 0.4% of Fe_3O_4 of the initial reagent NP solution into the final silica-based composite product. Nonetheless, as previously mentioned, we had deliberately decreased the amount of CdSe used in order to minimize the potential toxicity of the overall composite nanostructure while maintaining its favorable optical properties.

To demonstrate that the composites were noticeably magnetic, we confirmed that the behavior of a suspension of our multifunctional Fe_3O_4-based, luminescent silica-encapsulated composite nanotubes was highly responsive to the movement of an external magnet field of limited strength (Figure 7.10). The magnetic properties of our as-prepared silica composite structures were more precisely measured using a SQUID magnetometer.

Figure 7.11 shows the magnetization as a function of an applied magnetic field at 30 and 300 K for both samples. They both show a small coercive field at 30 K which becomes negligible at 300 K (Figure 7.11B and D). This indicates a clear transition from ferri- or ferromagnetism below the blocking temperature to superparamagnetism at high temperatures, which is characteristic of superparamagnetic nanoparticles.[60]

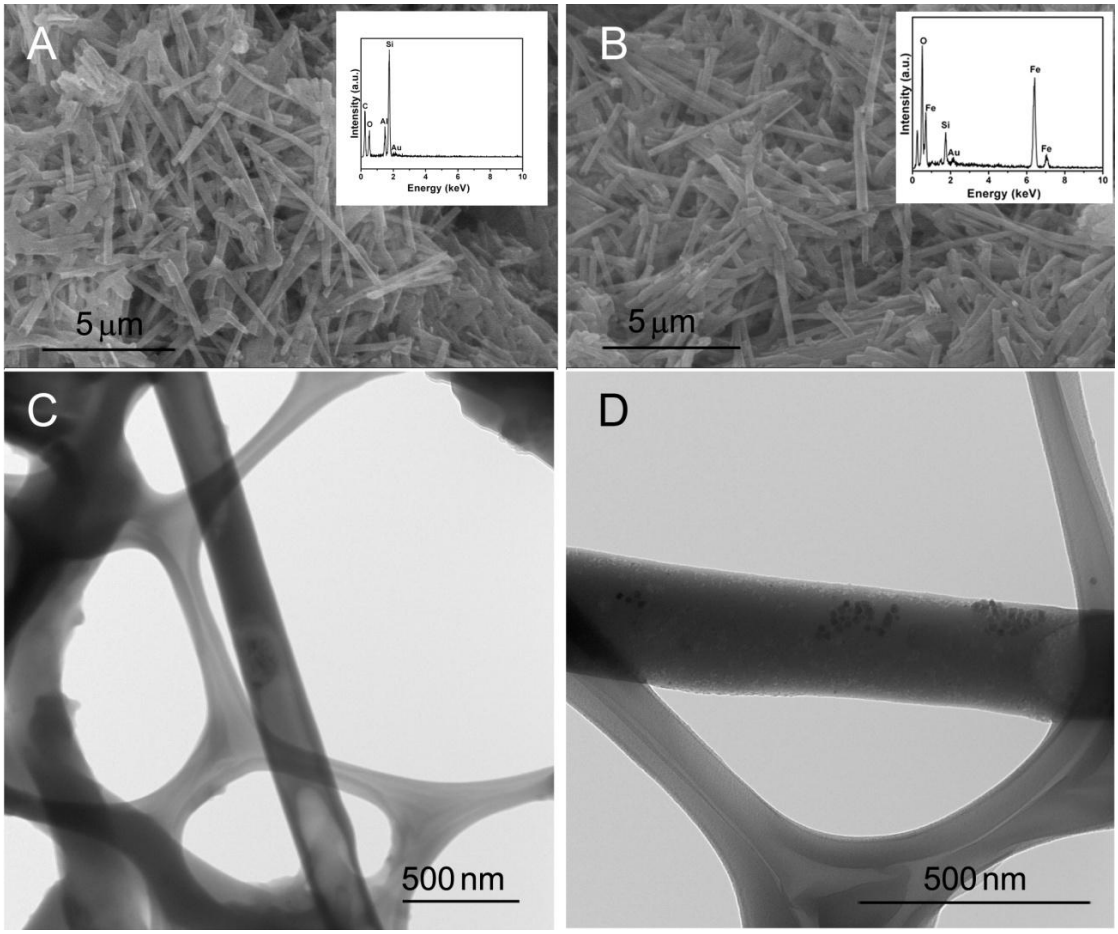

Figure 7.6 SEM and TEM images of silica nanotubes (A and C) as well as of $SiO_2/CdSe/Fe_3O_4$ composite nanostructure (B and D). Inset to (A) and (B) highlight EDS spectra of Au-coated samples of these materials. The presence of carbon can be ascribed to contamination within the SEM sample chamber itself.

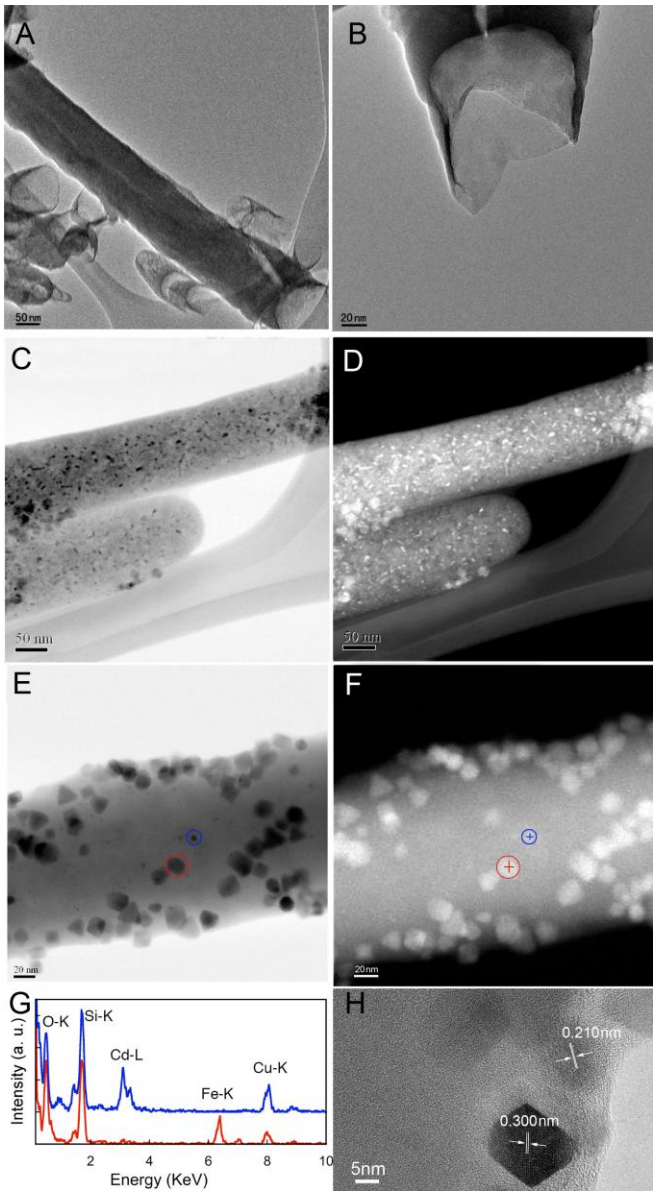

Figure 7.7 Control experiment: (A and B) Bright field STEM images of silica nanotubes. Desired product: (C and E) Bright field STEM image, (D and F) high-angle angular dark field STEM image, (G) EDS spectra, and (H) HRTEM image of a silica-encapsulated $CdSe/Fe_3O_4$ composite nanostructure. Individual spectra in (G) are associated with data taken at red and blue cross sites, respectively, which are spatially highlighted in (F).

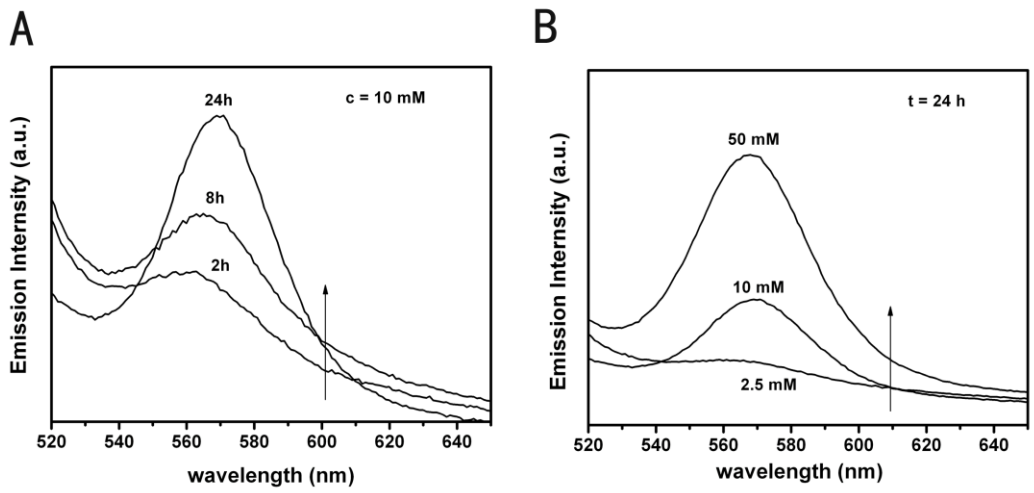

Figure 7.8 Room-temperature PL emission spectra (λex = 488 nm) of silica nanotube composites containing Fe_3O_4 NPs after immersion in (A) a constant 10 mM CdSe/cyclohexane solution for 2 h, 8 h, and 24 h, respectively; (B) a CdSe/cyclohexane solution for a constant 24 h period with varying nanoparticle concentrations of 2.5 mM, 10 mM, and 50 mM, respectively.

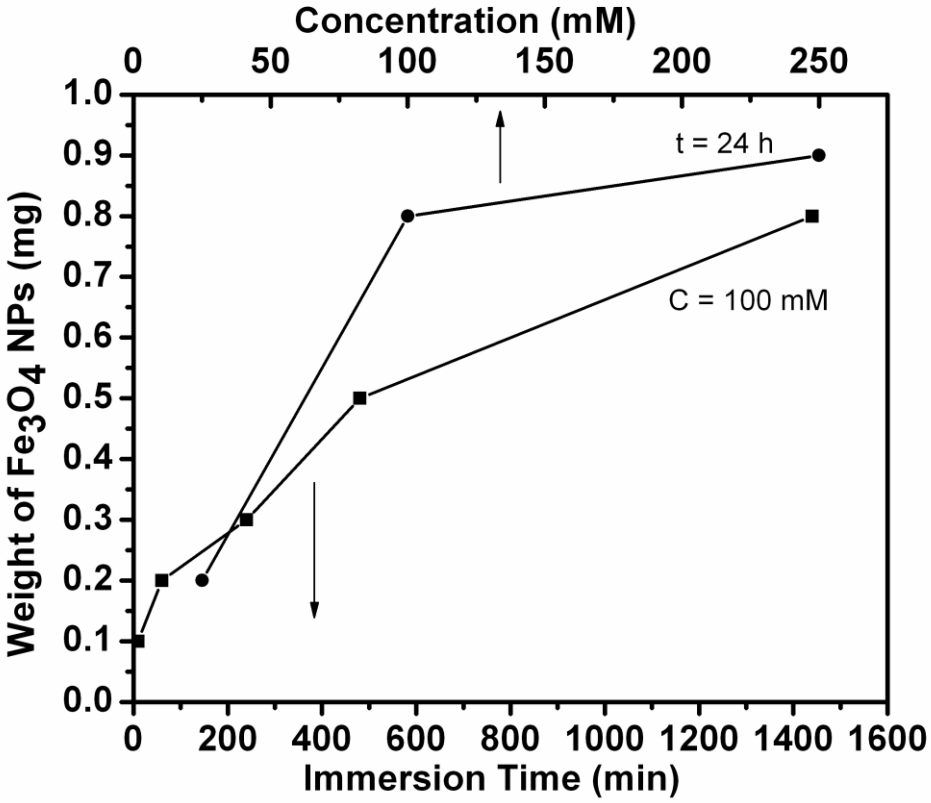

Figure 7.9 Amount of Fe_3O_4 NPs likely taken up by a silica nanotube composite containing CdSe QDs upon immersion into a Fe_3O_4/cyclohexane solution upon controlled incubation times (bottom) as well as rational variations in nanoparticle concentrations (top).

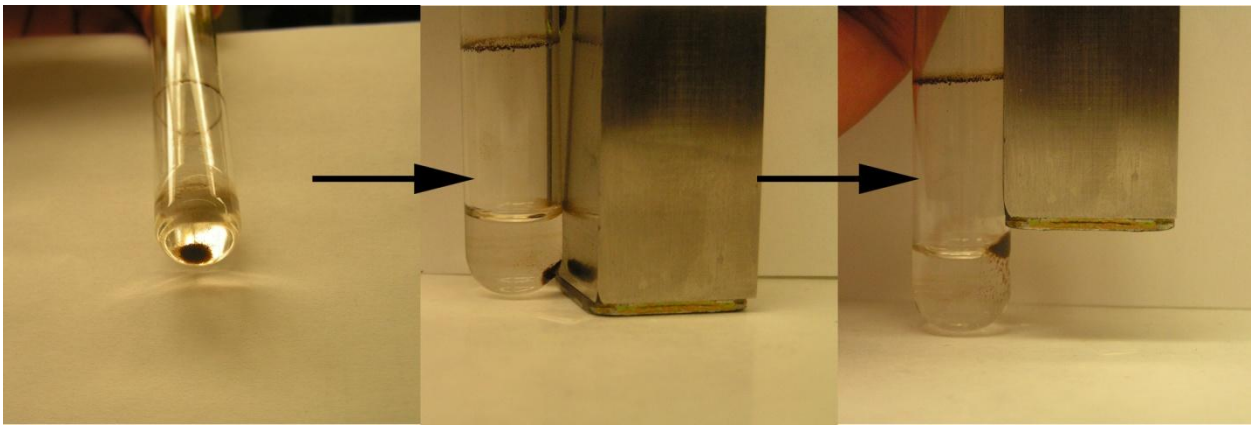

Figure 7.10 Series of photographs highlighting the responsiveness of our as-prepared silica-encapsulated multifunctional composite samples within a Pyrex test tube to the external application of a magnet (strength of 1400 to 1800 G).

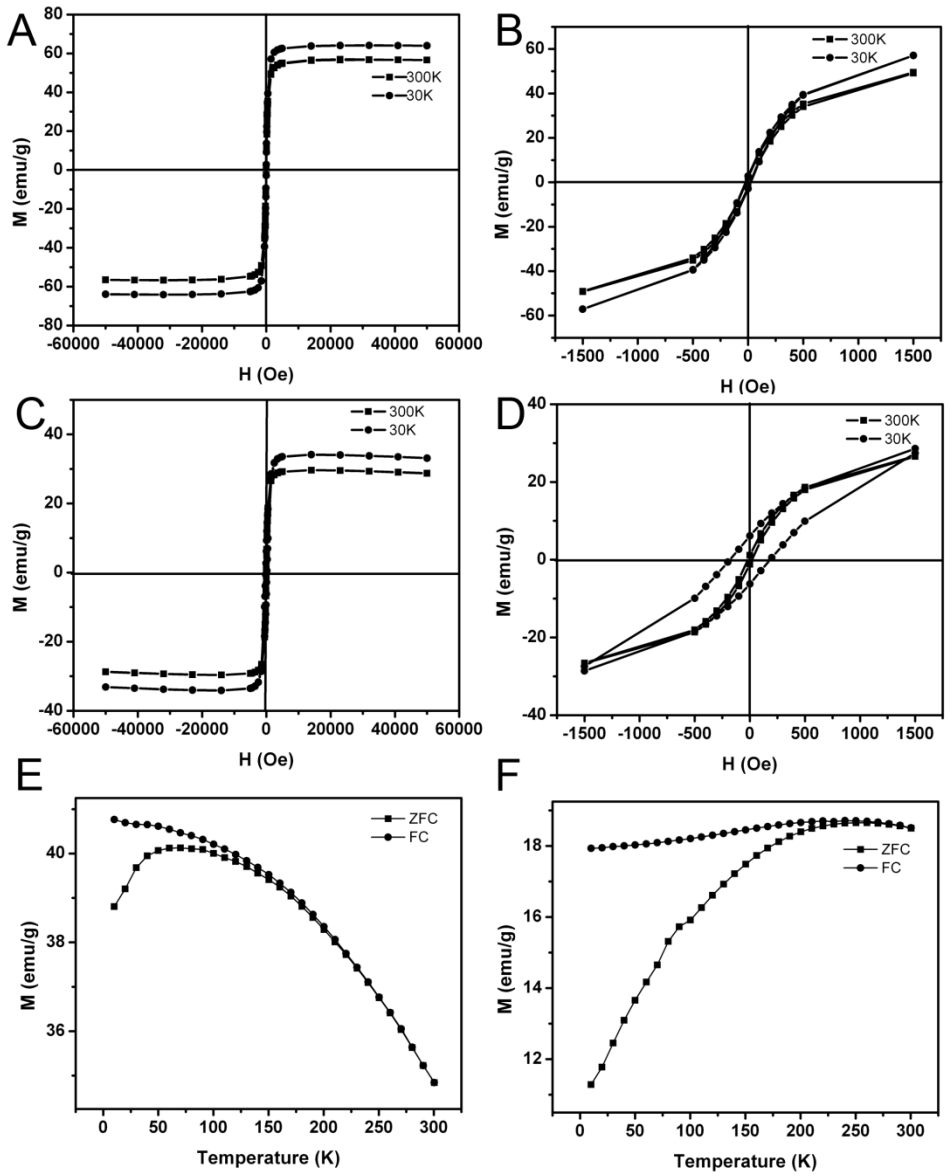

Figure 7.11 Plots of magnetization vs. applied field obtained at 30 K and 300 K, respectively, for (A) Fe_3O_4 nanoparticles and (C) Silica composite nanotubes containing Fe_3O_4 and CdSe. (B) and (D) show a magnified view of the hysteresis loops in (A) and (C), respectively. Temperature dependence of the magnetic susceptibility for (E) Fe_3O_4 nanoparticles and (F) silica composite nanotubes containing Fe_3O_4 and CdSe, showing zero field cooling (ZFC, closed square) and field cooling (FC, closed circle) curves, with an applied magnetic field set at 500 Oe.

We note the significant reduction of the saturation magnetization of Fe_3O_4/CdSe silica-based composite as compared with the Fe_3O_4 nanoparticles alone at both temperatures. Specifically, the saturation magnetization values at 30 K were 64 and 34 emu/g for the Fe_3O_4 nanoparticles and Fe_3O_4/CdSe silica-based composite, respectively, while at 300 K, the corresponding values were 57 and 29 emu/g. The observed reduction could be attributed to the normalization of the magnetization to the total mass of the composite including CdSe QDs and SiO_2 nanotubes. Thus, the magnetic contribution from the Fe_3O_4 nanoparticles was underestimated. A similar reduction of the saturation magnetization has been previously observed with Fe_3O_4/CdS bifunctional nanocomposites.[52, 53]

The zero-field-cooled (ZFC) and field-cooled (FC) magnetization measurements subject to an applied field of 500 Oe are shown in Figure 7.9E and F. Both ZFC and FC curves coincide at high temperatures but start to separate at blocking temperatures corresponding to 50 and 200 K for magnetite and silica-encapsulated magnetite, respectively. The large difference in the blocking temperature can explain the reduced coercive field of the bare Fe_3O_4 nanoparticles at 30 K as compared with that of the composite (see Figures 7.11B, D). Indeed, 30 K is well below the blocking temperature of 200 K for the composite, but it is very close to the blocking temperature of 50 K for bare, individual nanoparticles. The size distribution (12 – 14 nm) of bare Fe_3O_4 nanoparticles implies that smaller particles would have a lower blocking temperature. Hence, at 30 K, some of them are already in the superparamagnetic state with zero coercivity, whereas in the silica-based composite, all of the immobilized Fe_3O_4 nanoparticles are definitely blocked at 30 K, and possess non-zero coercive field.

We note that such a large observed difference in blocking temperature is a rather surprising result, considering the same size of the magnetite nanoparticles in each sample. The blocking temperature (T_B) of magnetic nanoparticles is related to the energy barrier ΔE separating two easy directions of magnetization via Arrhenius's law[61] namely, $T_B \sim \Delta E / 25 k_B$, where k_B is the Boltzmann's constant. For non-interacting nanoparticles, the energy barrier is $\Delta E = KV$, where K is the anisotropy constant and V is the volume of a nanoparticle. The dipole – dipole or exchange interactions between nanoparticles with an energy, E_{int}, increase the energy barrier: $\Delta E = KV + E_{int}$, as well as the blocking temperature of interacting nanoparticles.[62, 63] Thus, a significant increase of the blocking temperature of the silica-encapsulated CdSe/ Fe_3O_4 composite strongly suggests the presence of non-negligible interparticle interactions in this sample.

In order to examine the effect of magnetic interactions, we estimated the anisotropy constant, K, for Fe_3O_4 nanoparticles using Arrhenius's law for non-interacting nanoparticles, namely $K \sim 25 k_B T_B / V$. Using $T_B = 50$ K and an assumption that particles are spheres with an average diameter of 14 nm, the anisotropy constant K was computed to be $1.2 \cdot 10^4$ J/m^3. This value is in an excellent agreement with the anisotropy constant of the bulk magnetite, namely $K_{bulk} = 1.3 \cdot 10^4$ J/m^3.[64]

The fact that the anisotropy constant of our particles is similar to its bulk

counterpart is not surprising, if one takes into account their relatively large diameter of 14 nm. The anisotropy of nanoparticles significantly increases from its bulk value with

decreasing particle size, because of the emergence of an additional surface anisotropy. In the case of Fe_3O_4 nanoparticles generally, it is increased by an order of magnitude for particles with a diameter range of 4 – 7 nm.[65, 66] The fact that the energy barrier, ΔE, of Fe_3O_4 nanoparticles is consistent with the expected value for non-interacting nanoparticles suggests that the effect of magnetic interactions was reduced by dilution in paraffin. For bare Fe_3O_4 nanoparticles, the dilution in paraffin presumably increased the inter–particle distances and as a result, weakened the resulting magnetic interactions.

By contrast, in the Fe_3O_4/CdSe silica-based composite, the distance between individual Fe_3O_4 nanoparticles remained relatively intact upon dilution, because the particles are immobilized due to attachment to the silica nanotube surface. Hence, while the distance between silica nanotubes can surely be modified with dilution, spatial separations between individual Fe_3O_4 nanoparticles within the tubes remain unaffected.

Interactions between nanoparticles can also explain the difference in coercive fields of both samples. The coercive field of 180 Oe of the composite at 30 K is still larger than the highest coercive field of 100 Oe observed at 5 K in bare nanoparticles (Figure 7.12). Such an increase of the coercive field is consistent with an increase of the magnetic anisotropy of the nanoparticles in the composite due to the interparticle interactions. As was previously reported, those interactions not only increase the blocking temperature, but also enhance the coercive field of the magnetite nanoparticles.[67, 68]

Thus, we can conclude that the blocking temperature of Fe_3O_4/CdSe silica-based composite is noticeably increased due to magnetic interactions between discrete Fe_3O_4 nanoparticles incorporated within the silica nanotubes. In other words, our silica nanotubes create a higher confined density of magnetic nanoparticles immobilized within their 1-D structure, which invariably concentrates and strengthens the local magnetic interactions, thereby explaining the nature of our results.

To demonstrate the capability of our SiO_2-encapsulated composites as fluorescent probes, confocal microscopy images were taken, as shown in Figure 7.13. Figure 7.13A shows a typical phase contrast image of the composite nanotube suspension in PBS, highlighting its morphological profile within the field of view. We have previously inferred that our composites contain encapsulated CdSe nanoparticles. Hence, we excited our sample at 488 nm and noted an expected emission at ~520 nm (Figure 7.13B), which therefore yielded a readily-detectable green fluorescence in spite of the relatively low concentration of QDs present, implying the inherent sensitivity of our material. The superimposition of the phase contrast and the corresponding fluorescent image data in Figure 7.13C is indicative of a very strong overlap and correlation, strongly suggesting that the observed optical signal likely originated from CdSe incorporated within the SiO_2 nanotube matrix itself. As a control experiment, based on an analogous superposition of phase and fluorescence data, we noted that SiO_2 nanotubes associated with Fe_3O_4 nanoparticles alone did not appear to evince any such fluorescence, even under identical imaging conditions (Figure 7.13D).

To analyze their functional potential within a biomedical context, we further incubated our SiO_2 nanotube composites with HeLa cancer cells and studied their uptake using confocal microscopy. Prior to this, we had sonicated our nanotubes to yield intact

structures (Figure 14), measuring 1 $\pm$ 0.75 microns in length. Cell membranes were stained with the red Texas Red®-X conjugate of wheat germ agglutinin (TR-WGA) for enhanced visualization. Figures 7.15A suggested that nanotubes (highlighted in green) could indeed become internalized into HeLa cells after overnight incubation. As a control experiment, HeLa cells, which had not been exposed to any CdSe-containing silica nanotube composites, did not show any green fluorescence whatsoever, under identical experimental conditions (Figure 7.15B).

To confirm the spatial localization of nanotubes within a typical cell, we obtained a series of Z-stack images of the cell (e.g. top to bottom) at 1 μm 'slice' intervals (Figure 7.16). CdSe-containing silica nanotube composites evinced a green fluorescence that became apparent at slice 4, but which had faded in intensity by slice 9. We focused on the middle of slice 5. Data corresponding to orthogonal X, Y, and Z planes, respectively, within the cell interior are shown in Figure 7.15C. Specifically, the main, central portion of Figure 7.15C corresponds to fluorescence data measured in a plane in the Z direction, whereas the rightmost and uppermost edge regions of the image present data at planes in the X and Y direction, respectively. Because these three planes share a common focal center within the cell itself and moreover, as these intimately interconnected planes evidently all demonstrate green fluorescence simultaneously, we can reasonably conclude that the CdSe-containing silica nanotube composites are localized (and can therefore theoretically transport cargo) within the interior of the HeLa cells themselves.

Any practical biomedical device necessitates not only cell biocompatibility and penetrability, which we have discussed above, but also solubility in a biologically relevant medium. To deal with this latter issue, we took advantage of the robust chemistry of the outer silica shell of our nanocomposite. Specifically, as alluded to earlier, we grafted 3-aminopropyl triethoxysilane (APTES) onto its exterior surface.[69] This protocol increased the dispersibility of our samples in water (Figure 7.16), yielding a stability of up to 24 h at a concentration of 0.5 mg/mL.

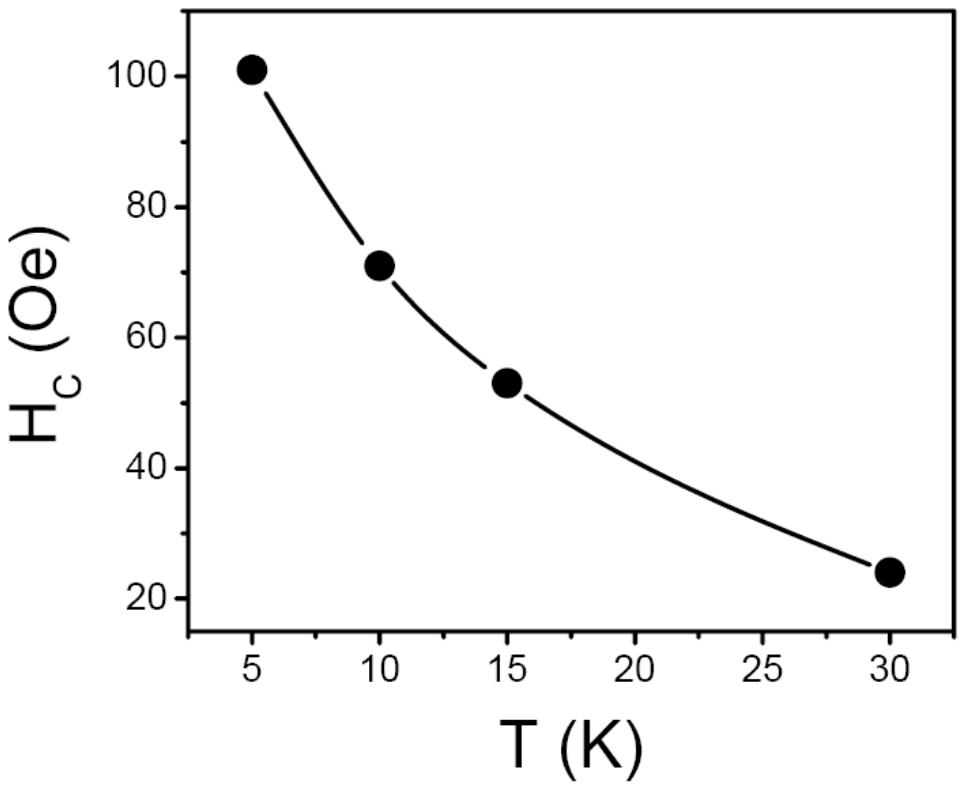

Figure 7.12 Behavior of the coercive field of bare Fe_3O_4 nanoparticles as a function of temperature. Solid line is drawn as a visual guide.

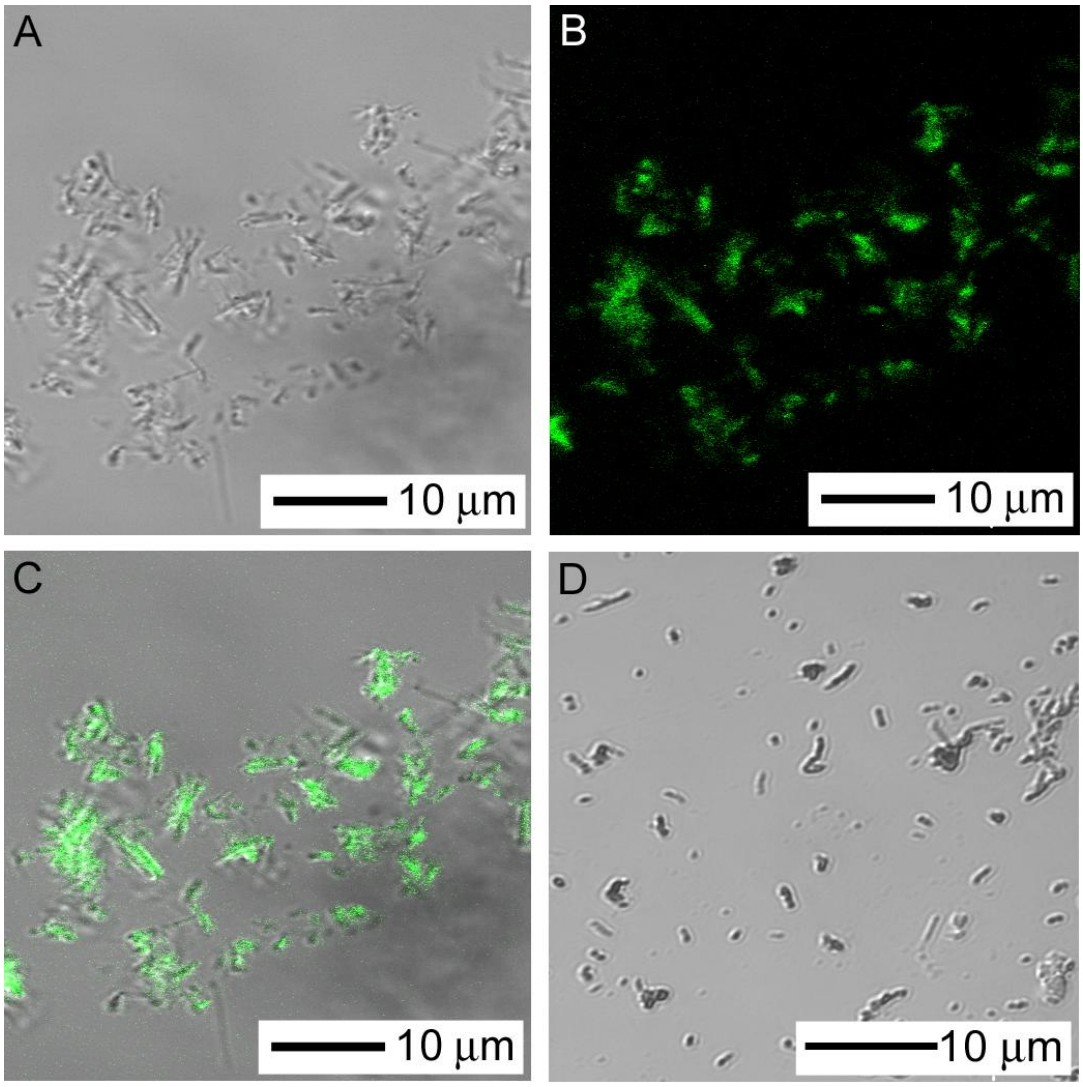

Figure 7.13 Confocal microscopy image characterization of silica-encapsulated composites containing both Fe_3O_4 and CdSe nanocrystals: (A) phase contrast image; (B) florescence image; and (C) superimposition of both (A) and (B). Control sample: (D) Superimposition of phase contrast and fluorescence images of silica-encapsulated nanotubes incorporating Fe_3O_4 alone. Data implied that neither the Fe_3O_4 nanoparticles nor the silica nanotubes alone evinced any noticeable fluorescence under identical imaging conditions.

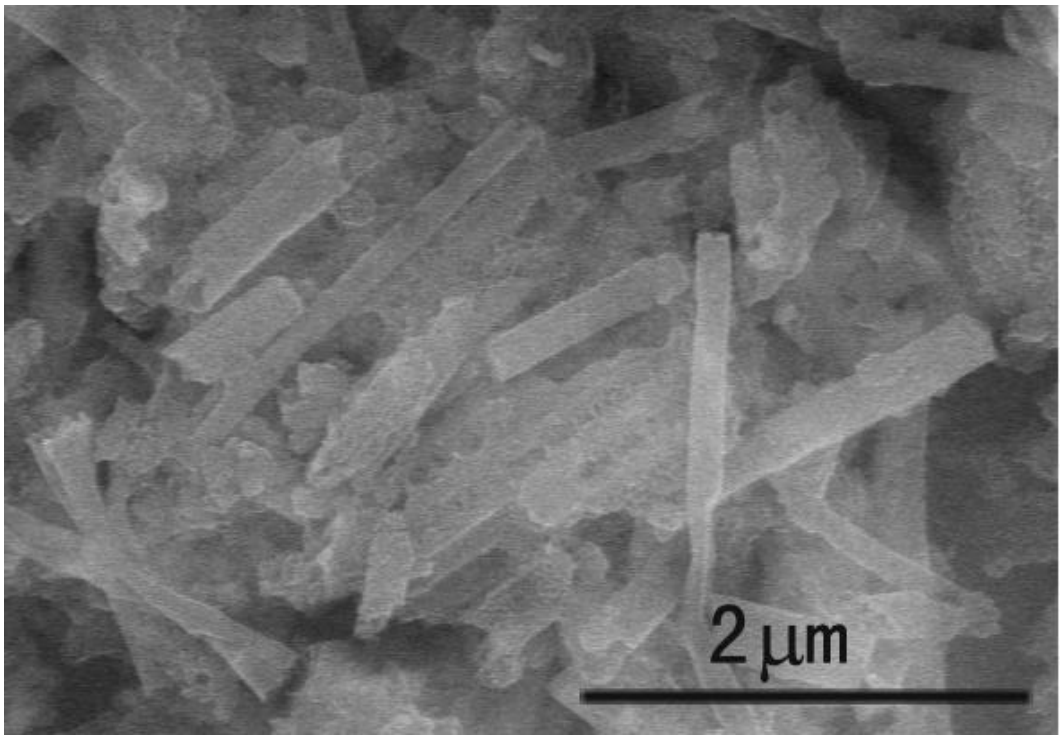

Figure 7.14 SEM image of silica composite nanotubes containing both CdSe QDs and Fe_3O_4 NPs after sonication for 12h.

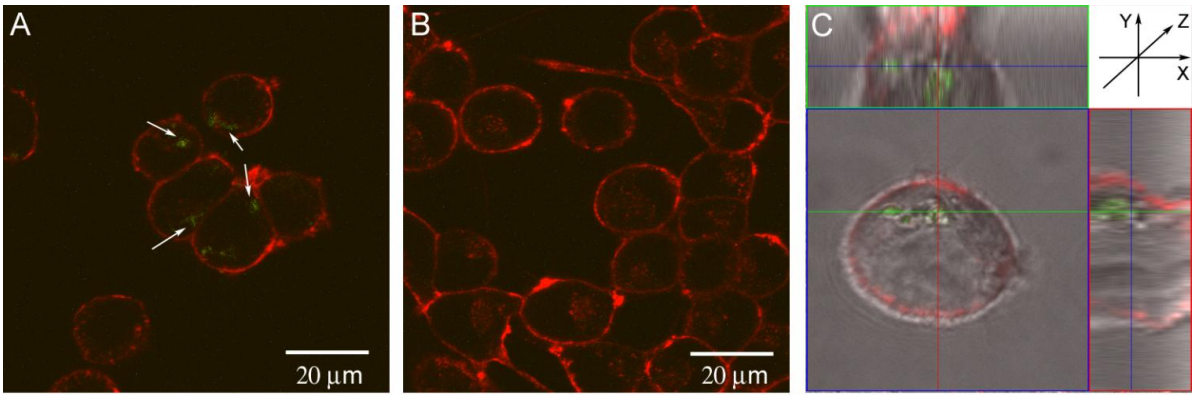

Figure 7.15 Confocal microscopy image characterization under identical conditions of HeLa cancer cells subjected to various treatments: (A) in the presence and (B) absence of silica-encapsulated nanotube composites containing Fe_3O_4 and CdSe nanocrystals. Cell membrane was red-stained with TR-WGA conjugates. Incidence of silica-encapsulated nanotube composites containing Fe_3O_4 and CdSe nanocrystals, that fluorescence green, is suggested by the presence of white arrows in (A). (C) A representative single orthogonal slice (slice 5) from 3D images (z-stacks) as shown in Figure 7.13, strongly indicating that the nanotubes were incorporated within the cells.

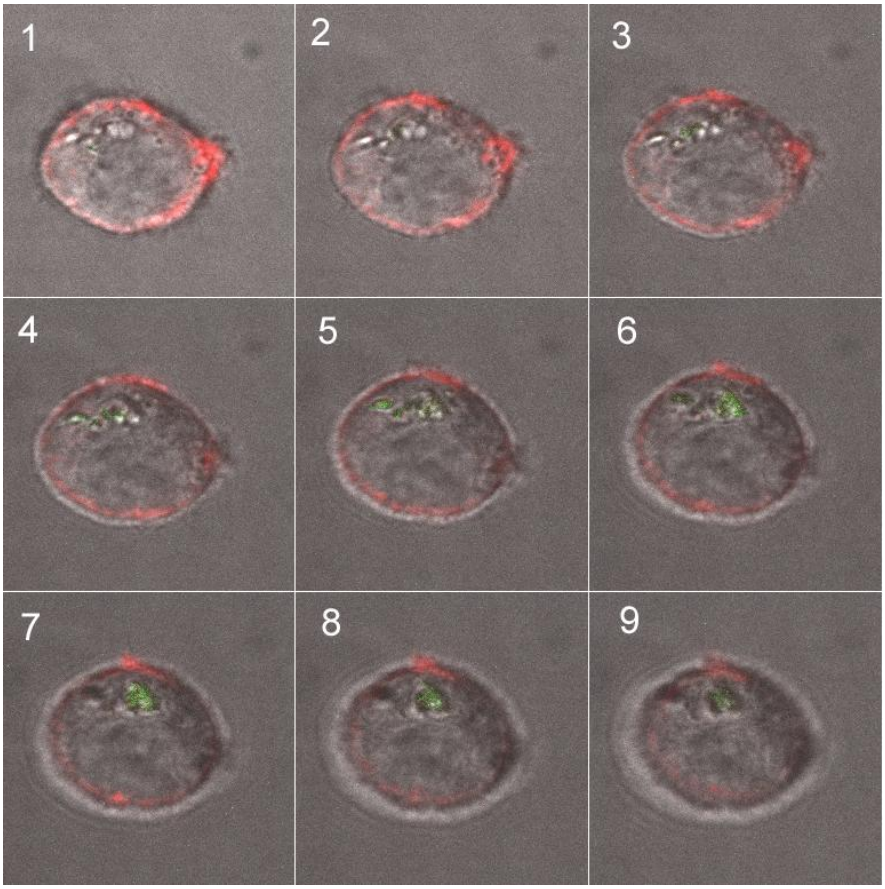

Figure 7.16 Z-stacked confocal images, representing a superposition of green and red fluorescence along with phase contrast, of a single cell incorporating our as-prepared silica-encapsulated nanotube composites containing Fe_3O_4 and CdSe nanoparticles. Slices were obtained from top to bottom in regular 1 micron intervals.

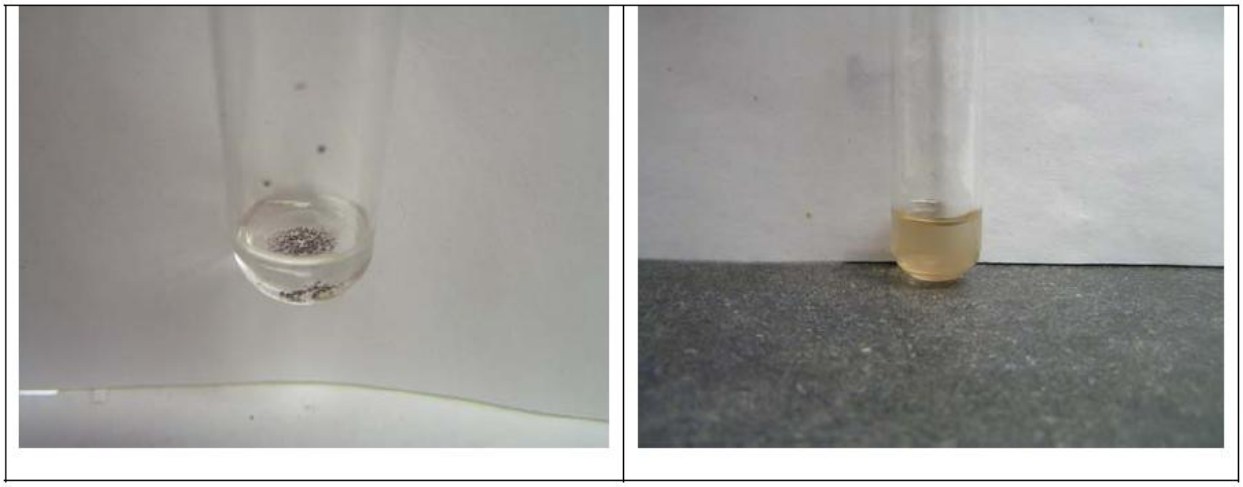

Figure 7.17 Aqueous solution containing as-prepared samples (left) prior to and (right) soon after surface modification with APTES.

7.4 Conclusions

In conclusion, we have prepared a novel multifunctional 1D nanostructure by incorporating CdSe QDs and Fe_3O_4 NPs into silica nanotubes via a hydrophobic quasi-self-assembly approach. The uniform size distribution and function of our nanoparticles were able to be preserved. The resulting nanostructure is luminescent and superparamagnetic which renders it ideal for biological applications. This was confirmed by cell experiment. The nanostructure was able to enter the HeLa cell, observed by fluorescence microscopy without further dye modification. Moreover, the biocompatibility of silica and superparamagnetic property render this nanostructure an excellent candidate for drug delivery.

Further research will include cytotoxicity research, and surface modification with other molecules. Also, other functional nanoparticles may also be tested so as to enrich the functionality of the resultingnanostructure.

7.5 Reference

1. Alivisatos, P. *Nat. Biotechnol.* **2004**, 22, 47.
2. Parak, W. J.; Gerion, D.; Pellegrino, T.; Zanchet, D.; Micheel, C. *Nanotechnology* **2003**, 14, R15.
3. Michalet, X.; Pinaud, F.; Lacoste, T. D.; Dahan, M.; Bruchez, M. *Single Mol.* **2001**, 2, 261.
4. Sutherland, A. J. *Curr. Opin. Solid State Mater. Sci.* **2002**, 6, 365.
5. Chan, W. C. W.; Maxwell, D. J.; Gao, X.; Bailey, R. E.; Han, M.; Nie, S. *Curr. Opin. Biotechnol.* **2002**, 13, 40.
6. Bruchez, M.; Moronne, M.; Gin, P.; Weiss, S.; Alivisatos, A. P. *Science* **1998**, 281, 2013.
7. Gao, X.; Nie, S. *Trends Biotechnol.* **2003**, 21, 371.
8. Larson, D. R.; Zipfel, W. R.; Williams, R. M.; Clark, S. W.; P., B. M. *Science* **2003**, 300, 1434.
9. Gao, X.; Cui, Y.; Levenson, R. M.; Chung, L. W. K.; Nie, S. *Nat. Biotechnol.* **2004**, 22, 969.
10. Lounis, B.; Bechtel, H. A.; Gerion, D.; Alivisatos, A. P.; Moerner, W. E. *Chem. Phys. Lett.* **2000**, 329, 399.
11. Dahan, M.; Laurence, T.; Pinaud, F.; S., C. D.; P., A. A. *Opt. Lett.* **2001**, 26, 825.
12. Neveu, S.; Bee, A.; Robineau, M.; Talbot, D. *J. Colloid Interface Sci.* **2002**, 255, 293.
13. Grasset, F.; Labhsetwar, N.; Li, D.; Park, D. C.; Saito, N.; Haneda, H.; Cador, O.; Roisnel, T.; Mornet, S.; Duguet, E.; Portier, J.; Etourneau, J. *Langmuir* **2002**, 18, 8209.
14. Sun, S.; Zeng, H. *J. Am. Chem. Soc.* **2002**, 124, 8204.
15. Park, S.-J.; Kim, S.; Lee, S.; Khim, Z.; Char, K.; Hyeon, T. *J. Am. Chem. Soc.* **2000**, 122, 8581.
16. Puntes, V. F.; Krishan, K. M.; Alivisatos, A. P. *Science* **2001**, 291, 2115.
17. Chen, Q.; Rondinon, A. J.; Chakoumakos, B. C.; Zhang, Z. J. *J. Magn. Magn. Mater.* **1999**, 194, 1.

18. Park, J.; An, K.; Hwang, Y.; Park, J.-G.; Noh, H.-J.; Kim, J.-Y.; Park, J.-H.; Hwang, N.-M.; Hyeon, T. *Nat. Mater.* **2004**, 3, 891.
19. Sun, S.; Murray, C. B.; Weller, D.; Folks, L.; Moser, A. *Science* **2000**, 287, 1989.
20. Shevchenko, E. V.; Talapin, D. V.; Rogach, A. L.; Kornowski, A.; Haase, M.; Weller, H. *J. Am. Chem. Soc.* **2002**, 124, 11480.
21. Xu, C.; Xu, K.; Gu, H.; Zheng, R.; Liu, H.; Zhang, X.; Guo, Z.; Xu, B. *J. Am. Chem. Soc.* **2004**, 126, 9938.
22. J.Widder, K.; Senyei, A. E.; Scarpelli, D. G. *Proc. Soc. Exp. Biol. Med.* **1978,** 58, 141.
23. Berry, C. C.; Curtis, A. S. G. *J. Phys. D* **2003**, 36, R198.
24. Mornet, S.; Vasseur, S.; Grasset, F.; Duguet, E. *J. Mater. Chem.* **2004**, 14, 2116.
25. Hiergeist, R.; Andra, W.; Buske, N.; Hergt, R.; Hilger, I.; Richter, U.; Kaiser, W. *J. Magn. Magn. Mater.* **1999**, 201, 420.
26. Brown, M. A.; Semelka, R. C., *MRI: Basic Principles and Applications.* Wiley-Liss: New York, **2003**.
27. Na, H. B.; Song, I. C.; Hyeon, T. *Adv. Mater,* **2009**, 21, 1.
28. Lee, S. B.; Mitcell, D. T.; Trofin, L.; Nevanen, T. K.; Soderlund, H.; Martin, C. R. *Science* **2002**, 296, 2198.
29. Fan, R.; Wu, Y.; Li, D.; Yue, M.; Majumdar, A.; Yang, P. *J. Am. Chem. Soc.* **2003**, 125, 5254.
30. Son, S. J.; Reichel, J.; He, B.; Schuchman, M.; Lee, S. B. *J. Am. Chem. Soc.* **2005**, 127, 7316.
31. Mitchell, D. T.; Lee, S. B.; Trofin, L.; Li, N.; Nevanen, T. K.; Soderlund, H.; Martin, C. R. *J. Am. Chem. Soc.* **2002**, 124, 11864.
32. Chang, T. M. S.; Prakash, S. *Mol. Biotechnol.* **2001**, 17, 249.
33. Nam, J.-M.; Thaxton, C. S.; Mirkin, C. A. *Science* **2003**, 301, 1884.
34. Langer, R. *Science* **2001**, 293, 58.
35. Michalet, X.; Pinaud, F. F.; Bentolila, L. A.; Tsay, J. M.; Doose, S.; Li, J. J.; Sundaresan, G.; Wu, A. M.; Gambhir, S. S.; Weiss, S. *Science* **2005**, 307, 538.
36. Park, S. A.; Taton, T. A.; Mirkin, C. A. *Science* **2002**, 295, 1503.
37. Tiefenauer, L. X.; Kuehne, G.; Andres, R. Y. *Bioconjugate Chem.* **1993**, 4, 347.
38. Hyeon, T.; Lee, S. S.; Park, J.; Chung, Y.; Na, H. B. *J. Am. Chem. Soc.* **2001**, 123, 12798.
39. Li, J. J.; Wang, Y. A.; Guo, W.; Keay, J. C.; Mishima, T. D.; Johnson, M. B.; Peng, X. J. *J. Am. Chem. Soc.* **2003**, 125, 12567.
40. Sun, S.; Murray, C. B.; Weller, D.; Folks, L.; Moser, A. *Science* **2000**, 287, 1989.
41. Pal, S.; Jagadeesan, D.; Gurunatha, K. L.; Eswaramoorthy, M.; Maji, T. K. *J. Mater. Chem.* **2008**, 18, 5448.
42. Lu, A.-H.; Salabas, E. L.; Schűth, F. *Angew. Chemie. Int. Ed.* **2007**, 46, 1222.
43. Zhang, M.; Bando, Y.; Wada, K. *J. Mater. Res.* **2001**, 16, 1408.
44. Okamaoto, K.; Shook, C. J.; Bivona, L.; Lee, S. B.; English, D. S. *Nano Lett.* **2004**, 4, 233.
45. Boatman, E. M.; Lisensky, G. C.; Nordell, K. J. *J. Chem. Edu.* **2005**, 82, 1697.
46. Park, J.; An, K.; Hwang, Y.; Park, J.-G.; Noh, H.-J.; Kim, J.-Y.; Park, J.-H.; Hwang, N.-M.; Hyeon, T. *Nature Mater.* **2004**, 3, 891.
47. Colorado, R.; Zeigler, S. Y.; Barron, A. R. *J. Mater. Chem.* **2008**, 18, 1911.

48. Zhai, T.; Gu, Z.; Dong, Y.; Zhong, H.; Ma, Y.; Fu, H.; Li, Y.; Yao, J. *J. Phys. Chem. C* **2007**, 111, 11604.
49. Wang, J.-X.; Wen, L.-X.; Wang, Z.-H.; Wang, M.; Shao, L.; Chen, J.-F. *Scr. Mater.* **2004**, 51, 1035.
50. Yu, W. W.; Qu, L.; Wenzhuo Guo; Peng, X. *Chem. Mater.* **2003**, 15, 2854.
51. Correa-Duarte, M. A.; Giersig, M.; Kotov, N. A.; Liz-Marz án, L. M. *Langmuir* **1998**, 14, 6430.
52. An, L.; Li, Z.; Wang, Z.; Zhang, J.; Yang, B. *Chem. Lett.* **2005**, 34, 652.
53. Liu, X.; Fang, Z.; Zhang, X.; Zhang, W.; Wei, X.; Geng, B. *Cryst. Growth Des.* **2009**, 9, 197.
54. Wang, Y. A.; Teng, X. W.; Wand, J. S.; Yang, H. *Nano Lett.* **2003**, 3, 789.
55. Yu, K.; Zaman, B.; Singh, S.; Wang, D.; Ripmeester, J. A. *Chem. Mater.* **2005**, 17, 2552.
56. Li, L.; Choo, E. S. G.; Liu, Z.; Ding, J.; Xue, J. *Chem. Phys. Lett.* **2008**, 461, 114.
57. Yi, D. K.; Selvan, S. T.; Lee, S. S.; Papaefthymiou, G. C.; Kundaliya, D.; Ying, J. Y. *J. Am. Chem. Soc.* **2005**, 127, 4990.
58. Chan, Y.; Zimmer, J. P.; Stroh, M.; Steckel, J. S.; Jain, R. K.; Bawendi, M. G. *Adv. Mater.* **2004**, 16, 2092.
59. Salgueirino-Maceira, V.; Correa-Duarte, M. A.; Spasova, M.; Liz-Marzan, L. M.; Farle, M. *Adv. Funct. Mater.* **2006**, 16, 509.
60. Lee, J.; Lee, Y.; Youn, J. K.; Na, H. R.; Yu, T.; Kim, H.; Lee, S.-M.; Koo, Y.-M.; Kwak, J. H.; Chang, H. N.; Hwang, M.; Park, J.-G.; Kim, J.; Hyeon, T. *Small* **2008**, 4, 143.
61. Wohlfarth, E. P. *J. Magn. Magn. Mater.* **1983**, 39, 39.
62. Hansen, M. F.; Morup, S. *J. Magn. Magn. Mater.* **1998**, 184, 262.
63. Petit, C.; Taleb, A.; Pileni, M.-P. *Adv. Mater.* **1998**, 10, 262.
64. Goya, G. F.; Berquot, T. S.; Fonseca, F. C.; Morales, M. P. *J. Appl. Phys.* **2003**, 94, 3520.
65. Balcells, L.; Iglesias, O.; Labarta, A. *Phys. Rev. B* **1997**, 55, 8940.
66. Si, S. K.; Mandal, T. K.; Gin, S.; Nakamura, H.; Kohara, T. *Chem. Mater.* **2004**, 16, 3489.
67. Arelaro, A. D.; Brandl, A. L.; Lima, E., Jr.; Grmarra, L. F.; Brito, G. E. S.; Pontuschka, W. M.; Goya, G. F. *J. Appl. Phys.* **2005**, 97, 10J316/1.
68. Wu, M.; Ma, Y.; Liu, Y.; Bi, H.; Fang, Q.; Niu, H.; Chem, Q. *Mater, Res. Bull.* **2008**, 43, 1321.
69. Jana, N. R.; Earhart, C.; Ying, J. Y. *Chem. Mater.* **2007**, 19, 5074.

Chapter VIII Conclusions

With improvements in characterization techniques and instruments, phenomena at the nano scale have attracted people's attention. Their unique, size, and shape-dependent properties are totally unlike their bulk counterparts. Prior to this, physical properties were believed to be only determined by composition and/or crystalline state. Nanomaterials' unique properties and intrinsic small size render them as highly promising for catalysis, sensor, biology, and information fields.

However, as compared with other science fields, nanoscience is still in its infancy. There are many challenges and obstacles that need to be overcome.

(5) Precise control of size, dimensionality, composition, crystal structure and assembly at the nanoscale.

(6) Development of an environmentally friendly, energy effective synthesis method, (e.g. low temperature, use of water as a solvent instead of a toxic solvent)

(7) Rational design and fabrication of novel nanomaterials and nanocomposites.

(8) A deep understanding of the relationship between size, shape and physical properties.

At the early stage of this research, synthesis is always very critical. It is the first step in the whole research. The relationship between size, shape and properties won't be understood until samples with high control over composition, size and shape are fabricated. Although many papers have been reported about synthesis of nanomaterials, there are still quite a number of materials that cannot be manipulated at the nano scale. In chapter II, we created $Bi_2Ti_2O_7$ nanotubes for the first time, which showed that nanotubes could be fabricated via the sol-gel technique coupled with use of an AAO template.

Moreover, the mechanism of nanoparticle synthesis is extremely important not only because it helps to understand how this specific material is formed, but also it can be used to make other materials with the same technique. In chapter III, we synthesized $BaZrO_3$ cubes and spheres by molten salt synthesis. We discussed its mechanism for the shape control. Moreover, we did a thorough investigation on the effects of parameters in MSS, which very few groups have referred to. All of these projects will greatly help in the design and synthesis of other nanomaterials in MSS. Also, in Chapter IV and VI, we discussed the mechanism of creating nanotubes vs. nanowires by the template method.

The synthesis techniques put forward for nanoscale synthesis have often involved toxic solvents, precursors, or high energy input. Today, the world we live in is facing

simultaneous energy and environmental crises. An environmentally and energy effective technique is therefore very important and necessary. In Chapters IV, V, and VI, we demonstrated a simple template method to effectively fabricate various 1D materials, including ternary metal oxides, transition metal oxides, and noble metals.

Nanocomposites can be created by applying nanomaterials as building blocks. The resulting nanocomposites may have collective or enhanced properties of their constituents. Hence, the selection of building blocks and assembly methods need to be carefully chosen and designed. Specifically in Chapter VII, we made a novel multifunctional nanostructure by incorporating CdSe QDs and Fe_3O_4 NPs into silica nanotubes. This compact nanostructure maintained both luminescent and superparamagnetic properties. Its promise for drug delivery was tested and demonstrated by successful entry into the HeLa cells.

In a word, research in this field will help to explore more materials at the nanoscale, with a deep understanding of the structure-property relationships, that will open up more opportunities in the area of nanoscience.

References

1. Booker, R.; Boysen, E., *Nanotechnology for Dummies*. Wiley Publishing, Inc.: NJ, **2005**
2. A report by the Interatency Working Group on Nanoscience, National Science and Technology Council, *Leading to the Next Industrial Revolution*; *National Nanotechnology Initiative*. **2000**
3. Tait, H., *Five thousand years of glass*. The British Museum Press London, **1991**.
4. Harden, D., *Glass of the Caesars*. The British Museum Press: London, **1988**.
5. Turkevich, J. *Gold. Bull.* **1985**, 18, 86.
6. Knoll, M.; Ruska, E. *Physik* **1932**, 12, 607.
7. Knoll, M.; Ruska, E. *Physik* **1932**, 12, 641.
8. Feynman, R. P. There's Plenty of Room at the Bottom, An Invitation to Enter a New Field of Physics. (http://www.zyvex.com/nanotech/feynman.html)
9. Kroto, H. W.; Heath, J. R.; O'Brien, S. C.; Curl, R. F.; Smalley, R. E. *Nature* **1985**, 318, 162.
10. Iijima, S. *Nature* **1991**, 354, 56.
11. Buzea, C.; Pacheco, I. I.; Robbie, K. *Biointerphases* **2007**, 2, MR17.
12. Rao, C. N. R.; Thomas, P. J.; Kulkarni, G. U., *Nanocrystals:: Synthesis, Properties and Applications.* Springer: Heidelberg, **2007**.
13. Klimov, V. I., *Semiconductor and Metal Nanocrystals: Synthesis and Electronic and Optical Properties.* Marcel Dekker, Inc.: New York, **2003**.
14. Schmid, G., *Nanoparticles: From Theory to Application.* WILEY-VCH Weinheim, **2004**.
15. Snider, G. L.; Orlov, A. O.; Lent, C. S., Quantum dots in nanoelectronic devices. In *Nano and Molecular Electronics Handbook*, Lyshevski, S. E., Ed. CRC: **2007**; 8, 1
16. Sargent, E. H. *Adv. Mater.* **2008**, 20. 3958
17. Pagan, J. G.; Patel, K. N.; Barletta, P. T.; Burkhart, C. C.; Stokes, E. B. *ECS Trans.* **2006**, 3, 333.
18. Peng, Y.; Zhao, X.; Fu, G. *Nanoscience* **2007,** 12, 30.
19. Bertolini, G.; Paleari, L.; Catassi, A.; Roz, L.; Cesario, A.; Sozzi, G.; Russo, P. *Curr. Pharm. Anal.* **2008**, 4, 197.
20. Steigerwald, M. L.; Alivisatos, A. P.; Gibson, J. M.; Harris, T. D.; Kortan, R.; Muller, A. J.; Thayer, A. M.; Duncan, T. M.; Douglas, D. C.; L, E. B. *J. Am. Chem. Soc.* **1988**, 110, 3046.
21. Wang, Y.; Herron, N. *J. Phys. Chem.* **1987**, 91, 257.
22. Cushing, B. L.; Kolesnichenko, V. L.; O'Connor, C. J. *Chem. Rev.* **2004**, 104, 3893.
23. Kuo, C.-L.; Huang, M. H. *J. Phys. Chem. C* **2008**, 112, 11661.
24. Das, S.; Basu, S.; Majumdar, G.; Chakravorty, D.; Chaudhuri, S. *J. Nanosci. Nanotechnol.* **2007**, 7, 4402.
25. Jiang, Y.; Yang, D.; Zhang, L.; Li, L.; Sun, Q.; Zhang, Y.; Li, J.; Jiang, Z. *Dalton Trans.* **2008**, 31, 4165.
26. Hu, Y.; Afzaal, M.; Malik, M. A.; O'Brien, P. *J. Crys. Growth* **2006**, 297, 61.
27. Kasai, S.; Asai, T. *Appl. Phys. Express* **2008**, 1, 083001/1.
28. Huang, M. H.; Mao, S.; Feick, H.; Yan, H.; Wu, Y.; Kind, H.; Webber, E.; Russo, R.; Yang, P. *Science* **2001**, 292, 1897.

29. Law, M.; Greene, L. E.; Hohnson, J. C.; Saykaly, R.; Yang, P. *Nat. Mater.* **2005**, 4, 455.
30. Lin, M. C.; Chu, C. J.; Tsai, L. C.; Lin, H. Y.; Wu, C. S.; Wu, Y. P.; Wu, Y. N.; Shieh, D. B.; Su, Y. W.; Chen, C. D. *Nano Letters* **2007**, 7, 3656.
31. Leao, C. R.; Fazzio, A.; Silva, A. J. R. d. *Nano Letters* **2007**, 7, 1172.
32. Kruyt, H. R.; Arkel, A. E. v. *Kolloid-Z* **1928**, 32, 29.
33. Furuta, N.; Ohasi, Y.; Itinose, H.; Igarashi, Y. *J. Appl. Phys.* **1975**, 14, 929.
34. Wu, Y.; Yang, P. *J. Am. Chem. Soc.* **2001**, 123, 3165.
35. Wu, Y.; Yang, P. *Chem. Mater* **2000**, 12, 605.
36. Chen, C. C.; Yeh, C. C. *Adv. Mater.* **2000**, 12, 738.
37. Duan, X.; Lieber, C. M. *Adv. Mater.* **2000**, 12, 298.
38. Martin, C. R. *Acc. Chem. Res.* **1995**, 28, 61.
39. T, M. W.; Jiang, J. S.; Searson, P. C.; Chien, C. L. *Science* **1993**, 261, 1316.
40. Yu, Y.-Y.; Chang, S. S.; Lee, C.-L.; Wang, C. R. C. *J. Phys. Chem. B* **1997**, 101, 6661.
41. He, R. R.; Law, M.; Fan, R.; F, K.; Yang, P. *Nano Letters* **2002**, 2, 1109.
42. Peng, X. G.; Manna, L.; Yang, W. D.; J, W.; Scher, E.; Kadavanich, A.; Alivatos, A. P. *Nature* **2000**, 404, 59.
43. Sun, Y.; Xia, Y. *Adv. Mater.* **2002**, 14, 833.
44. Lopes, W. A. *Phys. Rev. E* **2002**, 65, 031606.
45. Wilbur, J. L.; Kim, E.; Y, X.; Whitesides, G. M. *Adv. Mater.* **1997**, 7, 649.
46. Chesnel, K.; Fullerton, E. E.; Carey, M. J.; Kortright, J. B.; Kevan, S. D. *Phys. Rev. B: Condens. Matter Mater. Phys.* **2008**, 78, 132409/1.
47. Hale, R. L.; Lu, A. T.; Myers, D. J.; Rabinowitz, J. D.; Wensley, M. J. Thin-film drug delivery device. **2007**.
48. Kratschmer, W.; Lamb, L. D.; Fostiropoulos, K.; Huffman, D. R. *Nature* **1990**, 347, 354.
49. Dillon, A. C. *Nature* **1997**, 386, 377.
50. Gadd, G. E. *Science* **1997**, 277, 933.
51. Collins, P. G.; Zettl, A.; Bando, H.; Thess, A.; Smalley, R. E. *Science* **1997**, 278, 100.
52. Ghosh, S.; Sood, A. K.; Kumar, N. *Science* **2003**, 299, 1042.
53. Wagner, H. D.; Lourie, O.; Feldman, Y.; Tenne, R. *Appl. Phys. Lett.* **1998**, 72, 188.
54. Tanev, P. T.; Pinnavaia, T. J. *Science* **1995**, 267, 865.
55. Forster, S.; Antonietti, M. *Adv. Mater.* **1998**, 10, 195.
56. Cundy, C. S.; Cox, P. A. *Chem. Rev.* **2003**, 103, 663.
57. Jansen, J. C., In *Introduction to Zeolite Science and Pratice.*, Bekkum, H. v.; Flanigen, E. M.; Jacobs, P. A.; Jansen, J. C., Eds. Elsevier: Amsterdam, **2001**, 175.
58. Avnir, D.; Levy, D.; Reisfeld, R. *J. Phys. Chem.* **1984**, 88, 5956.
59. Levy, D.; Einhorn, S.; Avnir, D. J. *J. Non-Cryst. Solids* **1989**, 113, 137.
60. Siegel, R. W.; Chang, S. K.; Ash, B. J.; Stone, J.; Ajayan, P. M.; Doremus, R. W.; Schadler, L. *Scripta Mater.* **2001**, 44, 2063.
61. Tu, J. P.; Wang, N. Y.; Yang, Y. Z.; Qi, W. X.; Liu, F.; Zhang, X. B.; Lu, H. M.; Liu, M. S. *Mater. Lett.* **2002**, 52, 452.
62. Haruta, M.; Delmon, B. *J. Chim. Phys.* **1986**, 83, 859.
63. Murray, C. B.; Norris, D. J.; Bawendi, M. G. *J. Am. Chem. Soc.* **1993**, 115, 8706.
64. Hench, L. L.; West, J. K. *Chem. Rev.* **1990**, 90, 33.

65. Brinker, C. J.; Scherer, G. W., *Sol-Gel Science: The Physics and Chemistry of Sol-Gel Processing.* Academic Press, Inc.: San Diego, **1990**.
66. Brinker, C. J.; Scherer, G. W., *Sol-Gel Science.* Academic Press: New York, 1989.
67. Hench, L. L.; West, J. K. *Chem. Rev.* **1990,** 90, 33.
68. Jana, N. R.; Earhart, C.; Ying, J. Y. *Chem. Mater.* **2007,** 19, 5074.
69. Klein, L. C., *Sol-Gel Technology for Thin Films, Fibers, Preforms, Electronics and Specialty Shapes.* Noyes Publications: Park Ridge, NJ, **1988**.
70. Byrappa, K.; Yoshimura, M., *Hydrothermal Technology for Crystal Growth (Materials and Processing Technology).* Noyes Publications Park Ridge, New Jersey, 2001.
71. Blander, M., *Molten Salt Chemistry*. Interscience Publishers: New York, **1964**.
72. Bloom, H., *The chemistry of molten salts;an introduction to the physical and inorganic chemistry of molten salts and salt vapors.* W. A. Benjamin: New York, **1967**.
73. Mao, Y.; Banerjee, S.; Wong, S. S. *J. Am. Chem. Soc.* **2003**, 125, 15718.
74. Mao, Y.; Wong, S. S. *Adv. Mater.* **2005**, 17, 2194.
75. Park, T.-J.; Papaefthymiou, G. C.; Moodenbaugh, A. R.; Mao, Y.; Wong, S. S. *J. Mater. Chem.* **2005**, 15, 2099.
76. Jones, A. C.; Hitchman, M. L., *Chemical Vapour Deposition: Precursors, Processes and Applications.* Royal Society of Chemistry: Cambridge, **2009**.
77. Fanun, M., *Microemulsion:Properties and Applications*. CRC Press: London, **2008**.
78. Campbell, S. A., *The Science and Engineering of Microelectronic Fabrication.* Oxford University Press: Oxford, **2001**.
79. Xia, Y.; Whitesides, G. M. *Angew. Chem. Int. Ed.* **1998**, 37, 551.
80. Xia, Y.; Whitesides, G. M. *Annu. Rev. Mater. Sci.* **1998**, 28, 153.
81. Xia, Y.; Whitesides, G. M. *Annu. Rev. Mater. Sci.* **1998**, 28, 153.
82. Xia, Y. *Adv. Mater*, **2004**, 16 (special issue dedicated to George Whitesides).
83. Eigler, D. M.; Schweizer, E. K. *Nature* **1990**, 344, 524.
84. Baur, C.; Bugacov, A.; Koel, B. E.; Madhukar, A.; Montoya, N.; Ramachandran, T. R.; Requicha, A. A. G.; Resch, R.; Will, P. *Nanotechnology* **1998**, 9, 360.
85. Bentzon, M. D.; Tholen, A. *Ultramicroscopy* **1990**, 38, 105.
86. Huang, Y.; Duan, X.; Wei, Q.; Lieber, C. M. *Science* **2001**, 291, 630.
87. Robertson, D. H.; Brenner, D. W.; Mintmire, J. W. *Phys. Rev. B* **1992**, 45, 12592.
88. Niitzenadel, C.; Ziittel, A.; Chartouni, D.; Schmid, G.; Schlapbach, L. *Eur. Phys. J.* **2000**, 245, D8.
89. Reed, M. A.; Zhou, C.; Muller, C. J.; Burgin, T. P.; Tour, J. M. *Science* **1997**, 278, 252.
90. Cui, X. D.; Primak, A.; Zarate, X.; Tomfohr, J.; Sankey, O. F.; Moore, A. L.; Moore, T. A.; Gust, D.; Harris, G.; Lindsay, S. M. *Science* **2001**, 294, 571.
91. Collier, C. P.; Mattersteig, G.; Wong, E. W.; Luo, Y.; Beverly, K.; Sampaio, J.; Raymo, F. M.; Stoddart, J. F.; Heath, J. R. *Science* **2000**, 289, 1172.
92. Collier, C. P.; Wong, E. W.; Belohradsky, M.; Raymo, F. M.; Stoddart, J. F.; Kuekes, P. J.; Williams, R. S.; Heath, J. R. *Science* **1999**, 285, 391.
93. Tans, S. J.; Verschueren, A. R. M.; Dekker, C. *Nature* **1998**, 393, 49.
94. Liang, W.; Shores, M. P.; Bockrath, M.; Long, J. R.; Park, H. *Nature* **2002**, 417, 725.
95. Postma, H. W. C.; Peepen, T.; Yao, Z.; Grifoni, M.; Dekker, C. *Science* **2001**, 293, 76.
96. Liu, X.; Lee, C.; Zhou, C.; Han, J. *Appl. Phys. Lett.* **2001**, 79, 3329.

97. Kong, J.; Franklin, N. R.; Zhou, C.; Chapline, M. G.; Peng, S.; Cho, K.; Dai, H. *Science* **2000**, 287, 622.
98. Collins, P. G.; Arnold, M. S.; Avouris, P. *Science* **2001**, 292, 706.
99. O'Regan, B.; Grätzel, M. *Nature* **1991**, 353, 737.
100. Gur, I.; Fromer, N. A.; Geier, M. L.; Alivisatos, A. P. *Science* **2005**, 310, 462.
101. Hashmi, A. S. K.; Hutchings, G. J. *Angew. Chem. Int. Ed.* **2006**, 45, 7896.
102. Noda, S.; Tomoda, K.; Yamamoto, N.; Chutinan, A. *Science* **2000**, 289, 604.
103. Briner, A.; Wehrspohn, R. B.; Gosele, U.; Busch, K. *Adv. Mater.* **2001**, 13, 377.
104. Wanke, M. C.; Lehmann, O.; Muller, K.; Wen, Q. Z.; Stuke, M. *Science* **1997**, 275, 1284.
105. Xia, Y.; Gates, B.; Yin, Y.; Lu, Y. *Adv. Mater.* **2000**, 12, 693.
106. Pankhurst, Q. A.; Conolly, J.; Jones, S. K.; Dobson, J. *J. Phys. D: Appl. Phys.* **2003**, 36, R167.
107. Niemeyer, C. M.; Mirkin, C. A., *Nanobiotechnology: Concepts, Applications and Perspectives.* Wiley-VCH: Weinheim, **2004**.
108. Zhou, H.; Park, T.-J.; Wong, S. S. *J. Mater. Res.* **2006**, 21, 2941.
109. Zhou, H.; Mao, Y.; Wong, S. S. *J. Mater. Chem.* **2007**, 17, 1707.
110. Zhou, H.; Mao, Y.; Wong, S. S. *Chem. Mater.* **2007**, 19, 5238.
111. Zhou, H.; Wong, S. S. *ACS Nano* **2008**, 2, 944.
112. Zhou, H.; Yiu, Y.; Aronson, M. C.; Wong, S. S. *J. Solid State Chem.* **2008**, 181, 1539.
113. Zhou, H.; Zhou, W.-P.; Adzic, R. R.; Wong, S. S. *J. Phys. Chem. C* **2009**, 113, 5460.
114. Sleight, A. W. *Mater, Res. Bull.* **1974**, 9, 1185.
115. Longo, J. M.; Donohue, P. C.; Batson, D. A. *Inorg. Synth.* **1973**, 14, 146.
116. Wainer, E.; Wentworth, C. *J. Am. Ceram. Soc.* **1952**, 35, 207.
117. Lee, S.; Park, J.-G.; Adroja, D. T.; Khomskil, D.; Streltsov, S.; McEwen, K. A.; Sakai, H.; Yoshimura, K.; Anisimov, V. I.; Mori, D.; Kanno, R.; R, I. *Nat. Mater.* **2006**, 5, 471.
118. Hwang, G. W.; Kim, W. D.; Min, Y.-S.; Cho, Y. J.; Hwang., C. S. *J. Electrochem. Soc.* **2006**, 153, F20.
119. Yang, X. N.; Huang, B. B.; Wang, H. B.; Shang, S. X.; Yao, W. F.; Wei, J. Y. *J. Cryst. Growth* **2004**, 270, 98.
120. Wang, S. W.; Wang, H.; Wu, X.; Shang, S.; Wang, M.; Li, Z.; Lu, W. *J. Cryst. Growth* **2001**, 224, 323.
121. Wu, X. M.; Wang, S. W.; Wang, H.; Wang, Z.; Shang, S. X.; Wang, M. *Thin Solid Films* **2000**, 370, 30.
122. Wang, S. W.; Wang, H.; Shang, S. X.; Huang, J.; Wang, Z.; Wang, M. *J. Cryst. Growth* **2000**, 217.
123. Wu, W.; Fumoto, K.; Oishi, Y.; Okuyama, M.; Hamakawa, Y. *Jpn. J. Appl. Phys.* **1996**, 35, 1560.
124. Yao, W. F.; Wang, H.; Xu, X. H.; Zhou, J. T.; Yang, X. N.; Zhang, Y.; Shang, S. X. *Appl. Catal. A* **2004**, 259, 29.
125. Barringer, E. A.; Bowen, H. K. *J. Am. Ceram. Soc.* **1982**, 65, C199.
126. Fegley, B., Jr.; Barringer, E. A., In *Better Ceramics Through Chemistry*, Brinker, C. J.; Clark, D. E.; Ulrich, D. R., Eds. Elsevier: New York, **1984**, Vol. 32.
127. Fegley, B., Jr.; White, P.; Bowen, H. K. *Am. Ceram. Soc. Bull.* **1985**, 64, 1115.

128. Hardy, A.; Gowda, G.; McMahan, T. J.; Riman, R. E.; E., R. W.; Bowen, H. K., In *Ultrastructure Processing of Advanced Ceramics.*, Mackenzie, J. D.; Ulrich, D. R., Eds. Wiley: New York, **1988**.
129. Fegley, B., Jr.; Barringer, E. A.; Bowen, H. K. *J. Am. Ceram. Soc.* **1984,** 67, C113.
130. Carroll-Porczynski, C. Z., *Aduanced Materials*. Chemical Publishing Co.: New York, **1962**.
131. McCreight, L. R.; Rauch, H. W., Sr.; Sutton, W. H., *Ceramic Fibers and Fibrous Composite Materials.* Academic Press: New York, **1965**.
132. Rauch, H. W., Sr.; Sutton, W. H.; McCreight, L. R., *Ceramic Fibers and Fibrous Composite Materials.* Academic Press: New York, **1968**.
133. Seufert, L. E. US. Patent No. 3,808,015, **1974**.
134. Miyahara, K.; Nakayama, N. Process for Producing Polycrystalline Oxide Fibers. US. Patent 4,159,205, **1979**.
135. Leitheiser, M.; Snowman, H. G. Non-Fused Alumina Based Abrasive Material. . US. Patent Appl. 145,383, **1980**.
136. Schroeder, H. *Opt. Acta* **1962**, 9, 249.
137. Mackenzie, J. D. *J. Non-Cryst. Solids* **1982**, 41, 1.
138. Hench, L. L.; West, J. K. *Chem. Rev.* **1990**, 90, 33.
139. Rabin, Y.; Tanaka, M. *Phys. Rev. Lett.* **2005**, 94, 148103.
140. Sano, T.; Iguchi, N.; Iida, K.; Sakamoto, T.; Baba, M.; Kawaura, H. A. *Phys. Lett.* **2003**, 83, 4438.
141. Lira, H. D. L.; Paterson, R. *J. Membr. Sci.* **2002**, 206, 375.
142. Masuda, H.; Yamada, M.; Matsumoto, F.; Yokoyama, S.; Mashiko, S.; Nakao, M.; Nishio, K. *Adv. Mater.* **2006**, 18, 213.
143. Xia, Y.; Yang, P.; Sun, Y.; Wu, Y.; Mayers, B.; Gates, B.; Yin, Y.; Kim, F.; Yan, H. *Adv. Mater.* **2003**, 15, 353.
144. Zhu, H.; Gao, X.; Lan, Y.; Song, D.; Xi, Y.; Zhao, J. *J. Am. Chem. Soc.* **2004**, 126, 8380.
145. Armstrong, A. R.; Armstrong, G.; Canales, J.; Bruce, P. G. *Angew. Chem. Int. Ed.* **2004**, 43, 2286.
146. Tian, Z. R.; Voigt, J. A.; Liu, J.; Mckenzie, B.; Xu, H. *J. Am. Chem. Soc.* **2003**, 125, 12384.
147. Kasuga, T.; Hiramatsu, M.; Hoson, A.; Sekino, T.; Niihara, K. *Adv. Mater.* **1999**, 11, 1307.
148. Zhao, L.; Steinhart, M.; Yu, J.; Gosele, U. *J. Mater. Res.* **2006**, 21, 685.
149. Peng, H.; Li, G.; Zhang, Z. *Mater. Lett.* **2005**, 59, 1142.
150. Mao, Y.; Banerjee, S.; Wong, S. S. *Chem. Commun.* **2003**, 408.
151. Mao, Y.; Kanungo, M.; Hemraj-Benny, T.; Wong, S. S. *J. Phys. Chem. B* **2006**, 110, 702.
152. Patzke, G. R.; Krumeich, F.; Nesper, R. *Angew. Chem. Int. Ed.* **2002**, 41, 2446.
153. Lai, Y.; Sun, L.; Chen, Y.; Zhuang, H.; Lin, C.; Chin, J. W. *J. Electrochem. Soc.* **2006**, 153, D123.
154. Mao, Y.; Wong, S. S. *J. Am. Chem. Soc.* **2006**, 128, 8217.
155. Park, T.-J.; Mao, Y.; Wong, S. S. *Chem. Commun.* **2004**, 2708.
156. Hou, Y.; Huang, Z.; Xue, J.; Wu, Y.; Shen, X.; Chu, J. *Appl. Phys. Lett.* **2005**, 86, 112905.

157. Wang, Z.; Yang, C. H.; Sun, D. L.; Hu, J. F.; Wang, H.; Chen, H. C.; Fang, C. S. *Mater. Sci. Eng. B* **2003**, 102, 335.
158. Gu, H.; Dong, C.; Chen, P.; Bao, D.; Kuang, A.; Li, X. *J. Cryst. Growth.* **1998**, 186, 403.
159. Joshi, P. C.; Mansingh, A. *Appl. Phys. Lett.* **1991**, 59, 2389.
160. Su, W.-F.; Lu, Y.-T. *Mater. Chem. Phys.* **2003**, 80, 632.
161. Schwartz, R. W. *Chem. Mater.* **1997**, 9, 2325.
162. Yang, G.; Yue, Z.; Gui, Z.; Li, L. *J. Appl. Phys.* **2008**, 104, 074115/1.
163. Hu, H.; Krupanidhi, S. B. *J. Mater. Res.* **1994**, 1484.
164. Li, X. *J. Mater. Sci.* **2008**, 19, 271.
165. Davydov, B. L.; Yagodkin, D. I. *Quantum Electronics* **2005**, 35, 1071.
166. Feng, Z.; Luo, H.; Yin, Z.; Guang, C.; Ling, N. *Appl. Phys. A* **2004**, 81, 1245.
167. Wu, M. K.; Ashburn, J. R.; Torng, C. J.; Hor, P. H.; Meng, R. L.; L. Gao; Huang, Z. J.; Wang, Y. Q.; Chu, C. W. *Phys. Rev. Lett.* **1987**, 58, 908.
168. Noue, J.; Maekawa, S.; Physica C: Superconductivity : Amsterdam, **1994**.
169. Yajima, T.; Suzuki, H.; Yogo, T.; Iwahara, H. *Solid State Ionics* **1992**, 51, 101.
170. Shende, R. V.; Krueger, D. S.; Rossetti, G. A.; Lombardo, S. J. *J. Am. Ceram. Soc. Bull.* **2001**, 84, 1648.
171. Macmanus-Driscoll, J. L.; Foltyn, S. R.; Jia, Q. X.; Wang, H.; Serquis, A.; Civale, L.; Maiorov, B.; Hawley, M. E.; Maley, M. P.; Peterson, D. E. *Nat. Mater.* **2004**, 3, 439.
172. Koenig, J.; Jaffe, B. *J. Am. Ceram. Soc.* **1964**, 47, 87.
173. Kang, S.; Leonard, K. J.; Martin, P. M.; Li, J.; Goyal, A. *Supercond. Sci. Technol.* **2007**, 20, 11.
174. Viviani, M.; Buscaglia, M. T.; Buscaglia, V.; Leoni, M.; Nanni, P. *J. Eur. Ceram. Soc.* **2001**, 21, 1981.
175. Erb, A.; Traulsen, T.; Muller-Vogt, G. *J. Cryst. Growth.* **1994**, 137, 487.
176. L.Macmanus-Driscoll, J.; Foltyn, S. R.; Jia, Q. X.; Wang, H.; Serquis, A.; Civale, L.; Maiorov, B.; Hawley, M. E.; Maley, M. P.; Peterson, D. E. *Nat. Mater.* **2004**, 3, 439.
177. Boukamp, B. A. *Nat. Mater.* **2003**, 2, 296.
178. Hayashi, Y.; Kimura, T.; Yamaguchi, T. *J. Mater. Sci.* **1986**, 21, 757.
179. Volkov, S. V. *Chem. Soc. Rev.* **1990**, 19, 21.
180. Mao, Y.; Wong, S. S. *Adv. Mater,* **2005**, 17, 2194.
181. Zboril, R.; Mashlan, M.; Petridis, D. *Chem. Mater.* **2002**, 14, 969.
182. Yoon, K. H.; Cho, Y. S.; Kang, D. H. *J. Mater. Sci.* **1998**, 33, 2977.
183. Bloom, H., *The Chemistry of Molten Salts.* W. A. Benjamin, Inc.: New York, **1967**.
184. Badica, P.; Aldica, G.; Iyo, A.; Bradea, I.; Jaklovszky, J. *Mater. Lett.* **2003**, 58, 250.
185. Ling, H.; Li, A.; Wu, D.; Tang, Y.; Liu, Z.; Ming, N. *Mater. Chem. Phys. C* **2002**, 75, 170.
186. Sin, A.; Montaser, B. E.; Odier, P.; Weiss, F. *J. Am. Ceram. Soc.* **2002**, 85, 1928.
187. Brzezinska-Miecznik, J.; Haberko, K.; Bucko, M. M. *Mater. Lett.* **2002**, 56, 273.
188. Kirby, N. M.; Van Riessen, A.; Buckley, C. E.; Wittorff, V. W. *J. Mater. Sci. Eng. B* **2005**, 40, 97.
189. Lencka, M. M.; Nielsen, E.; Anderko, A.; Riman, R. E. *Chem. Mater.* **1997**, 9, 1116.
190. Lu, Z.; Tang, Y.; Chen, L.; Li, Y. *J. Cryst. Growth* **2004**, 266, 539.
191. Kutty, T. R. N.; Vivekanandan, R.; Philip, S. *J. Mater. Sci.* **1990**, 25, 3649.
192. Vivekanadan, R.; Philip, S.; Kutty, T. R. N. *Mater. Res. Bull.* **1987**, 22, 99.

193. Millot, N.; Xin, B.; Pighini, C.; Aymes, D. *J. Eur. Ceram. Soc.* **2005**, 25, 2013.
194. Kolen'ko, Y. V.; Burukhin, A. A.; Churagulov, B. R.; Oleinikov, N. N.; Vanetsev, A. S. *Inorg. Mater.* **2002**, 38, 252.
195. Azad, A.; Subramaniam, S. *Mater. Res. Bull.* **2002**, 37, 85.
196. Yamanaka, S.; Hamaguchi, T.; Oyama, T.; Matsuda, T.; Kobayashi, S.; Kurosaki, K. *J. Alloys Compd.* **2003**, 359, 1.
197. Robertz, B.; Boschini, F.; Cloots, R.; Rulmont, A. *Int. J. Inorg. Mater.* **2001**, 3, 1185.
198. Athawale, A. A.; Bapat, M. *J. Metastable Nanocryst. Mater.* **2005**, 23, 3.
199. Ubaldini, A.; Buscaglia, V.; Uliana, C.; Costa, G.; Ferretti, M. *J. Am. Ceram. Soc.* **2003**, 86, 19.
200. Boschini, F.; Robertz, B.; Rulmont, A.; Cloots, R. *J. Eur. Ceram. Soc.* **2003**, 23, 3035.
201. Niederberger, M.; Pinna, N.; Polleux, J.; Antonietti, M. *Angew. Chem., Int. Ed.* **2004**, 43, 2270.
202. Leonard, K. J.; Sathyamurthy, S.; Paranthaman, M. P. *Chem. Mater.* **2005**, 17, 4010.
203. Palchik, O.; Zhu, J.; Gedanken, A. *J. Mater. Chem.* **2000**, 10, 1251.
204. El-Sayed, M. A. *Acc. Chem. Res.* **2004**, 37, 326.
205. Lee, S.-M.; Jun, Y.-W.; Cho, S.-N.; Cheon, J. *J. Am. Chem. Soc.* **2002**, 124, 11244.
206. Jun, Y.-W.; Choi, J.-S.; Cheon, J. *Angew. Chem., Int. Ed.* **2006**, 45, 3414.
207. Liu, X.; McCandlish, E. F.; McCandlish, L. E.; Mikulka-Bolen, K.; Ramesh, R.; Cosandey, F.; Jr., G. A. R.; Riman, R. E. *Langmuir* **2005**, 21, 3207.
208. Bish, D. L.; Howard, S. A. *J. Appl. Crystallogr.* **1988**, 21, 86.
209. Orlhac, X.; Fillet, C.; Deniard, P.; Dulac, A. M.; Brec, R. *J. Appl. Crystallogr.* **2001**, 34, 114.
210. Toby, B., H. *J. Appl. Crystallogr.* **2001**, 34, 210.
211. Smith, D. K.; Newkirk, W. *Acta Crystallogr.* **1965**, 18, 983.
212. Robinson, K.; Gibbs, G. V.; Ribbe, P. H. *Am. Miner.* **1971**, 56, 782.
213. De Villiers, J. P. R. *Am. Miner.* **1971**, 56, 758.
214. Levin, I.; Amos, T. G.; Bell, S. M.; Farber, L.; Vanderah, T. A.; Roth, R. S.; Toby, B., H. *J. Solid State Chem.* **2003**, 175, 170.
215. Eckert, J. O., Jr.; Huang-Houston, C. C.; Gersten, B. L.; Lencka, M. M.; Riman, R. E. *J. Am. Ceram. Soc.* **1996**, 79, 2929.
216. Mao, Y.; Banerjee, S.; Wong, S. S. *J. Am. Chem. Soc.* **2003**, 125, 15718.
217. Park, J.-H.; Lee, D.-H.; Shin, H.-S.; Lee, B.-K. *J. Am. Ceram. Soc.* **1996**, 79, 1130.
218. Fuenzalida, V. M.; Pilleux, M. E. *J. Mater. Res.* **1995**, 10, 2749.
219. Lyapin, A.; Jeurgens, L. P. H.; Graat, P. C. J.; Mittemeijer, E. J. *Surf. Interface Anal.* **2004**, 36, 989.
220. Rao, B. V.; Rambabu, U.; Buddhudu, S. *Physica B.* **2006**, 382, 86.
221. Li, J.; Kuwabara, M. *Adv. Mater.* **2003**, 4, 143.
222. Gopolan, S.; Mehta, K.; Virkar, A. V. *J. Mater. Res.* **1996**, 11, 1863.
223. Barin, I.; knacke, O., *Thermochemical Properties of Inorganic Substances.* Springer-Verlag: New York, **1973**.
224. Deloume, J.-P.; Scharff, J.-P.; Marote, P.; Durand, B.; Abou-Jalil, A. *J. Mater. Chem.* **1999**, 9, 107.
225. Mamantov, G.; Braunstein, J., *AdVances in Molten Salt Chemistry;* . Plenum Press: New York, **1973**; Vol. 4.

226. Sundermeyer, W. *Chem. Ber*. **1964**, 97, 1069.
227. Liu, H.; Hu, C.; Wang, Z. L. *Nano Lett.* **2006**, 6, 1535.
228. Ito, Y.; Shimada, S.; Inagaki, M. *J. Am. Ceram. Soc.* **1995**, 78, 2695.
229. Ito, Y.; Jadidian, B.; Allahverdi, M.; Safari, A. In *Particle Shape Control of Molten Salt Synthesized Lead Titanate.*, Proceedings of the 2000 IEEE International Symposium on Applications of Ferroelectrics., Honolulu, HI, 2000; Institute of Electrical Engineers: New York: Honolulu, HI, 2000; p 389.
230. Murphy, C. J. *Science* **2002**, 298, 2139.
231. Puntes, V. F.; Krishnan, K. M.; Alivisatos, A. P. *Science* **2001**, 291, 2115.
232. Filankembo, A.; Giorgio, S.; Lisiecki, I.; Pileni, M. P. *J. Phys. Chem. B* **2003**, 107, 7492.
233. Xia, Y.; Yang, P.; Sun, Y.; Wu, Y.; Mayers, B.; Gates, B.; Yin, Y.; Kim, F.; Yan, H. *Adv. Mater*. **2003**, 15, 353.
234. Lee, S.-M.; Cho, S.-N.; Cheon, J. *AdV. Mater.* **2003**, 15, 441.
235. Park, T.-J.; Wong, S. S. *Chem. Mater.* **2006**, 18, 5289.
236. Yoon, K. H.; Cho, Y. S.; Lee, D. H.; Kang, D. H. *J. Am. Ceram. Soc.* **1993**, 76, 1373.
237. Wang, L.; Zhu, Y. *Chem. Lett.* **2003**, 32, 594.
238. Furneaux, R. C.; Rigby, W. R.; P.Davidson, A. *Nature* **1989**, 337, 147.
239. Fleisher, R. L.; Price, P. B.; Walker, R. M., *Nuclear Tracks in Solids.* University of California Press: Berkeley, CA, **1975**.
240. Tonucci, R. J.; Justus, B. L.; Campillo, A. J.; Ford, C. E. *Science* **1992,** 258, 783.
241. Possin, G. E. *Rev. Sci. Instrum.* **1970**, 41, 772.
242. Wu, C.; Bein, T. *Science* **1994**, 264, 1757.
243. Fan, S.; Chapline, M. G.; Franklin, N. R.; Tombler, T. W.; Cassell, A. M.; Dai, H. *Science* **1999**, 283, 512.
244. Enzel, P.; Zoller, J. J.; Bein, T. *Chem. Commun.* **1992**, 633.
245. Guerret-Piecourt, C.; Bouar, Y. L.; Loiseau, A.; Pascard, H. *Nature* **1994**, 375, 564.
246. Ajayan, P. M.; Stephan, O.; Redlich, P.; Colliex, C. *Nature* **1995**, 375, 564.
247. Keller, F.; Hunter, M.; Robinson, D. L. *J. Electrochem. Soc.* **1953**, 100, 411.
248. J.P.O'Sullivan; Wood, G. C. *Proc. R. Soc. Lond., Ser. A* **1970**, 317, 511.
249. Ebihara, K.; Takahashi, H.; Nagayama, M. *J. Surf. Fin. Soc. Jpn.* **1983**, 34, 548.
250. Reynolds, D. C.; Look, D. C.; Jogai, B.; Litton, C. W.; Collins, T. C.; Harsch, W.; Cantwell, G. *Phys. Rev. B* **1998**, 57, 12151.
251. Huang, M. H.; Mao, S.; Feick, H.; Yan, H.; Wu, Y.; Kind, H.; Webber, E.; Russo, R.; Yang, P. *Science* **2001**, 292, 1897.
252. Kind, H.; Yan, H.; Messer, B.; Law, M.; Yang, P. *Adv. Mater,* **2002**, 14, 158.
253. Soci, C.; Zhang, A.; Xiang, B.; Dayeh, S. A.; Aplin, D. P. R.; Park, J.; Bao, X. Y.; Lo, Y. H.; Wang, D. *Nano Lett.* **2007**, 7, 1003.
254. Law, M.; Greene, L. E.; Johnson, J. C.; Saykally, R.; Yang, P. *Nat. Mater.* **2005**, 4, 455.
255. Suh, D.-I.; Lee, S.-Y.; Kim, T.-H.; Chun, J.-M.; Suh, E.-K.; Yang, O.-B.; Lee, S.-K. *Chem. Phys. Lett.* **2007**, 442, 348.
256. Goldberger, J.; Sirbuly, D. J.; Law, M.; Yang, P. *J. Phys. Chem. B* **2005**, 109, 9.
257. Noh, Y.-Y.; Cheng, X.; Sirringhaus, H.; Sohn, J. I.; Welland, M. E.; Kang, D. J. *Appl. Phys. Lett.* **2007**, 91, 043109-1.

258. Wang, X.; Zhou, J.; Lao, C.; Song, J.; Xu, N.; Wang, Z. L. *Adv. Mater,* **2007**, 19, 1627.
259. Wang, Z. L.; Song, J. *Science* **2006**, 312, 242.
260. Gao, P. X.; Song, J.; Liu, J.; Wang, Z. L. *Adv. Mater,* **2007**, 19, 67.
261. Wang, X.; Liu, J.; Song, J.; Wang, Z. L. *Nano Lett.* **2007**, 7, 2475.
262. Park, W. I.; Yi, G.-C.; Kim, M.; Pennycook, S. J. *Adv. Mater,* **2002**, 14, 1841.
263. Jeong, M.-C.; Oh, B.-Y.; Nam, O.-H.; Kim, T.; Myoung, J.-M. *Nanotechnology* **2006**, 17, 526.
264. Yang, P.; Han, H.; Mao, S.; Russo, R.; Johnson, J.; Saykally, R.; Morris, N.; Pham, J.; He, R.; Choi, H.-J. *Adv. Funct. Mater.* **2002**, 12, 323.
265. Umar, A.; Kim, B.-K.; Kim, J.-J.; Hahn, Y. B. *Nanotechnology* **2007**, 18, 175606-1.
266. Sun, Y.; Fuge, G. M.; Ashfold, M. N. R. *Chem. Phys. Lett.* **2004**, 396, 21.
267. Vayssieres, L. *Adv. Mater,* **2003**, 15, 464.
268. Greene, L. E.; Law, M.; Goldberger, J.; Kim, F.; Johnson, J. C.; Zhang, Y.; Saykally, R. J.; Yang, P. *Angew. Chem. Int. Ed.* **2003**, 42, 3031.
269. Greene, L. E.; Law, M.; Tan, D. H.; Montano, M.; Goldberger, J.; Somorjai, G.; Yang, P. *Nano Lett.* **2005**, 5, 1231.
270. Jiang, X.; Herricks, T.; Xia, Y. *Nano Lett.* **2002**, 2, 1333.
271. Musa, A. O.; Akomolafe, T.; Carter, M. J. *Sol. Energy Mater. Sol. Cells* **1998**, 51, 305.
272. Reitz, J. B.; Solomon, E. I. *J. Am. Chem. Soc.* **1998**, 120, 11467.
273. Lanza, F.; Feduzi, R.; Fuger, J. *J. Mater. Res.* **1990**, 5, 1739.
274. Podhajecky, P.; Zabransky, Z.; Novak, P.; Dobiasova, Z.; Eerny, R.; Valvoda, V. *Electrochim. Acta* **1990**, 35, 245.
275. Cheng, C.-L.; Ma, Y.-R.; Chou, M. H.; Huang, C. Y.; Yeh, V.; Wu, S. Y. *Nanotechnology* **2007**, 18, 245604-1.
276. Cao, M.; Hu, C.; Wang, Y.; Guo, Y.; Guo, C.; Wang, E. *Chem. Commun.* **2003**, 1884.
277. Wen, X.; Xie, Y.; Choi, C. L.; Wan, K. C.; Li, X.-Y.; Yang, S. *Langmuir* **2005**, 21, 4729.
278. Du, G. H.; Tendeloo, G. V. *Chem. Phys. Lett.* **2004**, 393, 64.
279. Lu, C.; Qi, L.; Yang, J.; Zhang, D.; Wu, N.; Ma, J. *J. Phys. Chem. B* **2004**, 108, 17825.
280. Zhang, W.; Ding, S.; Yang, Z.; Liu, A.; Qian, Y.; Tang, S.; Yang, S. *J. Cryst. Growth* **2006**, 291, 479.
281. Wu, H.; Lin, D.; Pan, W. *Appl. Phys. Lett.* **2006**, 89, 133125-1.
282. Malandrino, G.; Finocchiaro, S. T.; Nigro, R. L.; Bongiorno, C.; Spinella, C.; Fragala, I. L. *Chem. Mater.* **2004**, 16, 5559.
283. Yi-Kun, S.; Cheng-Min, S.; Hai-Tao, Y.; Hu-Lin, L.; Hong-Jun, G. *Trans. Nonferrous Met. SOC. China* **2007**, 17, 783.
284. Gondal, M. A.; Hameed, A.; Yamani, Z. H.; Suwaiyan, A. *Chem. Phys. Lett.* **2004**, 385, 111.
285. Ohmori, T.; Takahashi, H.; Mametsuka, H.; Suzuki, E. *Phys. Chem. Chem. Phys.* **2000**, 2, 3519.
286. Chen, J.; Xu, L.; Li, W.; Gou, X. *Adv. Mater.* **2005**, 17, 582.

287. Fu, Y. Y.; Wang, R. M.; Xu, J.; Chen, J.; Yan, Y.; Narlikar, A. V.; Zhang, H. *Chem. Phys. Lett.* **2003**, 379, 373.
288. Wen, X.; Wang, S.; Ding, Y.; Wang, Z. L.; Yang, S. *J. Phys. Chem. B* **2005**, 109, 215.
289. Wang, X.; Chen, X.; Gao, L.; Zheng, H.; Ji, M.; Tang, C.; Shen, T.; Zhang, Z. *J. Mater. Chem.* **2004**, 14, 905.
290. Xiong, Y.; Li, Z.; Li, X.; Hu, B.; Xie, Y. *Inorg. Chem.* **2004**, 43, 6540.
291. Morber, J. R.; Ding, Y.; Haluska, M. S.; Li, Y.; Liu, J. P.; Wang, Z. L.; Snyder, R. L. *J. Phys. Chem. B* **2006**, 110, 21672.
292. Shen, X.-P.; Liu, H.-J.; Pan, L.; Chen, K.-M.; Hong, J.-M.; Xu, Z. *Chem. Lett.* **2004**, 33, 1128.
293. Sun, Z.; Yuan, H.; Liu, Z.; Han, B.; Zhang, X. *Adv. Mater.* **2005**, 17, 2993.
294. Hulteen, J. C.; Martin, C. R. *J. Mater. Chem.* **1997**, 7, 1075.
295. Martin, C. R. *Science* **1994**, 266, 1961.
296. Martin, C. R. *Chem. Mater.* **1996**, 8, 1739.
297. Mao, Y.; Wong, S. S. *J. Am. Chem. Soc.* **2004**, 126, 15245.
298. Mao, Y.; Zhang, F.; Wong, S. S. *Adv. Mater.* **2006**, 18, 1895.
299. Martin, C. R.; Dyke, L. S. V.; Cai, Z.; Liang, W. *J. Am. Chem. Soc.* **1990**, 112, 8976.
300. Liang, W.; Martin, C. R. *Chem. Mater.* **1991**, 3, 390.
301. Uekawa, N.; Iahii, S.; Kojima, T.; Kakegawa, K. *Mater. Lett.* **2007**, 61, 1729.
302. Ullah, M. H.; Kim, I.; Ha, C.-S. *J. Mater. Sci.* **2006**, 41, 3263.
303. Nashaat, N., N.; Maen, M., H. *Langmuir* **2007**, 23, 13093.
304. Klassen, N. V.; Marchington, D.; Mcgowan, H. C. E. *Anal. Chem.* **1994**, 66, 2921.
305. Prasad, V. D.; Souza, C.; Yadav, D.; Shaikh, A. J.; Vigneshwaran, N. *Spectrochim. Acta, Part A* **2006**, 65, 173.
306. Snitka, V.; Jankauskas, V.; Zunda, A.; Mizariene, V. *Mater. Lett.* **2007**, 61, 1763.
307. Wang, S.-B.; Min, Y.-L.; Yu, S.-H. *J. Phys. Chem. C* **2007**, 111, 3551.
308. Kaur, M.; Muthe, K. P.; Despande, S. K.; Choudhury, S.; Singh, J. B.; Verma, N.; Gupta, S. K.; Yakhmi, J. V. *J. Cryst. Growth* **2006**, 289, 670.
309. Mao, Y.; Wong, S. S. *J. Am. Chem. Soc.* **2006**, 128, 8217.
310. Huang, M. H.; Wu, Y.; Feick, H.; Tran, N.; Weber, E.; Yang, P. *Adv. Mater.* **2001**, 13, 113.
311. Vanheusden, K.; Warren, W. L.; Seager, C. H.; Tallant, D. R.; Voigt, J. A.; Gnade, B. E. *J. Appl. Phys.* **1996**, 79, 7983.
312. Maensiri, S.; Laokul, P.; Promarak, V. *J. Cryst. Growth* **2006**, 289, 102.
313. Xiong, G.; Pal, U.; Serrano, J. G. *J. Appl. Phys.* **2007**, 101, 024317-1.
314. Kaschner, A.; Haboeck, U.; Strassburg, M.; Strassburg, M.; Kaczmarczyk, G.; Hoffmann, A.; Thomsen, C.; Zeuner, A. H. R.; Alves, D. M. H.; Meyer, B. K. *Appl. Phys. Lett.* **2002**, 80, 1909.
315. Amores, J. M. G.; Escribano, V. S.; Busca, G.; Lorenzelli, V. *J. Mater. Chem.* **1994**, 4, 965.
316. Borgohain, K.; Singh, J. B.; Rao, M. V. R.; Shripathi, T.; Mahamuni, S. *Phys. Rev. B* **2000**, 61, 11093.
317. Wang, Y.; Muramatsu, A.; Sugimoto, T. *Colloids Surf., A* **1998**, 134, 281.
318. Music, S.; Czako-Nagy, I.; Salaj-Obelic, I.; Ljubesvic, N. *Mater. Lett.* **1997**, 32, 301.

319. Chernyshova, I. V.; Hochella, M. F.; Madden, A. S. *Phys. Chem. Chem. Phys.* **2007**, 9, 1736.
320. Morin, F. J. *Phys. Rev.* **1950**, 78, 819.
321. Liu, L.; Kou, H.-Z.; Mo, W.; Liu, H.; Wang, Y. *J. Phys. Chem. B* **2006**, 110, 15218.
322. Zysler, R. D.; Winkler, E.; Mansilla, M. V.; Fiorani, D. *Physica B.* **2006**, 384, 277.
323. Bandara, J.; Klehm, U.; Kiwi, J. *Appl. Catal. B* **2007**, 76, 73.
324. Drijvers, D.; Langenhove, H. V.; Beckers, M. *Water Res.* **1999**, 33, 1187.
325. Cochran, R. E.; Shyue, J.-J.; Padture, N. P. *Acta Mater.* **2007**, 55, 3007.
326. Smolenskii, G. A.; Chupis, I. E. *Usp. Fiz. Nauk* **1982**, 137, 415.
327. Smolenskii, G. A.; Chupis, I. E. *Sov. Phys. Usp.* **1982**, 25, 475.
328. Jona, F.; Shirane, G., *Ferroelectric Crystals*. Dover: New York, **1993**.
329. Schmid, H. *Ferroelectrics* **1994**, 162, 317.
330. Hill, N. A. *J. Phys. Chem. B* **2000**, 104, 6694.
331. Lines, M. E.; Glass, A. M., *Principles and Applications of Ferroelectrics and Related Materials*. Oxford Univeristy Press: Oxford, **2001**.
332. Khomskii, D. I. *Bull. Am. Phys. Soc. C* **2001**, 21.002.
333. Cheong, S.-W.; Mostovoy, M. *Nat. Mater.* **2007**, 6, 13.
334. Katsufuji, T. e. a. *Phys. Rev. B* **2001**, 64, 104419.
335. Kimura, T. e. a. *Phys. Rev. B* **2003**, 67, 180401.
336. Wang, J. e. a. *Science* **2003**, 299, 1719.
337. van Aken, B. B.; Palstra, T. T. M.; Filippetti, A.; Spaldin, N. A. *Nat. Mater.* **2004**, 3, 164.
338. Fennie, C. J.; Rabe, K. M. *Phys. Rev. B* **2005**, 72, 100103(R).
339. Ederer, C.; Spaldin, N. A. *Phys. Rev. B* **2006**, 74, 1.
340. Kimura, T. e. a. *Nature* **2003**, 426, 55.
341. Subramanian, M. A. e. a. *Adv. Mater*, **2006**, 18, 1737.
342. Ikeda, N. e. a. *Nature* **2005,** 436, 1136.
343. Taniguchi, K.; Abe, N.; Takenobu, T.; Iwasa, Y.; Arima, T. *Phys. Rev. Lett.* **2006**, 97, 097201.
344. Ehrenberg, H.; H.Weitzel; Heid, C.; Fuess, H.; Wltschek, G.; Kroener, T.; Tol, J. V.; Bonnet, M. *J. Phys.: Condens. Matter* **1997**, 9, 3189.
345. Arkenbout, A. H.; Palstra, T. T. M.; Siegrist, T.; Kimura, T. *Phys. Rev. B* **2006**, 74, 184431-1.
346. Heyer, O.; Hollmann, N.; Klassen, I.; Jodlauk, S.; Bohaty, L.; Becker, P.; Mydosh, J. A.; Lorenz, T.; Khomskii., D. *J. Phys.: Condens. Matter* **2006**, 18, L471.
347. Lautenschlager, G.; Weitzel, H.; Vogt, T.; Hock, R.; Bohm, A.; Bonnet, M.; Fuess, H. *Phys. Rev. B* **1993**, 48, 6087.
348. Lei, S.; Tang, K.; Fang, Z.; Huang, Y.; Zheng., H. *Nanotechnology* **2005**, 16, 2407.
349. Qu, W.; Wlodarski, W.; Meyer, J.-U. *Sensors Actuators B* **2000**, 64, 76.
350. Schultze, V. D.; Wilke, K. T.; Waligora, C. *Anorg. Allg. Chem.* **1967**, 352, 184.
351. Alvrecht, V. R.; Mobius, R. *Anorg. Allg. Chem.* **1972**, 392, 62.
352. Jang, M.; Weakley, T. J. R.; Doxsee, K. M. *Chem. Mater.* **2001**, 13, 519.
353. Chen, S.-J.; Chen, X.-T.; Xue, Z.; Zhou, J.-H.; Li, J.; Hong, J.-M.; You, X.-Z. *J. Mater. Chem.* **2003**, 13, 1132.
354. Zhang, L.; Lu, C.; Wang, Y.; Cheng, Y. *Mater. Chem. Phys.* **2007**, 103, 433.
355. Patzke, G. R.; Krumeich, F.; Nesper, R. *Angew. Chem. Int. Ed. Engl.* **2002**, 41, 2446.

356. Yu, S.-H.; Liu, B.; Mo, M.-S.; Huang, J.-H.; Liu, X.-M.; Y.-T. Qian. *Adv. Funct. Mater.* **2003**, 13, 639.
357. Jung, J.-S.; Ren, L.; O'Connor, C. J. *J. Mater. Chem.* **1992**, 2, 829.
358. Ingham, B.; Chong, S. V.; Tallon, J. L. *Curr. Appl. Phys.* **2006**, 6, 553.
359. Tarte, P.; Liegeois-Duyckaerts, M. *Spectrochim. Acta—Part A* **1972**, 28A, 2029.
360. Ehrenberg, H.; Weitzel, H.; Fuess, H. *Physica B.* **1997**, 560, 234.
361. Mao, Y.; Wong, S. S. *J. Am. Chem. Soc.* **2004**, 126, 15245.
362. Mao, Y.; Zhang, F.; Wong, S. S. *Adv. Mater.* **2006**, 18, 1895.
363. Mao, Y.; Park, T.-J.; Zhang, F.; Zhou, H.; Wong, S. S. *Small* **2007**, 3, 1122.
364. Zhang, F.; Mao, Y.; Park, T.-J.; Wong, S. S. *Adv. Funct. Mater.* **2008**, 18, 112.
365. Shi, H.; Qi, L.; Ma, J.; Cheng, H. *J. Am. Chem. Soc.* **2003**, 125, 3450.
366. Shi, H.; Qi, L.; Ma, J.; Cheng, H.; Zhu, B. *Adv. Mater.* **2003**, 15, 1647.
367. Shi, H.; Qi, L.; Ma, J.; Wu, N. *Adv. Funct. Mater.* **2005**, 15, 442.
368. Shi, H.; Wang, X.; Zhao, N.; Qi, L.; Ma, J. *J. Phys. Chem. B* **2006**, 110, 748.
369. Cheng, S.-F.; Chau, L.-K. *Anal. Chem.* **2003**, 75, 16.
370. Gates, A. T.; Fakayode, S. O.; Lowry, M.; Ganea, G. M.; Murugeshu, A.; Robinson, J. W.; Strongin, R. M.; Warner, I. M. *Langmuir* **2008**, 24, 4107.
371. Hunyadi, S. E.; Murphy, C. J. *J. Mater. Chem.* **2006**, 16, 3929.
372. Leong, W. L.; Lee, P. S.; Mhaisalkar, S. G.; Chen, T. P.; Dodabalapur, A. *Appl. Phys. Lett.* **2007**, 90, 042906-1.
373. Mitsudome, T.; Mikami, Y.; Funai, H.; Mizugaki, T.; Jitsukawa, K.; Kaneda, K. *Agew. Chem.* **2008**, 47, 138.
374. Thomas, J. M. *Pure Appl. Chem.* **1988**, 60, 1517.
375. Zhang, J.; Sakaki, K.; Sutter, E.; Zdzic, R. R. *Science* **2007**, 315, 220.
376. Pina, C. D.; Falletta, E.; Rossi, M. *Nanopart. Catal.* **2008**, 427.
377. Murphy, C. J.; Gole, A. M.; Hunyadi, S. E.; Orendorff, C. J. *Inorg. Chem.* **2006**, 45, 7544.
378. Keebaugh, S.; Kalkan, A. K.; Nam, W. J.; Fonash, S. J. *Electrochem. Solid-State. Lett.* **2006**, 9, H88.
379. Liu, Z.; Searson, P. C. *J. Phys. Chem. B* **2006**, 110, 4318.
380. Cusmà, A.; Curulli, A.; Zane, D.; Kaciulis, S.; Padeletti, G. *Mater. Sci. Engin. C* **2007**, 27, 1158.
381. Basu, M.; Seggerson, S.; Henshaw, J.; Jiang, J.; Cordona, R. d. A.; Lefave, C.; Boyle, P. J.; Miller, A.; Pugia, M.; Basu, S. *(GNWA). Glycoconj. J.* **2004**, 21, 487.
382. Wirtz, M.; Yu, S.; Martin, C. R. *Analyst* **2002**, 127.
383. Pang, Y. T.; Meng, G. W.; Fang, Q.; Zhang, L. D. *Nanotechnology* **2003**, 14, 20.
384. Jeong, D. H.; Zhang, Y. X.; Moskovits, M. *J. Phys. Chem. B* **2004**, 108.
385. Seo, B. I.; Shaislamov, U. A.; Kim, S.-W.; Kim, H.-K.; Hong, S. K.; Yang, B. *Physica E* **2007**, 37, 279.
386. Husain, A.; Hone, J.; Postma, H. W. C.; Huang, X. M. H.; Drake, T.; Barbic, M.; Scherer, A.; Roukes, M. L. *Appl. Phys. Lett.* **2003**, 83, 1240.
387. Jana, N. R.; Gearhart, L.; Murphy, C. J. *Adv. Mater.* **2001**, 13, 1389.
388. Jana, N. R.; Gearhart, L.; Murphy, C. J. *J. Phys. Chem. B* **2001**, 105, 4065.
389. Jana, N. R.; Gearhart, L.; Murphy, C. J. *Chem. Commun.* **2001**, 617.
390. Jana, N. R.; Gearhart, L.; Murphy, C. J. *Chem. Mater.* **2001,** 13, 2313.
391. Gai, P. L.; Harmer, M. A. *Nano Lett.* **2002**, 2, 771.

392. Xu, C.; Varghese, L.; Irudayaraj, J. *Langmuir* **2007**, 23, 9114.
393. Sun, Y.; Gates, B.; Mayers, B.; Xia, Y. *Nano Lett.* **2002**, 2, 165.
394. Sun, Y.; Xia, Y. *Adv. Mater.* **2002**, 14, 833.
395. Shen, Z.; Yamada, M.; Miyake, M. *Chem. Commun.* **2007**, 245.
396. Lee, E. P.; Peng, Z.; Cate, D. M.; Yang, H.; Campbell, C. T.; Xia, Y. *J. Am. Chem. Soc.* **2007**, 129, 10634.
397. Wroblowa, H.; Pan, Y. C.; Razumney, J. *J. Electroanal. Chem.* **1976**, 69, 1465.
398. Lee, J.-W.; Popov, B. N. *J. Solid State Electrochem.* **2007**, 11, 1355.
399. Garcıa-Contreras, M. A.; Fernandez-Valverde, S. M.; Vargas-Garcıa, J. R. *J. Alloys Compd.* **2007**, 434-435, 522.
400. Gong, K.; Du, F.; Xia, Z.; Durstock, M.; Dai, L. *Science* **2009**, 323, 760.
401. Waszczuk, P.; Barnard, T. M.; Rice, C.; Masel, R. I.; Wieckowski, A. *Electrochem. Commun.* **2002**, 4, 599.
402. Murphy, C. J.; Gole, A. M.; Hunyadi, S. E.; Stone, J. W.; Sisco, P. N.; Alkilany, A.; Kinard, B. E.; Hankins, P. *Chem. Commun.* **2008**, 544.
403. Chattopadhyay, S.; Shi, S. C.; Lan, Z. H.; Chen, C. F.; Chen, K.-H.; Chen, L.-C. *J. Am. Chem. Soc.* **2005**, 127, 2821.
404. Rex, M.; Hernandez, F. E.; Campiglia, A. D. *Anal. Chem.* **2006**, 78, (445-451).
405. Chen, Z.; Waje, M.; Li, W.; Yan, Y. *Angew. Chem. Int. Ed.* **2007**, 46, 4060.
406. Cepak, V. M.; Martin, C. R. *J. Phys. Chem. B* **1998**, 102, 9985.
407. Zhao, Y.; Guo, Y.-G.; Zhang, Y.-L.; Jiao, K. *Phys. Chem. Chem. Phys.* **2004**, 6, 1766.
408. Liz-Marzán, L. M. *Langmuir* **2006**, 22, 32.
409. Garrell, R. L.; Schultz, R. H. *J. Colloid Interface Sci.* **1985**, 105, 483.
410. Antonietti, M.; Thunemann, A.; Wenz, E. *Colloid Polym. Sci.* **1996**, 274, 795.
411. Wang, W.; Efrima, S.; Regev, O. *Langmuir* **1998**, 14, 602.
412. Satoh, N.; Hasegawa, H.; Tsujii, K.; Kimura, K. *J. Phys. Chem.* **1994**, 98, 2143.
413. Fu, X.; Wang, Y.; Wu, N.; Gui, L.; Tang, Y. *J. Mater. Chem.* **2003**, 13, 1192.
414. Sun, S.; Jaouen, F.; Dodelet, J.-P. *AdV. Mater.* **2008**, 20, 3900.
415. Mayrhofer, K. J. J.; Strmcnik, D.; Blizanac, B. B.; Stamenkovic, V.; Arenz, M.; Markovic, N. M. *Electrochimica Acta* **2008**, 53, 3181.
416. Takasu, Y.; Ohashi, N.; Zhang, X. G.; Murakami, Y.; Minagawa, H.; Sato, S.; Yahikozawa, K. *Electrochimica Acta* **1996**, 41, 2595.
417. Zhang, J. L.; Vukmirovic, M. B.; Xu, Y.; Mavrikakis, M.; Adzic, R. R. *Angew. Chem. Intl. Ed.* **2005**, 44, 2132.
418. Wang, J. X.; Zhang, J.; Adzic, R. R. *J. Phys. Chem. A* **2007**, 111, 12702.
419. Adzic, R. R.; Strbac, S.; Anastasijevic, N. *Mater. Chem. Phys.* **1989,** 22, 349-375.
420. Alivisatos, P. *Nat. Biotechnol.* **2004**, 22, 47.
421. Parak, W. J.; Gerion, D.; Pellegrino, T.; Zanchet, D.; Micheel, C. *Nanotechnology* **2003**, 14, R15.
422. Michalet, X.; Pinaud, F.; Lacoste, T. D.; Dahan, M.; Bruchez, M. *Single Mol.* **2001**, 2, 261.
423. Sutherland, A. J. *Curr. Opin. Solid State Mater. Sci.* **2002**, 6, 365.
424. Chan, W. C. W.; Maxwell, D. J.; Gao, X.; Bailey, R. E.; Han, M.; Nie, S. *Curr. Opin. Biotechnol.* **2002**, 13, 40.

425. Bruchez, M.; Moronne, M.; Gin, P.; Weiss, S.; Alivisatos, A. P. *Science* **1998**, 281, 2013.
426. Gao, X.; Nie, S. *Trends Biotechnol.* **2003**, 21, 371.
427. Larson, D. R.; Zipfel, W. R.; Williams, R. M.; Clark, S. W.; P., B. M. *Science* **2003**, 300, 1434.
428. Gao, X.; Cui, Y.; Levenson, R. M.; Chung, L. W. K.; Nie, S. *Nat. Biotechnol.* **2004**, 22, 969.
429. Lounis, B.; Bechtel, H. A.; Gerion, D.; Alivisatos, A. P.; Moerner, W. E. *Chem. Phys. Lett.* **2000**, 329, 399.
430. Dahan, M.; Laurence, T.; Pinaud, F.; S., C. D.; P., A. A. *Opt. Lett.* **2001**, 26, 825.
431. Neveu, S.; Bee, A.; Robineau, M.; Talbot, D. *J. Colloid Interface Sci.* **2002**, 255, 293.
432. Grasset, F.; Labhsetwar, N.; Li, D.; Park, D. C.; Saito, N.; Haneda, H.; Cador, O.; Roisnel, T.; Mornet, S.; Duguet, E.; Portier, J.; Etourneau, J. *Langmuir* **2002**, 18, 8209.
433. Sun, S.; Zeng, H. *J. Am. Chem. Soc.* **2002**, 124, 8204.
434. Park, S.-J.; Kim, S.; Lee, S.; Khim, Z.; Char, K.; Hyeon, T. *J. Am. Chem. Soc.* **2000**, 122, 8581.
435. Puntes, V. F.; Krishan, K. M.; Alivisatos, A. P. *Science* **2001**, 291, 2115.
436. Chen, Q.; Rondinon, A. J.; Chakoumakos, B. C.; Zhang, Z. J. *J. Magn. Magn. Mater.* **1999**, 194, 1.
437. Park, J.; An, K.; Hwang, Y.; Park, J.-G.; Noh, H.-J.; Kim, J.-Y.; Park, J.-H.; Hwang, N.-M.; Hyeon, T. *Nat. Mater.* **2004**, 3, 891.
438. Sun, S.; Murray, C. B.; Weller, D.; Folks, L.; Moser, A. *Science* **2000**, 287, 1989.
439. Shevchenko, E. V.; Talapin, D. V.; Rogach, A. L.; Kornowski, A.; Haase, M.; Weller, H. *J. Am. Chem. Soc.* **2002**, 124, 11480.
440. Xu, C.; Xu, K.; Gu, H.; Zheng, R.; Liu, H.; Zhang, X.; Guo, Z.; Xu, B. *J. Am. Chem. Soc.* **2004**, 126, 9938.
441. J.Widder, K.; Senyei, A. E.; Scarpelli, D. G. *Proc. Soc. Exp. Biol. Med.* **1978**, 58, 141.
442. Berry, C. C.; Curtis, A. S. G. *J. Phys. D* **2003**, 36, R198.
443. Mornet, S.; Vasseur, S.; Grasset, F.; Duguet, E. *J. Mater. Chem.* **2004**, 14, 2116.
444. Hiergeist, R.; Andra, W.; Buske, N.; Hergt, R.; Hilger, I.; Richter, U.; Kaiser, W. *J. Magn. Magn. Mater.* **1999**, 201, 420.
445. Brown, M. A.; Semelka, R. C., *MRI: Basic Principles and Applications.* Wiley-Liss: New York, **2003**.
446. Na, H. B.; Song, I. C.; Hyeon, T. *Adv. Mater,* **2009**, 21, 1.
447. Lee, S. B.; Mitcell, D. T.; Trofin, L.; Nevanen, T. K.; Soderlund, H.; Martin, C. R. *Science* **2002**, 296, 2198.
448. Fan, R.; Wu, Y.; Li, D.; Yue, M.; Majumdar, A.; Yang, P. *J. Am. Chem. Soc.* **2003**, 125, 5254.
449. Son, S. J.; Reichel, J.; He, B.; Schuchman, M.; Lee, S. B. *J. Am. Chem. Soc.* **2005**, 127, 7316.
450. Mitchell, D. T.; Lee, S. B.; Trofin, L.; Li, N.; Nevanen, T. K.; Soderlund, H.; Martin, C. R. *J. Am. Chem. Soc.* **2002**, 124, 11864.
451. Chang, T. M. S.; Prakash, S. *Mol. Biotechnol.* **2001**, 17, 249.
452. Nam, J.-M.; Thaxton, C. S.; Mirkin, C. A. *Science* **2003**, 301, 1884.

453. Langer, R. *Science* **2001**, 293, 58.
454. Michalet, X.; Pinaud, F. F.; Bentolila, L. A.; Tsay, J. M.; Doose, S.; Li, J. J.; Sundaresan, G.; Wu, A. M.; Gambhir, S. S.; Weiss, S. *Science* **2005**, 307, 538.
455. Park, S. A.; Taton, T. A.; Mirkin, C. A. *Science* **2002**, 295, 1503.
456. Tiefenauer, L. X.; Kuehne, G.; Andres, R. Y. *Bioconjugate Chem.* **1993**, 4, 347.
457. Hyeon, T.; Lee, S. S.; Park, J.; Chung, Y.; Na, H. B. *J. Am. Chem. Soc.* **2001**, 123, 12798.
458. Li, J. J.; Wang, Y. A.; Guo, W.; Keay, J. C.; Mishima, T. D.; Johnson, M. B.; Peng, X. J. *J. Am. Chem. Soc.* **2003**, 125, 12567.
459. Sun, S.; Murray, C. B.; Weller, D.; Folks, L.; Moser, A. *Science* **2000**, 287, 1989.
460. Pal, S.; Jagadeesan, D.; Gurunatha, K. L.; Eswaramoorthy, M.; Maji, T. K. *J. Mater. Chem.* **2008**, 18, 5448.
461. Lu, A.-H.; Salabas, E. L.; Schűth, F. *Angew. Chemie. Int. Ed.* **2007**, 46, 1222.
462. Zhang, M.; Bando, Y.; Wada, K. *J. Mater. Res.* **2001**, 16, 1408.
463. Okamaoto, K.; Shook, C. J.; Bivona, L.; Lee, S. B.; English, D. S. *Nano Lett.* **2004**, 4, 233.
464. Boatman, E. M.; Lisensky, G. C.; Nordell, K. J. *J. Chem. Edu.* **2005**, 82, 1697.
465. Park, J.; An, K.; Hwang, Y.; Park, J.-G.; Noh, H.-J.; Kim, J.-Y.; Park, J.-H.; Hwang, N.-M.; Hyeon, T. *Nature Mater.* **2004**, 3, 891.
466. Colorado, R.; Zeigler, S. Y.; Barron, A. R. *J. Mater. Chem.* **2008**, 18, 1911.
467. Zhai, T.; Gu, Z.; Dong, Y.; Zhong, H.; Ma, Y.; Fu, H.; Li, Y.; Yao, J. *J. Phys. Chem. C* **2007**, 111, 11604.
468. Wang, J.-X.; Wen, L.-X.; Wang, Z.-H.; Wang, M.; Shao, L.; Chen, J.-F. *Scr. Mater.* **2004**, 51, 1035.
469. Yu, W. W.; Qu, L.; Wenzhuo Guo; Peng, X. *Chem. Mater.* **2003**, 15, 2854.
470. Correa-Duarte, M. A.; Giersig, M.; Kotov, N. A.; Liz-Marzán, L. M. *Langmuir* **1998**, 14, 6430.
471. An, L.; Li, Z.; Wang, Z.; Zhang, J.; Yang, B. *Chem. Lett.* **2005**, 34, 652.
472. Liu, X.; Fang, Z.; Zhang, X.; Zhang, W.; Wei, X.; Geng, B. *Cryst. Growth Des.* **2009**, 9, 197.
473. Wang, Y. A.; Teng, X. W.; Wand, J. S.; Yang, H. *Nano Lett.* **2003**, 3, 789.
474. Yu, K.; Zaman, B.; Singh, S.; Wang, D.; Ripmeester, J. A. *Chem. Mater.* **2005**, 17, 2552.
475. Li, L.; Choo, E. S. G.; Liu, Z.; Ding, J.; Xue, J. *Chem. Phys. Lett.* **2008**, 461, 114.
476. Yi, D. K.; Selvan, S. T.; Lee, S. S.; Papaefthymiou, G. C.; Kundaliya, D.; Ying, J. Y. *J. Am. Chem. Soc.* **2005**, 127, 4990.
477. Chan, Y.; Zimmer, J. P.; Stroh, M.; Steckel, J. S.; Jain, R. K.; Bawendi, M. G. *Adv. Mater.* **2004**, 16, 2092.
478. Salgueirino-Maceira, V.; Correa-Duarte, M. A.; Spasova, M.; Liz-Marzan, L. M.; Farle, M. *Adv. Funct. Mater.* **2006**, 16, 509.
479. Lee, J.; Lee, Y.; Youn, J. K.; Na, H. R.; Yu, T.; Kim, H.; Lee, S.-M.; Koo, Y.-M.; Kwak, J. H.; Chang, H. N.; Hwang, M.; Park, J.-G.; Kim, J.; Hyeon, T. *Small* **2008**, 4, 143.
480. Wohlfarth, E. P. *J. Magn. Magn. Mater.* **1983**, 39, 39.
481. Hansen, M. F.; Morup, S. *J. Magn. Magn. Mater.* **1998**, 184, 262.
482. Petit, C.; Taleb, A.; Pileni, M.-P. *Adv. Mater.* **1998**, 10, 262.

483. Goya, G. F.; Berquot, T. S.; Fonseca, F. C.; Morales, M. P. *J. Appl. Phys.* **2003**, 94, 3520.
484. Balcells, L.; Iglesias, O.; Labarta, A. *Phys. Rev. B* **1997**, 55, 8940.
485. Si, S. K.; Mandal, T. K.; Gin, S.; Nakamura, H.; Kohara, T. *Chem. Mater.* **2004**, 16, 3489.
486. Arelaro, A. D.; Brandl, A. L.; Lima, E., Jr.; Grmarra, L. F.; Brito, G. E. S.; Pontuschka, W. M.; Goya, G. F. *J. Appl. Phys.* **2005**, 97, 10J316/1.
487. Wu, M.; Ma, Y.; Liu, Y.; Bi, H.; Fang, Q.; Niu, H.; Chem, Q. *Mater, Res. Bull.* **2008**, 43, 1321.